HYDRAULIC MECHANISMS OF CONCRETE-TIE RAIL SEAT DETERIORATION

BY

JOHN C. ZEMAN

THESIS

Submitted in partial fulfillment of the requirements
for the degree of Master of Science in Civil Engineering
in the Graduate College of the
University of Illinois at Urbana-Champaign, 2010

Urbana, Illinois

Advisers:

      Professor Christopher P.L. Barkan
      Lecturer J. Riley Edwards
      Professor David A. Lange

ABSTRACT

Rail seat deterioration (RSD) is considered the most critical problem with concrete-tie performance on North American freight railroads. RSD is the deterioration of the concrete underneath the rail that results in problems such as wide gauge, insufficient rail cant, and loss of fastening toe load. Currently, the problem is not sufficiently understood to enable development of effective solutions. The primary causes of RSD appear to be high stresses at the rail seat, a loosened fastening system, the presence of moisture, and the presence of abrasive fines. RSD is considered to have up to six potential mechanisms, and this research investigates three of them: hydraulic pressure cracking, hydro-abrasive erosion, and cavitation erosion. A laboratory test apparatus and procedure were devised to measure the surface water pressure in a laboratory rail seat using tie pads of differing material composition and surface geometry. To evaluate hydraulic pressure cracking, a model of the effective stress in a concrete-tie rail seat was developed to estimate the water pressures on the rail seat surface and whether they could lead to damaging pore pressures in the concrete. Comparing the effective stress model and the measured surface water pressures, hydraulic pressure cracking appears to be a feasible mechanism for RSD given the correct combination of high rail seat loads, sufficient moisture, and a tie pad surface that develops high pressure. The measured surface water pressures were used to estimate the potential water velocity. By comparing these estimates with critical velocities for concrete erosion, it appears feasible that hydro-abrasive erosion contributes to RSD. The uplift action of the rail was simulated in the test apparatus, and the resulting suction was at or near the vapor pressure of water for most of the tie pads considered, suggesting that cavitation occurs in a concrete-tie rail seat. However, considering the size of the cavitation bubbles that could fit underneath the tie pad, and the observation that no high collapse pressures were measured, cavitation erosion is not a feasible mechanism for RSD. Mitigation options for preventing hydraulic pressure cracking are using a tie pad or pad assembly that does not seal water, reducing the occurrence of high impact loads, and using high-strength, air-entrained, low-permeability concrete. Care should be exercised when using pads that do not seal water, as this could contribute to hydro-abrasive erosion or abrasion.

to Katie,

for all the miles you travelled,

and for standing by my side

ACKNOWLEDGMENTS

TABLE OF CONTENTS

CHAPTER 1: INTRODUCTION

1.1   Concrete Tie Functions and Components

Ballasted track provides support and stability for train traffic by properly distributing the loads

and maintaining the required track geometry. The role of concrete ties in this system is to support the

rails under load, distribute the stresses at the rail seat to acceptable levels for the ballast layer, and, along

with the ballast and subgrade, maintain proper geometry of the track structure. Because of their poor

dielectric qualities, concrete ties require an insulator in the fastening system to electrically isolate the rails

if a track circuit-based system of traffic control is used.

Concrete ties are prestressed, precast beams (Figure 1.1). The rail seats are locations on the tie

that bear the rails. The system that fastens the rail to the tie commonly consists of a thermoplastic pad or

pad assembly between the concrete rail seat and the base of the rail, cast-in, steel-shoulder inserts, spring

clips attached to the shoulder inserts that hold the rail, and plastic insulators between the clips/shoulders

and the rail.
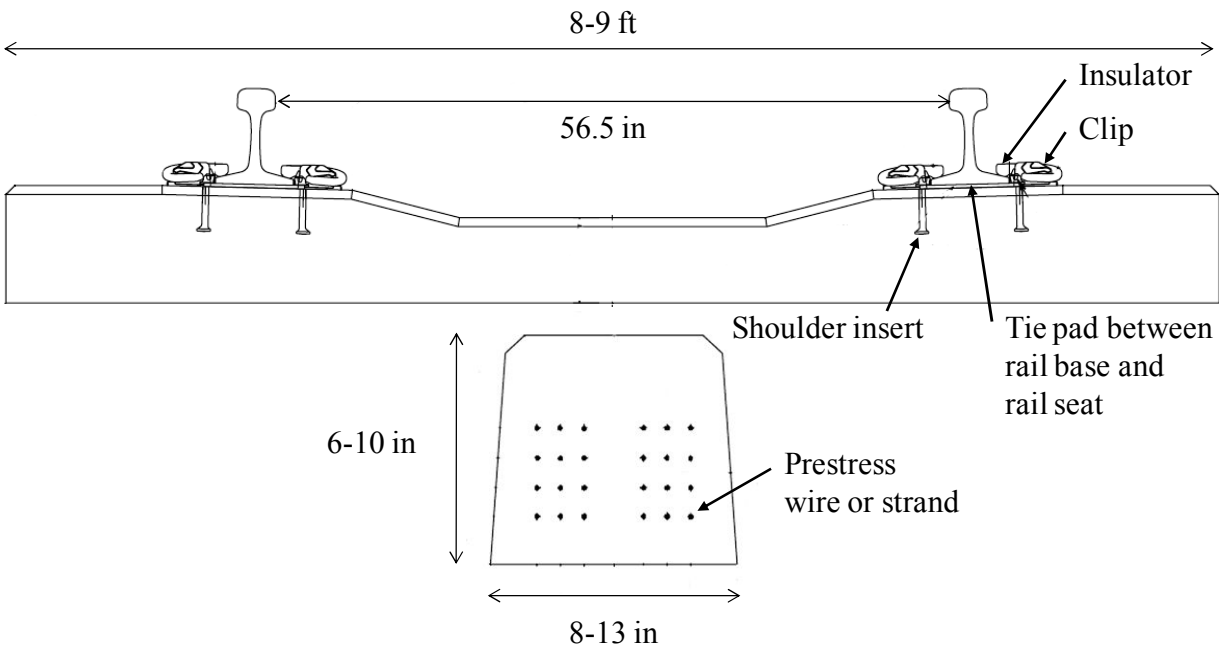
Figure 1.1 Typical prestressed concrete tie today (adapted from Amtrak 2006)

1.2   Background on Concrete Ties in North America

Ballasted timber-tie track is the most commonly used track structure in North America (Judge 2003). However, early US railroads used stone "sleepers" instead of timber ties, and the American Railway Engineering Association (AREA) proceedings include articles from as early as 1910 on "substitute ties." These substitute ties were creative solutions offered by engineers and entrepreneurs as an alternative to the standard timber ties, and they included a varied assortment of designs using concrete, steel, and wood materials. The motivation for pursuing different tie materials was to take advantage of their respective strengths – concrete's compressive strength and durability, steel's flexural strength and ductility, and wood's pliability and compatibility with cut spikes. In addition, the new designs were an attempt to avoid the weaknesses of each material – the brittleness of concrete, steel's tendency to corrode, and wood's problems with rot and decay. Multiple substitute-tie designs were tested in track but none gained widespread acceptance or extended use (Figures 1.2 through 1.6).
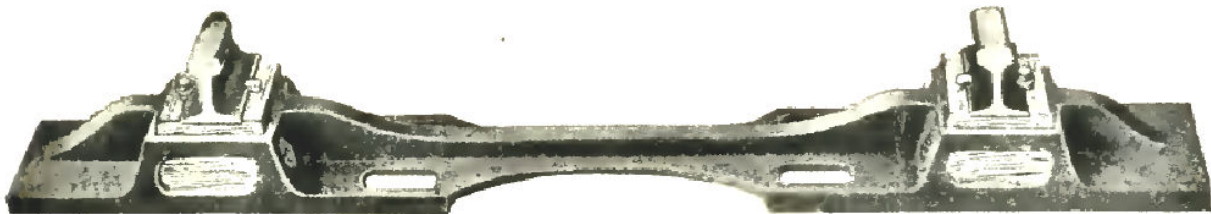
Figure 1.2 Metal Tie Company ties installed on a test section on the B&O Railroad, with a steel frame and wooden blocks pressure-fitted as rail seats (AREA 1910)
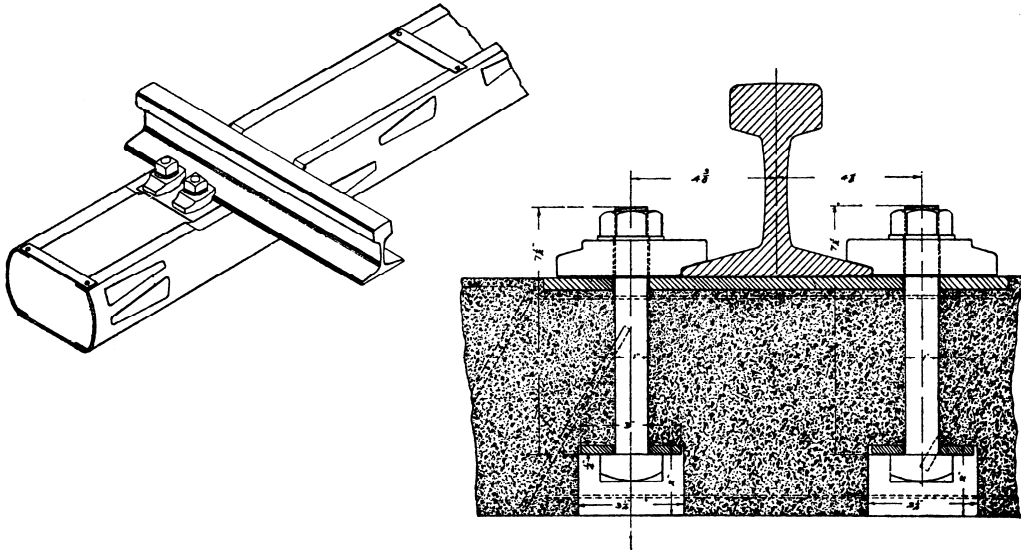
Figure 1.3 Kimball Concrete-filled Tie, installed on the Chicago and Alton Railroad (AREA 1910)
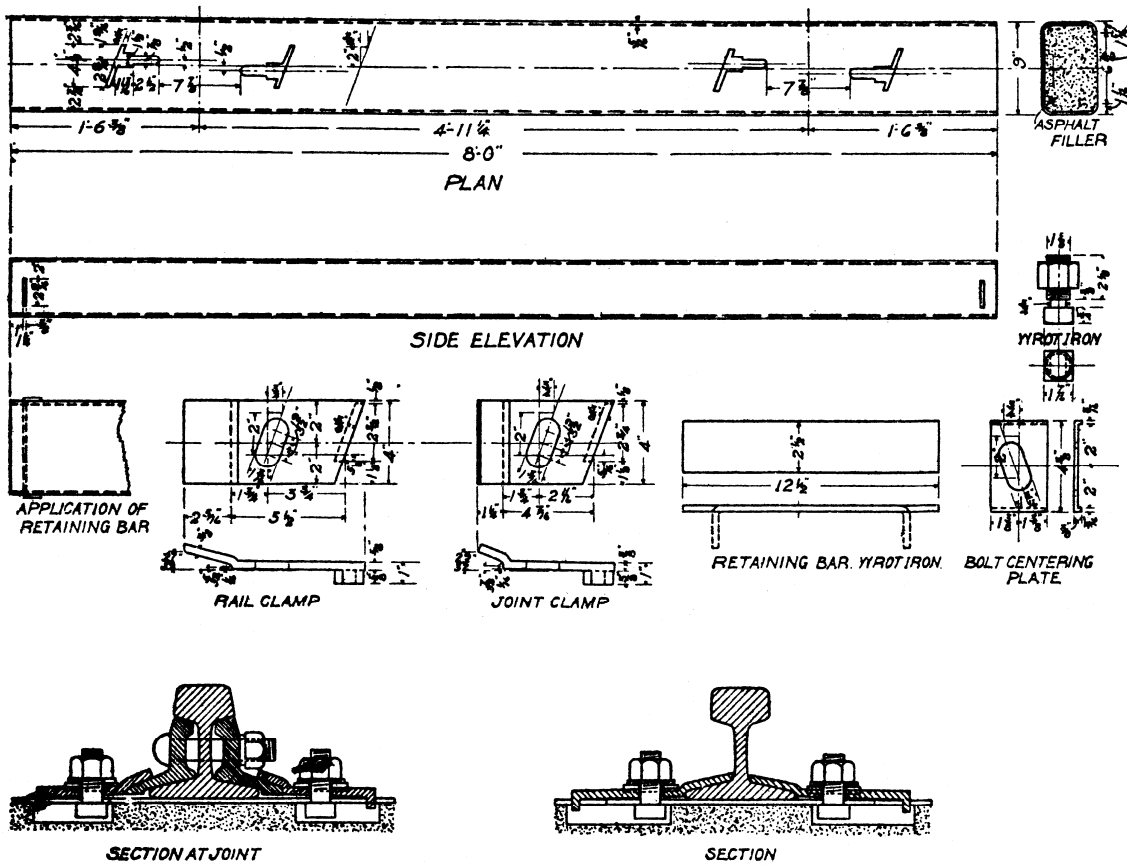
Figure 1.4 Snyder Steel Tie with asphalt and stone filler, installed on the Pennsylvania Railroad; the asphalt tended to deteriorate over time (AREA 1912)
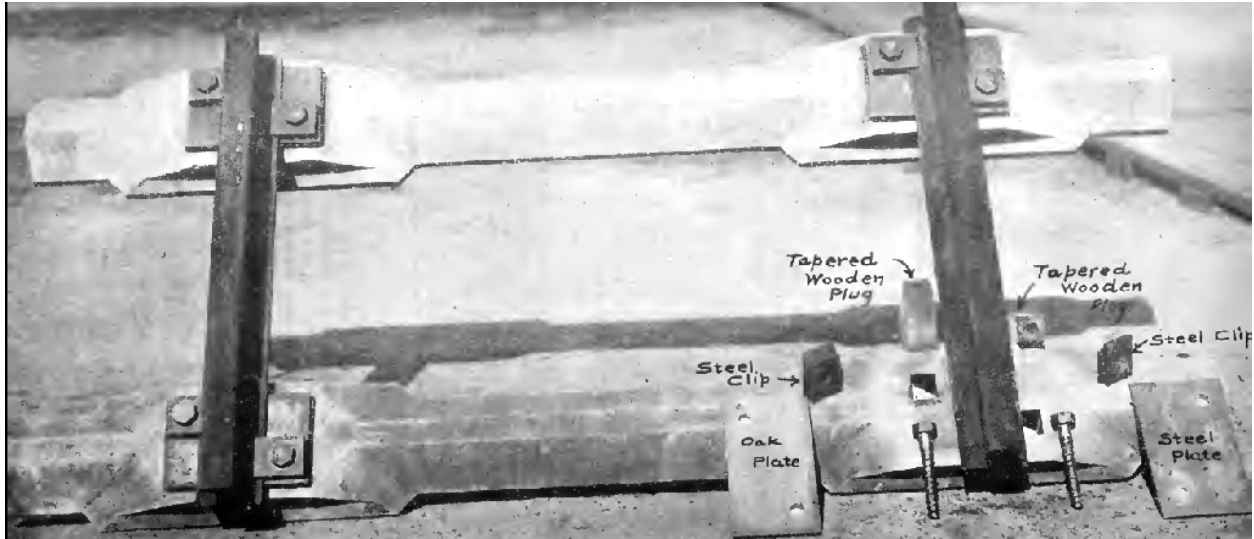
Figure 1.5 Reinforced concrete tie with steel and wood plates at the rail seat, installed on the Pittsburgh & Lake Erie Railroad (AREA 1912)
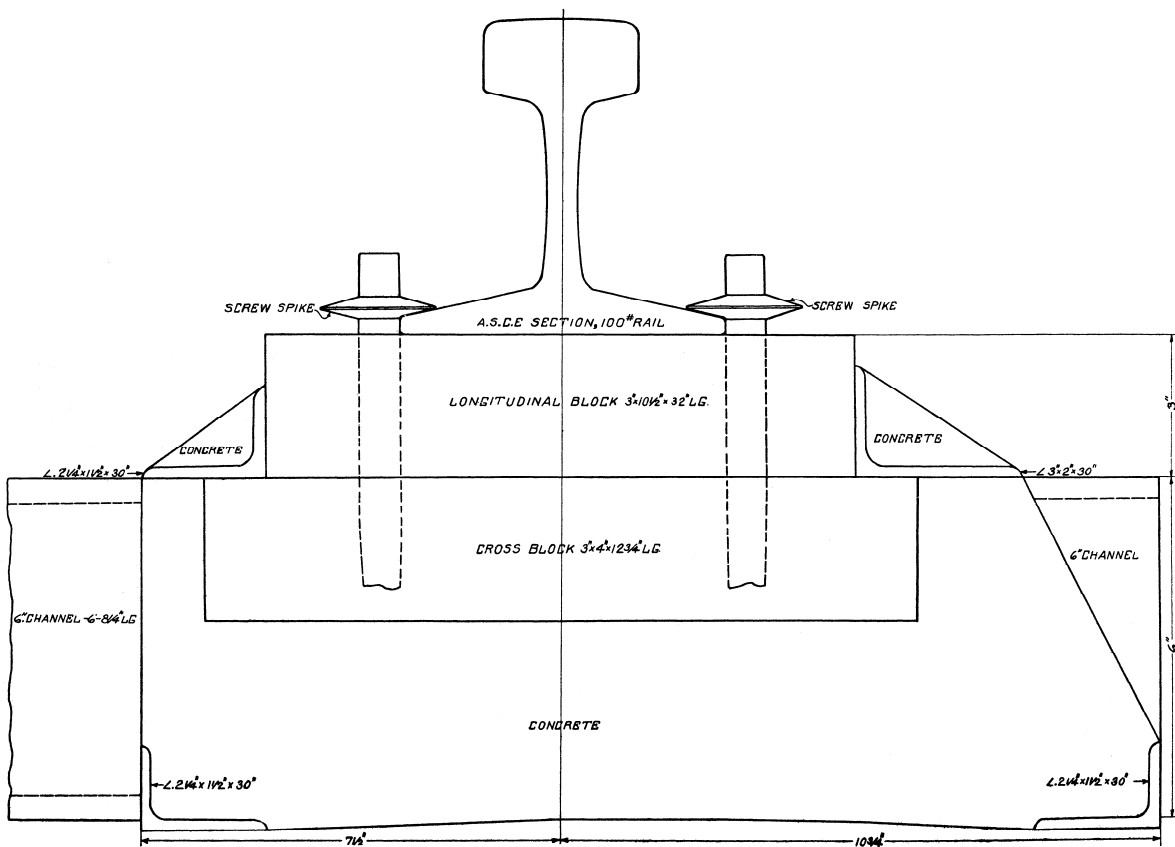
Figure 1.6 The International Steel Tie, a combination of steel frame, concrete filler, and wood rail seat, in the form of a ladder track, installed on the Pittsburgh & Lake Erie Railroad (AREA 1912)

A list of the common problems with substitute ties, compiled by the AREA in 1923, reveals problems similar, in some respects, to what would be listed today:

- Insufficient corrosion resistance
- Failure of fastenings or insulating materials
- Lower flexural strength at the location of the shoulder inserts due to the reduced sections
- Stress concentrations at sharp angles or square holes
- Low resistance to derailment damage
- Tie dimensions not compatible with tamping or other maintenance practices
- Difficult to maintain proper track alignment
- Flexural failure on non-uniform substructure support, abrasion of concrete by ballast
- Incompatible expansion and contraction of different materials in composite ties (AREA 1923)

By 1940, a number of test sites had been constructed and evaluated. The AREA summarized all the tests with the following statement:

> Practically all of the substitutes for wood ties in the original 193 installations reported have now been removed from track. Their performance generally was not satisfactory and their service life did not justify the extra cost over that of wood ties; however, it is felt that with the experience gained from the tests and the use of new materials developed within the last several years, satisfactory substitutes for wood railroad cross ties can be produced (AREA 1947).

When the previous statement was published, the primary motivation for pursuing substitute ties was to find a form of track support that would not have the durability problems of rot and decay experienced with timber ties. However, during the same period that the substitute ties were being developed and tested, great advancements were being made with timber ties, such as the introduction of creosote and other chemical treatments, as well as pressure-treatment techniques that made the chemical treatments more effective at preventing rot and decay (AREA 1954).

The combination of creosote and pressure-treatment changed the life-cycle economics of timber ties compared to substitute ties, improving wood's durability and making timber ties more economical given the abundant supply of timber in North America. This removed much of the motivation for pursuing innovative substitute-tie designs. In 1954, the AREA tie committee reported that "the necessity

5

for a substitute for wood ties is less urgent now than at any time for many years…the subject [should] be carried in a dormant state…until something of interest…develops…" (AREA 1954).

Prestressed concrete ties were first introduced in Europe in the early 1940's, motivated by constraints in timber supplies that became acute during World War II. Much of Europe continues to use prestressed concrete-tie track or slab track (Magee and Ruble 1960, White 1984). Encouraged by the success of prestressed concrete ties in Europe, the Association of American Railroads (AAR) developed three prototype tie designs based on a review of European practices (AREA 1960). These ties were referred to as A, B, and C and were tested in the laboratory under North American loads. The results were used to develop tie designs D and E. The AAR model E (also referred to as "MR" in honor of Magee and Ruble who developed the design, Figure 1.7) was first installed in track in test sections on the Atlantic Coast Line and the Seaboard Air Line railroads in 1960 (AREA 1960).

PRESTRESSED CONCRETE CROSSTIE
AAR DESIGN
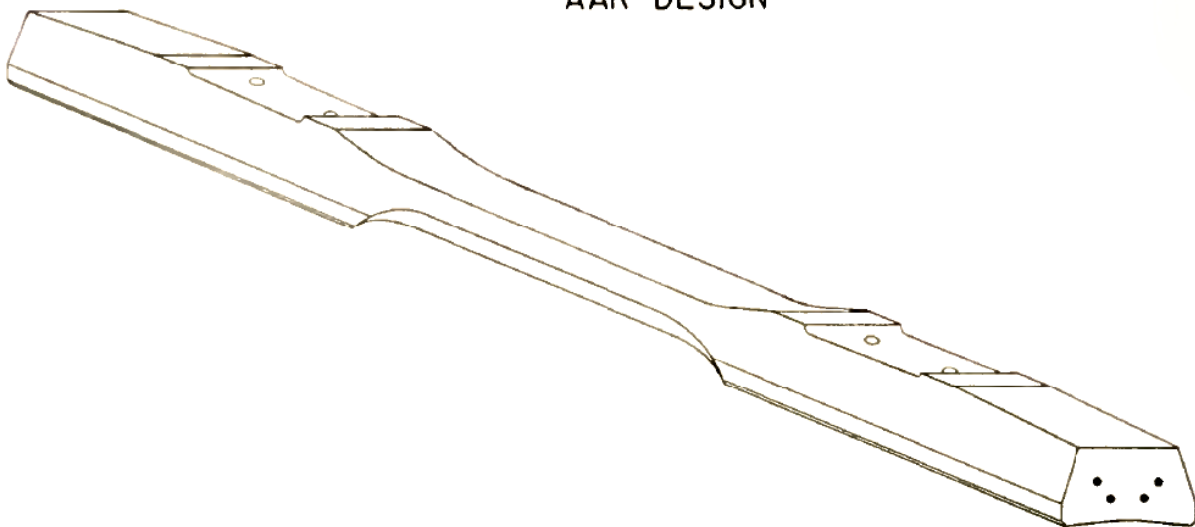
Figure 1.7 AAR Type E Concrete Tie (Magee 1966)

In 1962, the St. Louis-San Francisco (Frisco) Railway installed prestressed concrete ties at 30-inch (in) centers on a half-mile section of track with annual traffic of 15 million gross tons (MGT), 70 mile-per-hour (mph) passenger traffic, 55 mph freight traffic, and 132-pound (lb) welded rail (Fort 1968).

6

They also installed a comparable half-mile section of new timber-tie track. One representative from the railroad was quoted saying, "As far as suitability is concerned, each type of tie has advantages and disadvantages, and we feel that their relative economy will always be questionable until the life span of prestressed concrete ties is established" (Fort 1968). The Frisco's biggest problem with the concrete ties was center binding. Included in the report was a comparison between prestressed concrete ties and timber ties (Table 1.1), and many of the relative advantages and disadvantages remain true today.

Table 1.1 Relative advantages of prestressed concrete ties and timber ties (Fort 1968)

Advantages of Prestressed Concrete Ties	Advantages of Timber Ties
Rapid mass-production is possible	History of satisfactory performance
Better quality control	More flexible
Uniform quality of ties	Easier to handle
Increased track modulus	Predictable service life
Higher resistance for electrical insulation*	Less damage in derailments
Higher fire resistance	Maintenance crews are experienced with them
Greater tie spacing, fewer ties per mile	Current equipment designed for timber ties

*later disproved, see Weber 1969 and White 1984

By 1965, about 400,000 prestressed concrete ties were in track – of which, about 290,000 were on mainline tracks. The Florida East Coast Railroad installed 74,000 ties on its mainline between Jacksonville and Miami. Norfolk Southern installed 70,888 ties on an extension of its line near Marsden, North Carolina. The Baltimore & Ohio installed 18,000 near Lafferty, Ohio (Magee 1966). Magee, one of the developers of the AAR concrete tie, reported to the AREA in 1960: "We feel that we have solved most of the structural difficulties with the ties during this five-year service period but we still have the question of the service life of the ties" (AREA 1960). Early estimates placed the expected service life of concrete ties at 50 years (AREA 1962).

In North America today, concrete ties are used on freight lines with substantial annual tonnage, curvature, and heavy axle loads. A convention used by one Class I railroad in the past was that concrete ties are most economical for curves sharper than two degrees with annual tonnage greater than 20 MGT. Concrete ties are typically heavier than timber ties and can be spaced at greater intervals, typically around 24 inches compared to 20 inches for wood, depending on the location in track and the tie design (White 1984). The use of concrete ties on freight lines is uncommon in Canada, and they are seldom used in the eastern US. The exception is the Florida East Coast Railroad, which is mostly concrete-tie track, and certain locations on CSX Transportation's network. Currently, concrete ties are used more extensively on western railroad mainlines where tonnage, curvature, and axle load are such that concrete ties are most economical. Concrete ties account for approximately five percent of the ties in track in North America. By contrast, many other countries in the world use concrete ties as their primary form of track support and restraint (Judge 2003). Although concrete ties represent a small percentage of the ties in North America, they are used in some of the most demanding conditions in terms of track geometry and traffic volume.

Tests of concrete-tie track in revenue service and at the AAR's Facility for Accelerated Service Testing (FAST) in Pueblo, Colorado suggested that concrete ties with elastic fasteners provide much greater and more uniform rail restraint than timber ties with cut spikes. With a good ballast layer, the concrete ties held surface and alignment well. AAR researchers found higher center-binding strains on concrete ties under heavy axle loads (HAL) but nothing beyond its first cracking strain. No axle-load-related problems were identified in concrete ties at FAST after 1,300 MGT of HAL (Jimenez and LoPresti 2004).

1.3   Development of the Concrete Tie Part of the AREMA Manual's Tie Chapter

The American Railway Engineering and Maintenance-of-way Association (AREMA) Manual for Railway Engineering provides a set of industry-recommended best practices for concrete-tie design, manufacture, and installation. Chapter 30 of the Manual pertains to ties, and Part 4 focuses on concrete ties, primarily prestressed concrete ties. Each railroad that uses concrete ties has its own internal standards that are generally variations of the practices described in Chapter 30, Part 4 of the AREMA Manual.

In 1976, the original recommendations for concrete ties were published in Chapter 10 of the AREA Manual. The AREA merged with other railroad industry associations to form AREMA in 1997. When AREMA was formed, Committee 3 – Ties and Wood Preservatives and Committee 10 – Concrete Ties merged to form Committee 30 – Ties, and, in turn, Chapters 3 and 10 were combined in Chapter 30. In the following sections, I discuss the development of the current recommendations in the concrete-tie portion of the AREMA Manual, what assumptions were used, and how some of the design values were chosen.

1.3.1   Allowable Ballast Pressure

Part 4 of AREMA Chapter 30 has been using the same ballast pressure equation since 1976. It assumes uniform support and bearing area (A) underneath the tie, using an impact factor (IF) and a load distribution factor (DF) to amplify the static wheel load (P) (AREMA 2009):

$$\text{Average Ballast Pressure} = \frac{2P\left(1 + \dfrac{IF}{100}\right)\left(\dfrac{DF}{100}\right)}{A}$$

When this equation was first recommended, AREA Committee 10 stated that the calculated value of average ballast pressure may underestimate the maximum ballast pressure. This is because the maximum pressure typically occurs "several inches" below the bottom of the tie. AREA Committee 10 placed the allowable ballast pressure at 85 pounds per square inch (psi) for "high-quality, abrasion-resistant ballast.

If lower quality ballast materials are used, the ballast pressure should be reduced accordingly" (AREA 1975).

The concrete-tie chapter formerly included minimum specifications for the quality of ballast that should be used with concrete-tie track, but that now appears in Chapter 1 – Roadway and Ballast (AREA 1976). AREA Committee 10 worked on ballast recommendations until the mid-1980's when it determined that AREA Committee 1 – Roadway and Ballast had a similar section in its chapter (AREA 1988).

In recent concrete tie subcommittee meetings, it has been suggested that the ballast pressure calculation should include the speed and tonnage factors, used for flexural design, so that traffic conditions beyond the maximum axle load can be considered. If the ballast pressure calculation is multiplied by the speed and tonnage factors, then the ballast pressure may decrease by as much as 51% or it may increase by as much as 32%, depending on the speed and tonnage conditions (AREMA 2009).

1.3.2   Impact Factor

In the 1976 version of Chapter 10, the impact factor was 2.5 (150% increase) (AREA 1975), compared with the current 3.0 (200% increase) (AREMA 2009). The current impact factor was introduced in 1988 (AREA 1988). According to Jeff McQueen – a long-time Committee 10 and 30 member who contributed extensively to the development of concrete ties in North America – the original impact factor was 50% and then was increased to 100%, 150%, and eventually to 200% as a result of decades of experience with concrete ties in service. Within five years of installing concrete ties designed with a lower impact factor, cracks due to positive bending moments at the rail seat would appear. This encouraged the committee to increase the impact factor and make other design values more conservative. This type of iteration occurred several times (McQueen 2006).

1.3.3   Load Distribution Factor

AREA Committee 10 recognized that other factors such as rail stiffness, ballast and subgrade modulus, and axle spacing influence the distribution of loads to adjacent ties. For a simple, conservative estimate of load distribution, Committee 10 increased Talbot's relationship for percent-of-axle-load per

tie versus tie spacing for eight-foot (ft) long timber ties (AREA 1920) by ten percent to account for the extra weight of concrete ties for the 1976 chapter. The resulting line for distribution factor versus tie spacing is defined by (20 in, 45%) and (30 in, 60%) (AREA 1975) (Figure 1.8). The 2009 Manual has a nearly identical line defined by (19 in, 42.5%) and (31 in, 61%) (AREMA 2009) (Figure 1.8). Comparing the two lines, it is evident that the current load distribution factor was based on a ten-percent increase from Talbot's derivation for timber ties, with the weight of concrete ties circa 1976 in mind. The line was modified slightly in 1988, but it was still nearly identical to the current line (AREA 1988, AREMA 2009).
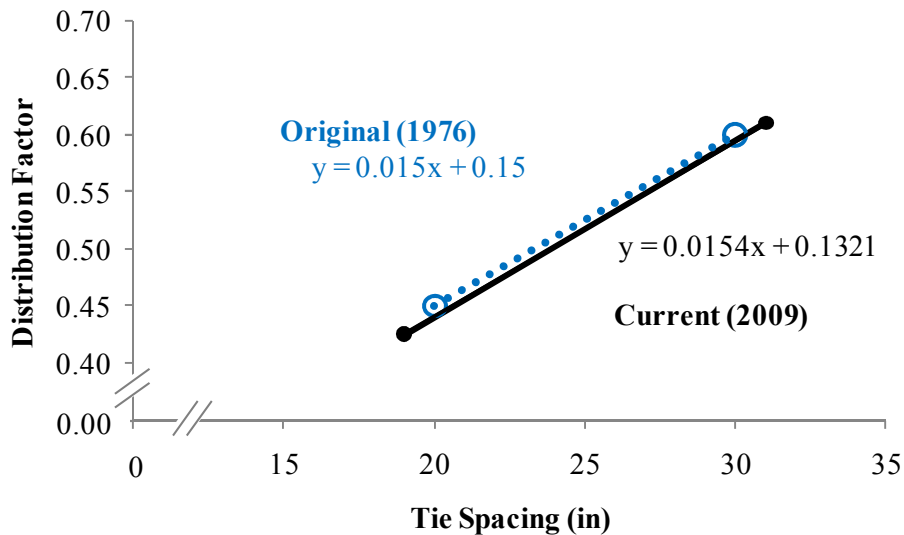
Figure 1.8 Comparison of the original and current axle load distribution factors as a function of tie spacing (AREA 1975, AREMA 2009)

1.3.4   Bending Moments

An important section of Part 4 of Chapter 30 in the current AREMA Manual is the recommendation for the required flexural capacity of the tie. Typically, the critical moments for design are the rail seat positive and center negative moments. The original AREA (1975) required values for the flexural strength of ties are presented in Table 1.2.

Table 1.2 1976 Required flexural capacity of monoblock concrete ties
(AREA 1975)

Length (ft)	Spacing (in)	Required flexural capacity (k-in) without cracking			
		Rail Seat +	Rail Seat -	Center -	Center +
8.00	21	220	115	200	90
	24	220	115	220	90
	27	220	115	240	90
	30	220	115	260	90
8.25	21	225	115	200	90
	24	235	115	210	90
	27	250	115	220	95
	30	260	115	230	100
8.50	21	225	115	200	90
	24	250	115	200	90
	27	275	115	200	100
	30	300	115	200	110
8.75	21	250	115	200	95
	24	275	115	200	100
	27	300	115	200	110
	30	325	115	200	120
9.00	21	275	115	200	100
	24	300	115	200	105
	27	325	115	200	115
	30	350	115	200	125

According to AREA Committee 10, the values in Table 1.2 came from an analysis of a beam on an elastic foundation, and the following disclaimer gives some insight into the committee members' assumptions and concerns:

> The values shown in the Rail seat (-) column are based on elastic foundations having an overall vertical upward spring rate in the range of 200,000 to 350,000 lb per inch. This spring rate is not necessarily linear and should be determined in the 0.00 to 0.02 inch deflection range. The Rail Seat (-) values may not be adequate for more rigid fastenings (AREA 1975).

The 2009 design moment procedure is different from the original in that it has a formula for calculating an unfactored moment based on tie spacing, tie length, design train speed, and annual traffic (in MGT). A quick comparison of the rail seat positive moments for three tie lengths and for tie spacing

from 21 to 30 inches (Figure 1.9) reveals differences between the 1976 and 2009 manuals. The 2009

unfactored moments are always higher than the 1976 required moments, but the factors for speed and

tonnage that are applied in the 2009 method may result in a factored moment lower than the 1976

required moments. The factored moments are shown for comparison (Figures 1.10 through 1.13).
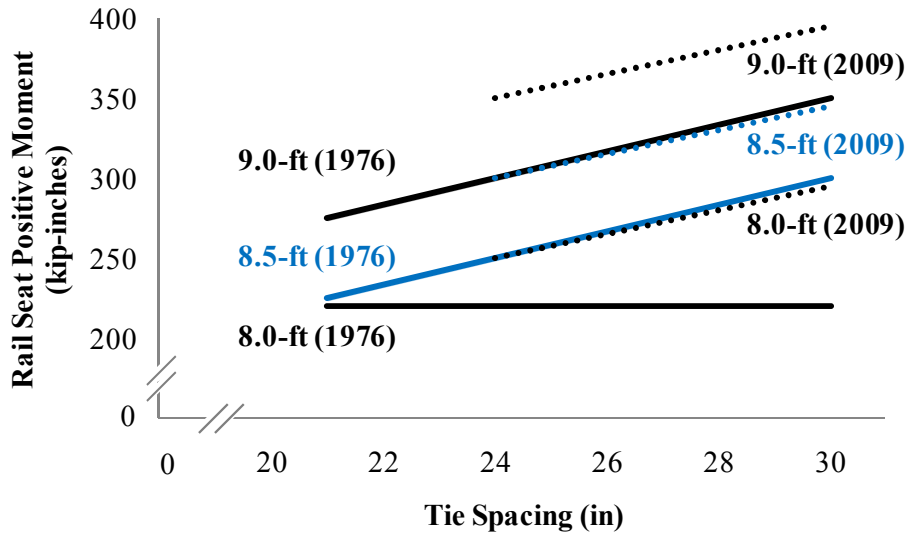
**Figure 1.9 Comparison of the 1976 required flexural capacity (solid lines) and the
2008 unfactored moments (dotted lines) for rail seat positive flexure
as a function of tie spacing (AREA 1975, AREMA 2009)**
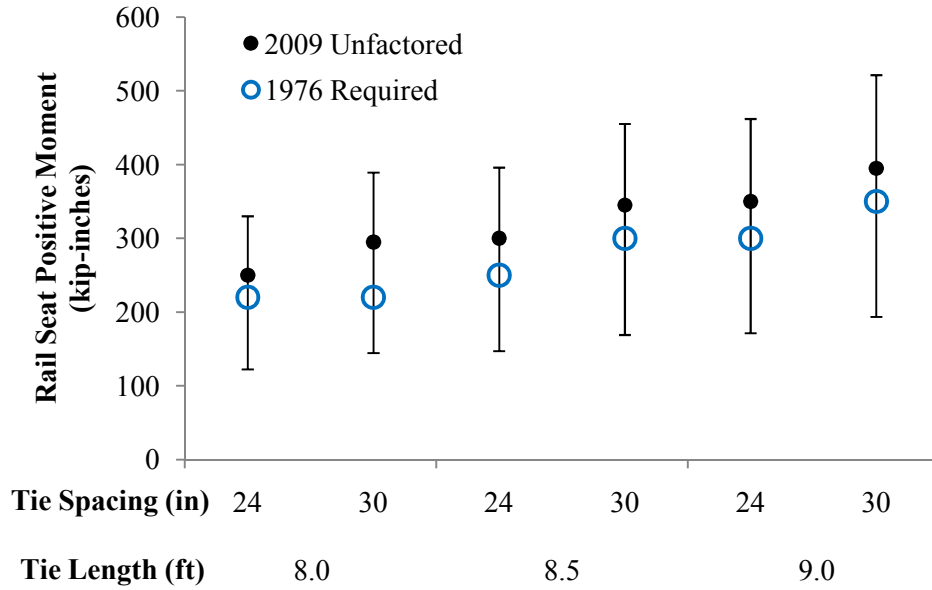
**Figure 1.10 Comparison of 1976 and 2009 requirements for
rail seat positive moment, including ranges for 2009 factored moments
(AREA 1975, AREMA 2009)**
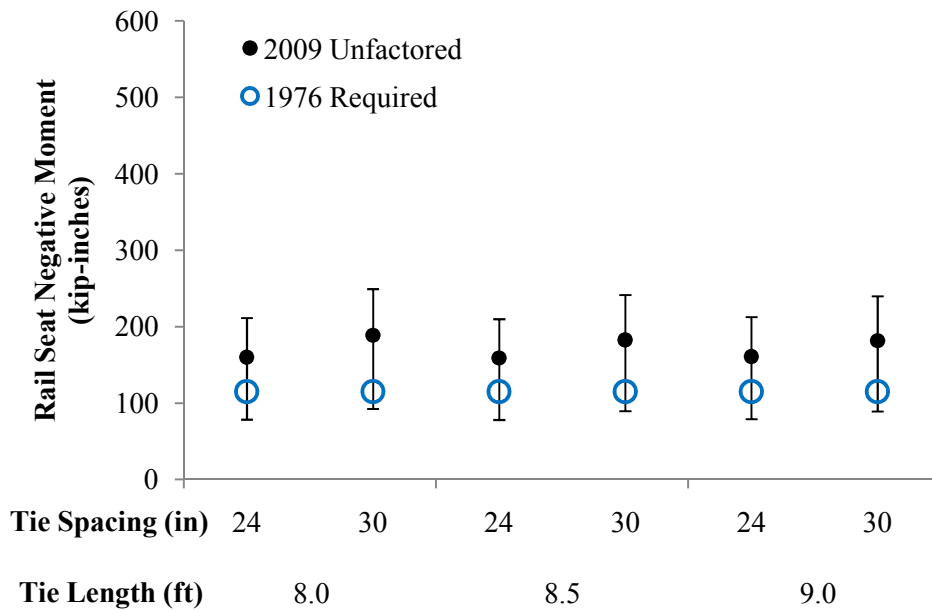
**Figure 1.11 Comparison of 1976 and 2009 requirements for
rail seat negative moment, including ranges for 2009 factored moments
(AREA 1975, AREMA 2009)**

14
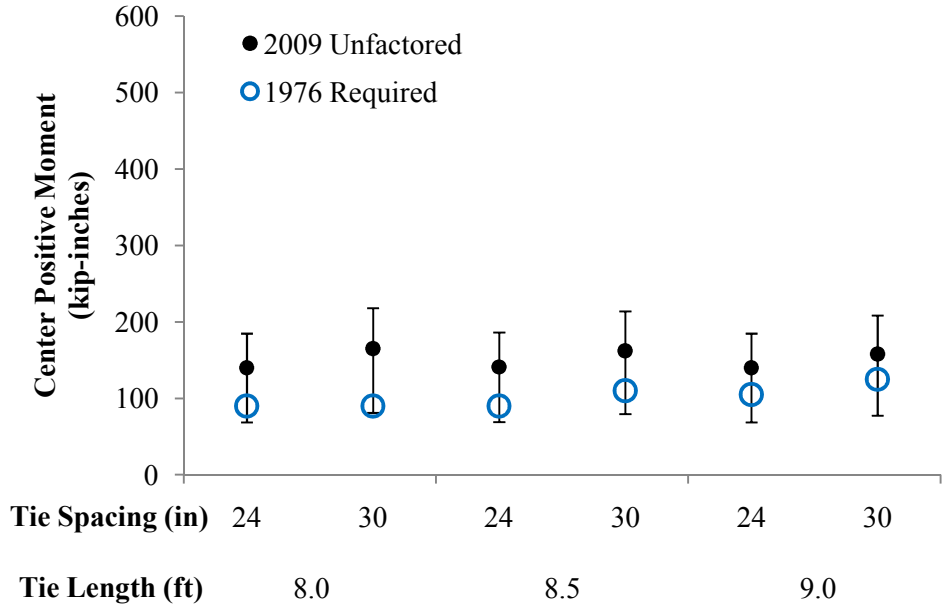
**Figure 1.12 Comparison of 1976 and 2009 requirements
for center positive moment, including ranges for 2009 factored moments
(AREA 1975, AREMA 2009)**
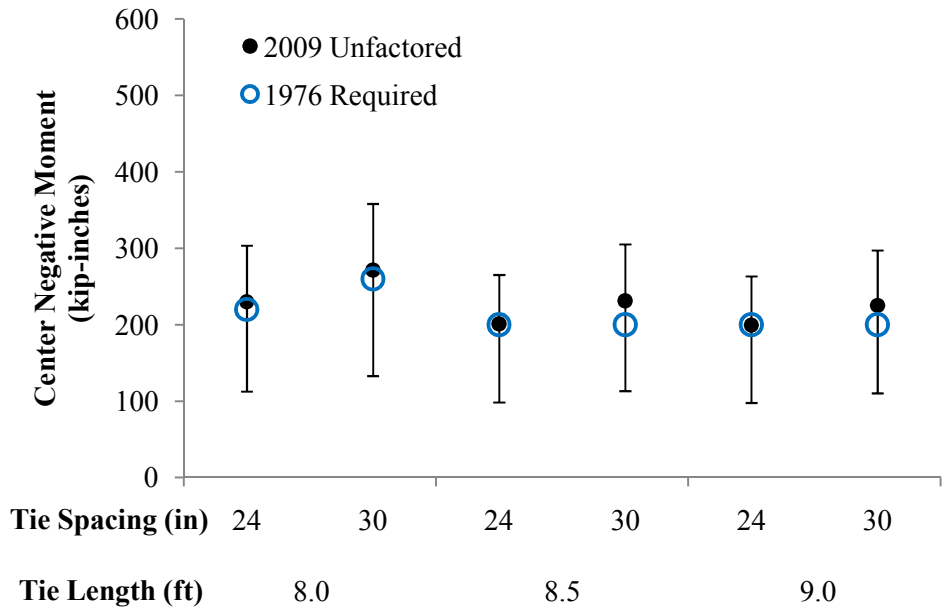
**Figure 1.13 Comparison of 1976 and 2009 requirements
for center negative moment, including ranges for 2009 factored moments
(AREA 1975, AREMA 2009)**

In 1982, AREA Committee 10 updated and simplified the flexural capacity table, basing all cases on 24-inch tie spacing and 61.5-kilopound (kip) rail seat loads. The required capacities were increased by 11-20% for rail seat positive, 39% for rail seat negative, 0-10% for center negative, and 33-56% for center positive. No explanation was given in the AREA bulletin for these changes (AREA 1981). The required capacities in the 1982 AREA Manual (Table 1.3) and the 2009 unfactored moments in Figures 1.10 through 1.13, are the same.

Table 1.3 1982 table for the required flexural capacity of monoblock concrete ties (AREA 1981)

		Required flexural capacity (k-in) without cracking			
Length (ft)	Spacing (in)	Rail Seat +	Rail Seat -	Center -	Center +
8'-3"	24	260	160	230	140
8'-6"	24	300	160	200	140
9'-0"	24	350	160	200	140

In 1988, AREA Committee 10 introduced the speed and tonnage factors, the rail seat positive moment plots for ties of length 8.0 ft, 8.5 ft, and 9.0 ft, and the factors to convert to the other design bending moments, all of which remain the same in the 2009 chapter (AREA 1988, AREMA 2009). The 7.75-ft tie length was added to the chapter in the 1991 edition (AREA 1991).

1.3.5   *Motivation to Improve Part 4 of Chapter 30 of the AREMA Manual*

Chapter 30, Part 4 of the AREMA Manual has been developed using an empirical approach in which ties are placed in service according to design recommendations, and subsequently tightening the design calculations if these ties did not perform satisfactorily. This process does not allow for increases in axle loads, frequency of wheel impact loads, environmental conditions, or load attenuation of the fastening system, among other factors. One can argue that the recommendations are sufficient for today's concrete ties and traffic demands, but the recommendations do not provide guidance for possible changes in demand. A more robust concrete tie design procedure could reduce some of the uncertainty in specifying and purchasing concrete ties, and improve the decision-making process for a product that is

16

purchased in mass quantities and represents a substantial capital investment. In particular, the ballast

pressure equation and limit, the impact factor, and the determination of the design bending moments,

should be investigated and improved. One concept for an improved bending moment design procedure,

based on a modified beam on an elastic foundation model (Section 4.5.4), is presented in Appendix C.

1.4   Motivation to Improve the Design and Performance of Concrete Ties

Since the Staggers Act was repealed in 1980, US railroads have dramatically increased their

profitability (Gallamore 1999). Motivated by a desire to increase productivity and efficiency, the AAR

increased the maximum gross axle load for four-axle cars in unrestricted interchange from 263,000 lbs to

286,000 lbs over the last two decades (Unsworth 2003). This has placed additional stress on all elements

of the track structure, and there has been a major effort to minimize track outages due to maintenance

activities in order to improve capacity. This combination of increased tonnage, increased axle loads, and

the demand for less maintenance has strained the limits of cut-spike, timber-tie track. From a life-cycle

cost perspective, the current state of the North American railroad industry is such that it can be

advantageous to invest in premium track materials.

As a material, prestressed concrete ties have the potential to withstand heavier axle loads and

higher traffic volumes than other tie materials. Another purported advantage of concrete ties is their

design life of up to 50 years, compared with timber ties that last approximately half as long. Concrete ties

provide a stiffer track support because of the increased mass and the premium fastening systems used,

they should require less maintenance, and gauge and cant are cast into the concrete rail seat. The increase

in track stiffness due to use of concrete ties can reduce fuel consumption by two to three percent,

compared to timber ties (White 1984).

A stiff track structure with premium fasteners, such as ballasted concrete-tie track or slab track, is

required to maintain the tight tolerances necessary for high speed operations. With the recent interest in

high-speed rail in the United States, premium track materials such as concrete ties will be needed. If

more lines with traffic characteristics like Amtrak's Northeast Corridor are planned – where high-speed

passenger trains are mixed with heavy axle load freight trains – then a track system like ballasted concrete-tie track will be needed.

The service life of concrete ties has often been quoted as 50 years (AREA 1962) and they are expected to require less maintenance than timber ties. However, certain durability problems have been observed in concrete ties that can shorten the service life and require more maintenance than anticipated. These problems can cause concrete ties, which have a significantly higher first cost than timber ties (White 1984), to have a higher life-cycle cost as well. Considering that some of these durability problems are not well understood and can be difficult to anticipate, there may be elevated financial risk when railroads select concrete ties.

Many of the concerns regarding concrete ties are the same today as they were decades ago. For railroad engineers and planners, a major challenge with concrete ties continues to be the inability to accurately predict the service life and maintenance requirements. Without understanding this, concrete ties can be a riskier alternative to timber ties, which typically have lower variability in terms of their service life and maintenance requirements.

The railway industry must solve the durability problems with concrete ties in order to take advantage of their potential as a safe, reliable, cost-effective track material that can withstand the service environment and provide greater line capacity. In order to effectively mitigate the problems that shorten the service life and increase the maintenance cost of concrete ties, the nature of these problems need to be better understood. The objective of this research is to investigate the most critical failure mechanisms of concrete ties in order to identify effective methods to address these problems and improve the performance of the ties.

CHAPTER 2: FAILURE MODE AND EFFECT ANALYSIS

OF CONCRETE TIES IN NORTH AMERICA[1]

2.1   Failure Mode and Effect Analysis

Failure mode and effect analysis (FMEA) is an efficient procedure for organizing and analyzing a complicated product or system, identifying potential problems, and addressing the most critical failures. Failure is defined as "the inability…to perform based on the design intent" (Stamatis 1995). The general analysis procedure (Figure 2.1) is to identify all the different ways a product can fail (failure modes), identify the potential consequences of the failures (failure effects), understand why these failures might occur (failure causes), determine which failures should be addressed first, and select the appropriate preventive measures to reduce the risk of failure (Stamatis 1995).
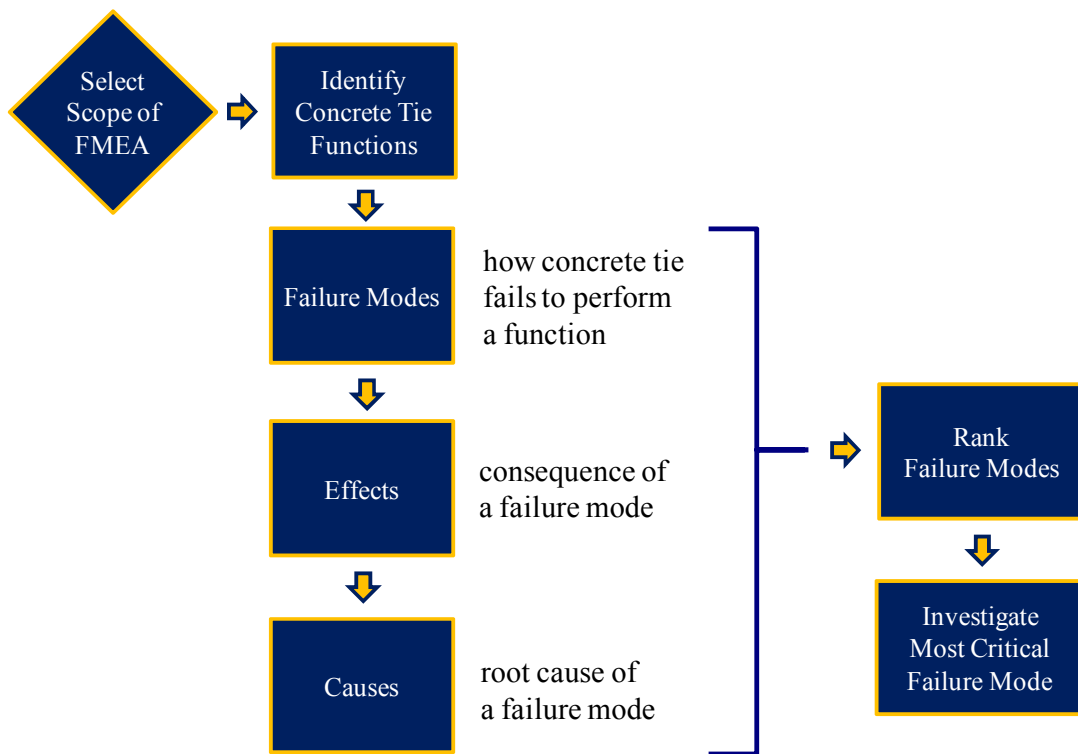
Figure 2.1 Flow chart of the general FMEA Process

2.2   Scope of FMEA

Using input from railroad engineers, concrete tie manufacturers, and railway industry committees, combined with my own knowledge of the subject, I applied a simplified form of a design FMEA to concrete ties in ballasted track in heavy haul service on major North American railroads. The purpose of the analysis was to identify the existing problems with concrete ties in North American heavy haul service, prioritize them, and investigate the most critical failures. In this analysis, "concrete tie" refers to a typical prestressed, monoblock tie that is an assembly of concrete, prestressed strands or wires, tie pads, shoulder inserts, insulators, and spring clips (Figure 1.1).

2.3   Concrete Tie Functions

Like any railway track system, ballasted concrete-tie track provides support and stability for train traffic by properly distributing the loads and maintaining the required track geometry. Concrete ties fit into this system by supporting the rails under load, distributing the stresses at the rail seat to acceptable levels for the ballast layer, and, with the ballast and subgrade, maintaining proper geometry of the track structure. Because of their poor dielectric qualities, concrete ties require an insulator in the fastening system to electrically isolate the rails if a track circuit-based system of traffic control is used.

2.4   Failure Modes

The failure modes of concrete ties in ballasted track can be categorized into support failure, stability failure, and electrical isolation failure. Each failure mode can be quite complex and may be related to failures of other track system components. It is important to understand the specific failure modes to get an idea of what causes the problems and how to reduce the probability that the failure effects will occur.

2.4.1   Support Failure

Failing to adequately distribute loads from the rails into the ballast may manifest itself through deterioration of other parts of the track system, as in ballast crushing, subgrade failure, rail flaws, or broken rails. These support failure modes relate to the strength, stiffness, spacing, and bearing area of the concrete ties.

The strength and stiffness of concrete ties come from the compressive strength of the concrete and the amount of prestress in the section (Hay 1982). Excessive stiffness can lead to higher stresses at the bottom of the tie and at the rail seat (White 1984). A loss of stiffness can lead to excessive deflections of the rail and pumping of the ballast and subgrade (Hay 1982).

Flexural strength and stiffness can be lost if the prestress force is lost through corrosion, concrete deterioration, or poor bond with the concrete due to improper manufacturing. The prestressing strands/wires may corrode if insufficient concrete cover or concrete cracking allows the intrusion of moisture and oxygen.

Concrete ties are sufficiently strong to withstand typical service loads in flexure without significant cracking. The kind of cracking that could reach the prestress and result in risk of corrosion would require high dynamic loads, such as those caused by out-of-round wheels, a center-bound condition (when the tie is supported at its center but not at its shoulders), or by impact damage from derailments or dragging equipment (White 1984). Ties can also be damaged during handling, including shipment, storage, installation, or maintenance. If concrete ties develop flexural cracks, these commonly correspond to high center negative moments (Figure 2.2) or to high rail seat positive moments (Figure 2.3).

**Figure 2.2 Example of a center-negative, flexural crack,
suggesting a center-bound condition**
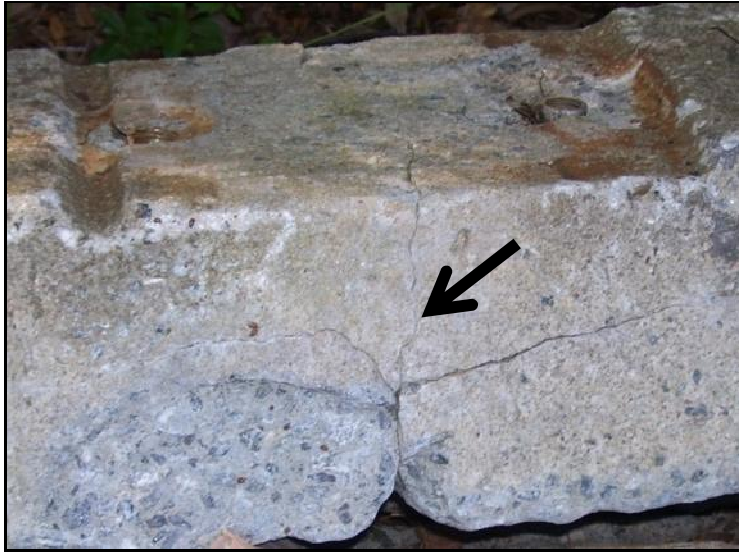
Figure 2.3 Example of a severe rail-seat-positive, flexural crack

Concrete that deteriorates due to chemical attack, environmental degradation (e.g. freeze-thaw expansion), or shear cracking may directly lose the bond with the prestressing strands or wires, or else cause cracking that leads to corrosion (Sahu and Thaulow 2004). Poor manufacturing can produce concrete that is not strong enough to sustain the high precompression, or it may be that the bond between the concrete and prestress never adequately developed because of an undesirable surface finish on the prestress strands or wires (White 1984, Weber 1969).

The bearing areas at the rail seats and at the bottom of the tie are important for distributing loads at acceptable stresses. If the bearing areas are reduced by concrete deterioration, damaged fasteners, or non-uniform ballast distribution, the stresses at these locations may increase and cause damage to the ballast, rail, or subgrade. Rail cant, referring to the inward tilt of the rails, is important for transferring the lateral and vertical loads through the web of the rail for stress distribution. Concrete deterioration, pad degradation, or damaged fasteners may lead to improper cant resulting in concentrated rail seat stresses.

The spacing of ties is also important for load distribution. Ties can become unevenly spaced, or bunched, if thermal, traction-, or braking-induced longitudinal forces in rails overcome the resistance of the crib ballast and the weight of the ties. Resistance to these forces is strongly affected by the effectiveness of the fastening system in providing adequate longitudinal restraint of the rail (Hay 1982).

2.4.2 *Stability Failure*

The stability failure modes all relate to track geometry. Failure to maintain proper track geometry includes problems with improper gauge, surface, line, or superelevation (Hay 1982). Track geometry problems are generally caused by insufficient restraint of the rails at the rail seats or by displacement of the ties.

Gauge problems are most commonly caused by failure modes like missing or damaged fasteners or rail seat deterioration. A weakened fastening system along a stretch of track allows gauge widening and possibly rail rollover. A typical fastening assembly on concrete ties in North America is comprised of cast-in, steel-shoulder inserts, spring clips attached to the shoulder inserts that hold the rail, insulators between the clips and the rail (some designs place insulation on the shoulder inserts instead), and a tie pad between the rail base and the concrete rail seat (Figure 1.1). Any one of these components can wear and allow the rail to rotate or translate laterally. Such deflections of the rail, whether permanent or only under load, may result in loss of gauge. Some examples of fastening component degradation are presented here (Figures 2.4 through 2.6).

Figure 2.4 Severe example of a shattered concrete shoulder and a yielded clip, caused by a derailment impact (Humphreys 2007)

Figure 2.5 Severe example of loss of clip toe load (sprung clip)

Figure 2.6 Example of tie pad wear (Humphreys 2007)

Aside from the fastening components, the concrete beneath the base of the rail can also deteriorate (Figure 2.7). In North America this failure mode is commonly referred to as "rail seat abrasion", but the preferred terminology is "rail seat deterioration" (RSD) (Figure 2.7). As with fastener wear, RSD may lead to loss of cant or loss of gauge. RSD and fastener wear are often concurrent failure modes and will be discussed in detail in Chapter 3.

Figure 2.7 Example of concrete-tie rail seat deterioration (RSD)

Vertical or lateral displacement of the ties can also cause geometry problems. Track buckling is an extreme failure mode that occurs when the lateral resistance from the ties and ballast is insufficient to restrain the thermal stresses in the rails. Generally, the weight of the concrete tie, the roughness of surfaces on the sides and bottom of ties, and the amount of shoulder ballast contribute to how much the ties will resist loads and thermal rail stresses that work to push the track out of line. Settlement is mostly caused by failures in the ballast and subgrade layers, but the ties influence these failures by how well they distribute traffic loads.

2.4.3   Electrical Isolation Failure

A shunted track circuit can occur if there is a failure to electrically isolate the rails. Electrical isolation is typically achieved by using an insulating material in the fastening assembly, since moist concrete ties conduct enough electricity to shunt the track circuit (Weber 1969). Broken, worn, or missing insulators or tie pads on each rail seat of a tie may cause the track circuit to shunt if the concrete has a high moisture content.

2.5 Failure Effects

The principal consequences or effects of the concrete tie failure modes – support failure, stability failure, and electrical isolation failure – such as reduced train performance, increased track maintenance costs, equipment damage, and increased risk of derailments could be the consequences of deterioration of any track structure and are not unique to concrete ties.

Reduced train performance refers to the effects that degraded track conditions have on operations: slower speeds, more delays due to maintenance, and reduced line capacity. These result in higher operating costs and lower service quality. Studies suggest that well-maintained concrete-tie track offers less train resistance (two to three percent) than comparable timber-tie track because of the higher track modulus (White 1984). This benefit from use of concrete ties is lost if the overall condition of the track is allowed to degrade to the point where this additional stiffness is lost.

2.6 Failure Causes

For each of the general failure modes listed above, there may be multiple potential root causes known as failure causes. Some potential causes for failure mode processes were listed which could be linked to the design and manufacture of concrete ties (Table 2.1). Understanding the underlying cause is important when trying to prevent the initiation of failure modes.

Table 2.1 Potential failure causes for processes within the failure modes

Failure Mode Processes	Potential Failure Causes
Concrete deterioration	low concrete strength; low prestress force; high curing temperature; reactive aggregates; fines intrusion; moisture intrusion; low abrasion resistance (concrete); improper pore system in cement; prestress diameter too large; too much steel in the cross-section; pad too soft; pad too hard; pad creates high hydraulic pressures; pad stiffness changes too much over time; fastener damage
Fastener damage	fines intrusion; moisture intrusion; pad too soft; pad too hard; pad creates high hydraulic pressures; pad stiffness changes too much over time; insulator not durable enough; fastener design leads to concentrated stresses; spring clip too stiff; spring clip too flexible; low fatigue strength for spring clip; concrete deterioration
Loss of prestress	low concrete strength; high prestress force; poor bonding surface on prestress; prestress diameter too large; concrete deterioration
Poor bearing	undersized bearing areas; concrete deterioration
Longitudinal shoving	low bottom and side friction with ballast; fastener damage
Lateral shoving	low bottom and side friction with ballast; fastener damage
Excessive stiffness	high concrete strength; high prestress force; spring clip too stiff; pad too stiff

It is important to remember that many failure modes in ballasted concrete-tie track are not caused by a deficiency in the ties. For example, internal rail defects, weak subgrade soil conditions, poor drainage, insufficient ballast depth, abrupt track modulus transitions, and other track problems may themselves lead to the failure modes discussed here, or they may be potential root causes for concrete tie problems.

2.7   Concrete Tie Survey

The criticality of each failure mode is influenced by how likely it is to cause the failure effect, the severity of its possible effects, and how difficult it is to detect the mode before the failure effect occurs. In a formal FMEA, these three factors are treated separately and are referred to as the occurrence, severity, and detection factors, respectively. One method for prioritizing failure modes is to assign

ranking values (typically from 1 to 10) to each of these factors. The product of these factors is a ranking metric called the "risk priority number" (Stamatis 1995).

A formal FMEA uses the risk priority numbers to prioritize failure modes. Determining the values for each of the factors is a collaborative effort that uses performance data, surveys, and expert opinion. For my analysis, a simplified ranking procedure was followed that applied the qualities of FMEA but with less detail. A rigorous FMEA of concrete ties was considered unnecessary and would have been mostly qualitative because adequate performance data are not available for some concrete tie failure modes. Most failure modes are often only recorded after severe failures such as derailments. A more involved analysis may lead to the same relative ranking of failure modes as achieved with this simpler approach.

Working in cooperation with Association of American Railroads (AAR) researchers at the Transportation Technology Center Inc. (TTCI), I conducted a survey of North American railroads, commuter agencies, and transit authorities to learn about their experiences with concrete ties. The survey consisted of a series of questions addressing the most critical concrete tie problems and how the railroads make decisions about the installation and maintenance of concrete ties. The eight-question surveys were distributed to 19 individuals with experience in the maintenance and performance of concrete-tie track.

Six major (Class I) railroads, two regional and shortline railroads, and four commuter agencies and transit authorities responded to the survey. The most critical problems that each group cited in the survey varied, primarily due to their different loading environments. The major freight railroads, with higher traffic volumes and heavier axle loads, had more load-related problems, such as RSD, fastener wear, and center binding. By comparison, the commuter agencies and transit authorities reported installation or tamping damage as their most critical problems. In response to an open question, "What are the most critical problems with concrete ties on your railroad?" most respondents cited rail seat maintenance, which could be attributed to either the fastening system or RSD.

Respondents were asked to rank a list of eight concrete tie failure modes, including "Other," in order of criticality (Table 2.2). The top two problems with concrete ties for major railroads are RSD and

fastener wear. Only one response had anything listed under "Other," so the truncated list of failure modes apparently was sufficient to encompass most heavy haul concrete tie problems in North America.

**Table 2.2 The most critical concrete tie problems for major North American railroads;
ranked from 1 to 8, with 8 being the most critical
(based on six Class I railroads' survey responses)**

Most Critical Concrete Tie Problems	Average Rank
Rail seat deterioration (RSD)	6.83
Shoulder/fastener wear or fatigue	6.67
Derailment damage	4.83
Cracking from center binding	4.58
Cracking from dynamic loads	1.83
Tamping damage	1.83
Other (ex: manufactured defect)	1.33
Cracking from environmental or chemical degradation	1.25

Two primary themes among the responses were that the concrete tie system is expensive and that there is substantial uncertainty in maintenance planning and estimation of the service life of concrete ties. Four of the twelve participants in the survey have largely ceased installing concrete ties in track for these reasons. Most of the survey participants, however, currently use concrete ties on a portion of their track.

The full set of survey responses, excluding confidential responses, is included in Appendix A: Summary of Concrete Tie Survey Results.

2.8   Selection of Research Topic

I selected RSD for further investigation due to the survey results shown in Table 2.2, guidance from AAR researchers at TTCI, and input from the concrete tie subcommittee of AREMA Committee 30 - Ties.

CHAPTER 3: RAIL SEAT DETERIORATION[2]

3.1   Introduction to Rail Seat Deterioration

Rail seat deterioration (RSD) is degradation underneath the rail on a concrete tie. It is often

referred to as rail seat abrasion (RSA), but RSD is a more appropriate term because the concrete wear

involves more than just abrasion. As will be discussed here, the deterioration of the concrete may result

from multiple mechanisms, or physical processes.

The concrete rail seat and the fastening assembly work together in concrete ties to hold the rails at

proper cant and gauge. Cant is the tilt of the rails toward the track centerline that maintains the proper

wheel/rail interface and directs the wheel loads through a stable pathway along the web of the rail (Hay

1982). Gauge is the distance between the inner sides of the heads of the rails that must be maintained

according to specification for proper operation and track-train dynamics. When a component in this rail

seat system deteriorates, the clamping force provided by the fasteners against the base flange of the rail is

loosened, allowing movement when the rail is loaded and unloaded. This loosened condition can initiate

a negative feedback loop in which the wear of other components accelerates due to their increased relative

motion and component wear. As a result, RSD and fastener wear are often concurrent failure modes, and

there is thought to be a cause-and-effect relationship between the two. In my research, I focused on

concrete deterioration, understanding that this is only one part of the RSD process.

The RSD wear patterns observed in track vary based on the specific climatic and traffic

conditions and the location of the concrete tie in track (Figures 3.1, 3.2, and 3.3). Figure 3.1 is a profile

view of the field side of the rail seat on the high side of a curve. This wear pattern is similar to that seen

in Figure 2.7 (a view from above). The rail seats in these images have worn more on one side because

high lateral forces on a curve may lead to eccentric stress distributions on the rail seat. The rail seat in

Figure 3.2 appears to be crushed on both its gauge and field sides. This could be the result of the rail

pivoting back-and-forth because of a loose fastening system. Figure 3.3 shows the concrete's coarse

---

[2] Portions of Chapter 3 were originally published in the Proceedings of the 2009 AREMA Annual Conference in
Chicago, Illinois, USA (Zeman et al. 2009b)

aggregate exposed after the mortar was worn away, leaving an appearance similar to a surface eroded by the movement of water or abraded by a flexible material. It has been reported that the deterioration begins along the perimeter of the tie pad and works its way toward the center of the rail seat (Bakharev 1994). In early stages, RSD can leave an impression of the tie pad surface on the rail seat, with deterioration occurring on the contact areas (Bakharev 1994). A more common example of RSD, with less severe wear, is presented in Figure 3.4.

RAIL SEAT PROFILE   **RAIL SEAT PROFILE (at fastener shoulder)**
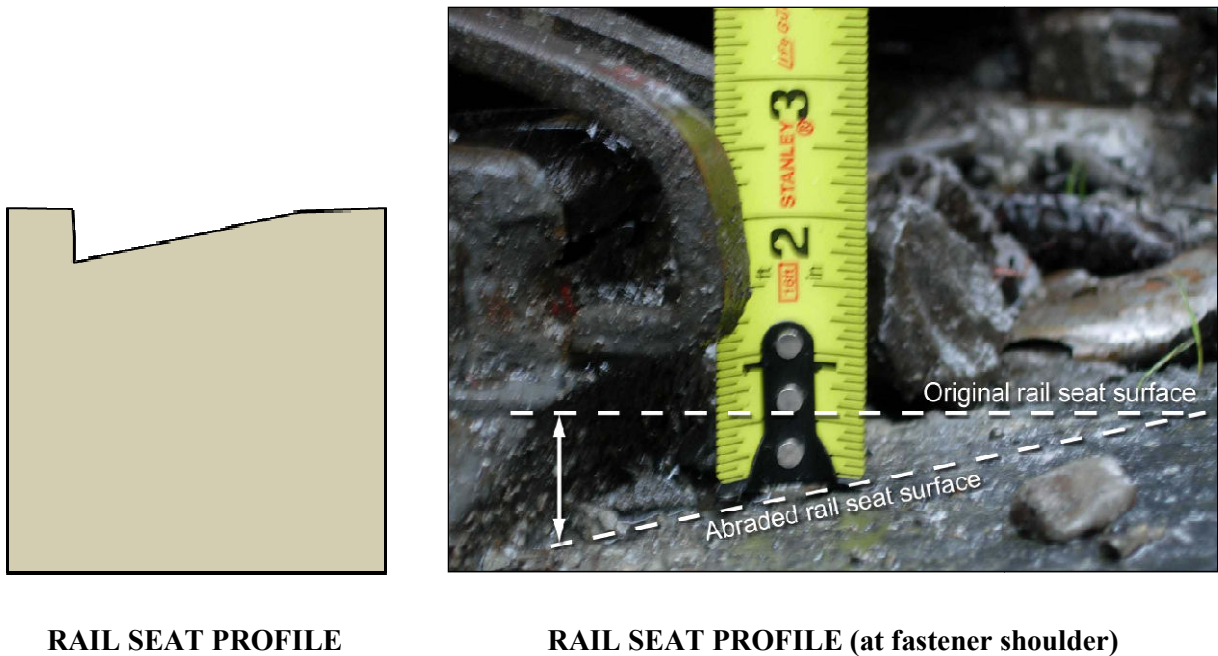
**Figure 3.1 Severe example of RSD, suggesting
excessive lateral forces on a curved section of track (NTSB 2006)**
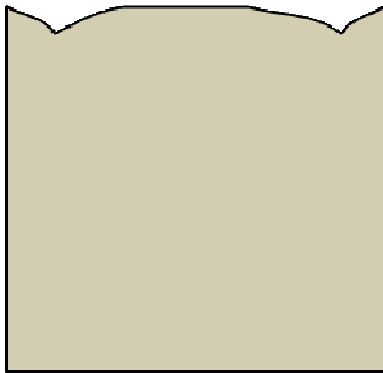
RAIL SEAT PROFILE   TOP OF RAIL SEAT

**Figure 3.2 Severe example of RSD,
suggesting loosened fastening components**
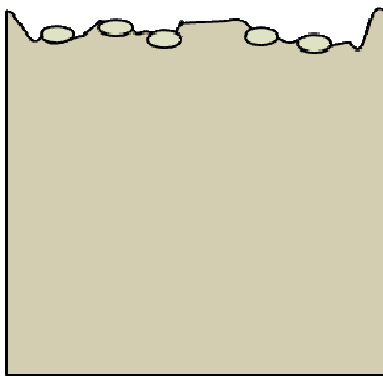
RAIL SEAT PROFILE   TOP OF RAIL SEAT

**Figure 3.3 Severe example of RSD, suggesting
erosion or abrasion of the cement paste (Peters and Mattson 2004)**

**Figure 3.4 Typical example of RSD, showing wear of the steel shoulder (on the left),
the top layer of cement (exposed aggregate on the left),
and the polyurethane coating (still intact on the right)**

RSD is a maintenance challenge because relatively small amounts of wear can lead to significant

track geometry problems, typically in the form of wide gauge. The site of a 2005 derailment in the state

of Washington had RSD as deep as two inches at one location. Researchers from the Volpe National

Transportation Systems Center studying this derailment estimated that, depending on the pivot point at

the base of the rail and the amount of rail head wear, one inch of RSD wear on the field side can result in

1 to 2.5 inches of gauge widening. To keep the track within gauge limits for the Federal Railroad

Administration (FRA) Track Classes 4 and 5, the researchers suggested that the depth of RSD wear on the

field side of the rail seat should be no more than 0.38 inch for new rail, 0.31 inch for 0.25-inch rail head

wear, and 0.19 inch for 0.50-inch rail head wear (Choros et al. 2007).

RSD is difficult to detect in its early stages and costly to repair, particularly if repairs are required

between rail replacement (relay) cycles. Currently, diagnosing and repairing RSD requires removing the

fastening system and lifting the rail from the rail seat, a time-consuming and expensive task. Several

automated vehicle-mounted inspection systems are being developed to identify RSD more rapidly and

efficiently (Reiff 2009a, Wamani and Villar 2009). Most of these systems try to correlate deviating cant measurements with RSD. So far, however, there is no reliable way to distinguish the cause of improper cant from the following possibilities (Reiff 2009a):

- RSD
- Worn tie pads
- Broken or worn insulators
- Loss of toe load

- Worn shoulders
- Excessive rail wear
- Broken ties
- Trains running at over-/under-balanced speeds on curves

Some automated inspection systems apply machine vision technology in an attempt to identify RSD (Reiff 2009a). It appears that these automated inspection technologies require more development before different inspection systems will be able to reliably identify RSD or even cant deficiencies using standard procedures and metrics (Reiff 2009a, Wamani and Villar 2009).

In the worst cases, RSD can develop on new ties within the first year a concrete tie is in service, though this is reportedly the exception, not the norm (Bosshart 2009). Fastening components, such as the insulators, tie pads, and spring clips, must be replaced periodically. In order to maximize track capacity and minimize maintenance-of-way track windows, it is more efficient to repair the rail seat and replace the fastening components during rail replacement (Read and Kalay 1996). As rail life continues to increase through practices such as rail lubrication, grinding, and the use of head-hardened rail, the rail seat and fastening components are being required to withstand more tonnage before repair or replacement (Kalay 2010). Therefore, in addition to preventing the initiation of RSD, an important objective of this research is to determine methods to increase the rail seat's resistance to RSD so that it can last one or two rail relay cycles.

3.2   History of RSD in North America

The Canadian National (CN) Railway was one of the first North American railroads to report RSD on its concrete ties (Bakharev 1994). In the early 1980's, CN was having problems with alkali-silica reaction (ASR) caused by high-alkali sand in their ties. It was not until the mid- to late-1980's that the

ASR problem was resolved. However, what later came to be called RSD was still occurring on the concrete-tie rail seats. Thus, in the late-1980's RSD was identified as a distinct problem (Johns 2009). The Canadian Pacific (CP) railroad first noticed RSD in 1986, and the Burlington Northern (BN) identified it in 1988 (Bakharev 1994).

In the early-1990's, an ad hoc Association of American Railroads (AAR) committee was formed to work on the RSD problem. Its members initiated a number of research projects, including tests at the Transportation Technology Center's (TTC) Facility for Accelerated Service Testing (FAST). The tests involved many different combinations of concrete ties, fasteners, rail seat treatments, and tie pads placed in the FAST high tonnage loop (Reiff 1995). The tests resulted in identification of certain pads and pad assemblies that mitigated RSD to a manageable level. These solutions were sufficient for the North American freight rail conditions in the mid-1990's. Since then, rail has been lasting longer due to improved materials and maintenance. In addition, axle loads have increased. Consequently, the materials that worked in the past are generally not adequate today (Reiff 2009b). In other words, the demands on the rail seat are higher, and there is incentive to perform RSD maintenance less frequently due to the added expense of lifting the rail before it is time to replace it.

A number of laboratory tests have been developed to simulate accelerated RSD. Pandrol developed accelerated tests with high-pressure water jets, creating a scoured surface that appeared similar to RSD. Using this test, Pandrol evaluated the resistance of different concrete mixes and surface finishes to this type of erosion mechanism (Bakharev 1994).

Frank Scott and others at the CN Railway Research Lab developed an accelerated wear test based on the company's experience with RSD (Johns 2009). This test was the direct predecessor of today's RSD lab test described in the American Railway Engineering and Maintenance-of-Way Association (AREMA) Manual for Railway Engineering Chapter 30, Part 2 (AREMA 2009). The test was intended to screen alternative tie designs for the best performance before a design was selected and placed in track. The test loads were based on strain-gauge measurements taken on ties in approximately five-degree curves. For setting the test loads, they also factored in an empty car for every loaded car to account for

35

the higher impact factors and lateral-to-vertical load ratios (L/V) with an empty car. Due to the dynamics

of a rail car suspension, the wheels on an empty car may have higher impact factors (the ratio of the

dynamic to the static wheel load), though not necessarily higher dynamic loads (Bhatti et al. 1985). Also,

the "hunting" action of trucks, where the axles of a truck oscillate laterally and lead to higher L/V ratios,

is more prevalent in empty cars (Hay 1982). In the test apparatus, the loads were applied by a single

actuator and transferred to rail sections, fastened to a tie, by a Y-shaped member. The angle of the "Y"

was selected to match a certain L/V ratio. The CN researchers found that the wear was much worse when

water was added to the rail seat during the test. They also found that three million cycles was a good

target that usually correlated with acceptable field performance. Early ties that were tested could not last

1,000 cycles before failing, while some of today's ties can last up to ten million cycles (most ties are only

tested to three million cycles, not until failure occurs) (Peters and Mattson 2004, Johns 2009).

The CN lab test was correlated with field performance by the research engineers studying three

different track locations – with varying climatic and geometric conditions – over the course of ten years.

At the time, they concluded that one lab cycle was equal to approximately seven to eight track cycles, so

that one million lab cycles was equivalent to approximately 320 cumulative million gross tons (MGT).

Three weeks of testing could simulate about a year of traffic on a high-density line (Johns 2009). CN

later sold the lab to an external research company and it is currently operated by Exova. CTL, in Skokie,

Illinois, also runs accelerated RSD tests similar to those developed by the CN research lab (Reiff 2009b).

Unit Rail, Inc. has a similar test apparatus capable of running accelerated service tests on concrete ties. It

is housed at the Advanced Transportation Research Engineering Laboratory (ATREL) in Rantoul, Illinois

and is operated by the University of Illinois at Urbana-Champaign.

Around the same time that CN was developing a laboratory test, the AAR developed a similar

RSD lab test that introduced another important element: a restoring force that returned the rail to its

original position – effectively rocking the rail back-and-forth. In track, the lateral forces on a rail induce

torsion in the rail, but since the rail has some torsional stiffness, there is a restoring force (in addition to

the restoring force provided by the spring clips and the trailing axle of a truck) that returns the rail to its

original position. This back-and-forth action has been found to lead to substantially more wear than if the spring clips are the only source of a restoring force. The AAR also found that adding water, as well as abrasive sand during the test accelerated RSD (Reiff 2009b).

The RSD test procedure described in AREMA is not very prescriptive. The description of Test 6 in Chapter 30, Part 2 of the AREMA Manual (2009) provides no guidance for the following details: the magnitude or application of the restoring force, the rate or manner of application of sand and water, the stiffness or type of support for the tie, the initial tightness or allowable tolerances for the fastening system, the criteria for whether to replace worn fastening components during the test, and the procedure for measuring the response or wear of the rail seat and fastening system. A consequence of the lack of a standard RSD test, results from different labs vary significantly, depending on each lab's specific test apparatus and procedure. Improving the standardization of the RSD test is currently a central topic of discussion in AREMA Committee 30 – Ties. Doing so would result in a better understanding of the problem and enhance the ability to objectively compare fastener system performance.

3.3   Contributing Factors

Factors that contribute to RSD are generally considered to be axle load, traffic volume, curvature, grade, the presence of abrasive fines (e.g. locomotive sand or metal shavings), the tightness of the fastening system, the durability of the pad and fastening components, and climate. Based on North American freight railroad experiences and concrete tie tests at FAST, heavy axle loads, abrasive fines, moisture, and rail movement appear to be the most important factors (Bakharev 1994, Peters and Mattson 2004, Reiff 1995).

Significant RSD tends to occur in certain regions. One Class I railroad specifically cites the worst-case scenario for RSD as (1) on the northwest slope of a mountain, (2) a wet climate, (3) track with sharp curves and steep grade, and (4) high annual tonnage.   The northwest slope is worse than other slopes because the northern part receives less sunlight in the northern hemisphere and the western part receives more rainfall (particularly in the western Cascade Mountains where the Washington state derailment occurred, see Figure 3.5) (Bosshart 2009). Unfortunately, there is presently no way to track

the occurrence of RSD, how rapidly it occurs, and the characteristics of the environment, tie material, track support, and train traffic. Much of what is known about RSD is based on anecdotal evidence. A large-scale investigation to collect data on the location and the characteristics of the ties, track, and traffic for RSD occurrences would be extremely valuable. The resultant database could be used to evaluate the prevailing theories on the cause of RSD and thus further inform consideration of possible solutions.
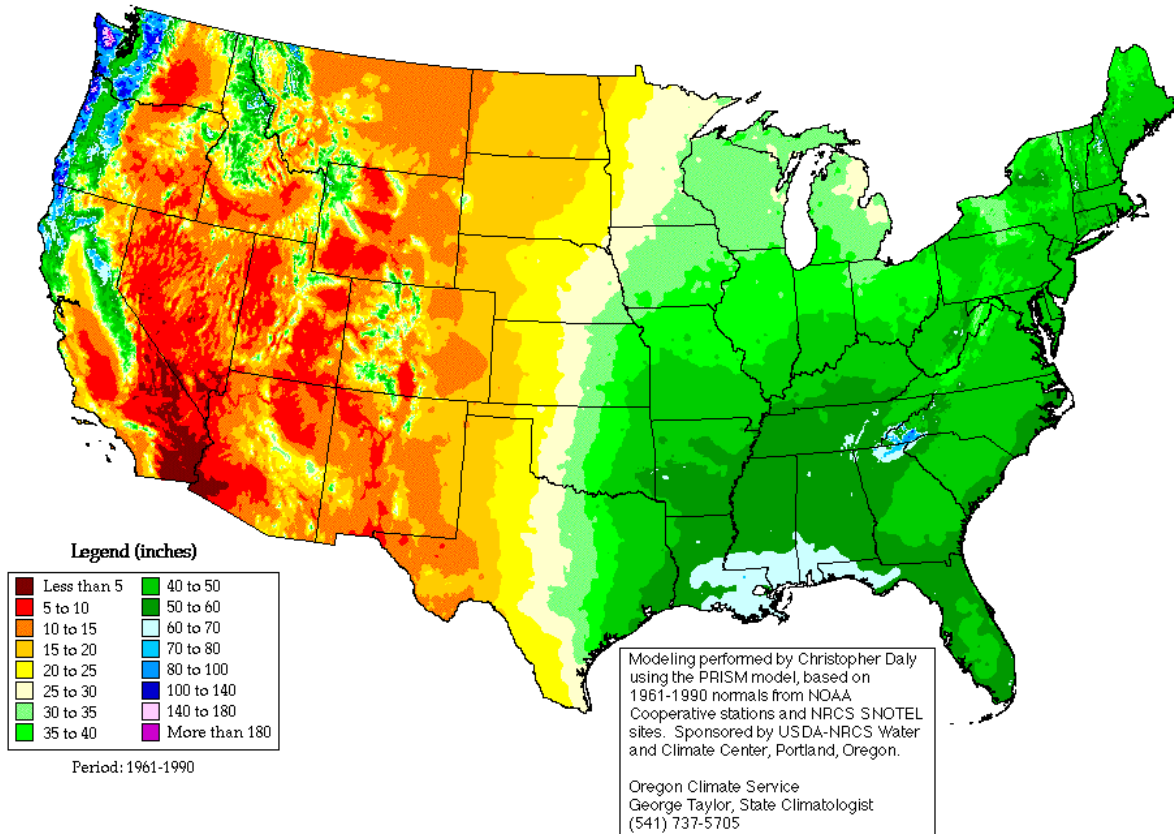
Figure 3.5 Map of average annual rainfall in the US (Oregon Climate Service)

Aside from the location of instances of RSD, the importance of moisture is also understood by means of field tests conducted at TTC in Pueblo, Colorado (located in eastern Colorado, see Figure 3.5) and the laboratory RSD test. Both have demonstrated that without adding moisture, the wear rate is minimal and little noticeable wear occurs. According to Reiff (2009b), who conducted the RSD tests on TTC's high tonnage loop at FAST:

…at FAST we rarely get RSA [rail seat abrasion] even after 600[-plus] MGT. To conduct our RSA mitigation test several years ago…we had to add a water drip system to the FAST loop in order to generate RSA. Where we did this, RSA developed in less than 100 MGT, where it was dry, no RSA, and even today, the same ties are in place with little or no RSA (Reiff 2009b).

Reiff highlights that it is also important to consider where RSD has not been found. The Florida East Coast (FEC) railroad was one of the first to install concrete ties in the 1960's, and its tracks have been almost solely concrete ties since then. The FEC is a regional freight railroad with minimal grades and few sharp curves that runs along the east coast of Florida from Jacksonville to the Port of Miami. Most of its mainline has traffic ranging from 30 to 50 MGT annually, with a maximum speed of 60 mph. Many of the FEC ties that were produced in the 1970's and some of the original AAR MR-2 ties from the 1960's are still in service today. The first generation FEC ties that were taken out of service were removed due to inadequate flexural strength because of relatively low initial precompression. The concrete mix was very dense and difficult to work with during manufacture, but this resulted in ties that were harder and more durable than other concrete ties. To date, the FEC has not found RSD on its ties (Riehl 2008).

Taking a broader perspective, an interesting aspect of RSD is that it appears to be unique to North America. Other than rumors of occurrences in Australia and India, RSD has not been specifically identified anywhere else in the world. In fact, most railroad engineers and concrete tie manufacturers in the world are unaware of RSD. Thus an important question is: what are the elements of North American freight railroad use of concrete ties that may be causing RSD?

One possibility is that North America uniquely combines heavy axle loads (HAL) and high annual tonnage, so the demands are much higher and the track sees more load cycles each year. Within North America, this argument seems to hold. Transit and commuter railroads using concrete ties, as well as Amtrak's Northeast Corridor, have seen no instances of RSD. It could also be argued that the magnitude and cumulative number of loads on the FEC ties is less than what some Class I railroads handle on their current routes. However, running HAL and high annual tonnage on concrete-tie track is

not unique to North American freight operations (Table 3.1). This comparison of a few international heavy haul rail lines did not provide enough evidence to support or reject the hypothesis that RSD is a problem in North America due to the uniqueness of its HAL rail lines. A corollary of the HAL hypothesis is that the maintenance practices in North America are such that the rail car fleet in general contains more wheel flats and irregularities that lead to greater and more frequent impact loads than are experienced elsewhere. The Fortescue Metals Group (FMG) ore line in Australia, for example, has one rail line dedicated to a single commodity. The mining company owns the track, operates the trains, and owns all the rolling stock and keeps it in good condition.

Table 3.1 Comparison of international heavy haul rail lines with concrete ties
(Thomas 2009, Kalay 2010, Kuys 2009,
Schoch and Frick 2007, Bhatnager 2009, Zhixiu 2009)

Rail Line	Country	Annual MGT	Train Load (ton)	Car Load (kip)	Axle Load (kip)
FMG Ore Line	Australia	40	38,720	352	88
Powder River Joint Line	USA	200	18,000	286	72
Transnet West	South Africa	--	44,000	263	66
Malmbanan	Sweden	30	9,000	263	66
Transnet East	South Africa	30 → 90	24,200	216	54
Future Freight	India	--	12,760	216	54
Current Freight	India	--	5,500	176	44
Da-Qin Line	China	340	22,000	176	44

Another possibility is that other locations with HAL do not have the same demanding climate with the potential for many wetting-drying and freeze-thaw cycles that may damage the concrete. For example, the HAL lines in South Africa and Australia generally run through arid or semi-arid regions with moderate to low potential for freeze-thaw cycles, similar to the Southwest US. Portions of India generally receive heavy rainfall but have tropical climates, thereby avoiding freeze-thaw cycles.

However, much of Sweden, as well as China's Datong-Qinhuangdao (Da-Qin) line near Beijing, can receive significant rainfall and multiple freeze-thaw cycles annually (Heritage 2007).

A third possible explanation as to why RSD only occurs in North America is related to the tie materials used. It has been pointed out that air-entrained concrete is not common to all countries, and that North America uses air entrainment more than other regions with freeze-thaw conditions. This higher air content may weaken the concrete's resistance to abrasion. Others argue that the tie pads used in North America are too stiff and poorly designed, and therefore the pad does not provide much load attenuation and transfers higher stresses to the rail seat.

It is possible that RSD is not actually unique to North America; rather, that other heavy haul railroads in the world have not experienced RSD to the extent that it has become a problem. As will be discussed in the following section, RSD appears to be a deterioration process that occurs under demanding loading conditions that can be exacerbated by environmental factors such as moisture and abrasive fines. Given HAL, it seems likely that RSD will occur, and it may simply be a question of how long this will take. With the correct combination of high rail seat stresses, looseness in the fastening system, moisture, abrasive fines, and high traffic (many annual load cycles), RSD can develop quickly enough that it either shortens tie service life or requires attention within the service life of the tie or the rail, making it a problem. To date, parts of North America are the only locations in the world with the combination of track, operating, and environmental conditions that cause RSD to be a problem.

3.4   Concrete Deterioration Mechanisms

Industry opinion and previous studies suggest that concrete deterioration in RSD may be due to abrasion, crushing, freeze-thaw cracking, hydraulic pressure cracking, hydro-abrasive erosion, cavitation erosion, or some combination of these mechanisms.

A previous microscopy study concluded that a sample of concrete ties taken out of service with RSD showed characteristics of abrasion and possibly hydraulic pressure cracking or freeze-thaw cracking. Hydraulic pressure cracking and freeze-thaw cracking have similar appearances because they both result from high pore water pressures in the concrete. The study did not find microstructural evidence of hydro-

abrasive or cavitation erosion in the samples, nor did it find evidence that ASR was an active mechanism (Bakharev 1994). Evidence for cavitation erosion has been suggested in examples of worn rail seats such as the one documented by Peters and Mattson (2004) in Figure 3.3 and a video recorded at TTCI's FAST showing bubbles forming at the edge of the tie pad during loading (Bakharev 1994). The bubbles could be evidence of sudden pressure changes in the water, which could cause cavitation. In regards to crushing, an investigation into the Washington state derailment concluded that poor track geometry may have caused concentrated stresses at the rail seat sufficient to crush or fatigue the concrete (Choros et al. 2007).

3.4.1   Abrasion

Generally, abrasion is surface wear that results from a friction force acting over some displacement. What is required for rubbing abrasion to occur is a normal force that joins the surfaces in question, a coefficient of friction between the surfaces, and a lateral, shearing displacement. Abrasion is the result of dynamic forces and displacements that are cycled many times. In concrete ties, abrasion could be caused by some combination of rubbing of the tie pad, grinding of abrasive fines, and the impact between the rail and tie.

A surface abraded by two-body wear is smooth if the abrading element is smooth and the abraded material is homogeneous. Heterogeneous materials like concrete do not abrade evenly. For the rail seat, abrasion is typically thought of as two- or three-body wear, involving the concrete rail seat, the tie pad surface, and possibly abrasive fines like sand or metal shavings. If the pad is soft and flexible, it may conform to the aggregate shapes and create an uneven surface (Figure 3.3) (Bakharev 1994). By contrast, a harder pad surface would create more uniform concrete wear.

The abrasion resistance of concrete is a complex parameter that does not fit neatly into an analytical formula or simple guidelines. It is largely understood through empirical results of fatigue-style tests that measure surface wear in terms of depth, surface area, or volume lost. Abrasion resistance depends on the concrete strength, paste content, aggregate characteristics, concrete porosity, curing techniques, compaction, and surface finish (De Almeida 1994). Nearly every measurable concrete

characteristic appears to have some influence on abrasion resistance. Following is a summary of a literature review on the influence of concrete properties on abrasion resistance.

Abrasion resistance is largely determined by the surface cement pore structure. It is mostly the micropores that influence toughness and wear resistance (Bakharev 1994). One study found a strong inverse relationship between concrete absorption and abrasion resistance, whether the concrete was made with ordinary Portland cement, fly ash, or slag (Dhir et al. 1994). Absorption, or permeability, is one indication of the porosity and pore structure of concrete. Some experiments have shown a positive correlation between wear rate and the water-to-cement ratio (w/c). As w/c, cement paste volume, or porosity of concrete increased, abrasion resistance decreased (De Almeida 1994).

Air-entrained concrete may be less resistant to abrasion than normal concrete because of its increased porosity. Some researchers advise that air content should be less than five percent and that air entrainment reduces wear resistance more than it reduces compressive strength (Bakharev 1994). However, there is not a consensus among researchers about the relationship between air entrainment and abrasion resistance. Some have found that air-entraining admixture (AEA) increases abrasion resistance for low w/c concrete. Others found that AEA does not affect abrasion resistance, except through its effects on compressive strength (Bakharev 1994).

In some studies, concrete that had been cured at 100% relative humidity, under a wax seal, with the aid of a curing compound, or under plastic or burlap covers had up to 50% higher abrasion resistance than concrete that had been air-dried or cured with low-quality compounds (Senbetta and Malchow 1987, Kettle and Sadegzadeh 1987). At least one study demonstrated that abrasion resistance increases with concrete age (Naik et al. 1997).

Depth of abrasion is strongly related to surface pore structure, which is partly influenced by the finishing procedure. Bakharev (1994) suggested that it is best to finish the surface by compacting the local matrix and eliminating capillary channels, thereby increasing the microhardness and abrasion resistance. Compared with hand finishing, slabs that were power trowelled or vacuum dewatered in one study had greater abrasion resistance, supposedly because the surface w/c was reduced (Kettle and

Sadegzadeh 1987). In one test, sawn concrete surfaces had more abrasion resistance than those surfaces cured against the forms (Sustersic et al. 1991).

The influence of fly ash has been studied extensively, and there are conflicting results. Generally class C fly ash provides more abrasion resistance than class F fly ash or plain concrete (Naik et al. 1997, Carrasquillo 1987). In most tests, adding fly ash increased the abrasion resistance of the concrete (Kettle and Sadegzadeh 1987, Naik et al. 1997, Carrasquillo 1987), though in some cases, adding class F fly ash reduced the abrasion resistance of concrete (Naik et al. 1997). In these studies, replacement rates of fly ash ranged from 25% to 60% (Kettle and Sadegzadeh 1987, Naik et al. 1997, Carrasquillo 1987). One study reported that abrasion resistance increased by approximately 50% with 35% class C fly ash replacement (Carrasquillo 1987). It has even been shown that the source of the fly ash influences abrasion resistance (Naik et al. 1997).

Some studies found that silica fume and superplasticizers have little effect on abrasion resistance. Other researchers observed that the use of a superplasticizer reduces the volume of paste and thus the potential for wear, and that using silica fume reduces abrasion as a result of smaller pores and lower permeability (Bakharev 1994, De Almeida 1994). One study showed that abrasion resistance was actually lowest for high strength concrete with silica fume (Bakharev 1994).

Replacing cement by mineral admixtures reduced abrasion resistance by 10-25%, with condensed silica fume concrete showing the lowest resistance. Poor performance of condensed silica fume concrete may be due to self-desiccation because the super fine particles increase water demand. Generally, the cementitious compositions with the highest to lowest abrasion resistance were: 100% Portland cement, 10% natural pozzolan (volcanic) replacement, 10% fly ash (type F) replacement, and 10-20% silica fume replacement (De Almeida 1994).

Generally, high compressive strength – greater than 10,000 pounds per square inch (psi) – concrete has high abrasion resistance (Bakharev 1994, Sustersic et al. 1991, De Almeida 1994), though this is not always a strong correlation when other factors are isolated (De Almeida 1994). There are many

combinations of mix designs and curing techniques that could achieve the target strength, but they will not necessarily result in consistent abrasion resistance.

Aggregate durability, size, and shape can also affect abrasion resistance. Coutinho found that very fine aggregate may reduce abrasion resistance (De Almeida 1994). Popovics found that coarse aggregate did not have a great influence on abrasion resistance (De Almeida 1994). Others found a strong relationship between the abrasion resistance of concrete and abrasion resistance of the coarse aggregate and mortar. Concrete with larger coarse aggregate sized 1-3/8" to 1-5/8" has lower resistance. Angular, rough aggregate is better for abrasion resistance than smooth aggregate because of the stronger bond with the cement paste (Bakharev 1994).

Multiple studies have demonstrated that fiber-reinforced concrete (FRC) provides effective abrasion resistance (Sustersic et al. 1991, Hoff 1987, Nanni 1989). One study showed that steel-FRC reduced abrasion by over 50%, while polypropylene-FRC reduced wear by about 25% (Hoff 1987).

Testing under wet conditions generally results in more wear than testing under dry conditions. This is because paste bond strength is susceptible to ambient moisture content, and wet-dry cycles in the concrete may reduce its abrasion resistance (Nanni 1989).

An example of the use of abrasion-resistant concrete is that some barges in British Columbia were topped with high-strength concrete decks containing corrugated steel fibers (Woodhead 1991). The surfaces were finished by adding a mineral aggregate surface hardener and then power trowelling. The contractor for the project found that the surface hardener made the top cure faster than the bottom, resulting in surface cracking, so the surface hardener was rejected. After six months, the concrete showed little wear or distress. The use of abrasion-resistant concrete in this application was due to the introduction of front-end loaders for removal of wood chips from the barges and the requisite need for a more wear-resistant surface (Woodhead 1991).

3.4.2 *Crushing*

"Crushing," in the context of this research, refers to localized concrete damage caused by concentrated stresses that either exceed the concrete's strength or are high enough to lead to damage after

many loading cycles. The latter would be considered a type of fatigue damage. It was first proposed as a mechanism for RSD by Volpe researchers studying a derailment near Home Valley, Washington (Figure 3.1). Crushing concentrated stresses may come from poor load-distribution among adjacent ties, changes in track-substructure stiffness, or track-geometry defects, particularly in curves. Choros et al (2007) considered the stress distribution under the rail as an eccentrically-loaded foundation, assuming a trapezoidal or triangular stress distribution resulting from a given L/V ratio. As the L/V ratio increases, the stress on the field side of the rail seat increases, and this effect becomes magnified if the rail is allowed to roll (torsion) and loose contact on the gauge side. Choros (2009) suspected that both crushing and abrasion were occurring simultaneously in this case.

The researchers made their predictions by using the railroad's track geometry measurements recorded shortly before the derailment to show that trains were running at overbalanced speeds and used these data as input to NUCARS simulations to get calculated L/V ratios (Choros et al. 2007).

This particular derailment and its proposed cause were considered by both the railroad and the researchers to be a rare case with potentially catastrophic consequences (Choros 2009). One example of some of the most extreme wear at this derailment site is shown in Figure 3.1. The Volpe researchers also considered that stopping the initiation of this mechanism would be the best approach, since once it develops and becomes self-accelerating wear, the stress distributions become more eccentric. According to their calculations, extreme stresses in excess of 16,000 psi could be expected, and there is no cost-effective way to design a tie or a concrete mix to resist such stresses (Choros 2009). The more effective approach would be to target the track problems that lead to concentrated stresses at the rail seat, reducing the demands on the material.

In general, though, higher strength concrete with a dense, strong paste and strong aggregate would be expected to provide better resistance to crushing. Currently, concrete ties are made with mixes that have 28-day compressive strengths well above the AREMA minimum of 7,000 psi, reaching 11,000 psi or more.

3.4.3   Freeze-Thaw Cracking

Freeze-thaw cracking results from the expansion of freezing water, flow of water during freezing, or other processes during freeze-thaw cycles that create damaging stresses in the concrete. Bakharev (1994) hypothesized that if the concrete pores reached critical saturation (greater than 90% by volume), then the paste cannot relieve the pressures caused by freezing expansion.

Bakharev listed a number of factors that affect the durability of concrete to freeze-thaw cycles. In general, the distribution and size of air voids in the cement paste play a major role in determining whether freezing pore water results in damaging pressures. The pore size and distribution are largely controlled by the addition of an air-entraining admixture, the w/c ratio, methods of placing and finishing the concrete, and curing conditions. If the coarse aggregate in the concrete is itself susceptible to deterioration by freeze-thaw cycles, or if any cracks are present in the concrete and become saturated, these could be other mechanisms by which freeze-thaw cycles lead to damage (Bakharev 1994).

Chapter 30, Part 4 of the AREMA Manual for Railway Engineering (AREMA 2009) recommends a minimum of 4.5% air content in the fresh paste, 3.5% air content in the hardened paste, and a maximum air void spacing of 0.2 mm for adequate freeze-thaw durability. AREMA (2009) also recommends regularly testing the concrete mix with ASTM C666 Method A to 90% at 300 cycles to ensure freeze-thaw durability. According to the American Concrete Institute (ACI), a desirable air content is between four percent and eight percent of the concrete by volume, depending on maximum aggregate size. The smaller the aggregate, the more paste is typically required to obtain the proper workability, and, therefore, more entrained air has to be added to the mix (Mindess et al. 2003).

It is well understood that freeze-thaw cracking can be a primary mechanism for concrete durability problems in highway pavements and bridge decks, as well as other applications (Mindess et al. 2003). Bakharev (1994) found microcracks in concrete ties with RSD which could have been caused by freeze-thaw cycles or hydraulic pressure. The next step toward understanding the role that freeze-thaw cracking actually plays in RSD would be to gather data on the occurrences of RSD in track, noting the air content of the concrete ties in use, and compare this with the annual number of freeze-thaw cycles in each

location where RSD has (and has not) been found. Of particular interest would be to consider the air content of concrete ties and slab track used around the world, in regions with many annual freeze-thaw cycles, to see if these international cases have freeze-thaw durability problems. The areas of the US receiving the most annual freeze-thaw cycles are typically the Midwest and the central Great Plains, although a large percentage of the US receives multiple cycles annually (Zhang et al. 2003).

3.4.4   *Hydraulic Pressure Cracking*

Hydraulic pressure cracking is thought to be the result of high pore pressures in saturated concrete caused by the wheel loads forcing water in and out of the concrete pores. Hydraulic pressure cracking may occur when water beneath the tie pad is forced into the pore system near the surface, creating tensile stresses in the solid concrete skeleton. If the tensile stresses exceed the tensile strength of the concrete, then microcracking may result. This cracking may propagate with further hydraulic pressure cycles. Because compressive stresses are also acting near the surface, resulting from both the wheel loads and the prestressing steel, the net stress in some direction has to be tensile in order for damage to occur. Also, the concrete may need to be saturated, at least locally, for damaging pressures to develop. If the concrete pores are not saturated, water might flow into air voids, relieving the pressure. Related to this consideration, Bakharev (1994) suggested that with proper air entrainment, the pores could be closely spaced to prevent pressures from getting too high.

Bakharev tested the hydraulic pressure cracking hypothesis with a simple two-dimensional model. The location of stresses predicted by her model was consistent with the subsurface cracking she observed in the sample RSD ties. The ties had characteristic cracks described as vertical cracks reaching as deep as 0.8 inch below the surface and horizontal cracks at depths of 0.2 inch and 0.6 inch. According to her model, there should be a section of the concrete two to four inches below the rail seat surface that will experience significant tensile stresses, even when the compressive wheel stresses are superimposed onto the pore pressures (Bakharev 1994). This analysis did not account for the effects of the prestress, which results in a horizontal compressive stress that may counteract tensile pore pressures in the horizontal direction. Concrete ties are prestressed so that the concrete is in compression at rest. When the

ties are loaded in flexure by axle loads, the precompression from the prestress cancels out the flexural tension, allowing the ties to withstand higher loads without cracking. Part 4 of AREMA Chapter 30 (2009) recommends that precompression at any point in the tie should be at least 500 psi but no more than 2,500 psi. The precompression is significant and should be superimposed on the pore pressure and load stresses in a hydraulic pressure cracking model.

The hydraulic pressure cracking hypothesis hinges on tensile stresses damaging the concrete. Concrete is much weaker in tension than in compression and a general rule is that the tensile strength is approximately ten percent of the compressive strength. Another relevant approximation is that cyclic stresses greater than half of the concrete's strength can lead to fatigue damage (Mindess et al. 2003). AREMA (2009) recommends a minimum 28-day compressive strength of 7,000 psi. For hydraulic pressure cracking to be plausible, net tensile stresses in the concrete should be on the order of 350 to 700 psi or greater.

Models have been created to characterize the distribution of water pressure in saturated asphalt pavements under highway traffic, similar to the hydraulic pressure cracking theory for concrete ties. One model predicted that higher pressure gradients, water velocities, and shear stresses would be found in the upper 0.4-1.6 inches of the pavement and that the pore pressures and water velocity varied nonlinearly as a function of depth due to the heterogeneity of the asphalt concrete (Kutay and Aydilek 2007). Another model predicted that, in the upper pavement layer, hard asphalt (characterized by high stiffness and low porosity) experienced higher pore pressures (290 psi) and lower water velocities (70 microns per second), while soft asphalt (low stiffness and high porosity) experienced lower pore pressures (2.9 psi) and higher water velocities (20,000 microns per second) (Kettil et al. 2005). These models suggest that pore pressures near the surface could be in the magnitude of stresses that could lead to fatigue cracking if sufficient repeated loading occurs.

3.4.5   *Hydro-Abrasive Erosion*

Concrete wear through the action of flowing water and suspended-particle abrasion has been studied in many contexts, from wear of concrete pipes and walls in hydraulic structures (Momber and

Kovacevic 1994) to the application of abrasive erosion to decontaminate nuclear facilities (Goretta et al. 1999). Here, this action is referred to as hydro-abrasive erosion, though it is also referred to in the literature as abrasive erosion or suspended-particle erosion. The parameters that influence wear rate are flow velocity, the angle of impact relative to the concrete surface, exposure time, concentration of suspended particles, and particle size, shape, and hardness (Momber and Kovacevic 1994, Goretta et al. 1999, Finnie 1960). Similar to abrasion, analytically predicting the potential for hydro-abrasive erosion may be difficult. Finnie noted that "if a prediction of erosion is required, there appears to be no satisfactory approach except that of testing under the specific conditions of interest" (1960).

The erosion process is typically initiated at the interface between the hardened cement paste and the aggregate grains. Damage results when high-velocity flow generates and expands microcracks, while the toughening mechanisms from the aggregate-crack interaction resist this erosion process. Similar to what would be expected with hydraulic pressure cracking, it is only when the microcracks connect that mass loss results. Before mass loss occurs, there is an "incubation period" when microcracks form in the interfacial zone (Momber and Kovacevic 1994).

Water jet flow without suspended particles and oriented perpendicular to concrete, resulted in a critical flow velocity of approximately 400 feet per second (ft/s) that induced erosion. The critical exposure time varied with the water velocity, but it was at least 0.2-1.0 seconds with a 525-400 ft/s jet velocity (Momber and Kovacevic 1994). The critical flow velocity for erosion by water alone is higher than the critical velocity for suspended particles abrading a surface. Goretta et al (1999) conducted experiments with different sizes of angular or rounded abrasive particles suspended in water, impacting the concrete surface at either 20 or 90 degrees. The particle velocity was 165 ft/s, and particle sizes ranged from 42 to 390 micrometers, corresponding to fine sand. An unexpected result was that the finest particles led to the highest wear rate. Hu et al (2002) demonstrated that, under their test conditions, the particle velocity was between 60% and 72% of the overall flow velocity, since the particles would come in and out of suspension as they impacted the concrete surface. They measured wear due to particle

velocity between 180 ft/s and 550 ft/s (Hu et al. 2002). Based on the available literature, an estimate for critical suspended-particle velocity of parallel flow is 165 ft/s.

Considering the geometry of the tie-pad/rail-seat interface, abrasive particles that intrude from the outside or are the result of internal wear would only be a few millimeters in diameter or less. Many of the abrasive particles might be lodged in the tie pad or rail seat material. Only the very fine particles would be in suspension in the surface water, but some of the larger particles might become dislodged and enter into suspension when flow is present. Additionally, the majority of flow will be parallel to the concrete surface. When flow is mostly parallel to a surface, researchers commonly consider the angle of attack of a suspended particle as 15-20 degrees, as it falls out of suspension. For hydro-abrasive erosion to occur in this case with parallel flow, the surface water would have to propel very fine abrasive particles at 165 ft/s or greater.

3.4.6   *Cavitation Erosion*

Cavitation erosion is surface wear due to bursts of high pressure created by sudden changes in water flow over the concrete surface. It is possible that this might occur when water trapped beneath the tie pad is accelerated by wheel loads. Cavitation is a phase transition from liquid to vapor that occurs during a drop in the liquid's pressure to the vapor pressure at a given temperature. This process is sometimes referred to as "cold boiling" and is analogous to the phase transition from liquid to vapor that occurs due to an increase in temperature (Figure 3.6). The vapor bubbles that form are unstable, and when they burst against a surface, pressures as high as tens of thousands of psi can be released over very small areas, which over time can cause surface erosion (Franc and Michel 2004).
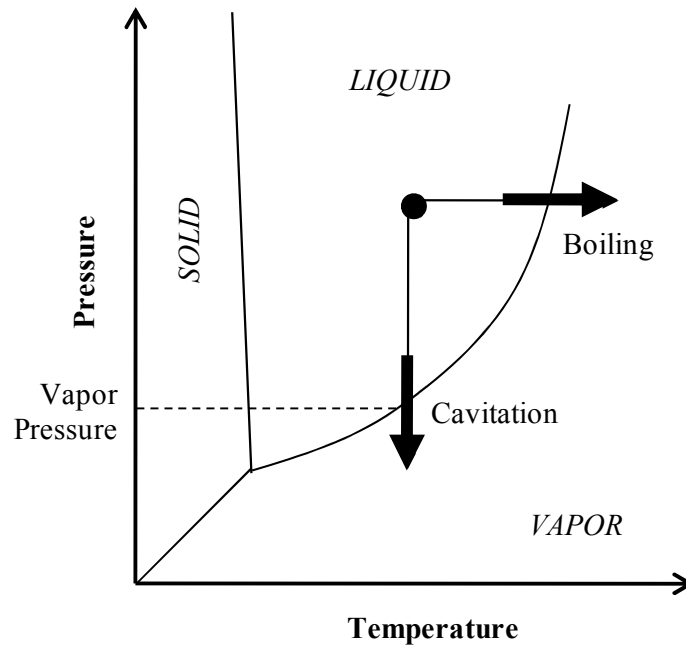
Figure 3.6 Phase diagram of water, illustrating the distinction between cavitation and boiling (adapted from Franc and Michel 2004)

Cavitation can have multiple causes, such as flow obstructions at dams, spillways, or turbine blades; ultrasonic vibrations (20 kiloHertz (kHz) or greater frequency) in fluids; water jet demolition of concrete surfaces; and sudden changes of flow in hydraulic systems, such as those caused by a water hammer (Franc and Michel 2004, Momber 2000, Haestad Methods et al. 2003). It is the water hammer example that is most like the rail seat cavitation hypothesis that I am discussing. In each of the previous examples, the velocity of the fluid changes rapidly, causing the fluid pressure to change to maintain conservation of energy, and, under the right conditions, this can lead to cavitation (Franc and Michel 2004). Cavitation may occur when water trapped beneath the tie pad is accelerated by wheel loads if the resulting pressure fluctuation reaches negative gauge pressures, or suction, on the order of the vapor pressure of water (0.36 psi absolute (psia); -14.34 psi gauge (psig) at 70°F) (Munson et al. 2006).

On concrete surfaces, cavitation tends to erode the weaker cement paste, exposing the coarse aggregate. Although most examples of cavitation erosion of concrete result from continuous exposure to

cavitating flows, it has been found that as little as two seconds of exposure to cavitation can lead to measurable damage (Momber 2000).

As part of an earlier investigation into the mechanics of RSD, Pandrol developed the Jetmil test to create cavitation erosion by spraying a concrete surface with water at a pressure of 6,000 psi from a set of rotating nozzles (Bakharev 1994). Bakharev used the Jetmil test apparatus on different concrete mixes and recorded depths of wear between 0.06 and 0.10 inch on a 5.25-inch-diameter surface after ten minutes. The Jetmil created surfaces that appeared similar to the RSD surfaces found in service (Figure 3.3), but at the microscopic level, the wear on new ties subjected to Jetmil tests was inconsistent with that found in the RSD field samples (Bakharev 1994). Although Bakharev did not find evidence of cavitation in her sample set of RSD ties, she also did not find conclusive evidence to eliminate cavitation erosion as a potential deterioration mechanism.

3.5   Focus on Hydraulic Mechanisms

Experimentation and field knowledge suggest that moisture is necessary for substantial RSD to occur. Possible explanations for this are that hardened concrete is less resistant to abrasion or crushing when it is wet, higher stresses can develop during freeze-thaw cycles when concrete is saturated, or the acceleration of water under traffic load may deteriorate the concrete through hydraulic pressure cracking, hydro-abrasive erosion, or cavitation erosion. These last three are jointly referred to as the hydraulic mechanisms of RSD.

Concrete deterioration due to abrasion, freeze-thaw cracking, or crushing in wet versus dry conditions is understood through standard laboratory tests and experience with structural concrete and highway pavements. Researchers have shown that concrete abrasion under wet testing conditions may be as little as 10% or as much as 100% more than the abrasion under air-dry conditions (Nanni 1989). The conditions for abrasion have been observed when locomotive sand and metal shavings (from rail or wheels) enter beneath the tie pad (Reiff 1995). Freeze-thaw damage is possible in regions with the necessary climate, though the entrained air in concrete ties should prevent this. Volpe researchers

presented evidence that rail seat stresses can become highly concentrated under certain combinations of degraded track geometry and damaged rail seats on a curve, leading to crushing (Choros et al. 2007).

Compared with abrasion, freeze-thaw cracking, and crushing, it is not as clear whether conditions exist for hydraulic pressure cracking, hydro-abrasive erosion, or cavitation erosion to contribute to RSD. Simple models have suggested that these theories are feasible, but little experimental data exists that is relevant to the theories. The major questions pertaining to the hydraulic mechanisms are whether they are feasible and, if so, how they can be mitigated in the design and maintenance of concrete ties. These questions led me to further refine the focus of my investigation to the hydraulic mechanisms, the least understood of the potential concrete deterioration mechanisms.

CHAPTER 4: ANALYTICAL MODELS OF THE RAIL SEAT SYSTEM

4.1   Introduction and Definitions

In this chapter I discuss multiple analytical models that describe the idealized actions and responses of the rail seat system. The forces that act on the rail seat, the vertical motion of the track, the flow and pressurization of water, and the effective stress of the concrete beneath the rail seat are considered. The objective of this chapter is to lay the theoretical framework that will aid in interpreting the experimental results, comparing the laboratory test conditions with track conditions, and estimating damaging values of water pressure or velocity. The variable symbols considered in this chapter are listed here for reference, and the coordinate system is defined (Figure 4.1).
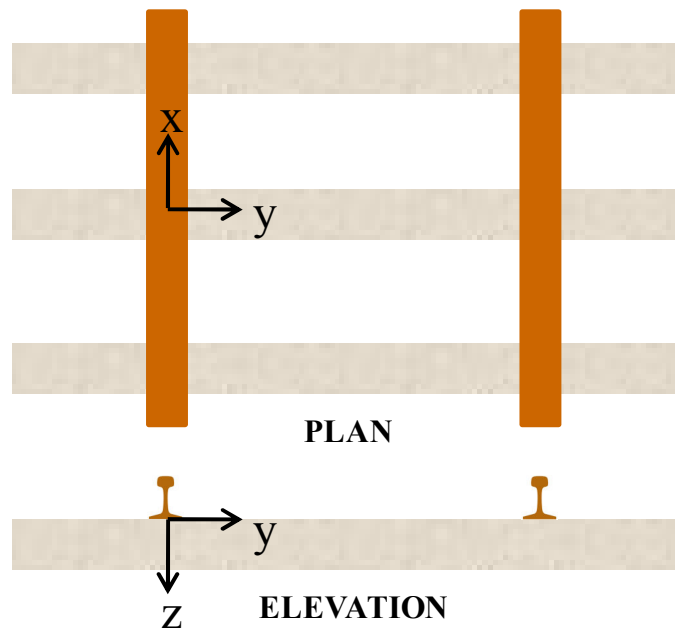

Figure 4.1 Coordinate system, with the center of the rail seat as the origin

A Cross-sectional area of the tie

b_r Base width of the rail

b_{rs} Base width of the rail seat area

b_t Base width of the tie

c Distance from neutral axis of section to extreme fiber, assumed to be half the section height

E Young's modulus of the tie

E_{Rf} Effective resilient modulus of the foundation

E_{Ri}	Resilient modulus of foundation layer i
e	Eccentricity of the prestress force
F_i	Force terms for the Galerkin method
f	Loading frequency, in cycles per second or Hertz (Hz)
f_c'	28-day compressive strength of concrete
f_t'	28-day tensile strength of concrete
G	Shear modulus of the tie
H	Thickness of ballast and subballast layers ($h_1 + h_2$)
h_i	Thickness of foundation layer i
I	In-plane moment of inertia of the tie
K_{ij}	Stiffness terms for the Galerkin method
k	Permeability of the concrete
L	Length of the tie
L/V	Ratio of lateral component to vertical component of wheel load
M	In-plane bending moment in the tie
m	In-plane moments applied to the beam, including eccentric prestress moment
N	Axial prestress force in the tie
O_i	The ith term in Odemark's method
P	Component of wheel load supported by the tie, normal to the rail seat surface
p	Surface water pressure at the rail seat
Q	Shear force in the tie section
q	Vertical forces applied to beam, including rail seat load and foundation reaction
R_i	Geometric terms in Holl's equations, for $i = 1, 2, 3$
r	Radius of the loaded area in Odemark's method
S	Principal state of total stress, a 3 x 3 diagonal matrix containing the principal stresses
S'	State of effective stress, a 3 x 3 diagonal matrix in principal coordinates
S_B	Contributions from a prestressed beam on an elastic foundation to the total stress-state, a 3x3 matrix in *xyz* coordinates
S_H	Contributions from a uniform horizontal load to the total stress-state, a 3x3 matrix in *xyz* coordinates
S_V	Contributions from a uniform vertical load to the total stress-state, a 3x3 matrix in *xyz* coordinates
S_{xyz}	State of total stress, a 3x3 matrix in *xyz* coordinates
U	State of stress expression for pore water pressure, a 3x3 diagonal matrix
u	Pore water pressure in the concrete
V	Train speed

v	Surface water velocity
w	Vertical deflection of beam section
x	Longitudinal direction, along the axis of the rail
y	Lateral direction, along the axis of the tie
z	Vertical direction, positive downward; also refers to vertical position or displacement of the rail
α_i	Coefficients for the vertical displacement of the beam
β_i	Coefficients for the in-plane rotation of the beam
δ	Virtual work operator
θ	In-plane rotation of beam section
λ	Damping factor for beams on elastic foundation
μ	Track modulus, pounds per inch per inch (lb/in/in)
μ_f	Modulus of the foundation reaction, psi
v_f	Poisson's ratio for the foundation
v_t	Poisson's ratio for the tie
ξ	Vector of shape functions for the in-plane rotation of the beam, used for Galerkin's method
σ_i	Normal stress on a face perpendicular to the i-direction, positive when compressive (i could refer to x, y, z, 1, 2, or 3)
σ_H	Uniform, horizontal rail seat stress
σ_V	Uniform, vertical rail seat stress
τ_{ij}	Shear stress on a face perpendicular to the i-direction, positive when acting in the j-direction (i and j could refer to x, y, or z)
ψ	Vector of shape functions for the vertical displacement of the beam, used for Galerkin's method

4.2   Track Forces

Because hydraulic pressure cracking and hydro-abrasive erosion, as well as abrasion and crushing, are direct consequences of the loads applied to the rail seat, it is important to estimate and analyze the forces to which the rail seat is subjected.

The wheel load magnitudes were estimated assuming 286-kilopound (kip or k) cars, 1:40 rail cant, 0.52 lateral-to-vertical (*L/V*) ratio, 28-inch tie spacing, and a 200% impact factor for high dynamic loads. The 0.52 *L/V* was taken from the accelerated rail seat deterioration (RSD) test, which is documented in the American Railway Engineering and Maintenance-of-Way Association (AREMA) Manual for Railway Engineering Chapter 30, Part 2 (AREMA 2009). The 28-inch tie spacing was used to ensure a conservative load distribution factor (AREMA 2009, Chapter 30, Part 4). The 200% impact factor was also taken from AREMA Chapter 30, Part 4 (AREMA 2009). From Figure 1.8, using the 2009 curve, 28-inch tie spacing results in a distribution factor (DF) equal to 55%. With these assumptions, the static normal force on one rail seat is approximately 20 kips, while the dynamic normal force on one rail seat is as high as 60 kips (Figure 4.2 and subsequent calculations).
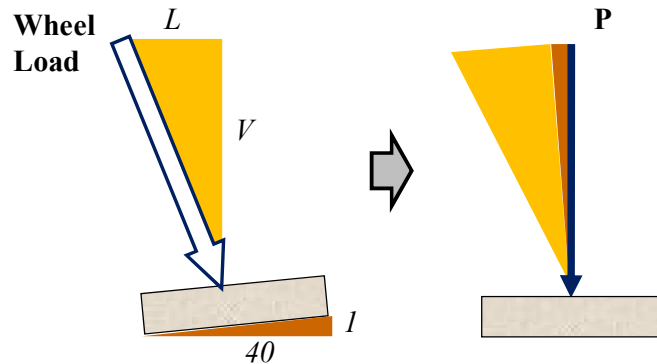

**Figure 4.2 Conversion of the wheel load vector
to its component normal to the rail seat surface, P**

$$P = \cos\left[\arctan\left(\frac{L}{V}\right) - \arctan\left(\frac{1}{40}\right)\right](DF)\frac{286 \text{ kips}}{8 \text{ wheels}}$$

$$P = \cos\left[\arctan(0.52) - \arctan\left(\frac{1}{40}\right)\right](0.55)\frac{286\,kips}{8\,wheels} = (0.90)(0.55)(35.75\,kips) = 17.7\,kips$$

$$P \cong 20\,kips$$

$$P_{max} = (1 + IF)\,P = (1 + 2)\,20\,kips = 60\,kips$$

To estimate frequency of wheel loads and vertical track motion, a 50-foot rail car with simple axle spacing (Figure 4.3) was selected because it is representative of many heavy axle load cars in service in North America. In general, the axle spacing varies among different sizes and types of rail cars. For this study, the axle spacing in Figure 4.3 is sufficiently representative of 50-foot rail cars in service.

3'   6'   32'   6'   3'
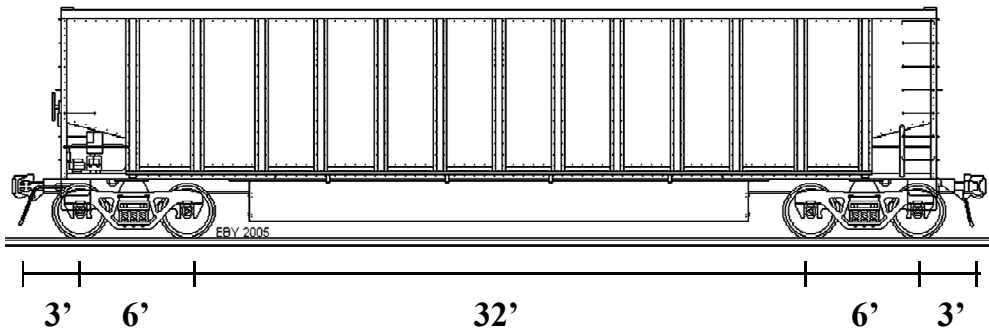
Figure 4.3 50-foot rail car, with idealized axle spacing
(adapted from Trainiax.net 2010)

To estimate the frequency of wheel loads, 6-foot (ft) and 32-ft axle spacings were considered (Figure 4.3), as well as an "average" axle spacing which was the length of the rail car divided by four axles. A selected set of loading frequencies were converted to equivalent train speeds (in miles per hour (mph)) for the three axle spacings (Table 4.1). These values were calculated by multiplying a selected frequency by an axle spacing and then converting to mph. The frequency is in Hertz (Hz) and the axle spacing is in feet. This loading frequency assumes a continuous, sinusoidal loading waveform. Due to the limitations of the available test frame and hydraulic equipment, the load frequency for the laboratory tests was limited to four Hz (see Section 6.2.3).

**Table 4.1 Equivalent speed for different axle spacing,
as a function of the selected load frequency, f**

	Train Speed (mph)		
f (Hz)	Minimum Axle Spacing, 6.0-ft	Average Axle Spacing, 12.5-ft	Maximum Axle Spacing, 32.0-ft
0.5	2	4	11
1.0	4	9	22
2.0	8	17	44
4.0	16	34	87
10.0	41	85	218
15.0	61	128	327

The magnitude of the rail seat load is a function of many factors, such as the static wheel load, the train speed, the quality of the wheel/rail interface, the stiffness and uniformity (both transverse and longitudinal) of the track substructure (the ballast, subballast, and subgrade), the stiffness and load attenuation of the tie pads and fastening system, and the distribution of the loads among adjacent ties (tie spacing and support transitions). One of the aforementioned factors that is easy to monitor is the dynamic wheel load, and a network of wheel impact load detectors (WILD) have been installed across North America to identify wheels that produce high impacts and flag these wheels for removal. High impact wheels are those with out-of-round treads that result in irregular, dynamic wheel/rail contact forces that can be very damaging. The Association of American Railroad's (AAR) guidelines require that wheels producing over 90 kips be flagged for opportunistic repair, while wheels producing over 140 kips must be removed immediately (AAR 2010). The implementation of WILD has been quite successful, resulting in a significant decline in the number of high impact wheels in service (Kalay 2010). This trend holds true for the two WILD distributions compared here (Table 4.2), though these two data sets are quite different in size. The WILD distribution from 2003 came from the Chicago Freight Car Leasing Company, and the

WILD data is specifically for the company's fleet of cars (Weed and Lonsdale 2004). The 2008 WILD distribution came from a Class I railroad, and the data is from multiple WILD sites across the railroad's network, including all cars that passed these sites.

Table 4.2 Distributions of rail seat loads from WILD measurements (assuming that the rail seat load is 50% of the wheel load)

Rail seat load, P, half of wheel load (kips)	Percent of loads, Rail Car Lease Fleet* (2003)	Percent of loads, Class I railroad (2008)
0-25	80.93%	94.21%
25-35	12.38%	4.69%
35-45	4.50%	0.94%
45-55	1.59%	0.14%
> 55	0.60%	0.02%
Sample size:	0.03 million	59.6 million

*(Weed and Lonsdale 2004)

The most typical value used to quantify the restraint the fastener system provides to the rail is the spring-clip toe load. The original e-clip system had a rated toe load of 2.75 kips per clip, with a stiffness of 6,300 pounds per inch (lb/in) (Pandrol USA 2004a). The first Safelok system had a rated toe load of 4.5 to 5.6 kips per clip, with a stiffness of 8,800 lb/in (Pandrol USA 2004b). The load on the rail seat at rest could be approximately five to ten kips, depending on the system in use. The toe load tends to decrease over the life of the clips, due to plastic deformation of the clips or reduction of clip deflection due to loss of the materials at the rail seat – wear of the pad, the concrete, or the insulators. The tightness of the fastening system influences the amount of movement of the rail relative to the tie, as well as the intrusion of moisture and abrasive fines under the tie pad.

4.3 Track Motion

In order to estimate the practical range of vertical deflection, velocity, and acceleration for railroad track, Talbot's equation for vertical track deflection was considered and compared with measurements of track motion in the literature. The Talbot equation was originally derived assuming the rail to be a beam on a uniform elastic foundation that represents everything supporting the rail (tie pad/plate, tie, ballast, subballast, and subgrade). It is a static model that cannot account for the dynamic vibrations that characterize actual track-train interaction. Using the coordinate system defined in Section 4.1, Talbot's equation for vertical track deflection is expressed as (Hay 1982):

$$z = \frac{P_{wheel}}{(64EI\mu^3)^{0.25}} e^{-\lambda|x|} \left(\cos\left(\lambda|x|\right) - \sin\left(\lambda|x|\right) \right)$$

The wheel load was based on a 286-kip car (P_{wheel} = 40 kips), the Young's modulus of the rail was taken as 30,000 kips per square inch (ksi), 136 RE rail was selected (I = 94.9 in^4) (NS Railway 2001), the track modulus μ represents the stiffness of the track supporting the rail, and the damping factor is:

$$\lambda = \left(\frac{\mu}{4EI} \right)^{0.25}$$

The above equation is for the deflection under one wheel, and it is important to take the absolute value around x to get a symmetric function about the point of load application (x = 0). To consider the effect of train speed on the rate of change of this static deflection, I considered that the location of the load x varied with time t at a constant speed V: $x(t) = Vt + x_0$. So considering the deflection as a function of time, the deflection will be a maximum at the time when $x(t)$ is zero – this can be controlled by selecting the appropriate offset x_0.

The track deflection under multiple axles can be considered by enforcing superposition with individual wheel loads. This is effectively done by choosing different offsets for each wheel load according to a given axle spacing. For this study, four 50-foot cars were considered (Figure 4.3), totaling 16 axles. With the resulting superposition, it is convenient to consider the axles as sets of four that surround a coupler. The deflection of these four axles affect the deflection under each of the respective

wheels, while being effectively independent of the deflections due to wheels in other four-axle sets (for most realistic cases of track modulus rail moment of inertia). To distinguish axles within the car, the axles nearest to the couplers will be referred to as "outer axles" while the others as "inner axles."

The vertical velocity and acceleration were estimated with numerical differentiation of the total deflection-time curve under 16 axles. The resulting theoretical track motion (Figure 4.4) shows the vertical motion experienced by a single location on track over time – positive motion is directed downward. The acceleration is given in units of acceleration due to gravity ($g = 9.81$ m/s^2 = 32.2 ft/s^2). The Talbot model predicts that, for uniform wheel loads, uplift occurs on either side of a four-axle or two-axle set, which is approximately where the maximum velocity and upward acceleration occur. The maximum downward acceleration is expected underneath the coupler, and the outer axles surrounding the couplers are where the greatest deflection is expected.
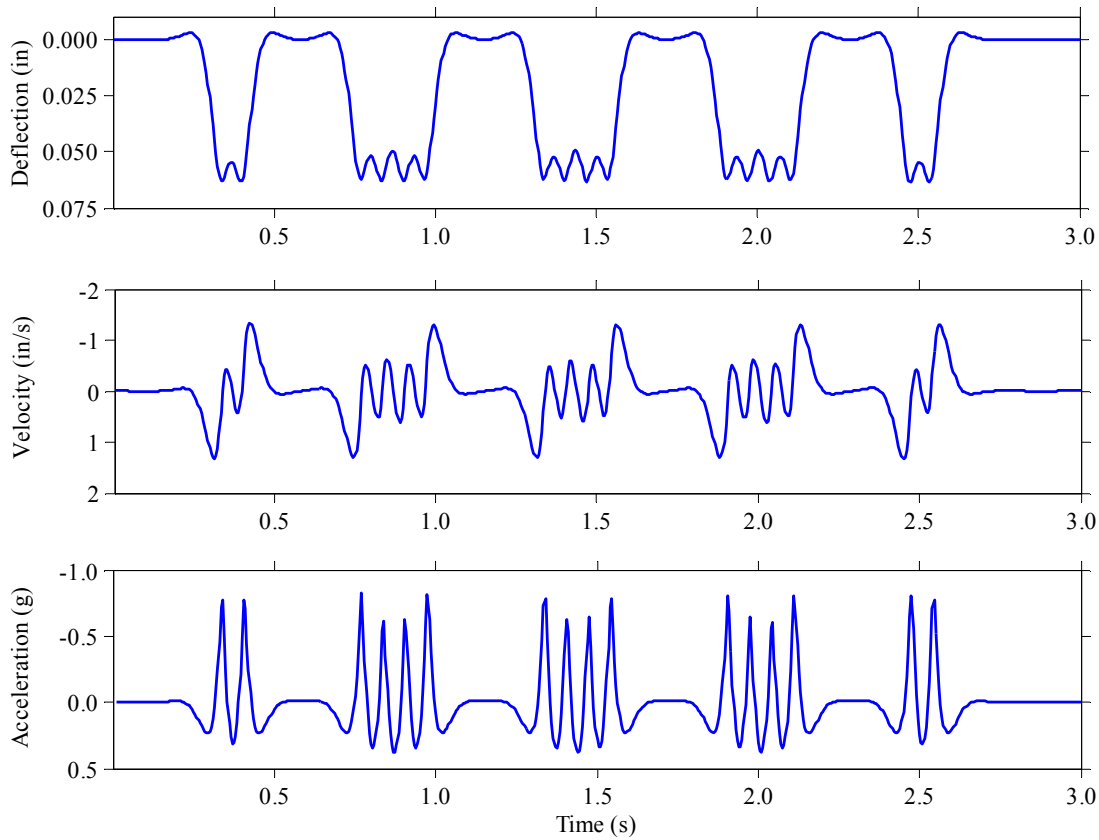

Figure 4.4 Talbot model of track motion under base conditions

The Talbot model is very sensitive to the track modulus, which can vary substantially depending on the characteristics of the ties and fastening system, the quality of the ballast and subballast, and the subgrade stiffness. In temperate climate regions, the track modulus is seasonal, as the subgrade may be stiff in the winter and soft in the spring (Hendry 2007). Deflection and uplift are nonlinear, inverse functions of track modulus (Figure 4.5).
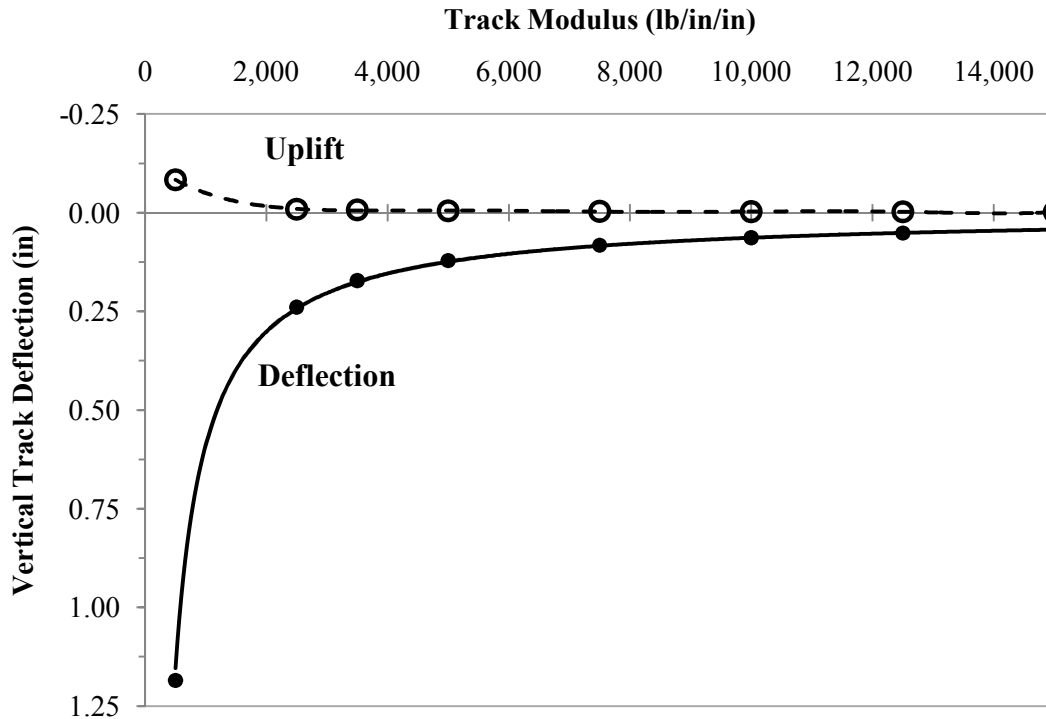

Figure 4.5 Relationship between track modulus and peak track deflection and uplift

The deflection between wheel loads is nonzero (Figure 4.4), and this implies that there is some effective force being felt at these points. The amount of "return deflection" between adjacent axles - referring to the minimum deflection that occurs between two maxima deflections (Figure 4.4) - depends on the track modulus and the rail moment of inertia. By considering this return deflection relative to the maximum deflection under a single wheel load, the effective load due to deflection from multiple axles is defined as:

$$P_{eff}(x) = z(x) \cdot (64EI\mu^3)^{0.25}$$

Plotting the effective load under the outer axle and the coupler versus track modulus (Figure 4.6) reveals that the ratio of the effective return load to the maximum effective load goes to unity as the track modulus goes to zero. With a low track modulus, a fixed point on the track feels a single load pulse with each four-axle set, whereas with a stiff track modulus, each wheel load is a distinct load pulse. According to Talbot's model, for track modulus up to 15,000 lb/in/in, the minimum effective return load is approximately 72% of the maximum effective load. This suggests that during the passage of a four-axle set over a rail seat, the load cycles between some maximum value and at least 72% of this maximum. In other words, less than 30% of the load is released between adjacent axles in a four-axle set. Talbot modeled the track as a continuous elastic support for the rails, but in reality, the rails are supported by rail seats at discrete points. Considering this factor would probably result in more distinct load cycles than Talbot predicts.
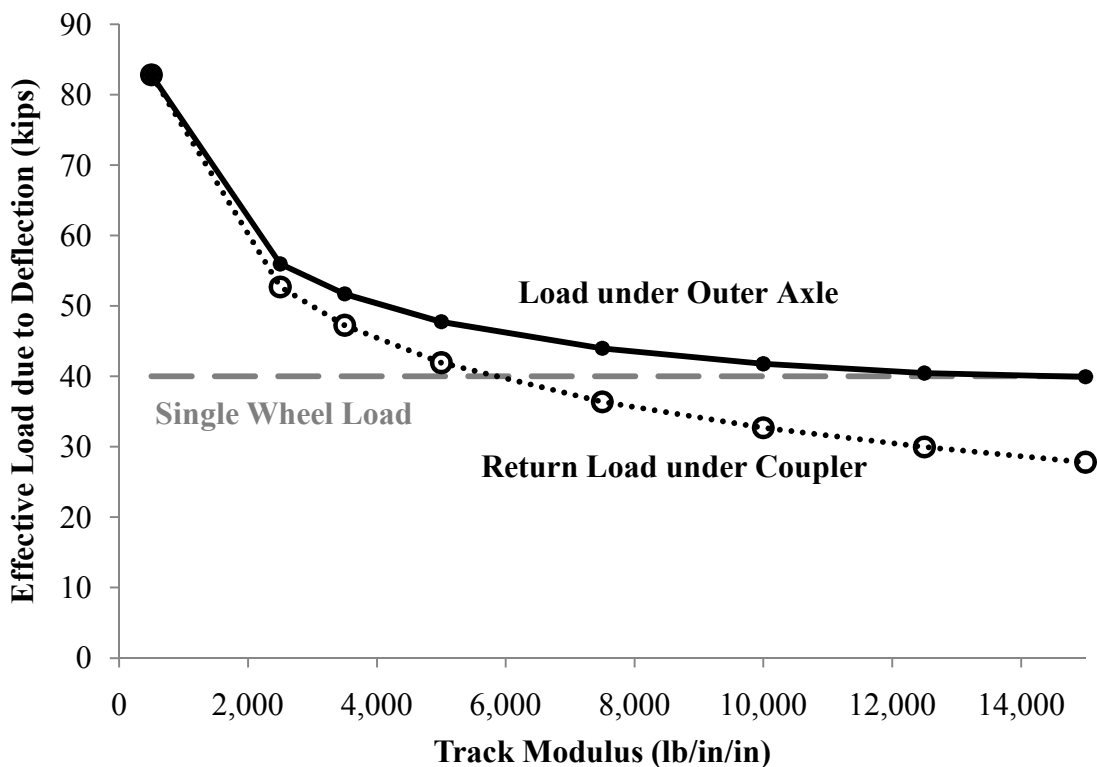

Figure 4.6 Relationship between track modulus and the effective load due to deflection

To estimate the range of vertical motion of the track, the Talbot model was run within the limits given in Appendix C (Table C.1) to find upper bounds of deflection, velocity, and acceleration (Table 4.3). More detailed results from the Talbot model, including the introduction of high impact wheels, are given in Appendix C. Also included in Table 4.3 are some extreme track motion values that were found in the literature. The deflection and uplift measurements came from a study of concrete-tie track on soft, peaty soil in Northern Ireland. The subgrade had an estimated resilient modulus between 370 and 670 psi, and the measurements were taken during the passage of a passenger train at 55 mph, with car static wheel loads of 11 kips and locomotive static wheel loads of 20 kips (Hendry 2007). The vertical track velocity and acceleration measurements came from a study of the vibrations caused by the passage of a high-speed Thalys train in Europe. The Thalys train was traveling at 194 mph, the rail had a moment of inertia of 73 in^4, and the car static wheel loads were probably 20 kips or less (Degrande and Schillemans 2001).

Table 4.3 Upper bounds of vertical track motion

Parameter	Units	Talbot Model	Measurements
Deflection	in	0.67	0.55*
Uplift	in	0.03	0.04*
Velocity	in/s	11.0	7.9[†]
Acceleration Down	g	1.71	12[†]
Acceleration Up	g	4.40	25[†]

[*]From track deflections on soft, peaty soils in Northern Ireland (Hendry 2007)
[†]From vertical rail motion during passage of a high-speed Thalys train
(Degrande and Schillemans 2001)

For deflection, uplift, and velocity, there is fairly good agreement between the observed values found in the literature and the values calculated using Talbot's model. However, the acceleration was about five to seven times higher than what the static Talbot model predicted. This is most likely due to the dynamics and vibrations of the track that a static model like Talbot's model cannot account for.

Talbot's model predicts that the track acceleration is largely a function of train speed, so the acceleration of the track with trains operating at 194 mph may be very different than what typical North American freight trains would generate (maximum allowable speed of 80 mph) (FRA 2010).

4.4   Hydraulics at the Rail Seat

A sudden change in flow in hydraulic systems, such as a system of pipes, is referred to as transient flow.   The abrupt type of transient flow is referred to as a "water hammer." A water hammer is a pulse of pressure that is created by a sudden acceleration of flow that was originally in a steady state. In piping systems, this can be caused by suddenly opening or closing a valve. The water hammer often oscillates between maximum and minimum pressures and dissipates over time until the flow returns to a steady-state condition (Haestad Methods et al. 2003). The hydraulic mechanisms of RSD rely on a water hammer, or pulse of water pressure, developing in the thin film of water between the tie pad and the concrete rail seat during a load cycle.

As wheels pass over a stationary point on a section of track, the rail is subjected to a vertical wave action that causes uplift of the rail ahead and behind a wheel and a downward deflection beneath the wheel, as illustrated in Figure 4.4. If the rail is not restrained vertically to the rail seat by the fastening system, some relative motion will occur, allowing a gap to form between the rail and the tie pad and/or between the tie pad and the concrete rail seat. This vertical wave action in a loose rail seat generates two distinct actions: a downward applied load and an uplift deflection of the rail relative to the rail seat.

Water may enter the pad/concrete interface in several ways: precipitation may enter directly between the pad and rail seat via tiny gaps and irregularities, it may enter if loading and uplift occur during or after precipitation, or the concrete may become saturated, allowing water to enter the interface by diffusion or by suction during a load cycle that draws water up from the concrete pores.

4.4.1   Surface Water

To look at how the interfacial water at the rail seat might respond to a normal force, two ideal scenarios may be considered. The first considers the case where there is a perfect seal around the perimeter of the rail seat and the concrete is impermeable so that all the energy from the wheel is

manifested as pressure in the water. In this ideal case, the water pressure would be the load, P, divided by the rail seat area, A. This is the case that Bakharev considered in her model of hydraulic pressure and effective stress (1994).

The second case is where the concrete is again considered impermeable but there is no seal around the perimeter of the rail seat. The water is accelerated by the wheel load and ejected from underneath the tie pad. This assumes that water is an incompressible fluid, so that all the water is ejected rather than being pressurized.

Considering Bernoulli's equation for pipe flow without losses, the energy in the water is divided among the pressure energy and the velocity energy (Munson et al. 2006):

$$\text{Water Energy} = p + \tfrac{1}{2}\rho v^2$$

Here, p is the pressure, v is the velocity, and ρ is the density of water (1000 kg/m^3). Theoretically, the water energy would be, at most, the energy imparted by the normal stress on the rail seat:

$$\text{Load Energy} = \frac{P}{A} \cong p + \tfrac{1}{2}\rho v^2$$

$$v \cong \sqrt{\frac{2}{\rho}\left(\frac{P}{A} - p\right)}$$

This derivation represents the maximum velocity that the water could have, assuming that all the load energy is transferred to the interfacial water at the rail seat. In reality, all of the load energy might not be transferred through the water, particularly if the water is not evenly distributed over the rail seat. There will also be energy losses to friction, heat, noise, and compressibility of the pad, among other possibilities. Other factors such as the permeability of the concrete, wetness of the pad surface, and volume losses to the outside, will play a major role. However, the Bernoulli equation, as presented here, illustrates the theoretical maxima for pressure and velocity in the cases where there is (1) a perfect seal ($v = 0$), (2) no seal ($p = 0$), or (3) an imperfect seal ($p \neq 0$, $v \neq 0$). The third case is probably closest to reality.

In this discussion I am considering a downward movement of the pad that generates a compressive force, but the same principles may also apply when there is an upward movement of the pad with tensile forces. The former case of an applied load would create positive water pressure, while the latter case of rail uplift would create negative water pressure, or suction. One important distinction between the load and uplift strokes is that the uplift stroke could draw water in from the surface of the tie surrounding the rail seat or from the concrete pores underneath the rail seat.

4.4.2   Pore Water

Concrete is a composite material containing coarse aggregate, fine aggregate, hardened cement paste, water, and air. The cement paste is a porous material that has some measurable permeability. The pores in the cement paste typically contain water and/or air. If the concrete is fully saturated, then all of its pores are filled with water. In an unsaturated concrete, the pore volume not taken up by water is filled with air. The movement of water through the pore system is complex, involving flow through capillaries (approximately on the micro-scale) and water stored in the intrinsic gel pores (on the nano-scale) (Mindess et al. 2003). Theoretically, at these scales, the water flow is complicated by viscous effects that generally do not govern pipe flow (Munson et al. 2006). A saturated porous media was analyzed in this study (Section 4.5.1), though some consideration was given to concrete that is unsaturated (Section 6.5.4).

4.5   Effective Stress Model[3]

The theory on hydraulic pressure cracking claims that pore pressures in the concrete become large enough that the concrete's tensile strength is exceeded, resulting in cracking or spalling (Bakharev 1994). In order to evaluate the feasibility of this theory, two elements were examined: (1) the specific pore pressure required to damage the concrete, and (2) the expected pore pressure in a typical concrete railroad tie.

To estimate the pore pressure required to do damage to the concrete, a model was created to calculate the effective stress beneath the center of the rail seat. This model is an adaptation of an

---

[3] Much of the discussion of the effective stress model was originally published in the Proceedings of the 2010 Joint Rail Conference in Urbana, Illinois, USA (Zeman et al. 2010b)

approach developed by Bakharev (1994). The effective stress of the concrete is the total stress – the sum

of all the mechanical stresses acting on an element of concrete – minus the pore pressure. With this

formulation, stress is taken as positive when it is compressive, and the pore pressure exerts a tensile stress

on the concrete, similar to what is experienced by the walls of a pressure vessel. It is the effective stress

that must be compared with the concrete's strength to determine if damage will occur.

Bakharev's effective stress model was for two-dimensional stresses, considering only the vertical

wheel load's contribution to total stress. My model also incorporates the contributions of lateral loads,

prestress, and flexure in three dimensions. I directly use Bakharev's formula for pore pressure

distribution, expanded to three dimensions.

Considering the effective stress in a concrete tie in three dimensions, the total stress state was

taken as the sum of the stress states from a uniform vertical load, a uniform horizontal load, and a

prestressed beam on an elastic foundation. The total stress state was converted to a principal stress state

that can be expressed by three mutually-perpendicular normal stresses and no shear stress (Hjelmstad

2005). The minimum of these three stresses is referred to as the minor principal stress. It represents the

direction in which the concrete is most susceptible to damage from pore pressure. The minor principal

stress is the total stress term used in the effective stress equation.

4.5.1   Pore Water Pressure

To estimate the pore pressure in the concrete for this study, the following approach was adapted

from Bakharev's (1994) work on hydraulic pressure modeling. The pore water is assumed to obey

Darcy's law. In three dimensions, neglecting changes in elevation, Darcy's law states that the flow

velocity (v) is equal to the permeability of the porous media (k) multiplied by the change in water pressure

(u):

$$v = k\nabla u = k\left(\frac{\partial u}{\partial x} + \frac{\partial u}{\partial y} + \frac{\partial u}{\partial z}\right)$$

If the concrete is assumed to be fully saturated, then conservation of mass applies:

$$\nabla v = \frac{\partial v}{\partial x} + \frac{\partial v}{\partial y} + \frac{\partial v}{\partial z} = 0$$

Imposing the conservation of mass in Darcy's law yields:

$$k\left(\frac{\partial^2 u}{\partial x^2} + \frac{\partial^2 u}{\partial y^2} + \frac{\partial^2 u}{\partial z^2}\right) = 0$$

Concrete has some measurable permeability, so k does not equal zero, implying that:

$$\frac{\partial^2 u}{\partial x^2} + \frac{\partial^2 u}{\partial y^2} + \frac{\partial^2 u}{\partial z^2} = 0$$

This is the Laplace equation for pore water pressure, and its solution is a harmonic function that satisfies the following boundary conditions (referencing the coordinates in Figure 4.1):

$u(x,y,z) = 0$ for $z < 0$

$u(x,y,0) = p$ for $-0.5b_{rs} \leq x \leq 0.5b_{rs}$

for $-0.5b_{rs} \leq y \leq 0.5b_{rs}$

$u(x,y,0) = 0$ elsewhere

where p is the surface water pressure and b_{rs} is the width of the rail seat area. For the x-z plane, Bakharev used the following solution (1994):

$$u(x,z) = \frac{p}{\pi}\left[\arctan\left(\frac{x}{z}\right) - \arctan\left(\frac{x - b_{rs}}{z}\right)\right]$$

It can be shown that the superposition of half of this solution with half of the same solution for the y-z plane yields a three-dimensional solution that fulfills the boundary conditions and Laplace's equation:

$$u = \frac{p}{2\pi}\left[\arctan\left(\frac{x}{z}\right) - \arctan\left(\frac{x - b_{rs}}{z}\right) + \arctan\left(\frac{y}{z}\right) - \arctan\left(\frac{y - b_{rs}}{z}\right)\right]$$

This equation can be used to estimate the pore pressure in a fully saturated concrete tie resulting from pressurized water at the rail seat surface. For the pore pressure at the center of the rail seat, x and y become zero, resulting in the following expression:

$$u = \frac{2p}{\pi}\left[\arctan\left(\frac{b_{rs}}{2z}\right)\right]$$

The solution for different values of p results in a family of curves versus depth into the concrete (Figure 4.7).
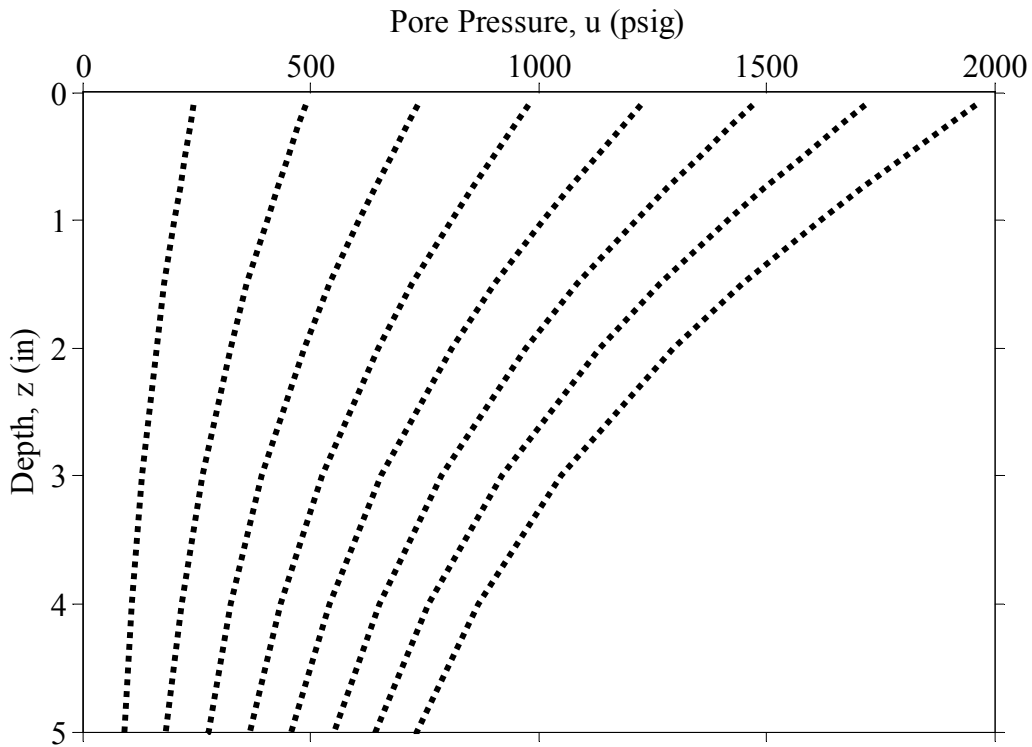

Figure 4.7 Predicted pore pressure dissipation with depth in a saturated concrete tie; a family of curves representing different surface water pressures

4.5.2   *Total Stress from a Uniform Vertical Load*

For the uniform vertical load (normal to the rail seat), Holl's equations were used to find the total stress beneath the center of a square 42.25 square-inch rail seat, assuming an elastic stress distribution with a Poisson's ratio of 0.5 (Poulos and Davis 1974). The Poisson's ratio of concrete is typically around 0.2 (Mindess et al. 2003). This discrepancy between the model and the actual concrete material was accepted because the resulting equations for a three-dimensional state of stress were readily available. For elastic stress distributions, choosing a larger Poisson's ratio generally results in a stiffer material, thus

greater confining stresses than would be observed with a smaller Poisson's ratio (Poulos and Davis 1974). The normal stress on the rail seat was estimated as the set of normal forces from Section 4.2, divided by the rail seat area.

Holl's general solution, where b and l are sides of the rectangular area and σ_V is the applied load stress, is (Poulos and Davis 1974):

$$R_1 = \sqrt{l^2 + z^2}$$

$$R_2 = \sqrt{b^2 + z^2}$$

$$R_3 = \sqrt{l^2 + b^2 + z^2}$$

$$\{\sigma_z\}_V = \frac{\sigma_V}{2\pi}\left[\arctan\left(\frac{lb}{zR_3}\right) + \frac{lbz}{R_3}\left(\frac{1}{R_1^2} + \frac{1}{R_2^2}\right)\right]$$

$$\{\sigma_x\}_V = \frac{\sigma_V}{2\pi}\left[\arctan\left(\frac{lb}{zR_3}\right) - \frac{lbz}{R_1^2 R_3}\right]$$

$$\{\sigma_y\}_V = \frac{\sigma_V}{2\pi}\left[\arctan\left(\frac{lb}{zR_3}\right) - \frac{lbz}{R_2^2 R_3}\right]$$

$$\{\tau_{xz}\}_V = \frac{\sigma_V}{2\pi}\left[\frac{b}{R_2} - \frac{z^2 b}{R_1^2 R_3}\right]$$

$$\{\tau_{yz}\}_V = \frac{\sigma_V}{2\pi}\left[\frac{l}{R_1} - \frac{z^2 l}{R_2^2 R_3}\right]$$

$$\{\tau_{xy}\}_V = \frac{\sigma_V}{2\pi}\left[1 + \frac{z}{R_3} - z\left(\frac{1}{R_1} + \frac{1}{R_2}\right)\right]$$

Superposition can be used to obtain the stresses under any location on the rail seat. Considering the center of the rail seat, Holl's equations directly apply to one fourth of the loaded area, so they were multiplied by four to apply superposition. Also, for the center case, b and l in Holl's equations are both equal to half of the rail seat width. For the center of the rail seat, the contributions of the uniform vertical load to the total stress are summarized in the following stress tensor:

$$S_V = 4 \begin{bmatrix} \{\sigma_x\}_V & \{\tau_{xy}\}_V & \{\tau_{xz}\}_V \\ \{\tau_{xy}\}_V & \{\sigma_y\}_V & \{\tau_{yz}\}_V \\ \{\tau_{xz}\}_V & \{\tau_{yz}\}_V & \{\sigma_z\}_V \end{bmatrix}$$

A stress tensor represents the three-dimensional state of stress of an infinitesimal element. The diagonals are the normal stresses, while the off-diagonal entries are the shear stresses. Typically, the tensor matrix is presented such that the first, second, and third rows and columns are for the *x-, y-,* and *z-*directions, respectively. For example, the shear stress in entry {1, 3} is the shear stress with an *xz-*orientation. The advantage of representing states of stress as tensors is that they can be easily manipulated as matrices by programs such as Matlab.

The assumption of elastic stress distribution could result in higher confining stresses than would be reasonable if the predicted stress in the concrete begins to approach its compressive strength. Depending on the specific concrete in use, the stress-strain curve may exhibit inelastic strain-softening behavior at moderate to high strains, which would result in lower stresses at the same strain (Mindess et al. 2003).

4.5.3   Total Stress from a Uniform Horizontal Load

Similar to the calculation of total stress from a uniform vertical load, the total stress from a uniform horizontal load was calculated using equations from Holl – again assuming a Poisson's ratio of 0.5. The lateral load on the rail seat was estimated as 52% of the normal load – considering the *L/V* ratio chosen in Section 4.2. Holl's equations for a uniform horizontal load are

$$\{\sigma_z\}_H = \frac{\sigma_H}{2\pi} \left[\frac{b}{R_2} - \frac{z^2 b}{R_1^2 R_3} \right]$$

$$\{\sigma_x\}_H = \frac{\sigma_H}{\pi} \left[\ln\left(\frac{R_1(b+R_2)}{z(b+R_3)} \right) - \frac{l^2 b}{2R_1^2 R_3} \right]$$

$$\{\sigma_y\}_H = \frac{\sigma_H}{2\pi} \left[\ln\left(\frac{R_1(b+R_2)}{z(b+R_3)} \right) - b\left(\frac{1}{R_2} - \frac{1}{R_3} \right) \right]$$

$$\{\tau_{xz}\}_H = \frac{\sigma_H}{2\pi}\left[\arctan\left(\frac{lb}{zR_3}\right) - \frac{lbz}{R_1^2 R_3}\right]$$

$$\{\tau_{yz}\}_H = \frac{\sigma_H}{2\pi}\left[1 + \frac{z}{R_3} - z\left(\frac{1}{R_1} + \frac{1}{R_2}\right)\right]$$

$$\{\tau_{xy}\}_H = \frac{\sigma_H}{2\pi}\left[\ln\left(\frac{(R_1+l)(R_3-l)}{zR_2}\right) + l\left(\frac{1}{R_3} - \frac{1}{R_1}\right)\right]$$

Holl's coordinates were such that the horizontal load was in the positive *x*-direction (Poulos and Davis 1974), but my coordinates have the horizontal load in the negative *y*-direction (left-hand rail seat in Figure 4.1). To transform Holl's stress tensor into my coordinate system, the following transformation map is applied, with the resulting stress tensor (referencing Holl's equations given above) shown here:

$$S_H = \begin{bmatrix} 0 & 1 & 0 \\ -1 & 0 & 0 \\ 0 & 0 & 1 \end{bmatrix} 4 \begin{bmatrix} \{\sigma_x\}_H & \{\tau_{xy}\}_H & \{\tau_{xz}\}_H \\ \{\tau_{xy}\}_H & \{\sigma_y\}_H & \{\tau_{yz}\}_H \\ \{\tau_{xz}\}_H & \{\tau_{yz}\}_H & \{\sigma_z\}_H \end{bmatrix} \begin{bmatrix} 0 & -1 & 0 \\ 1 & 0 & 0 \\ 0 & 0 & 1 \end{bmatrix}$$

$$S_H = 4 \begin{bmatrix} \{\sigma_y\}_H & -\{\tau_{xy}\}_H & \{\tau_{yz}\}_H \\ -\{\tau_{xy}\}_H & \{\sigma_x\}_H & -\{\tau_{xz}\}_H \\ \{\tau_{yz}\}_H & -\{\tau_{xz}\}_H & \{\sigma_z\}_H \end{bmatrix}$$

4.5.4 *Total Stress from a Timoshenko Beam on an Elastic Foundation*

To consider the contributions of flexure and prestress, a model of a prestressed Timoshenko beam on an elastic foundation was developed. The section properties of the beam, the loading conditions, and the layers of the elastic foundation are illustrated (Figure 4.8) using the variables defined in the first section of this chapter. A Timoshenko beam is a planar beam where the vertical deflection and in-plane rotation of the beam are considered independent variables. The bending moment and shear in the beam were determined by constitutive relationships with the deflection and rotation. Typically the axial strain is neglected, as was done here. The principal of virtual work was applied using the Galerkin method, which is a special form of the Ritz approximation, to estimate the deflection and rotation for many different scenarios (Hjelmstad 2005). The resulting model of a beam on an elastic foundation that was

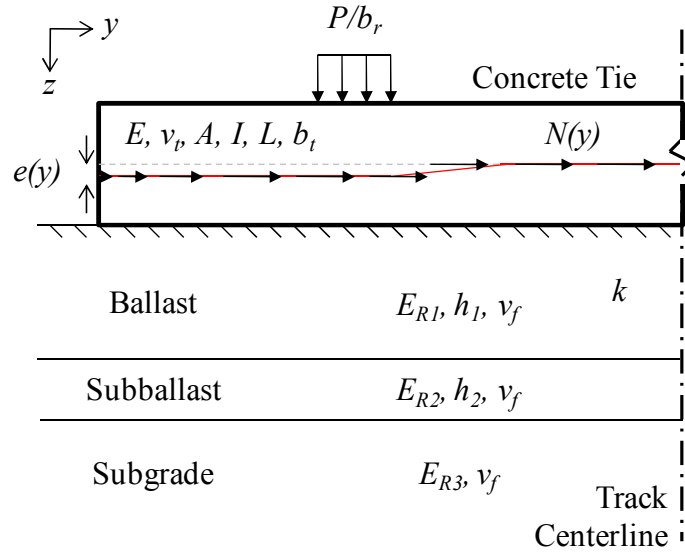derived with the Galerkin method, as described by Hjelmstad (2005), is referred to as the "Galerkin model."

Figure 4.8 Galerkin model of a prestressed beam on an elastic foundation

The following derivation of the approximate solution for the assumed Timoshenko beam is from Hjelmstad (2005). It begins by assuming a planar (2D) beam and stating the governing equations:

$$\frac{dQ}{dy} + q = 0 \qquad\qquad Q = GA\left(\frac{dw}{dy} - \theta\right)$$

$$\frac{dM}{dy} + Q + m = 0 \qquad\qquad M = EI\frac{d\theta}{dy}$$

where Q and M are the shear force and bending moment in the beam, respectively; q and m are the applied vertical force and bending moments, respectively; w and θ represent the vertical displacement and the in-plane rotation, respectively; and $E, A, I,$ and G are material and section properties of the beam (constants). Typically the axial strain is neglected, as is done here. For this derivation, the shear is taken as positive upward, which is the opposite of the convention used in structural engineering in the US. This discrepancy is handled in post-processing, so that the output of the model follows the US convention.

76

The principal of virtual work can be applied using the Galerkin method, which is a special form of the Ritz approximation where the real displacements and the virtual displacements are assumed to have the same shape function. The displacements are approximated as a linear combination of shape functions, such that (Hjelmstad 2005):

$$w(y) = \psi(y) \cdot \alpha \qquad\qquad \theta(y) = \xi(y) \cdot \beta$$

$$\delta w(y) = \psi(y) \cdot \delta\alpha \qquad\qquad \delta\theta(y) = \xi(y) \cdot \delta\beta$$

$$\alpha = [\alpha_1, \ldots, \alpha_5]^T \qquad\qquad \beta = [\beta_1, \ldots, \beta_5]^T$$

$$\psi(y) = [1, \sin\left(\frac{\pi y}{L}\right), \sin\left(\frac{3\pi y}{L}\right), \sin\left(\frac{5\pi y}{L}\right), \sin\left(\frac{7\pi y}{L}\right)]^T$$

$$\xi(y) = [1, \cos\left(\frac{\pi y}{L}\right), \cos\left(\frac{3\pi y}{L}\right), \cos\left(\frac{5\pi y}{L}\right), \cos\left(\frac{7\pi y}{L}\right)]^T$$

where the δ operator indicates a virtual displacement or a virtual coefficient. The shape functions ψ_i and ξ_i were chosen as trigonometric functions to create realistic deflected shapes and to ensure that Q and M would be zero at the boundaries (see the Timoshenko definitions of Q and M, given on the previous page). The coefficients α_i and β_i ($i = 1,\ldots,5$) are unknowns. The principal of virtual work states that the sum of all virtual work done on the beam must be zero, and Hjelmstad expressed this as

$$\delta\alpha: \qquad K_{\alpha\alpha}\alpha + K_{\alpha\beta}\beta = F_\alpha$$

$$\delta\beta: \qquad K_{\beta\alpha}\alpha + K_{\beta\beta}\beta = F_\beta$$

$$K_{\alpha\alpha} = \int_0^L GA\left[\frac{d\psi}{dy}\right]\left[\frac{d\psi}{dy}\right]^T dy \qquad\qquad K_{\alpha\beta} = -\int_0^L GA\left[\frac{d\psi}{dy}\right][\xi]^T dy$$

$$K_{\beta\alpha} = -\int_0^L GA[\xi]\left[\frac{d\psi}{dy}\right]^T dy \qquad K_{\beta\beta} = \int_0^L \left\{ EI\left[\frac{d\xi}{dy}\right]\left[\frac{d\xi}{dy}\right]^T + GA[\xi][\xi]^T \right\} dy$$

$$F_\alpha = \int_0^L q\psi \, dy$$

77

$$F_{\beta} = \int_0^L m\xi dy$$

The solution to the matrix equation can be summarized as

$$\begin{bmatrix} \alpha \\ \beta \end{bmatrix} = \begin{bmatrix} K_{\alpha\alpha} & K_{\alpha\beta} \\ K_{\beta\alpha} & K_{\beta\beta} \end{bmatrix}^{-1} \begin{bmatrix} F_{\alpha} \\ F_{\beta} \end{bmatrix}$$

where the coefficient vectors $\boldsymbol{\alpha}$ and $\boldsymbol{\beta}$ are found by multiplying the force vector (the right-hand side) by the inverse of the combined stiffness matrix (composed of $\mathbf{K_{ij}}$) (Hjelmstad 2005).

The rail seat load was assumed to be uniformly distributed over the width of the rail base (typically six inches) – this rail seat load becomes part of the q term. The other part of the applied transverse load, q, is the foundation reaction, which is $\mu_f w(y)$. Because the foundation reaction depends on the vertical deflection $w(y)$, it needs to be moved to the left-hand side of the $\delta\alpha$ equation – the foundation reaction will supplement the $\mathbf{K_{\alpha\alpha}}$ matrix (Hjelmstad 2005).

For simplicity, this model of the tie was assumed to have a uniform rectangular cross-section, choosing an effective cross-sectional area and an effective moment of inertia for the tie. The prestress at the ends of the tie is zero because of the open boundary. Over a certain development length, the prestress in the tendons builds up to its nominal value. This development length was assumed to be 60 times the diameter of the tendons (wires or strands) (Naaman 2004). The prestress in a real concrete tie is placed eccentrically relative to the neutral axis of the section to create the prestress bending moment, and the eccentricity changes as the section changes along the tie's length. In the absence of a changing section, the change in eccentricity was modeled to mimic what is common in many concrete ties currently in use in North America (note the section change along the length of the tie shown in Figure 1.1). Next, the prestress force was multiplied by the eccentricity along the length to get the applied prestress bending moment, m.

Estimating the foundation stiffness μ_f is important but also difficult because of the great variability of quality of ballast, subballast, and subgrade with both location and time. For the purpose of approximating the stresses in a concrete tie, a range of values for the resilient moduli of the layers can

bound the problem and provide a reasonable solution (Selig and Li 1994). There are many different

approaches to estimating the foundation reaction from a granular material. The following approach was

adapted from Cai et al (1994), selecting a different approach to estimate E_{Rf}. Vesic and Johnson's

equation (Cai et al. 1994) for estimating the modulus of foundation reaction is:

$$\mu_f = \frac{0.65 E_{Rf}}{(1-v_f)^2} \sqrt{\frac{E_{Rf} b_t^4}{EI}}$$

Odemark's method (Poulos and Davis 1974) was selected for estimating E_{Rf} because it has been

found to perform best when the relative stiffness of the foundation layers decrease with depth – the top

layer is the stiffest, while the bottom layer is the least stiff. The method assumes $v_f = 0.5$, which is

generally not correct for ballast, subballast, and subgrade materials (Poulos and Davis 1974, Selig and Li

1994) as was discussed in Section 4.5.2. The solution is found using an iterative approach by selecting a

value for E_{Rf}, solving for the other unknowns, then solving for E_{Rf}, and continuing this process until E_{Rf}

converges to a constant value. Odemark's system of equations, as described by Poulos and Davis (1974),

is:

$$O_1 = 0.9 \frac{h_1}{H} \left(\frac{E_{R1}}{E_{Rf}} \right)^{\frac{1}{3}}$$

$$O_2 = O_1 + 0.9 \frac{h_2}{H}$$

$$O_3 = O_1 + 0.9 \frac{h_2}{H} \left(\frac{E_{R2}}{E_{R3}} \right)^{\frac{1}{3}}$$

$$E_{Rf} = \frac{E_{R3}}{\sqrt{\frac{1+O_1^2 \left(H/r \right)^2}{1+O_3^2 \left(H/r \right)^2}} + \frac{E_{R3}}{E_{R2}} \left[1 - \sqrt{\frac{1+O_1^2 \left(H/r \right)^2}{1+O_2^2 \left(H/r \right)^2}} \right]}$$

Where r is the radius of a circularly loaded area. This radius was approximated using a circle with an

area equal to that of the base of the concrete tie:

$$r = \sqrt{\frac{Lb_t}{\pi}}$$

Other considerations were included in subsequent versions of the Galerkin model, such as changing section along the length of the tie and different support conditions at the shoulders than at the middle (center bound or freshly tamped, for example). The output of the model for different tie section considerations (Figure 4.9) shows half of the tie with $y = 0$ at the end of the tie. Including the section changes results in larger center moments, while including the prestress reduces the rail seat moment considerably. More detailed results from the Galerkin model are given in Appendix C.
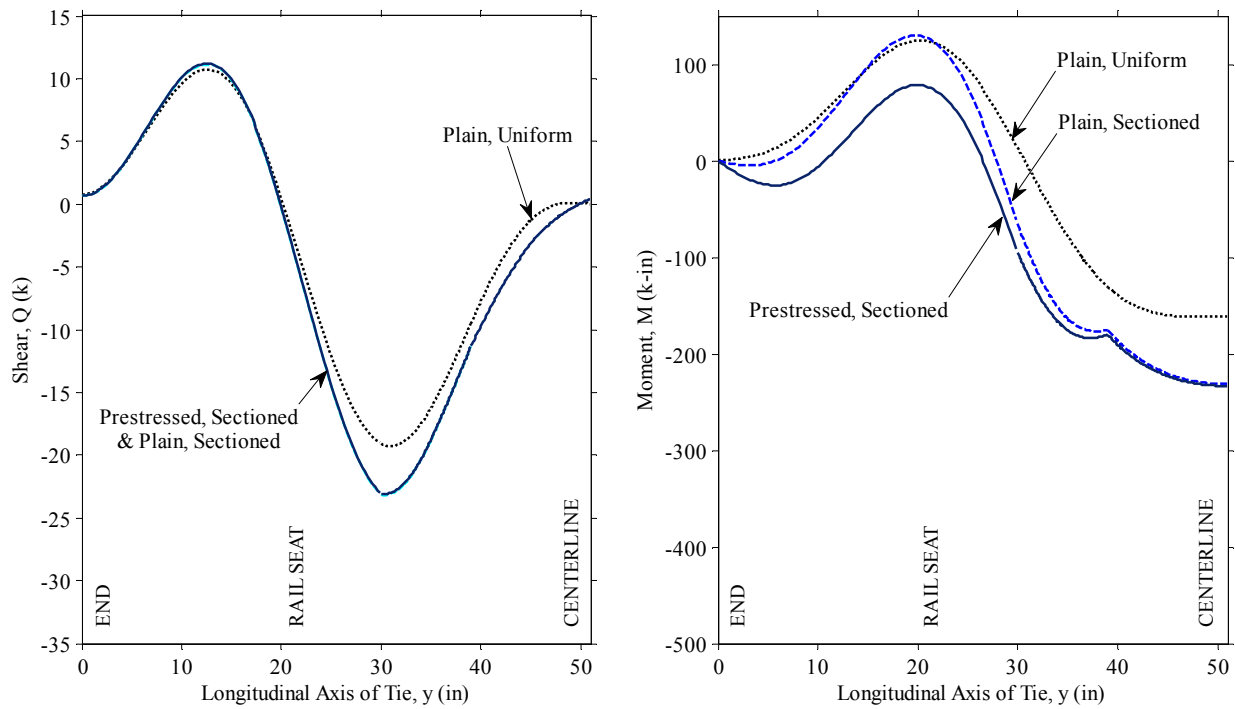
**Figure 4.9 Comparison of different tie section considerations
with the Galerkin model of a beam on an elastic foundation**

To check the output of the Galerkin model, Hetenyi's closed-form solution to a railroad crosstie on an elastic foundation was considered. Hetenyi worked with the Euler-Bernoulli beam assumptions which state that all initially plane sections remain plane and perpendicular to the beam's neutral axis. Hetenyi solved the differential equation for an elastic line (Hetenyi 1946):

$$EI\frac{d^4w}{dy^4} = -\mu_f w + q$$

Assuming that:

$$\frac{dw}{dy} = \tan\theta$$

This results in the relationship:

$$Q = \frac{dM}{dy}$$

This assumption and its consequence are the primary differences between Euler-Bernoulli beams and Timoshenko beams. The output from Hetenyi's equations is given here and compared with output from the Galerkin model (Table 4.4). For the uniform, plain tie, Hetenyi's solution is slightly conservative compared with the Galerkin method. The major advantage of the Galerkin model over the simple Hetenyi solution is that Galerkin can directly account for important factors such as prestress, changing sections, and non-uniform support conditions.

Table 4.4 Comparison of Hetenyi's closed-form solution of an Euler-Bernoulli beam with the Galerkin method approximation of a Timoshenko beam

	Shear, Q (k)				Moment, M (k-in)		
	End	Field Peak	Gauge Peak	Center	End	Rail Seat	Center
Hetenyi (1946)	0.0	16.7	-23.3	0.0	0	167	-173
Galerkin							
Uniform, plain	0.8	10.7	-19.3	0.0	0	124	-161
Sectioned, plain	0.6	11.2	-23.2	0.4	0	126	-231
Sectioned, prestressed	0.7	11.2	-23.1	0.4	0	76	-235
Center-bound	-0.3	8.4	-32.5	0.6	0	32	-491
Freshly tamped	0.9	11.8	-16.9	0.0	0	87	-103

For use in the effective stress model, the rail seat shear force and bending moment from the Galerkin model were converted to shear stress and normal stress at different depths, assuming constant (average) shear stress in the section and a linear flexural stress distribution (Craig 2000):

$$\{\tau_{yz}\}_B = \frac{Q}{A}$$

$$\{\sigma_y\}_B = \frac{M(c-z)}{I} + \frac{N}{A}$$

By assuming planar bending and an isotropic material, the stress components not on the face of a beam's cross-section are unaffected by prestress or flexure (Craig 2000):

$$S_B = \begin{bmatrix} 0 & 0 & 0 \\ 0 & \{\sigma_y\}_B & \{\tau_{yz}\}_B \\ 0 & \{\tau_{yz}\}_B & 0 \end{bmatrix}$$

4.5.5   *Principal Stresses and Effective Stress*

The total stress from the contributions of a uniform vertical load, a uniform transverse load, and Timoshenko bending can be calculated by superposition of the stress tensors:

$$S_{xyz} = S_V + S_H + S_B$$

The total stress tensor S_{xyz} is in the *xyz* coordinate system. For stress tensors, in general, it is possible to find a coordinate system – or effectively rotate the concrete element – such that there is no shear on the element. This case is called the principal coordinate system because the state of stress is summarized by three principal normal stresses and no shear stresses. The principal stresses are referred to as major, intermediate, and minor, symbolized by σ_1, σ_2, and σ_3, respectively, with the distinction that $\sigma_1 > \sigma_2 > \sigma_3$ (Hjelmstad 2005).

The principal stress tensor can be found by solving an eigenvalue problem with the *xyz* stress tensor, where the eigenvalues are the principal stresses, and the eigenvectors are the principal directions, relative to the *xyz* coordinate system. The eigenvalue problem for this model is stated as such (Hjelmstad 2005):

$$S_{xyz}\phi_i = \sigma_i\phi_i \quad for \quad i = 1,2,3$$

$$(S_{xyz} - \sigma_i I)\phi_i = 0$$

$$det(S_{xyz} - \sigma_i I) = 0$$

Having solved this eigenvalue problem, the resulting principal stress tensor is

$$S_{123} = \begin{bmatrix} \sigma_1 & 0 & 0 \\ 0 & \sigma_2 & 0 \\ 0 & 0 & \sigma_3 \end{bmatrix}$$

Pascal's Law states that a fluid exerts pressure equally to all surfaces that it is contacting, and that these pressures are normal to the contact surfaces (Munson et al. 2006). So in terms of a stress tensor, the pore pressure can be expressed as equal normal stresses without any shear:

$$U = \begin{bmatrix} u & 0 & 0 \\ 0 & u & 0 \\ 0 & 0 & u \end{bmatrix}$$

Then the effective stress tensor is the result of the principal stress tensor minus the pore pressure tensor:

$$S' = S_{123} - U = \begin{bmatrix} \sigma_1 - u & 0 & 0 \\ 0 & \sigma_2 - u & 0 \\ 0 & 0 & \sigma_3 - u \end{bmatrix}$$

The resistance of the concrete to spalling due to effective tensile stresses in one direction was simply assumed to be the uniaxial tensile strength of the concrete, which is approximately ten percent of the 28-day compressive strength. A further simplification can be made to estimate the fatigue limit for concrete under any kind of action as approximately 50% of the ultimate strength. The actual tensile strength of the concrete is dependent on the stress state and is complicated because this is a triaxial state of stress (Mindess et al. 2003). It is possible that the variability of the actual strength of the concrete would be large enough that considering a complex model of the triaxial tensile strength would not provide a substantially different solution. One example dataset for the 28-day compressive strength of structural concrete is normally distributed (Figure 4.10) with target strength equal to 7,000 psi, which is the

minimum strength recommended by AREMA (2009). It is likely that the actual probability distribution for concrete used in concrete ties will be different from this example, so Figure 4.10 is presented here just as an illustration.
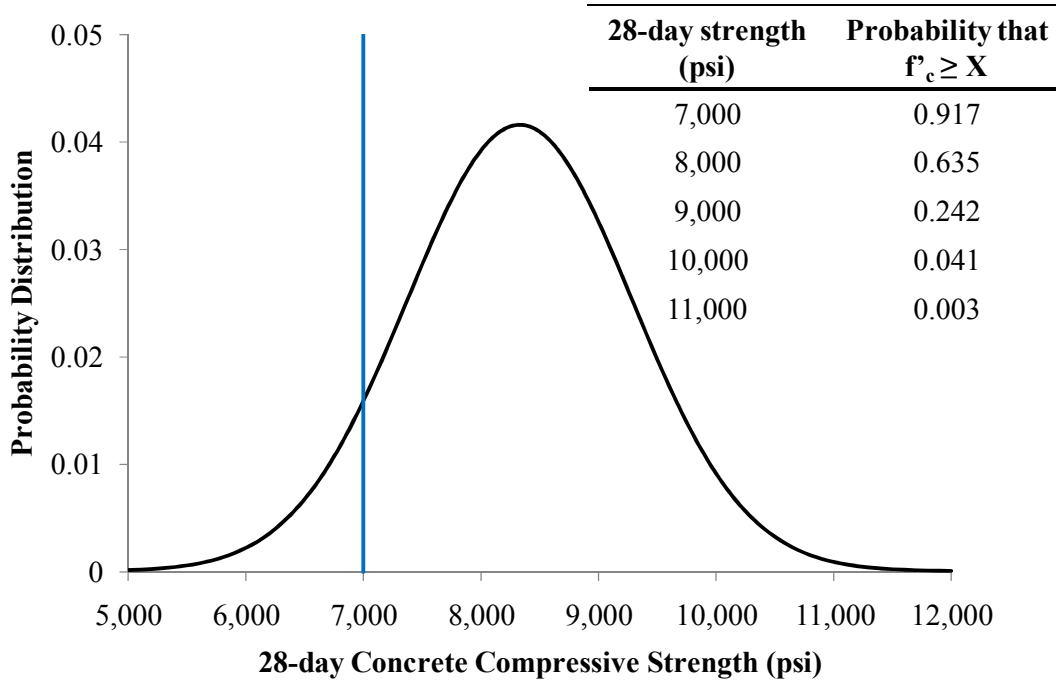
28-day strength (psi)	Probability that $f'_c \geq X$
7,000	0.917
8,000	0.635
9,000	0.242
10,000	0.041
11,000	0.003

**Figure 4.10 Example probability distribution of compressive strength
for structural concrete with target strength equal to 7,000 psi
(Wight and MacGregor 2009)**

Given the recommended minimum strength of 7,000 psi and the stated assumptions, the tensile strength was approximated as 700 psi, while the fatigue limit was approximated as 350 psi. These estimated damage limits were imposed on the effective stress, and these relationships were rearranged to put limits in terms of pore pressure as shown:

$$\min(S') = \sigma_3 - u \geq \begin{Bmatrix} \left\{ \tfrac{1}{2} f'_t \right\}_{fatigue} \\ \left\{ f'_t \right\}_{strength} \end{Bmatrix}$$

$$u \leq \begin{Bmatrix} \sigma_3 - \left\{ \tfrac{1}{2} f'_t \right\}_{fatigue} \\ \sigma_3 - \left\{ f'_t \right\}_{strength} \end{Bmatrix} = \begin{Bmatrix} \sigma_3 + 350\,psi \\ \sigma_3 + 700\,psi \end{Bmatrix} = \begin{Bmatrix} u_{fatigue} \\ u_{strength} \end{Bmatrix}$$

84

The limits on surface pressure, p, were defined by finding the minimum pore pressure, u, curves that intersected the damage limits (Figure 4.11). The solid, black curves corresponding to $p = 720$ psi gauge (psig) and $p = 1180$ psig are the minimum curves that intersect the fatigue limit and strength limit curves, respectively. The damage limits were defined by the effective stress at points around one to two inches below the rail seat surface (Figure 4.11) and for other magnitudes of load as well, due to the curvature of the damage limit curves. In a microscopy study of deteriorated rail seats, Bakharev (1994) found microcracks originating at approximately the same depth. She concluded that these microcracks could have been caused by either hydraulic pressure or freeze-thaw cycles. The surface pressure damage limits were found by performing similar procedures for the other applied load cases (Table 4.5).
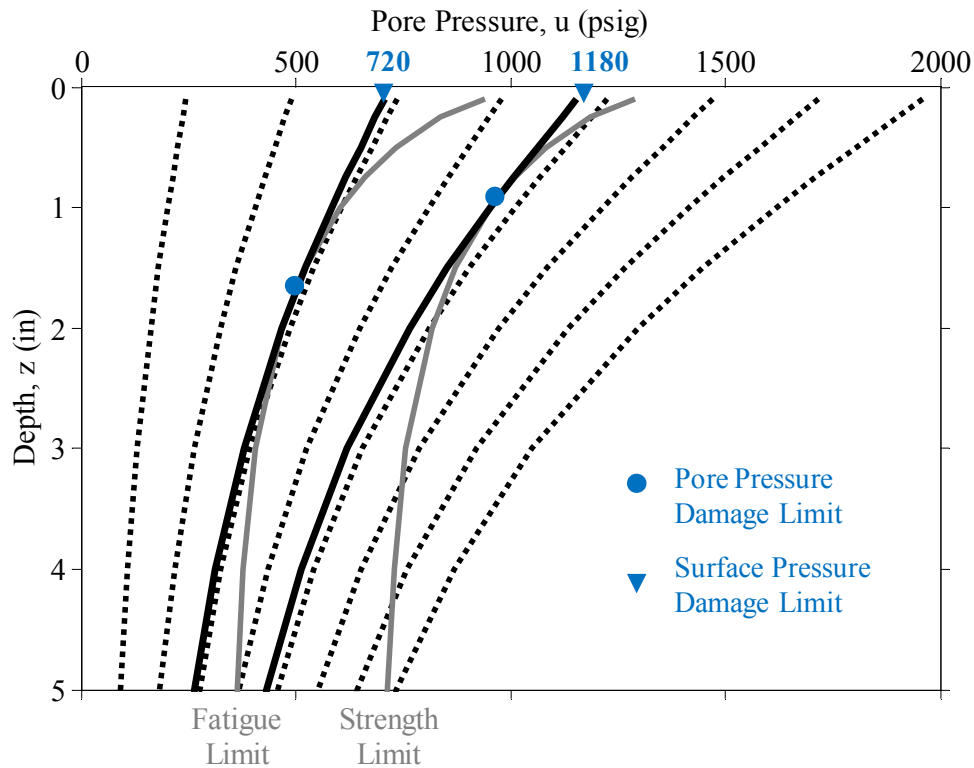
Figure 4.11 Graphical conversion of damage limits from pore pressure to surface pressure values for 40-kip applied load, assuming saturated concrete

Table 4.5 Summary of the surface pressure limits derived from the effective stress model, assuming saturated concrete

	Applied Load, P (kips)				
	20	**30**	**40**	**50**	**60**
Fatigue Limit (psig)	580	660	720	770	810
Strength Limit (psig)	945	1090	1180	1260	1320

By performing a sensitivity analysis on the effective stress model (see Appendix C), I determined that the uniform vertical load made the most significant contribution to the minor principal stress; therefore, it had the greatest impact on the damage limits. The uniform lateral load and prestressed beam contributions only affected the minor principal stress in the upper two inches of the tie, accounting for the curvature of the damage limits in Figure 4.11. Below approximately two inches, the lateral load and prestress/flexure have little influence on the minor principal stress. This is because the minor principal stress was mostly oriented along the axis of the rail, in the *x*-direction. That is the direction of least total stress because the applied loads considered were only vertical, in the *z*-direction, or along the axis of the tie, in the *y*-direction.

CHAPTER 5: MANUAL TESTS[4]

5.1   Motivation

As an initial step in the experimental phase of this research, a manually-driven (hand-operated) test apparatus was developed to quickly test several initial hypotheses about water pressure between two plates. These hypotheses were that (a) changes in tie pad material and surface geometry would affect the pressure generated, (b) the pressure generated would be a function of the load and/or the relative acceleration between the two plates, (c) the pressure would be less if there was a nonzero contact angle between the two plates, and (d) the pressure may not be uniformly distributed beneath the tie pad. The advantage of the manual apparatus was that preliminary tests could be conducted quickly and inexpensively to gain insight about the behavior and dynamics of the tie-pad/rail-seat interface in terms of water pressurization, load application, and pressure measurement. The observations and data produced with the manual apparatus enabled me to more efficiently design the tests for the mechanically-driven test apparatus, used for the load and uplift tests (described in Chapters 6 and 7, respectively).

The primary requirements of the manual test apparatus were to (1) pressurize water by manually applying normal load and generating relative motion between the tie pad and the rail seat, and (2) measure this water pressure with a pressure transducer. Another requirement was that most of the materials were available in the laboratory supply inventory or could easily be purchased.

5.2   Materials and Equipment

The manually-driven test apparatus (Figure 5.1) included a stainless steel plate at the base of a plastic tub that could be filled with water or some other fluid. The steel plate was drilled and tapped so that a pressure transducer with a male 1/4-inch NPT-18 pipe thread end could be positioned flush with the steel plate. The water tank was elevated on two blocks to allow the transducer to protrude below the

---

[4] The tests described in this chapter were mostly performed by Edgardo Santana-Santiago as part of his Summer Research Opportunities Program (SROP) internship. Mr. Santana-Santiago wrote about his work in a report to the SROP entitled "Characterizing the Dynamic Water Pressure in a Concrete Tie Rail Seat."

plate. A garden hose nozzle was attached to one corner of the plastic tub to drain the fluid. A water-sealing caulk was placed around the steel plate and the nozzle to prevent leakage.
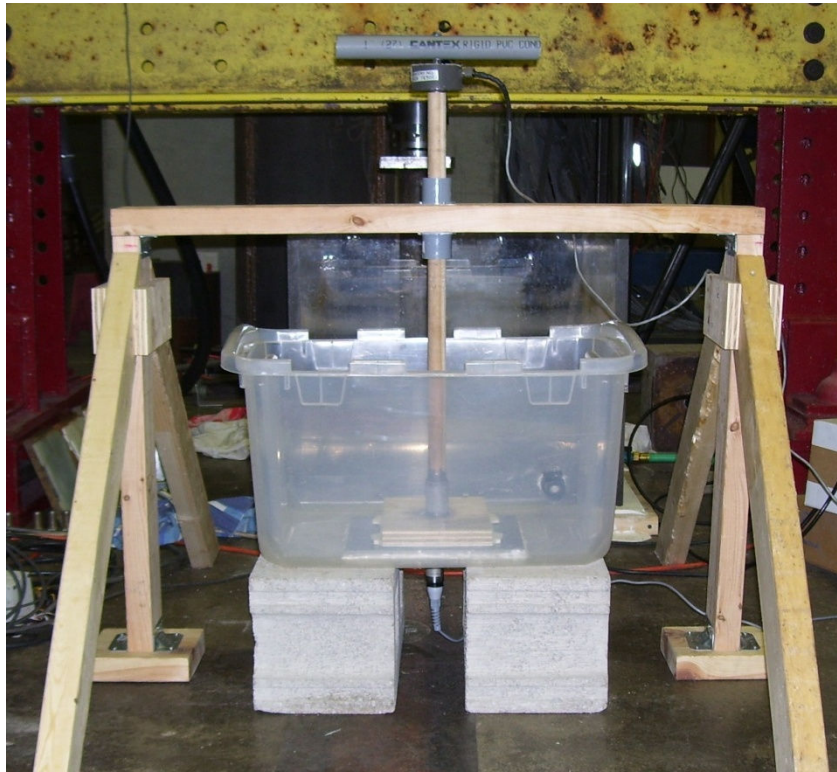

Figure 5.1 Manually-driven test apparatus

Tie pads commonly used on concrete ties were adhered to a wooden plate and dowel rod with a two-part epoxy. At the other end of the dowel rod, a 200-pound (lb) load cell and PVC pipe handle were attached. This manual load applicator was stabilized by a wooden frame. A clamp was attached to the dowel rod to control the range of vertical motion of the tie pad, restricting the maximum uplift of the pad above the rail seat plate.

5.2.1   Tie Pads

In this study, the primary component that was varied during the each of the laboratory tests was the tie pad. Tie pads are thermoplastic pads or assemblies of different materials placed between the rail base and the concrete rail seat. They provide many functions including stress distribution at the rail seat, abrasion resistance, and impact attenuation / damping. According to some literature on rail seat

88

deterioration (RSD), certain tie-pad designs seemed to increase rail seat wear. An often cited example is that the flat ethyl-vinyl actetate (EVA) pad, common in the 1980's and early 1990's, was found to be a poor material for abrasion resistance (Clark and Bosshart 2010). Replacing that pad with materials like polyurethane provided an improvement. Bakharev (1994) discussed the effect that different pads may have on trapping moisture. What has not been considered is the potential influence of pad material and surface geometry on water pressurization at the rail seat. For instance, in her model of hydraulic pressure at the rail seat, Bakharev (1994) assumed that the tie pad produces a surface water pressure equal to the applied load divided by the tie pad's area (equal to the applied load stress). One objective of my study was to measure surface water pressure under different tie pads to check the validity of this assumption.

Nine tie pads of different materials and surface geometries were analyzed in this study, including three types of pad assemblies. The tie pad surfaces that were tested were flat polyurethane, grooved polyurethane, dimpled polyurethane, flat EVA, dimpled EVA, dimpled santoprene, a studded pad with a flat plastic bottom (2-part C), a two-part assembly with a flat plastic bottom (2-part B), and a three-part assembly with a flat foam bottom underneath a steel plate (3-part A). Appendix D contains photos and details about each tie pad in terms of dimensions, surface geometry, load-deflection behavior, and other characteristics.

5.2.2   *Pressure Transducers*

The pressure transducers used in this study were all purchased from Transducers Direct and were variations of transducer model TDG 03/04. The transducers have pipe-threaded ends (1/4" NPT-18 male) with an open chamber and an inner diameter of 0.6 inches (in) and a depth of 3.75 inches (Figure 5.2). Fluid fills this chamber and the fluid pressure bends a strain gauge near the bottom of the chamber. The flexure in the strain gauge changes its electrical resistance such that the change in output voltage can be calibrated and converted to pounds per square inch absolute (psia) or psi gauge (psig) pressure. Gauge pressure is relative to the atmosphere, which is approximately 14.70 psia at the location where the tests were conducted. According to the manufacturer, the calibration curve for each transducer is

$p = (Voltage - 1)(Capacity/4)$. Nominally, a reading of zero pressure (absolute or gauge) is reported

as one Volt.

Figure 5.2 Submersible pressure transducer used in the load tests

Multiple transducers were used to measure the different ranges of water pressure developed in the

manual, load, and uplift tests, respectively. The manual tests required transducers with a capacity of 100-

psig. The load tests required a pressure transducer with a capacity of 6,000-psig for the much higher

pressures generated by railroad-magnitude loads. The uplift tests required a 135-psia transducer which

was specially designed to measure suction, or negative pressure. The 6,000-psig and 135-psia transducers

were customized to be submersed in water during operation.

The calibration curves for the 6,000-psig and 135-psia transducers are presented in Appendix D.

The 135-psia transducer had a calibration curve that deviated significantly from the manufacturer's

equation relating Voltage to pressure, and this correction is included in Appendix D.

5.3   Procedure

The general procedure for a manual test was for an individual to hold the load applicator by the handle and apply cycles of downward force and uplift to the steel plate which represented the rail seat. The variables in this experiment were the tie pad, the fluid level above the rail seat surface, the fluid material filling the water tank, the location of the resultant applied force relative to the location of the transducer (which was fixed), the depth of the transducer's orifice below the surface of the rail seat plate, the contact angle between the tie pad and the rail seat plate, the amount of uplift for each cycle, the rate of load application, and the maximum compressive force.

The load application frequency is the number of load cycles per second. The following load frequencies were used in various tests: 1 Hertz (Hz), 2 Hz, 3 Hz, 0.5 Hz, and 1/3 Hz. In some tests, the actual load frequency varied significantly from the targeted value because this was a manual process. The operator attempted to maintain the proper load frequency by monitoring a stop watch during the test. In general, lower frequencies resulted in higher applied loads, more repeatable results, and better data resolution.

The manual loading process was most similar to the position control mode for an actuator, in that the amount of uplift was controlled by an adjustable stopper, while the applied force was largely a resultant and could not be easily controlled. Multiple factors affected the resulting applied force, such as the loading frequency, the uplift displacement, and the fluid material. This meant that the applied force was not an independent variable. The control case was selected as the flat polyurethane pad, one-inch uplift, six-inch water level, a centered horizontal alignment, and a zero contact angle between the pad and the rail seat plate.

The data acquisition period was originally set at ten milliseconds (ms) but was reduced to five ms following initial tests to obtain better data resolution.

5.4 Results and Discussion

5.4.1 Basic Pressure Generation

Typically, the water pressure directly responded to rapidly applied load and uplift strokes (Figures 5.3 and 5.4). The negative force indicates compression (load), while the positive force indicates tension (uplift). In each cycle, the large positive pressure peak is a direct response to the applied load. This peak is referred to as the pressure peak. The relative magnitudes of the load peaks corresponded to the relative magnitudes of the positive pressure peaks (Figure 5.3). The peaks in order of greatest to least, for both applied load and positive pressure, are 2, 1, 3, 4, and 5.
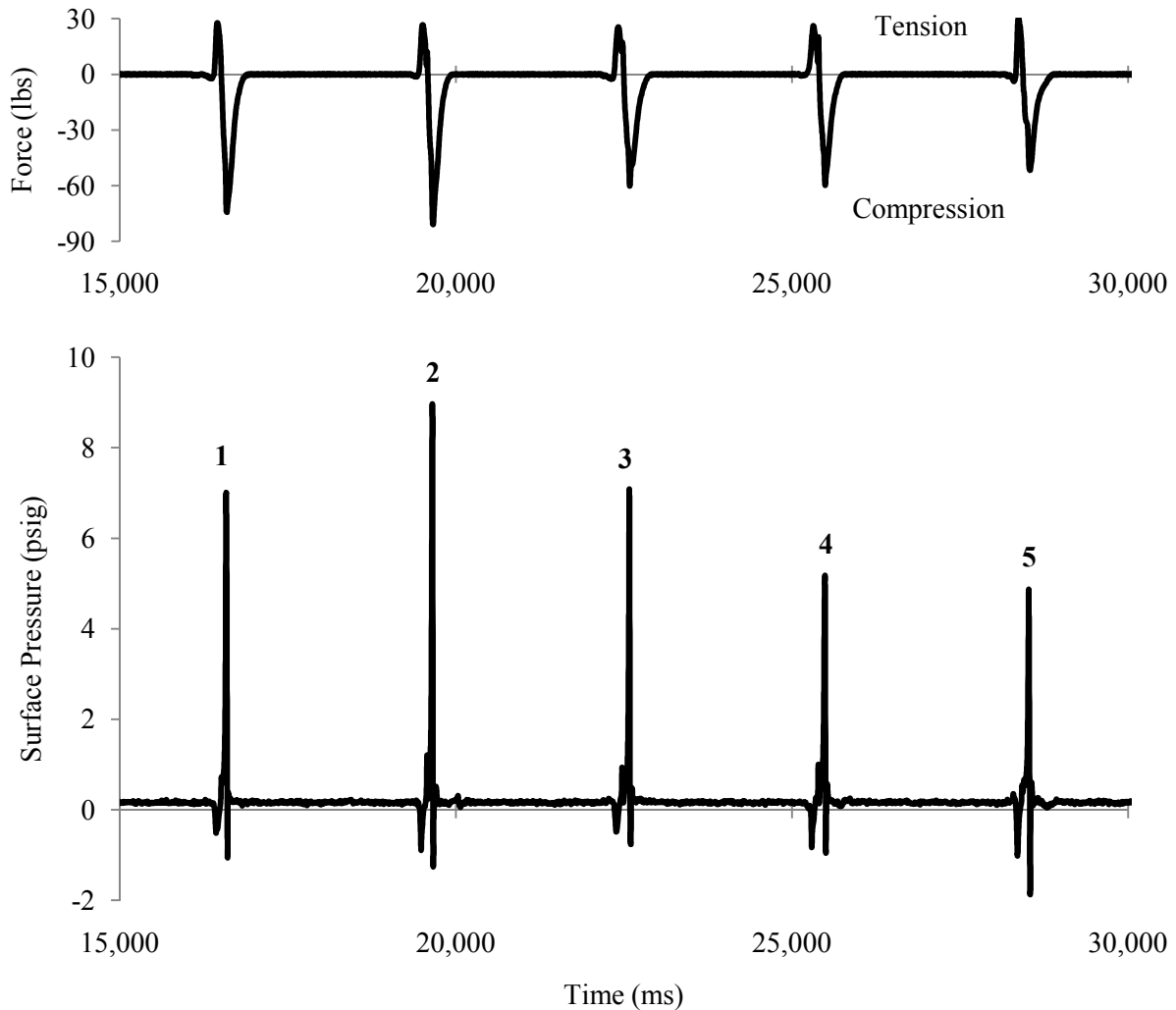
Figure 5.3 Example measurements showing the relationship between applied load and surface water pressure in the manual test

92
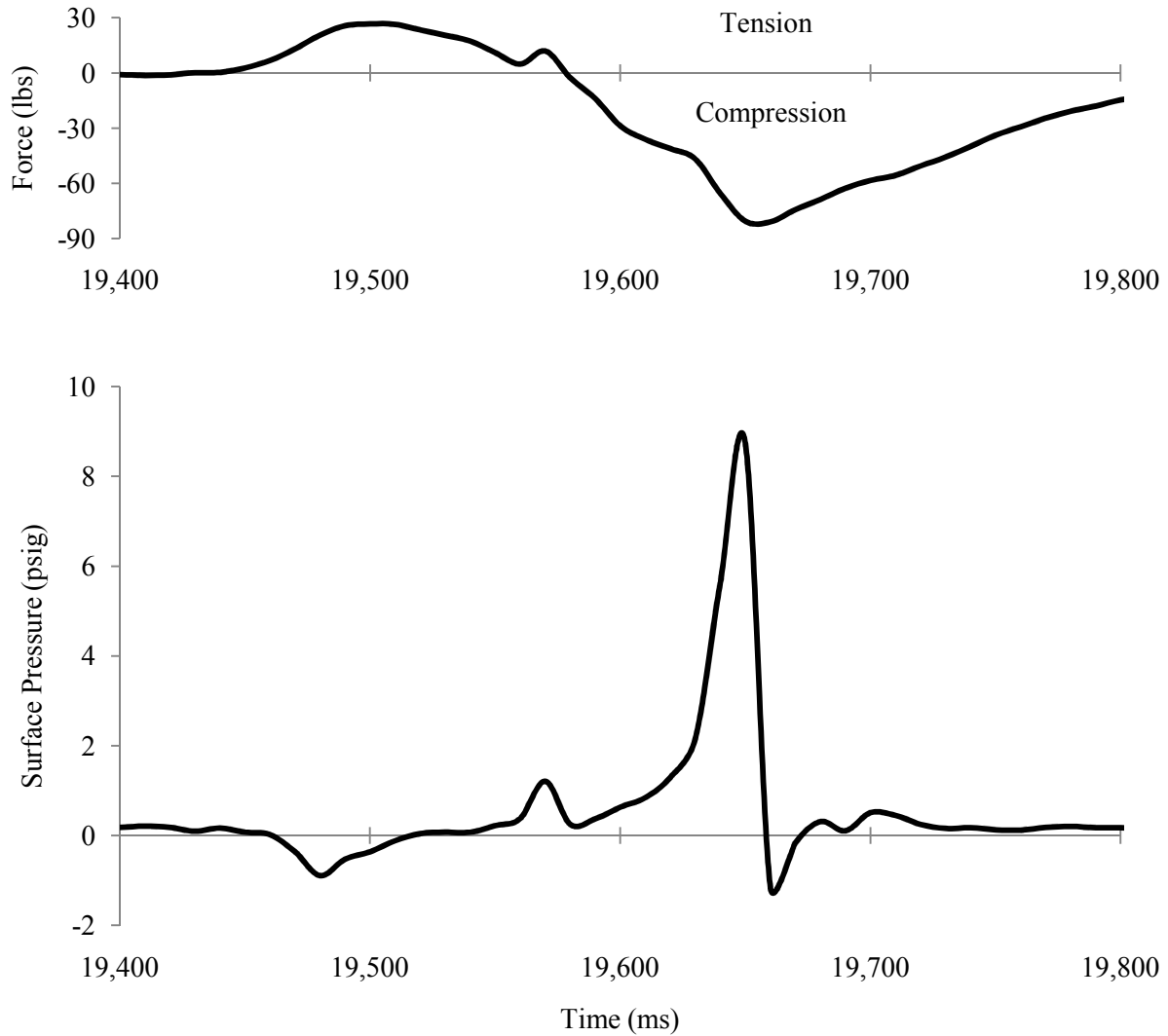
**Figure 5.4 One example cycle showing general relationships
between applied load and surface water pressure**

The first negative pressure peak was a direct response to lifting the loading plate (this was

inferred from the observed tensile force). This peak is referred to as the initial suction peak. Immediately

following the pressure peak, there was another negative pressure peak. This peak is referred to as the

rebound suction peak, and it appears to be either a pressure oscillation similar to a water hammer or a

response due to the quick release of the applied load.

Figure 5.4 shows a close-up view of one set of peaks. The tension peak lined up with the initial

suction peak, and the compression peak lined up with the pressure peak. The rebound suction peak

93

closely followed the pressure peak, with a short delay. If the load applicator was not lifted (no uplift), no noticeable initial suction peaks were observed. The time delay between different peaks was summarized with histograms for all of the manual test data (Figures 5.5, 5.6, and 5.7). In nearly half of the trials, the rebound suction peak occurred within 25 ms of the pressure peak. In general, the respective delay between applied load and surface pressure for the tension-suction and compression-pressure pairs was also usually less than 25 ms. In light of these data, I determined that a data collection rate of at least five ms would be needed. These pressure responses occur rapidly and a slower data collection rate might miss the peak values.

Time Delay from Pressure Peak to Rebound Peak (ms)
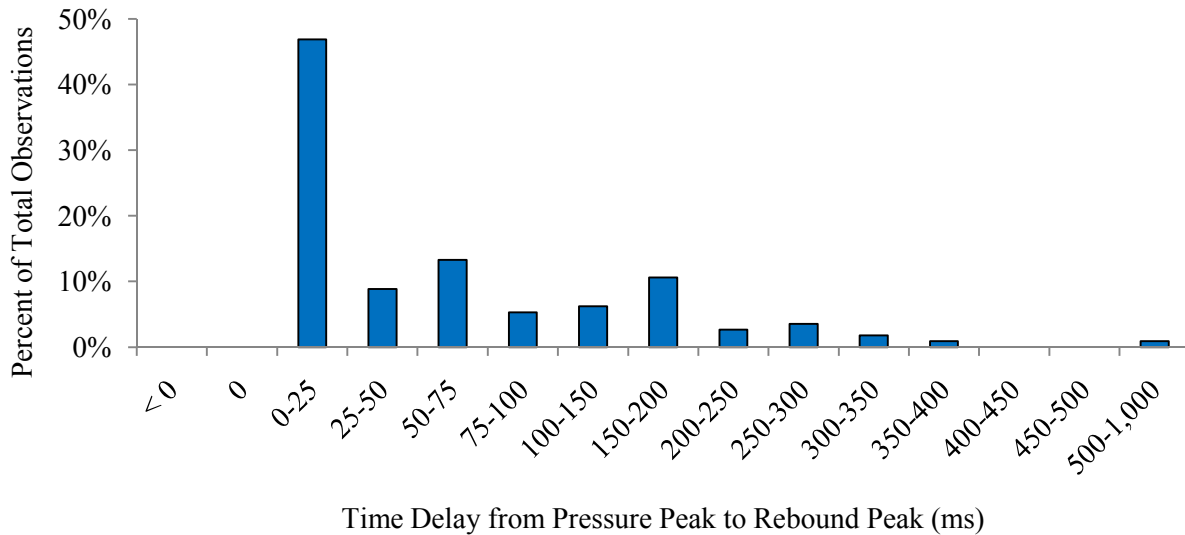
**Figure 5.5 Histogram of time delay from pressure peak
to rebound suction peak for manual test data**

94
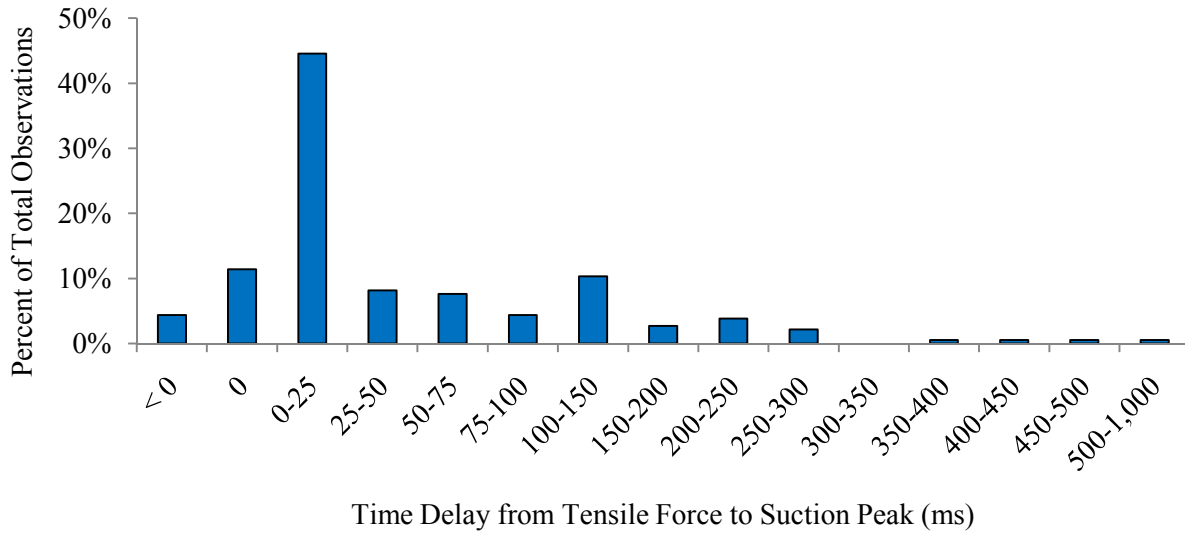
**Figure 5.6 Histogram of time delay from tensile force
to initial suction peak for manual test data**
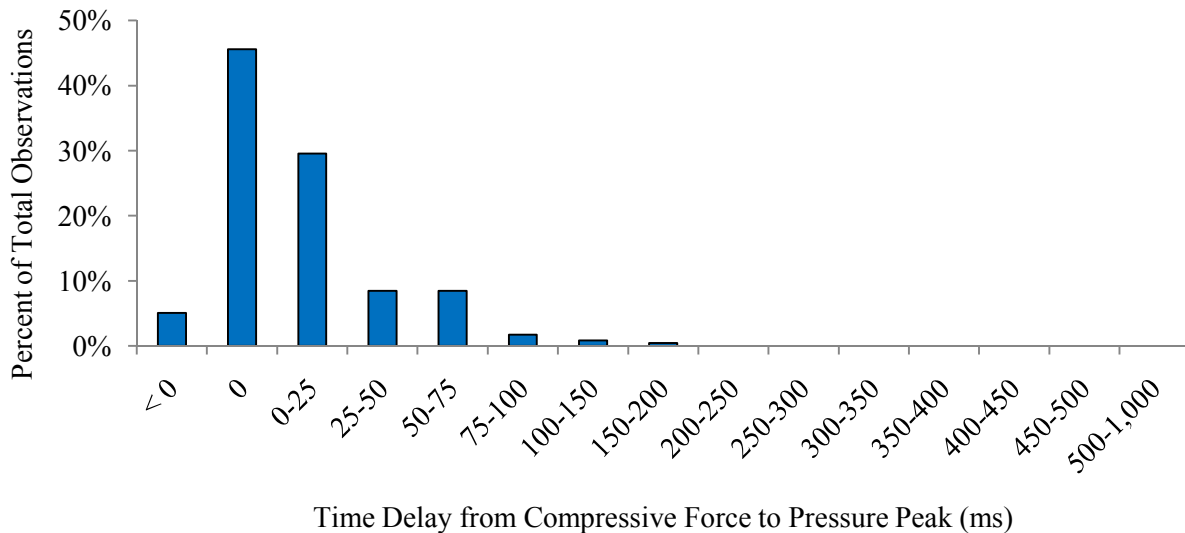
**Figure 5.7 Histogram of time delay from compressive force
to pressure peak for manual test data**

5.4.2   Rebound Suction

The rebound suction peaks appeared in some – but not all – of the different test conditions. The

amount of uplift had a significant influence on the rebound suction, at least for the flat polyurethane pad

(Figure 5.8). One possible explanation is that a greater uplift meant that the compressive stroke was

95

longer and thus could have transferred more energy to the water, resulting in more water-pressure oscillations (water hammer). The most challenging aspect of interpreting the results of varying the uplift or frequency in the manual test was that these factors also influenced the applied force.
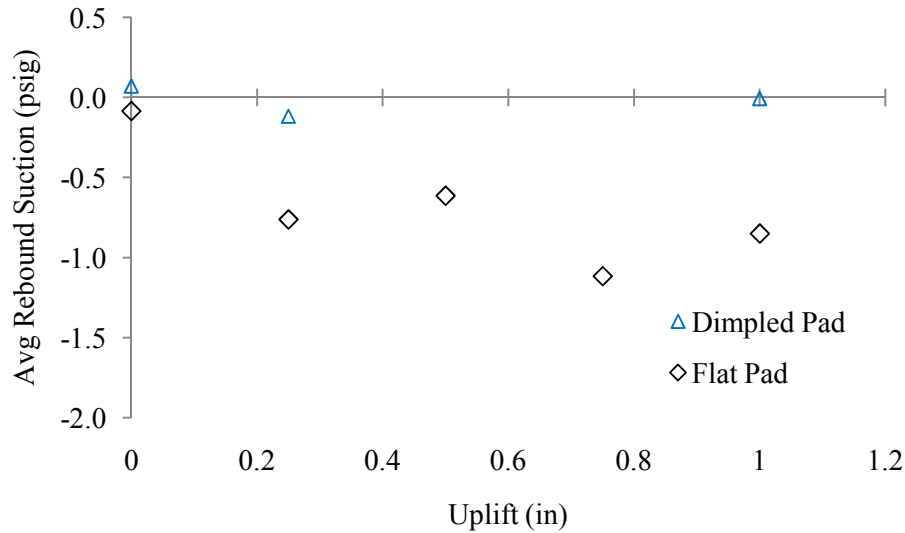
Figure 5.8 Relationship between applied uplift and average rebound suction

Generally, increased viscosity and hydrostatic pressure result in lower rebound suction (Table 5.1 and Figure 5.9). The glycerin tests did not generate any rebound suction peaks, perhaps because the higher viscosity of the glycerin dampened any water hammer reverberations. Increasing the hydrostatic pressure at rest also reduced the rebound suction. This is partially accounted for by the change in the overall water pressure. The extra decrease, at least for the flat polyurethane pad, could be due to increased damping with a larger mass of water.

Table 5.1 Number of rebound suction peaks for different fluids

Fluid Material	Number of Rebound Suction Peaks*	
	Dimpled Pad	Flat Pad
Air	0	1
Water (W)	10	0
2:1 W:G Solution	10	1
Glycerin (G)	0	0

*Each cell represents a trial consisting of ten load cycles
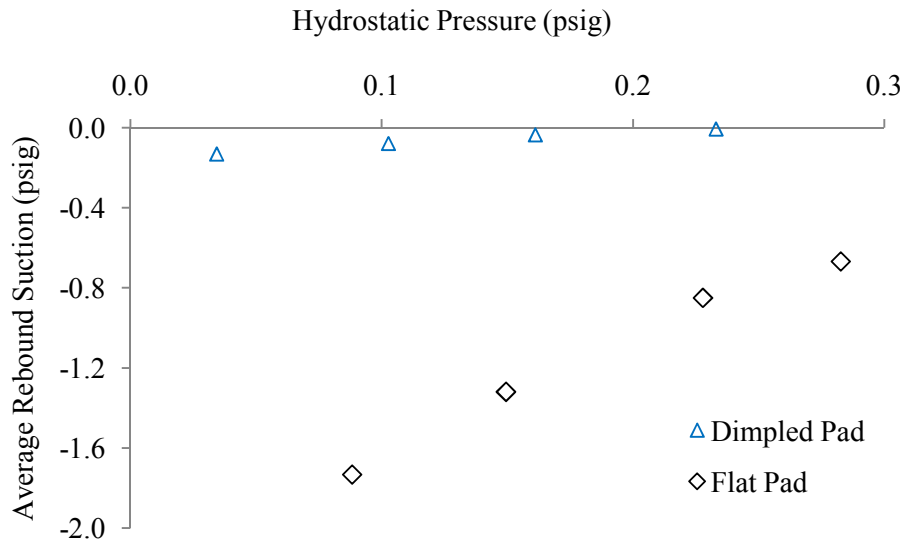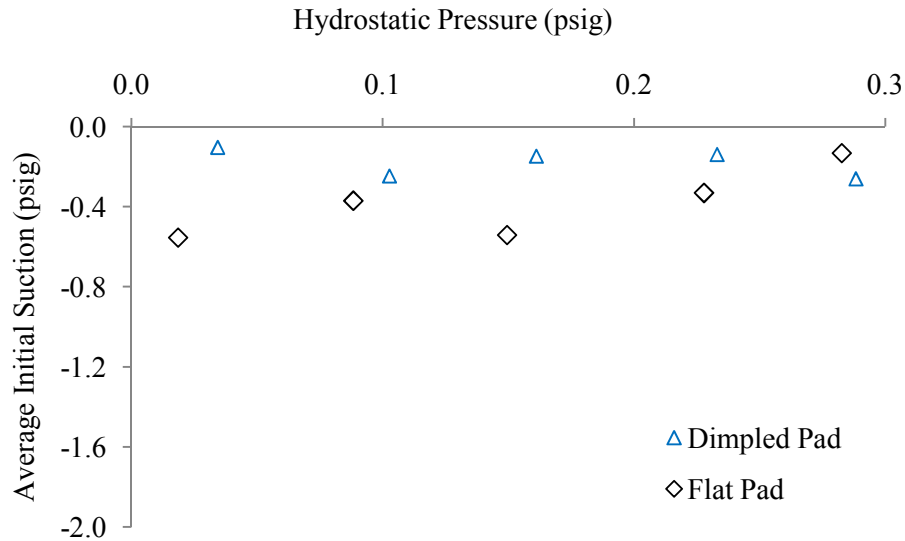

Figure 5.9 Relationship between hydrostatic pressure and average rebound suction

5.4.3   *Factors with Insignificant Correlation to Pressure*

The applied uplift, fluid material, and hydrostatic pressure did not have strong influences on the

pressure or initial suction peaks (Figures 5.10 through 5.14). It appeared that there was a difference

between no uplift and some measurable amount of uplift (Figures 5.10 and 5.11), but further uplift

displacements had little effect. It is difficult to draw conclusions from Figure 5.12 because the flat pad

only showed a distinction between air and the liquids, while the dimpled pad exhibited increasing

pressure with increasing viscosity, suggesting a difference between glycerin and the other fluids. Less surface pressure was generated with a lower hydrostatic pressure, but that from 0.15 to 0.30 psig there was little difference (Figure 5.13). For the lower water levels, the transducer's chamber may not have been sufficiently filled to ensure that load application would pressurize the water. There was no influence on the initial suction due to variations in the hydrostatic pressure.
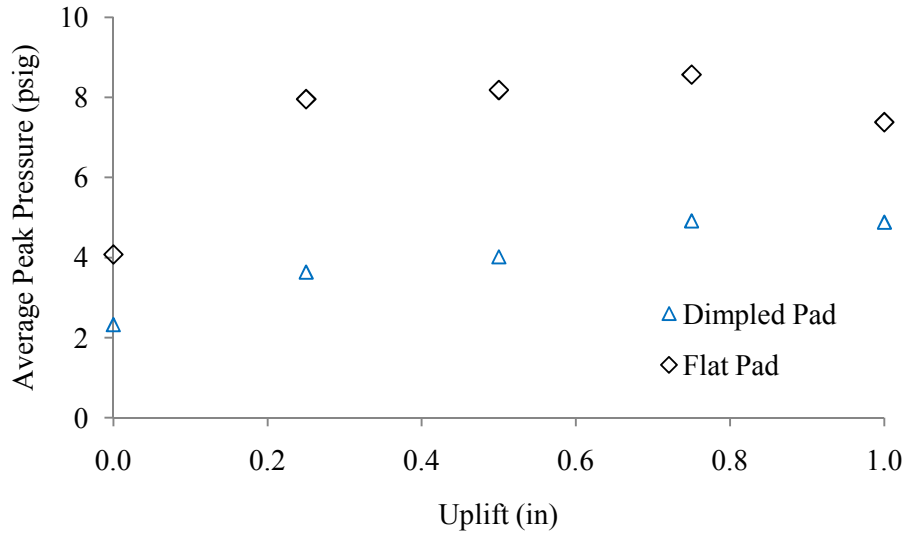
Figure 5.10 Relationship between applied uplift and average peak pressure
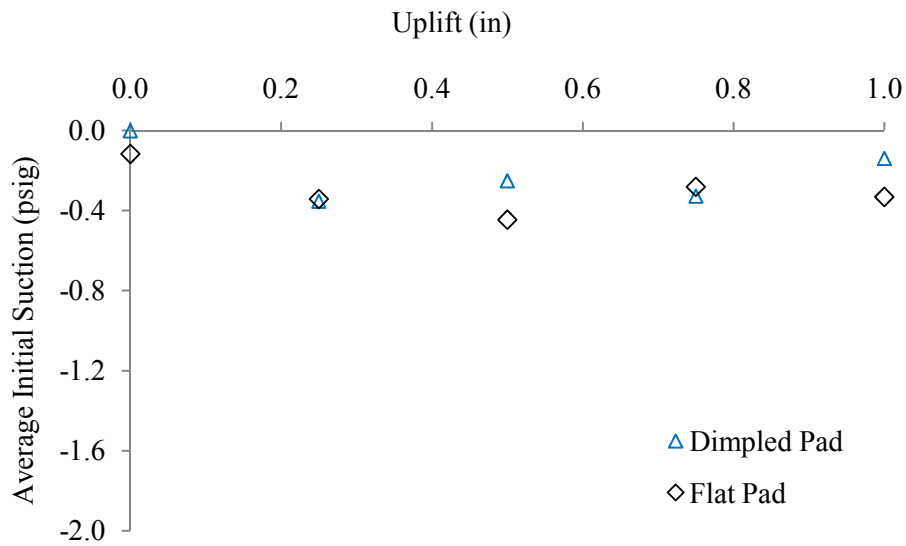
Figure 5.11 Relationship between applied uplift and average initial suction
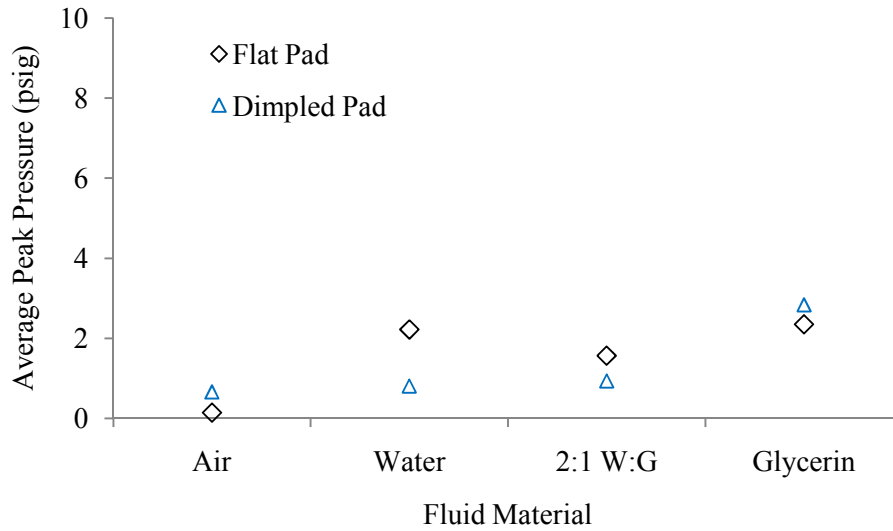
Figure 5.12 Relationship between fluid material and average peak pressure
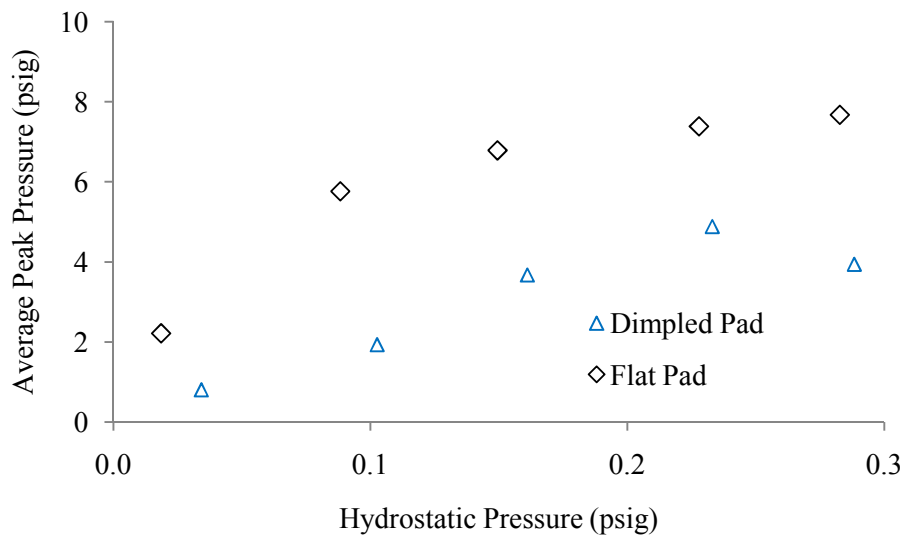
Figure 5.13 Relationship between hydrostatic pressure and average peak pressure

Figure 5.14 Relationship between hydrostatic pressure and average initial suction

5.4.4   Factors with Significant Correlation to Pressure

The proceeding graphs present both the pressure and suction peaks as functions of the compressive force peaks (Figures 5.15, 5.16, 5.17, and 5.19). The positive pressure peaks directly corresponded to the compressive forces. The suction peaks were included as reference, but there was no evidence that a relationship existed between the applied compressive force and the measured suction.

For the low range of forces used in the manual tests, there was a subtle distinction between the pad geometries (Figure 5.15). In particular, the flat pad consistently exhibited higher peak pressures than the indented pads. The indented pads generated similar positive pressure. The dimpled pad generated slightly greater suction, though the measurements were so small that it was difficult to distinguish them.
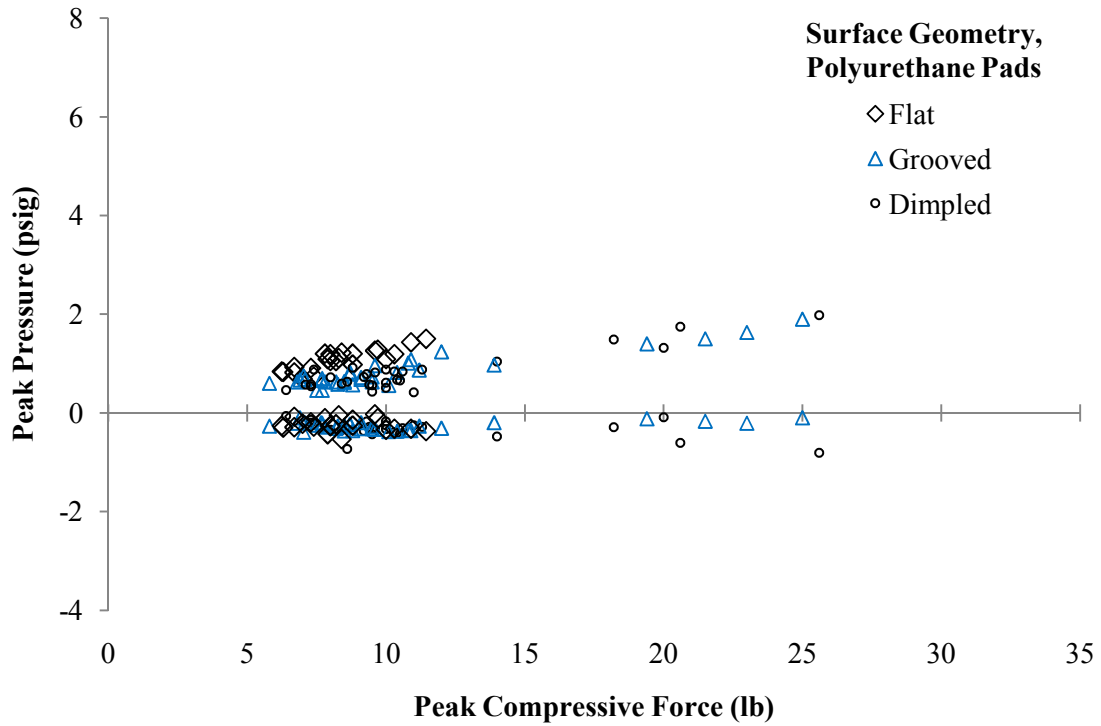
Figure 5.15 Peak pressures for different polyurethane pad geometries

The transducer was placed at varying depths below the rail seat surface (Figure 5.16). The slight differences between the average pressure values are not as noteworthy as the increase in the variance of the pressure measurements as the depth to the transducer orifice increased. This is consistent with findings in fluid mechanics that exposed rough surfaces, such as burs or pipe threads, can induce turbulence near a transducer's orifice that can lead to artificially higher or smaller measurements (Munson et al. 2006).
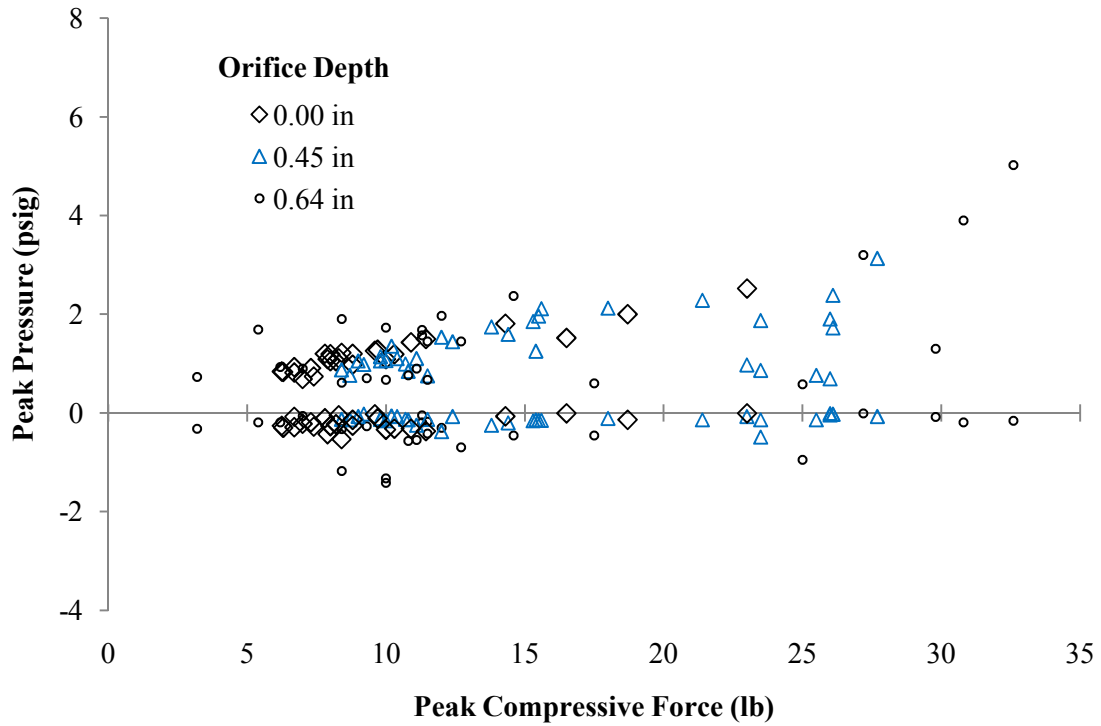
**Figure 5.16 Peak pressures for adjusted depths
of the transducer orifice beneath the rail seat surface**

By adjusting the contact angle between the loading plate and the rail seat plate, the measured water pressure was reduced (Figure 5.17). It appears that there was little measurable difference between a two-degree and a six-degree contact angle. In other words, as long as there was a slight mismatch between the two plates, the pressure was reduced.
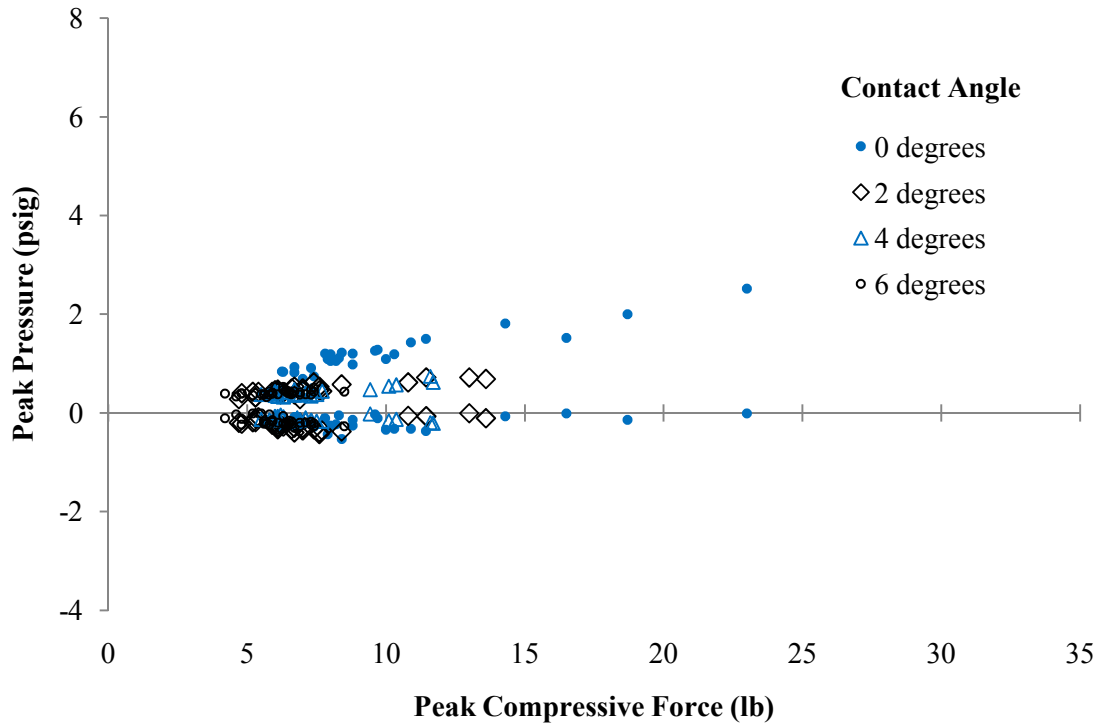
**Figure 5.17 Peak pressures for different contact angles between
the loading plate and the rail seat surface**

Different horizontal alignments of the loading plate relative to the pressure transducer (Figure 5.18) were tested to understand the distribution of water pressure under the tie pad (Figure 5.19 and Table 5.2). It is difficult to draw strong conclusions from the results in Figure 5.19 due to the high variability, but it appears that the bottom alignment produced some of the highest pressure and suction peaks. The side alignment produced the greatest suction but some of the lowest pressures. The center alignment, the alignment used in the subsequent, full-scale load and uplift tests, generated the second highest pressures, with considerably less scatter than the bottom alignment.
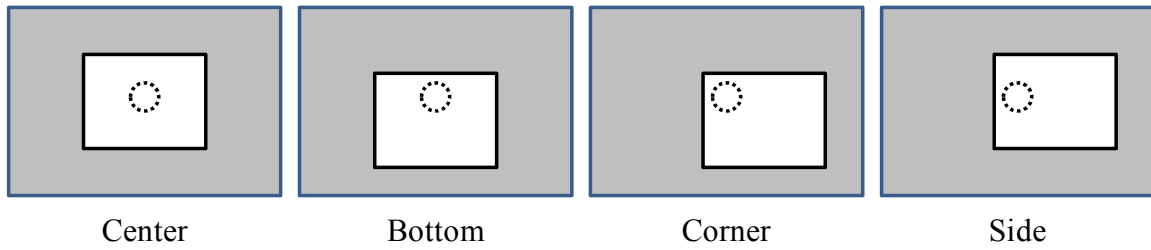
Figure 5.18 Horizontal alignments of the loading plate (white rectangle) relative to the pressure transducer (dotted circle), with center as the control alignment
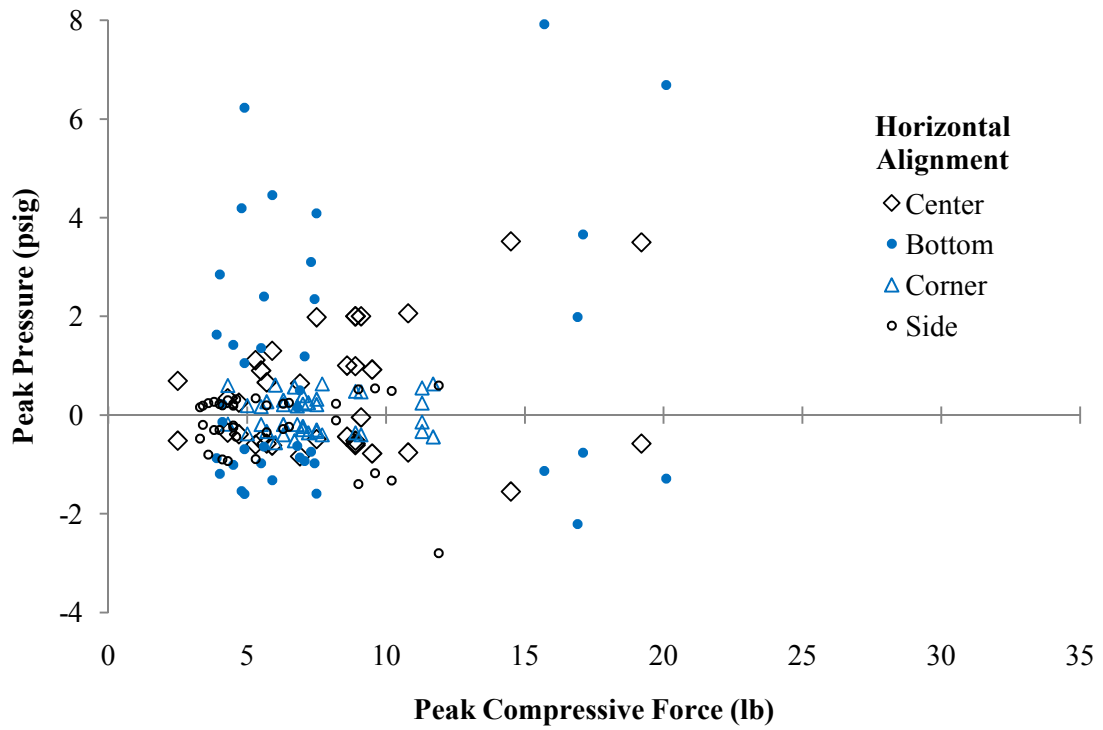

Figure 5.19 Peak pressures for different horizontal alignments of the loading plate relative to the pressure transducer's location

**Table 5.2 Statistical analysis of the peak pressure data for different
horizontal alignments of the loading plate relative to the pressure transducer**

	Horizontal Alignment			
	Center	Bottom	Corner	Side
Regression on Positive Pressure versus Compressive Force				
Slope (psig/lb)	0.21	0.22	0.02	0.04
Intercept (psig)	-0.30	1.11	0.20	0.04
R-squared	0.75	0.25	0.08	0.73
Peak Suction Values				
Average (psig)	-0.60	-1.06	-0.33	-0.71
Twice the Standard Error (psig)	0.14	0.20	0.05	0.30
No. of Data	18	20	20	19

5.5 Conclusion

Observations from the manual tests helped guide the development of the mechanically-driven load and uplift tests. Due to the high variability of both the pressure measurements and the applied load rate and magnitude, it was difficult to have confidence in the manual test data or draw distinct conclusions. Some important observations that guided later tests were:

- The pressure transducer should be flush with the rail seat surface to minimize error

- A nonzero contact angle between the loading plate and the rail seat reduced the surface pressure

- The data acquisition period should be at most five ms to capture the rapid pressure responses

- Increasing the uplift amplitude above a small amount had little effect on the surface pressure

Returning to the four hypotheses listed at the beginning of this chapter, the manual tests confirmed that varying the contact angle produced lower pressure and that varying the horizontal alignment of the loading plate revealed a non-uniform water pressure distribution. The manual tests did not show a strong distinction between tie pad geometries, but they did reveal the linear increase of positive pressure with increasing compressive force.

When trend lines were fitted to the data from one set of tests it suggested that there were distinctions between the three polyurethane pad geometries (Figure 5.20). Each trend line had an R-squared value greater than 0.80. As was shown in Figure 5.15, the flat pad produced higher average pressures, but it also had a steeper force-pressure slope than the other two pads, which behaved similarly in these manual tests. This concept of relating the peak pressure to the applied force was continued in the load tests. The force-pressure relationships observed in the manual tests (Figure 5.20) were extrapolated to develop rough estimates of what could be expected in the higher load, mechanically-driven tests that were a primary objective of this research (Figure 5.21). These extrapolations predict pressures up to seven times greater than expected based on Bakharev's (1994) assumption equating the surface water pressure to the applied load divided by the rail seat area. Based on these results, a 6,000-psig transducer was purchased for the load tests. The results of the load test later disproved the extrapolations in Figure 5.21, suggesting that applied loads from zero to 20 kips (k) generate a nonlinear pressure curve (Figure 6.17).
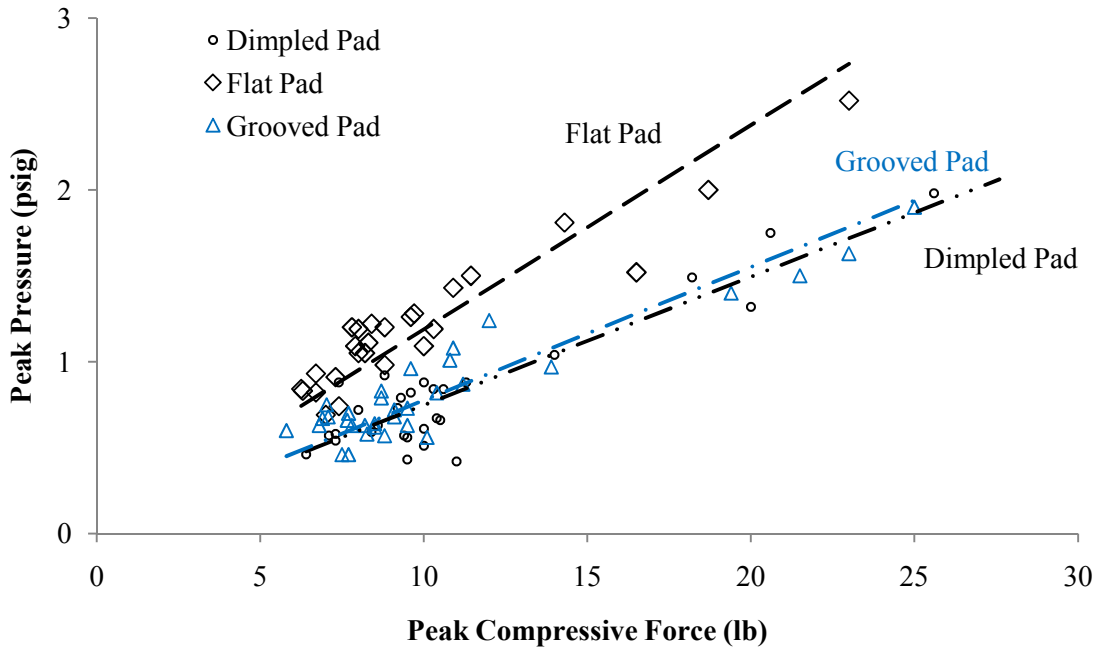
**Figure 5.20 Relationship between peak compressive force
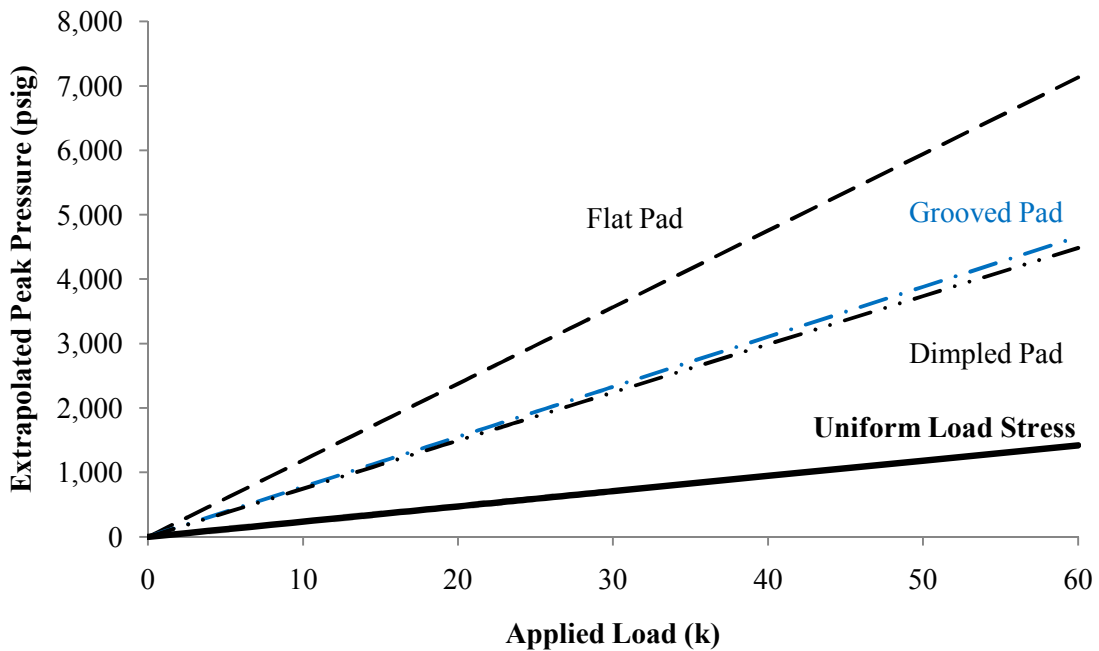and peak pressure for three polyurethane pads**

**Figure 5.21 Extrapolated relationship between applied load and peak pressure, based on
the manual test results, compared with the theoretical pressure due to applied load**

CHAPTER 6: LOAD TESTS[5]

6.1   Motivation

In a previous study of hydraulic pressure cracking, it was assumed that the surface pressure p was equal to the uniform vertical load stress (Bakharev 1994). A linear extrapolation of the manual tests at low loads resulted in pressures much higher than this, and it appears that the pressure, at least in part, depends on the type of tie pad being used (Figure 5.21). A laboratory test apparatus and procedure were devised to measure p in a saturated rail seat for different tie pads and loading scenarios to determine the validity of these predictions and whether the tie pad material or surface geometry affects the pressure generated.

In this study, the primary goal was to measure the water pressure at the interface between the concrete rail seat and the tie pad. Mock rail seats constructed of concrete were instrumented and tested in the laboratory. Only a normal force was considered because it was assumed that lateral forces would have little effect on the pressure or would reduce the pressure, relative to the normal force case.

6.2   Materials & Equipment

6.2.1   Concrete Block Specimens

To mimic the height and width of a concrete tie (Figure 1.1), the concrete blocks were eight inches high and eight inches wide (in the longitudinal direction of the rail). To make the third dimension longer than the other two while still keeping the weight of the block around 50 pounds (lb), the length of the block (perpendicular to the rail) was designed to be ten inches.

The bearing strength of the concrete block was estimated according to the American Concrete Institute (ACI) 318-08 Building Code (ACI 2008). The bearing area was assumed to be 6 x 8 inches, the concrete strength was assumed to be at least 7,000 pounds per square inch (psi), and the strength

---

[5] Parts of Chapter 6 were originally published in the Proceedings of the 2010 Transportation Research Board Conference in Washington, DC, USA (Zeman et al. 2010a) and in the Proceedings of the 2010 Joint Rail Conference in Chicago, Illinois, USA (Zeman et al. 2010b)

reduction factor was 0.65 for concrete bearing (Section 9.3.2.4 of ACI 318). According to ACI Section

10.14.1, the bearing strength for this case was (ACI 2008):

$$\phi_b P_n = \phi_b (0.85) f_c' A = (0.65)(0.85)(7 ksi)(8")(6") = 186 kips$$

Using the American Society of Civil Engineer's ASCE-7 load factor of 1.6 for live load (Section 9.2.1 of

ACI 318), and considering the full capacity of the actuator of 100 kips, the ultimate design load would be

160 kips (ACI 2008). According to these calculations, the bearing capacity of the block was adequate.

The specimens were unreinforced concrete with Type III cement, made using a mix design from

Bakharev's previous concrete tie research (1994) that is similar to mix designs presently used by US

concrete tie manufacturers (Table 6.1). The concrete was batched by manually adding the dry

components to a two-cubic-foot (ft^3) mixing drum. The dry components were mixed for one minute, the

water and air-entraining admixture (AEA) were added slowly over the course of a minute, the

superplasticizer was added, and everything was mixed for an additional minute. Daravair 1400 and

Advacast 530 were used for the AEA and super plasticizer, respectively. Each two-cubic-foot batch was

distributed among three blocks, three 4 x 8 inch cylinders, a 0.25 ft^3 bucket for air content and unit weight

measurements, and a slump cone test. The fresh concrete properties for each batch are summarized in

Table 6.2. The concrete blocks were cast with a 1.25-inch diameter stainless steel pipe and a cylindrical

opening 1.75 inches in diameter and 0.75-inch deep to provide space for a stainless steel coupling (Figure

6.1). Appendix D contains photographs of the forms used to cast the blocks. The cylinders were placed

in three lifts, with each lift rodded 25 times according to ASTM C192. The blocks were placed in three

lifts, with each lift compacted by placing the form on a vibrating table for ten seconds at 10,000

revolutions per minute.

Table 6.1 Mix design for the concrete blocks

	SSD Weights (lb per yd^3)	Stock Batch Weights (lb)	Moisture Content (%)
3/4" Limestone	1,809	139.2	-1.38
Sand	1,242	95.0	-2.00
Type III Cement	640	49.9	
Water	205	19.90	
Target Air Content	5%		
Target Batch Volume	2.0 ft^3		
Water-to-cement ratio (w/c)	0.32		

Table 6.2 Properties of the four concrete batches

	Batch W	Batch X	Batch Y	Batch Z
Air entraining admixture (mL)	28	36	17	12
Super plasticizer (mL)	177	190	200	200
Air content	10.3%	10.8%	7.3%	7.8%
Slump (in)	0.75	0.50	3.00	4.50
Unit weight (pcf)	139.0	140.8	144.6	143.4
28-day strength (psi)	8,014	7,731	8,420	8,843
	8,431	7,983	8,708	9,225
	7,511	7,865	8,613	6,199
Average strength (psi)	**7,985**	**7,860**	**8,580**	**8,089**

The blocks and cylinders were allowed to cure for 24 hours before being demolded. The hardened concrete specimens were placed in a moist cure room with 100% relative humidity at 72° Farenheit (F) for the remainder of the four weeks of curing. After curing for 28 days, the concrete specimens were removed and capped with a sulfur compound according to ASTM C617, and the cylinders were tested in compression according to ASTM C39. The resulting 28-day compressive strengths for each batch are summarized here (Table 6.2).

The top surface of each concrete block was cast against the form, while the bottom surface was open to the atmosphere, resulting in a rough, unfinished surface. To avoid problems with the concrete block bearing on the steel base plate, the same sulfur compound used for the ASTM C39 cylinders was used to cap the bottom of the blocks. The procedure to cap the bottom of a block involved arranging a temporary mold with an aluminum plate, two short walls, and solid metal blocks to stabilize this arrangement. Two adjustable clamps were used as handles to lift the blocks. A dowel rod was placed inside the steel pipe to ensure that sulfur compound did not penetrate inside the pipe. One person rapidly poured the molten sulfur compound to cover the metal plate, and a second person immediately lowered the block's bottom surface onto the molten sulfur. The result was a smooth bearing surface, though it was not always parallel to the block's top surface.

Once a block's bottom had been capped, the pressure transducer could be installed. A stainless steel coupling was secured on the end of the transducer so that the transducer's orifice was flush with the coupling's surface. The transducer-coupling assembly was threaded through the steel pipe in the concrete block so that the coupling rested on top of the steel pipe and was flush with the concrete block's surface, as shown in Figure 6.1. A high strength, two-part epoxy was applied to the circumference of the coupling to create a seal and secure the transducer in place. An attempt was made to leave the "rail seat" surface as flat and undisturbed as possible. An example of an instrumented concrete block is shown in Figure 6.2, with the transducer's cable running out the bottom of the block.
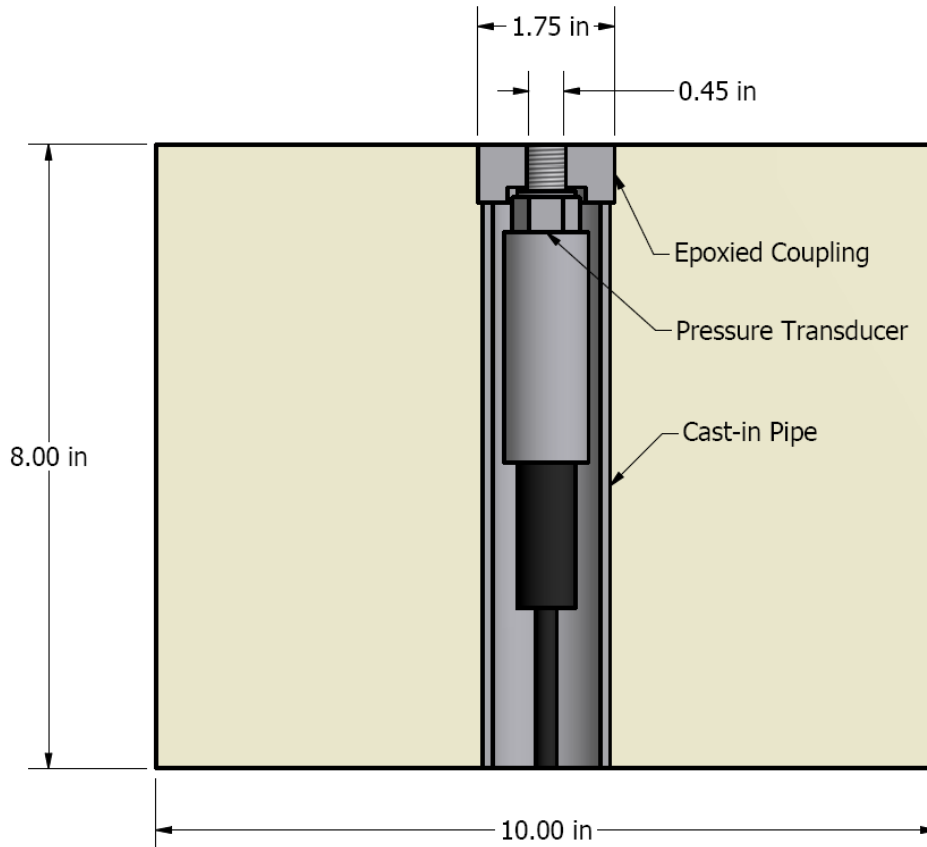
Figure 6.1 Cross-section drawing of pressure transducer placement within concrete block

Figure 6.2 Concrete block prepared with pressure transducer

112

To remove a pressure transducer from the concrete block, a set of chisels would be used to chip around the coupling and remove it. Because this process would remove a small amount of concrete surrounding the coupling, a block could only withstand a few cycles of installing and removing transducers before the surface appeared to be unacceptably disturbed. Then a new block would be used.

6.2.2   *Test Frame and Water Tank*

A test frame was assembled from available stock columns and channels (Figure 6.3). The position of the top channels was specified based on the length of the actuator, which was between 86 and 92 inches since its piston had a six-inch stroke. During initial tests, the frame swayed and vibrated noticeably, particularly at loads above 40 kips. To reduce the swaying, a second set of channels was attached to the frame to provide lateral stiffness.
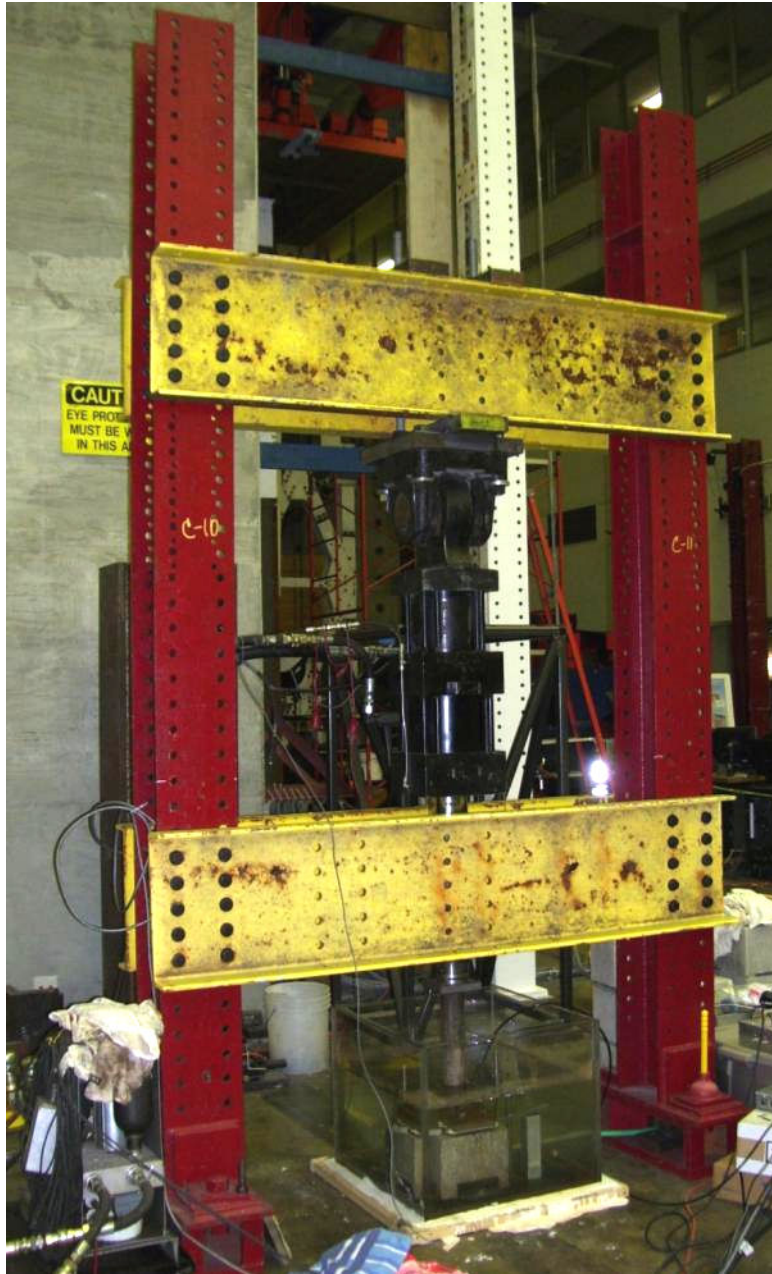
Figure 6.3 Mechanically-driven test apparatus

Initially, the actuator was connected to the top channels by tack welding a plate to each

connecting element. This tack weld fractured after about a week of testing due to local flexing of the

channel at the connection. The second connection was a pair of large-diameter threaded rods extending

from the actuator's hinge to a point above the top of the top channels. These threaded rods were bolted to

two plates to clamp the actuator to the channels. This connection was adequate at first and was used

throughout most of the load tests described in this chapter. However, with each trial at high loads, the actuator shifted slightly at the connection point. The local flexure of the channels during a downstroke caused the top plates to lose contact with the top of the channels. It was by this mechanism that the actuator was able to slowly slip along the channels. It eventually became a problem because the loading plate had shifted too far from the center of the concrete block. The solution was to slide the actuator back into position, keep the bolted clamp connection, and add a more substantial weld between the actuator and the bottom of the channels to prevent slip. This bolted-welded connection was adequate for these tests and was also used for the uplift tests, described in Chapter 7.

The base plate thickness was designed using the American Institute of Steel Construction (AISC) Steel Construction Manual, part 14 (AISC 2006), assuming A36 steel (yield strength of 36 ksi), and using the initial plate dimensions 16 x 16 inches, with a four-inch overhang. As with the bearing check for the concrete block, the load considered here was the 100-kip actuator capacity with the 1.6 ASCE-7 load factor. The resulting base plate thickness to minimize deflections would be (AISC 2006):

$$t_{\min} = l\sqrt{\frac{2P_u}{0.9F_y BN}} = (4")\sqrt{\frac{2(1.6)100kips}{0.9(36ksi)(10")(8")}} = 1.41" \rightarrow 2.0"$$

Two inches was selected as the base plate thickness. In subsequent designs, the concrete block was offset from the center of the plate and the plate dimensions were increased for easier access to the block, increasing the overhang threefold to 12 inches. The plate thickness was not increased, which resulted in significant flexure observed in the plate during tests. Accounting for the increased overhang, the plate thickness should have been:

$$t_{\min} = (12")\sqrt{\frac{2(1.6)100kips}{0.9(36ksi)(10")(8")}} = 4.22" \rightarrow 4.25"$$

Another reason for the visible flexure in the base plate during initial tests was the slight mismatch between the bottom of the base plate and the testing floor, such that the base plate was not uniformly bearing on the floor. To fill in the gaps under the base plate, the water tank was lifted (using the actuator), a high-strength plaster (Hydrocal®) was poured within a set of forms, and the water tank was

lowered. This plaster performed well until the water tank began leaking around its bottom edges. In general, plaster degrades when exposed to water. In this case, the plaster began to slowly break down once the leaking began. Initially, the water tank only leaked during trials at 60 kips, presumably because such a high load flexed the plate enough that the O-rings around the screws connecting the base plate and the plexiglass walls were not adequate to seal the water. After running many trials, the water tank would leak without any applied load. At this point, the water tank had to be removed and re-assembled with more extensive sealing around the base of the plate-plexiglass connection. The water tank was re-installed with a new layer of plaster and this proved to be adequate.

A groove was cut into the surface of the base plate to allow the pressure transducer cable to exit the bottom of the concrete block and out the top of the water tank. It was cut one-inch deep, based on the flexibility of the submersible cable, to prevent straining the cable.

Angle sections (visible in Figure 6.4) were included to secure the concrete block laterally and aid in achieving the proper alignment of the actuator and the block. The size of the angles was specified to fit short-slotted holes (SSH's) and bear on the side of the concrete block. The SSH's allowed room for the adjustments required due to variability of block dimensions and the alignment of the loading plate. The bolts for the angles were sized at 3/4" to match the bolts chosen for the base-of-rail plate (see Section 6.2.3). The bolts had a design strength similar to or higher than that of the bolts in the base-of-rail plate.

Figure 6.4 Close-up of the water tank of the mechanically-driven test apparatus

Initial uplift tests demonstrated that vertical restraint of the block was required. The suction created by the uplift of the loading plate was sufficient to lift the block off its base. This movement of the block could have damaged the test apparatus, so aluminum bars were installed as clamps, acting as flexible springs to hold down the block (Figure 6.4).

As with the plastic tub for the manual test apparatus, a drainage valve was attached to the water tank near its base, and this can be seen in the right-hand side of Figure 6.4. After each day of testing, the water tank needed to be drained and cleaned to prevent excessive rusting of the non-stainless steel components (the base plate, the loading plate, and the angles). Another motivation for cleaning the water tank regularly was that the mixture of rust particles and the sulfur compound – either partially crushing into a powder or dissolving into the solution – resulted in an odorous, black compound forming around the base of the block.

6.2.3   Actuator and Controller

A 100-kip MTS servo-hydraulic actuator was used to apply normal loads to the tie pads on top of the instrumented concrete blocks. The actuator loaded the block through a loading arm and a loading plate that extended its reach below the water level so as to not wet the actuator. The lab coordinator recommended that for cyclic loads, at frequencies greater than three Hertz (Hz), the load should be kept below 70% of the actuator's capacity. The ultimate service load for the actuator was selected as 60 kips.

For the 60-kip service load, using the ASCE-7 live load factor of 1.6, the ultimate design load was 96 kips. The design length of the actuator's loading arm was 16 inches. The actuator was pinned to the channels at the top of the frame, and the loading plate bearing on the pad and the concrete block was idealized as a pinned connection. Therefore, the effective length factor (K) of the loading arm was selected as 2.0, from case (f) in Table C-C2.2 in the AISC Commentary. The KL was conservatively taken as three feet, in AISC Manual Tables 4-4 (square tubes) and 4-5 (circular tubes). From these tables, the most economical sections were HSS3x3x3/8 (square) with a design strength of 135 kips and HSS4.000x0.250 (circular) with a design strength of 99.7 kips (AISC 2006). Any tube or circular section used for the loading arm had to be these sizes or greater. A circular section that exceeded the minimum size was selected from available materials.

A typical rail base is six inches wide, and a typical concrete tie is approximately 7.5 inches wide at the rail seat, so the "base-of-rail" plate was chosen to be six inches by eight inches. The base flange of a typical 136 RE rail section has an area just under five square-inches (NS Railway 2001), so a one-inch thick base-of-rail plate was selected. The plate welded to the actuator arm was designed to be 3/4-inch thick to provide shear resistance in the event that lateral forces developed due to misalignments in the load arm or actuator. For convenience, 3/4-inch A325 bolts were chosen, and the loading plate connection was checked for strength according to the AISC Manual.

Table J3.4 in the AISC Code specifies that 3/4-inch bolts should have a minimum 1-1/4-inch distance from the nearest sheared edge, and this was observed in the design. From AISC Table 7-1, the design shear strength of four 3/4-inch bolts on a single plane of shear, with the threads included, is 64

118

kips. From ASIC Table 7-5, the design bolt-hole bearing strength based on bolt spacing was 58 kips,

considering the closest spacing of three inches on the 3/4-inch plate. From AISC Table 7-6, the design

bolt-hole bearing strength based on edge distance was 33 kips, considering the shortest edge distance of

1-1/4 inches on the 3/4-inch plate (AISC 2006). Subsequently, the design strength of this connection in

shear was 33 kips. This shear strength would resist the lateral component of the actuator's load, assuming

that the actuator was misaligned by some angle. Using the 1.6 ASCE-7 load factor on the full capacity

100-kip load, the misalignment angle required to exceed the connection's design strength would be:

$$\text{Max Actuator Angle } = \arcsin\left(\frac{33kips}{1.6(100kips)}\right) = 12°$$

For the average length of the actuator of 89 inches, this maximum angle would result in a shift at the

loading plate of approximately 18 inches. Such a large shift in the loading plate would make it lose

contact with the rail seat block, so this load appeared to be theoretically unachievable. Therefore, the

shear strength of the loading plate connection was deemed adequate for this test apparatus.

The actuator arm was originally planned to be bolted to the actuator via a plate welded to the

structural tube, but it was determined that using a circular tube and threading it to mate with the actuator

would make assembly and adjustment easier. Spiral washers/shims were used to secure the actuator arm

to the actuator.

The servo-hydraulic actuator had a piston area of 33.3 in^2, and its servo-valve had an oil flow rate

capacity of ten gallons per minute (gpm). The following equation was used to estimate the flow rate

required to produce a motion with a certain frequency (Hz) and amplitude:

$$\text{Oil flow rate} = 2(\text{double amplitude})A_{piston}f\left(\frac{60}{231}\right)(1.10)$$

where the double amplitude is the range of displacement in one cycle. With input units of inches and

square-inches, the output of this equation is in gpm. The equation includes a factor for ten percent losses.

The required oil flow rate was estimated for a range of frequencies and double amplitudes (Table 6.3),

and these estimates served to bound the available frequency and double amplitude combinations for my test apparatus.

Table 6.3 Limits on the frequency and amplitude of the actuator's motion

Flow Rate (gpm)	Frequency (Hz)				
	1	2	3	4	5
0.06	1.1	2.3	3.4	4.6	5.7
0.08	1.5	3.0	4.6	6.1	7.6
0.10	1.9	3.8	5.7	7.6	9.5
0.12	2.3	4.6	6.9	9.1	11.4
0.14	2.7	5.3	8.0	10.7	13.3
0.16	3.0	6.1	9.1	12.2	15.2
0.18	3.4	6.9	10.3	13.7	17.1
0.20	3.8	7.6	11.4	15.2	19.0
0.22	4.2	8.4	12.6	16.8	21.0
0.24	4.6	9.1	13.7	18.3	22.9

(Double Amplitude (in) is the row label for the 0.06–0.24 values.)

▮ Actuator operation limited by the flow rate

6.3   Procedure

After applying simplifying assumptions about a 286,000 lb gross rail car load, the static normal force on one rail seat was approximated as 20 kips, while an upper bound of dynamic normal force was approximated as 60 kips (see Section 4.2).

The pressure transducer used for the load tests was a 6,000-psi gauge (psig), submersible TDG 03/04 unit, purchased from Transducers Direct (see Section 5.2.2 for more information).

Over 180 unique scenarios were tested for the load experiments, and at least one replication was conducted per scenario. The tests involved cyclic loading of the concrete block, cycling the load from a minimum of five kips up to a maximum load, chosen from 20, 30, 40, 50, or 60 kips. The waveform of the load was chosen from trapezoidal wave (ramping at 200 kips per second), square wave, or sinusoidal wave (at a frequency of two or four Hz). The trapezoidal and square wave tests were conducted at a frequency of one half Hz. The water level in the tank was varied from zero to six inches above the rail seat surface, with six inches selected to be the typical water level.

When running the tests, water was filled to the desired level, the pad under consideration was placed on the block, and the actuator was lowered to a point of contact (arbitrarily defined as 200 lb of force) to secure the pad in place. When a pad with indentations was used, the dimensions of the pad and the block were used to align the pad indentations in a specific way relative to the transducer orifice. The following three alignments were tested (Figure 6.5): (1) indentations were centered over the transducer's orifice (aligned), (2) the transducer was centered between two indentations (misaligned), and (3) an alignment between the previous two (half-aligned). All tests were run for 30 seconds, so that a four-Hz test contained 120 cycles, whereas a one-half-Hz test contained 15 cycles. As with the manual tests, the data acquisition rate was set at five milliseconds (ms). Between trials with no changes in the water level or pad, the pad was secured to the block while the actuator was raised to allow relaxation of the pad and return of any water that had been expelled from the rail seat during the previous trial. This seemed to be an effective method for creating repeatable results.

Aligned   Misaligned   Half-aligned
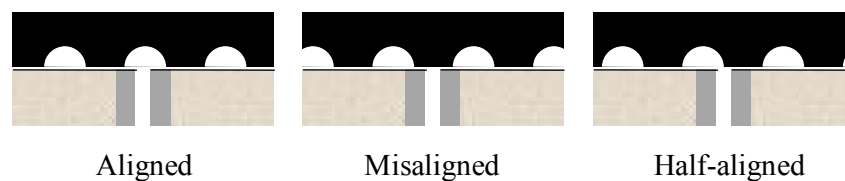
**Figure 6.5 Elevation view of three alignments of pad indentations
relative to the transducer's orifice**

In an attempt to understand the effect of different pad geometries, a set of grooved and dimpled polyurethane pads were modified in one of three ways: (1) the center indentation on the pad was filled with epoxy (local fill), (2) all indentations except the center one were filled with epoxy (bulk fill), or (3) two small, perpendicular channels that intersected at the center indentation were saw-cut (channelized).

6.4   Results

The data were processed so that the peak pressure values were identified for each trial, using the Matlab code "processdata" and "assembly" given in Appendix B. Examples of the raw data from a load test are presented in Appendix E (Figures E.1 through E.5).

At the beginning of each test, the actuator took approximately five seconds or more to reach a steady state at the specified cycled load. This occurred because as the actuator began to apply the load, its first application was slightly off from the target, and the controller corrected for this error by adjusting the motion. After enough cycles, the errors would be minimized through an integration correction process, and the cycled load became steady. This results in a subtle initial error in terms of applied force, but for some tests, it made a significant impact on the surface pressure generated with each load cycle. Appendix E contains data from trials where this effect was observed.

The sensitivity of the maximum surface pressure to different testing parameters was evaluated by varying the loading waveform (Figure 6.6), the water level (Figure 6.7), the indentation alignment (Figure 6.8), and the pad geometry modifications (Figure 6.9). Each figure plots all of the data for the given variable at a 40-kip applied load, sorted by pad type. Otherwise, the data plotted in each figure were not sorted to consider other variables or an interaction between the variables – i.e., the data under the "square wave" category in Figure 6.6 contain data from multiple indentation alignments and water levels. Of the four variables plotted, the only one that had a significant effect on maximum surface pressure was the channelized pad geometry modification (Figure 6.9). Otherwise, in terms of the surface pressure generated, there was little observable difference between different waveforms, water levels, or indentation alignments. An analysis of variance (ANOVA) was performed on the data in Figures 6.6 through 6.8 (Appendix E, Tables E.1, E.2, and E.3), and it indicated that loading waveform and water level did not significantly affect surface pressure.
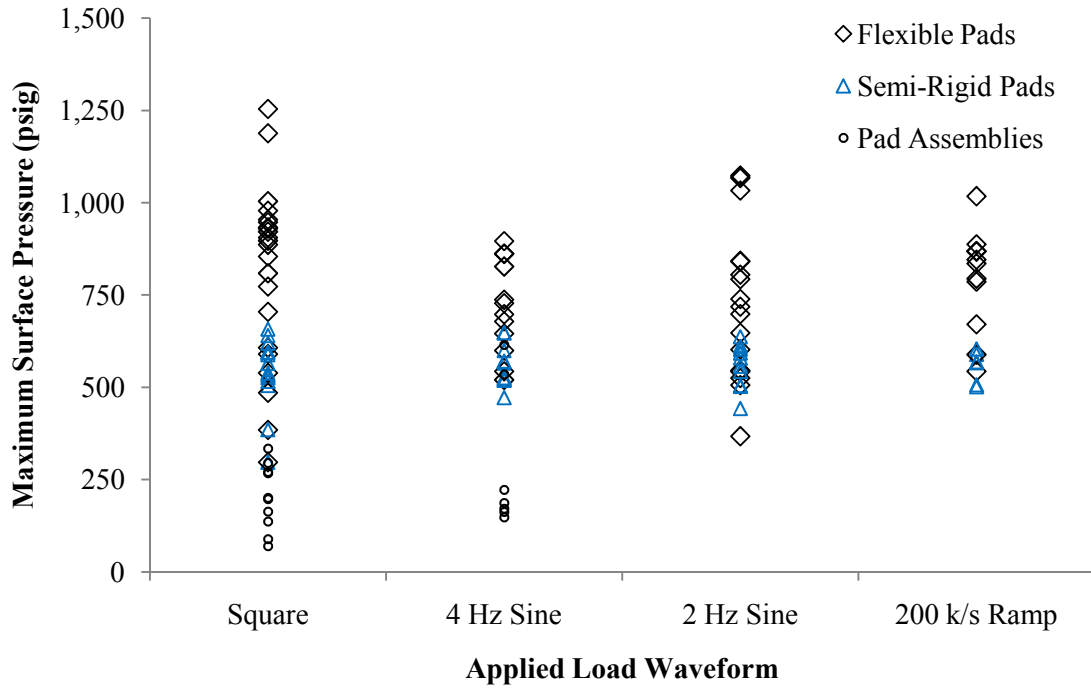
**Figure 6.6 Comparison of the maximum surface pressure
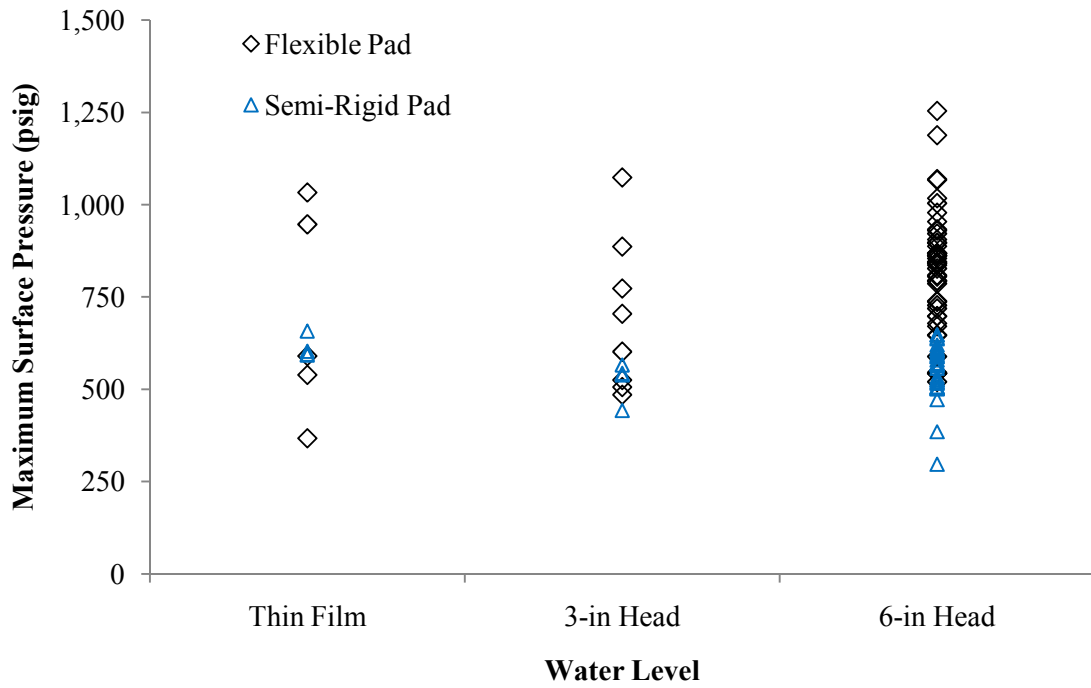for four loading waveforms, 40-kip applied load**

**Figure 6.7 Comparison of the maximum surface pressure
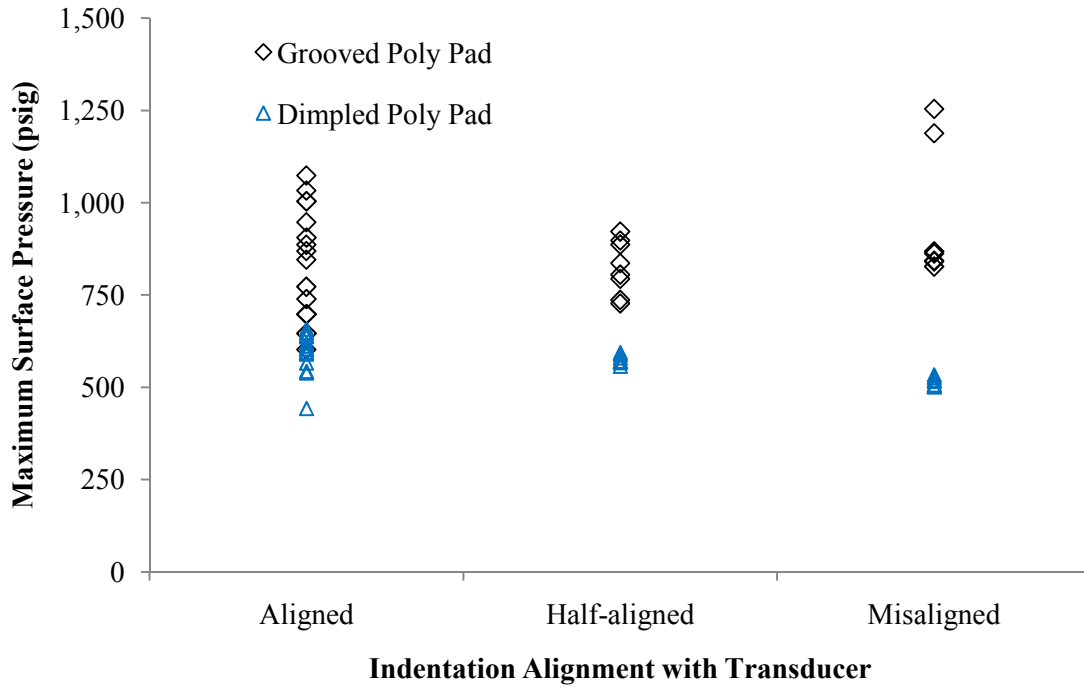for three water levels, 40-kip applied load**

**Figure 6.8 Comparisons of the maximum surface pressure
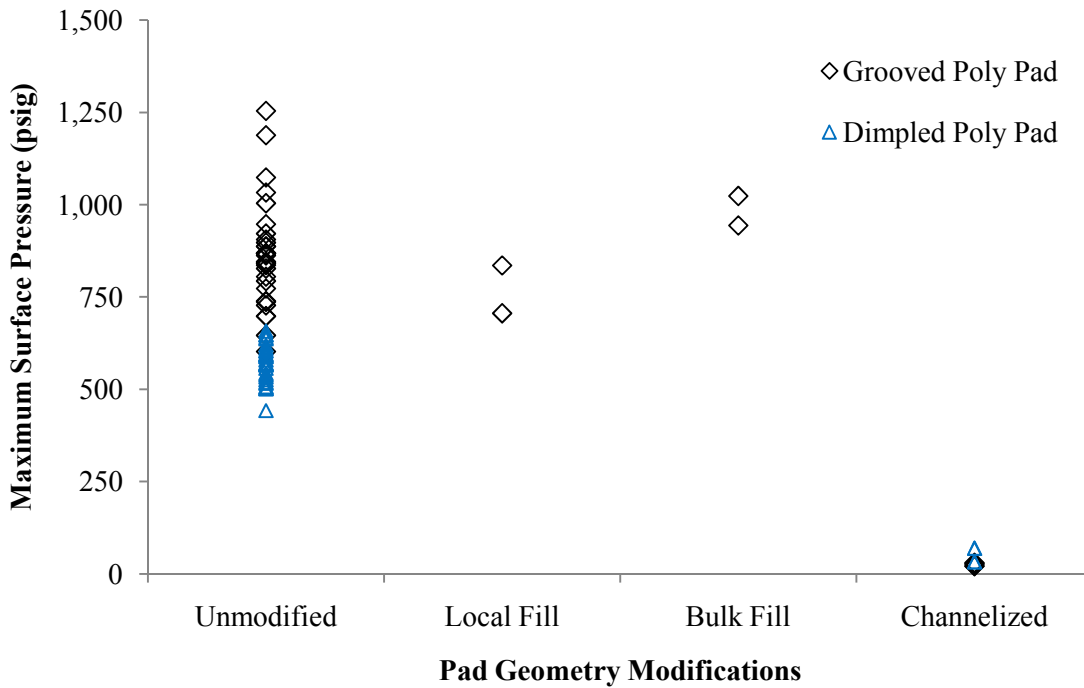for three pad indentation alignments, 40-kip applied load**

**Figure 6.9 Comparison of the maximum surface pressure
for unmodified pads and three types of pad modification, 40-kip applied load**

While running a series of tests, it was often observed that the actuator's loading plate would shift position relative to the block as a result of the flexibility of the frame. If the actuator-to-block interface was mismatched or if there was a nonzero contact angle it would have an effect on the pressure-versus-time curves and the maximum pressure. Data from four tests performed in sequence demonstrated this problem (Figure 6.10). The only difference between the four trials A through D was that the contact angle between the loading plate and the rail seat surface was adjusted. This had a major effect on the peak surface pressure in each cycle. It appears that some optimal contact angle (presumably zero, see Section 5.4.4) was found in trial C, since further adjustment reduced the peak pressures in trial D. However, there was no procedure to measure this contact angle or control it. Its impact was merely observed, and attempts were made to mitigate its effect on the results.
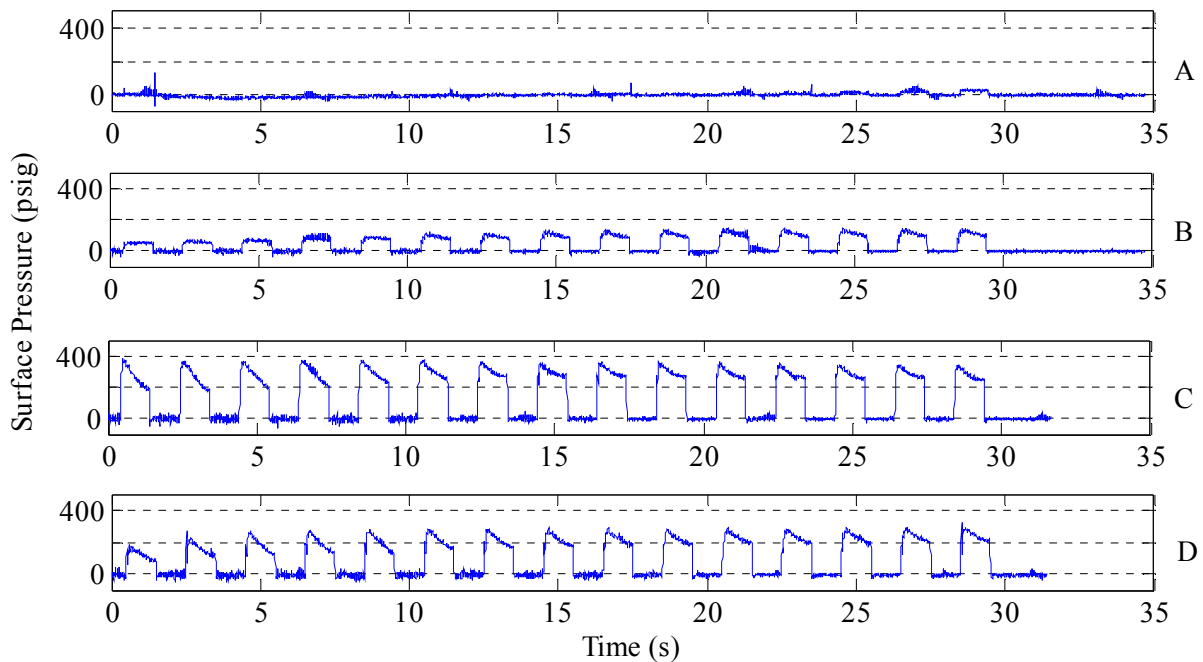
Figure 6.10 Demonstration of the influence of the contact angle on surface pressure; trials A, B, C, and D only differed by the contact angle in each

The maximum surface pressure p was plotted versus the applied load P to illustrate the correlation between load and surface pressure. By plotting these p-P graphs, it became apparent that the pads exhibited three distinct behaviors related to how much pressure they developed with the same

125

applied load. The first group was referred to as "flexible pads" (Figure 6.11) because these thermoplastic pads were relatively flexible when bent and twisted by hand, compared with the others. These pads produced pressure close to, though slightly below, the uniform rail seat load stress that Bakharev (1994) had assumed. The second group of "semi-rigid pads" produced trend lines significantly below, though parallel to, the ideal uniform rail seat stress (Figure 6.12). The third set of pads, the pad assemblies (each of which had a rigid layer of either metal or stiff plastic), generated little, if any, pressure relative to the other pads (Figure 6.13).
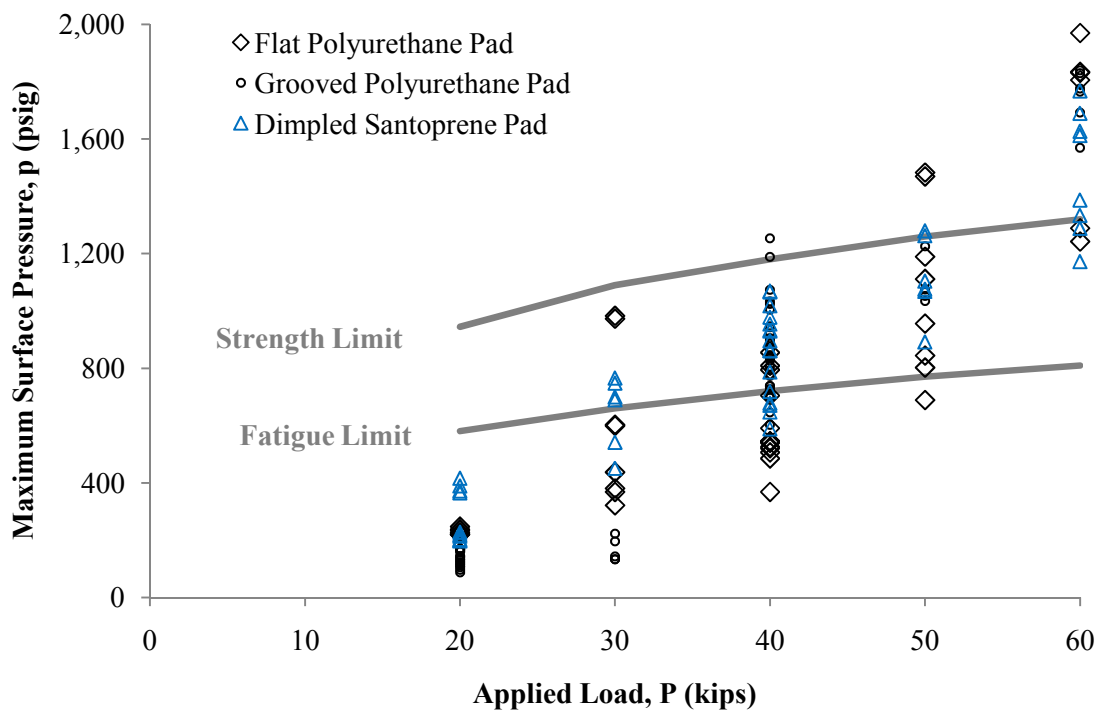
Figure 6.11 Comparing maximum surface pressure and damage limits, for flexible pads
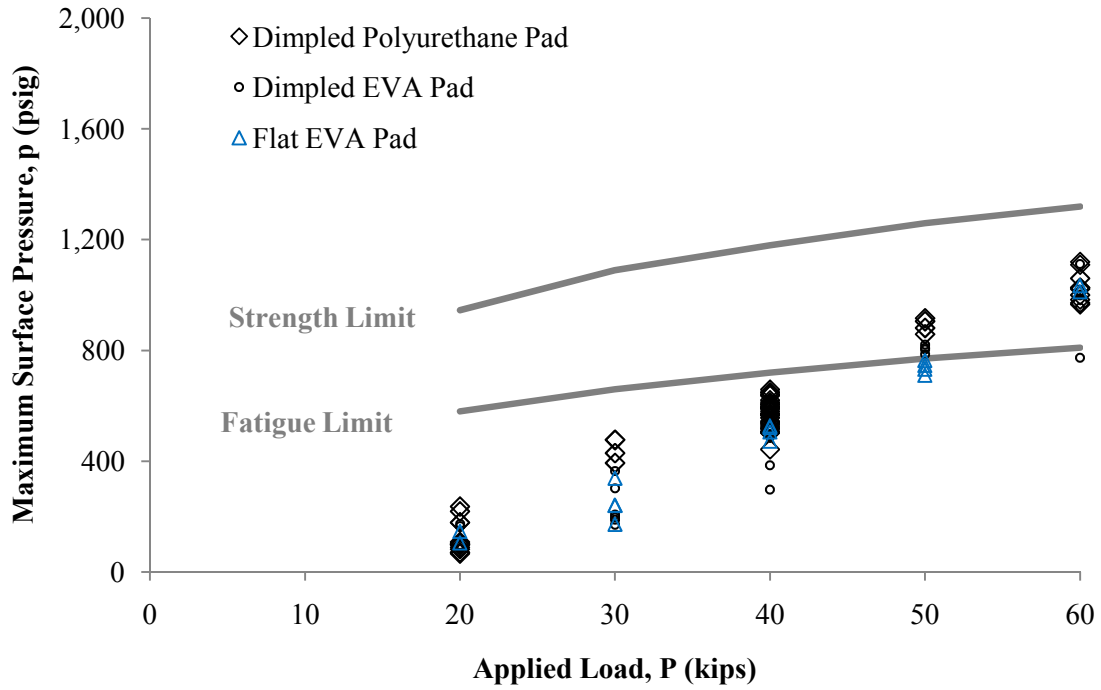
**Figure 6.12 Comparing maximum surface pressure and damage limits,
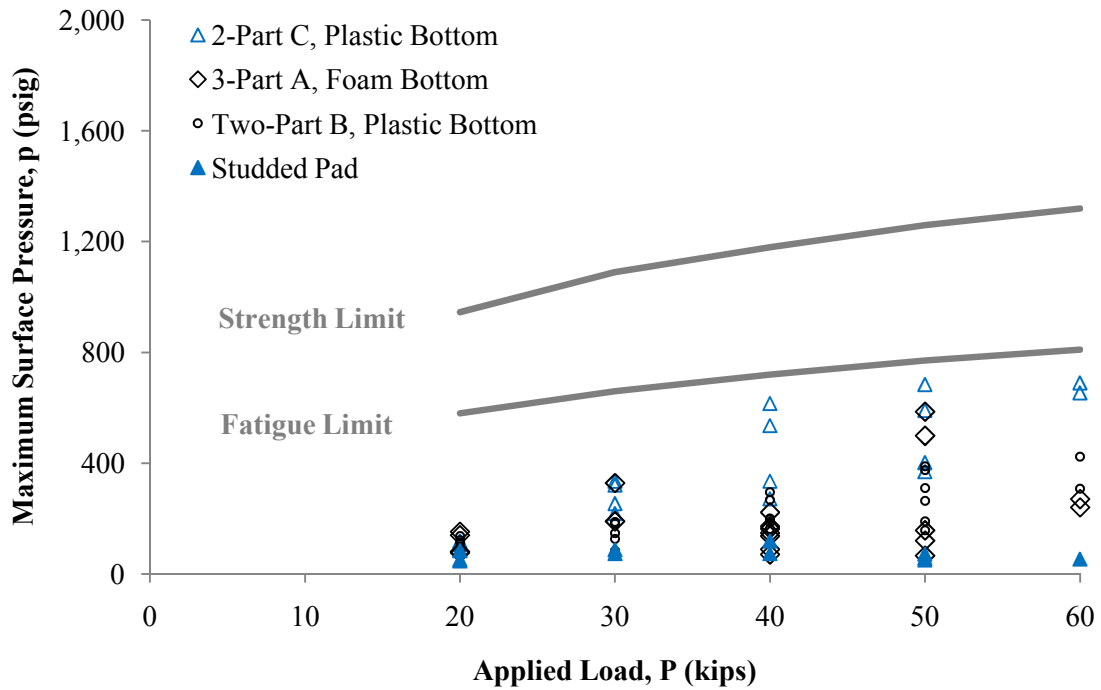for semi-rigid pads**

**Figure 6.13 Comparing maximum surface pressure and damage limits,
for pad assemblies with rigid layers**

The studded pad (the top layer of the 2-part C assembly), which was the only pad to have narrow channels running along its full length (providing openings at the pad boundaries), did not generate any significant pressure in any of its trials (Figure 6.13). The same results were observed when a dimpled pad and a grooved pad were modified to provide two-millimeter-wide channels from the indentation above the transducer to the pads' edges (Figure 6.9).

After plotting the maximum surface pressure for each pad and sorting the pads (Figures 6.11, 6.12, and 6.13), it was determined that all the tie pads could be grouped into one of three categories: flexible, semi-rigid, or assembly with a rigid layer. The pads were placed in these categories solely by their p-P behavior, and these names were assigned to the groups in an attempt to explain the differences between them. All of the data from Figures 6.11 through 6.13 were plotted on the same graph, sorted by these pad groups (Figure 6.14).
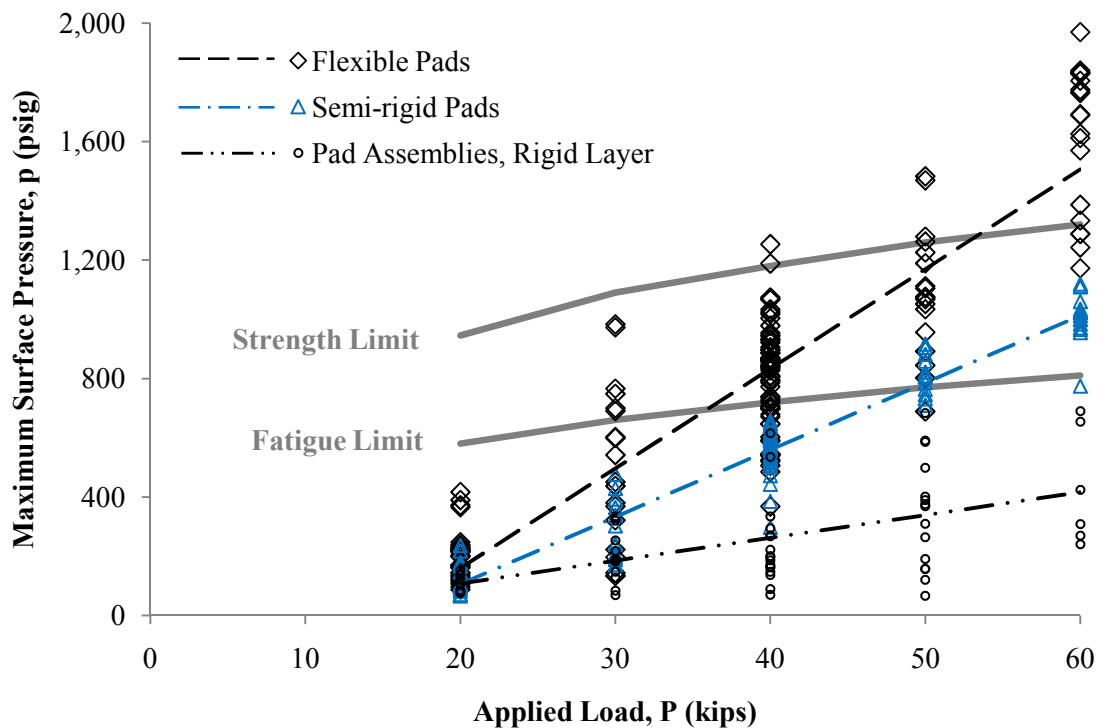

Figure 6.14 All maximum surface pressure measurements, sorted by pad group

The peak pressures p were plotted versus the load cycle count n to illustrate how the pressure varied over the course of a test. Some p-n data for a 40-kip applied load are presented here for the flexible pads (Figure 6.15) and for the semi-rigid pads (Figure 6.16). Typically, the maximum pressure occurred in the first few cycles of the trial. In some trials, the peak surface pressure was constant with continued load cycles. In other trials, the peak surface pressure dissipated from an initial maximum to either a steady state pressure that it sustained to the end of the trial, or a negligible value that was nominally zero pressure. The p-n data shown here for 40 kips are representative of the range of behavior that was observed for other magnitudes of applied load.
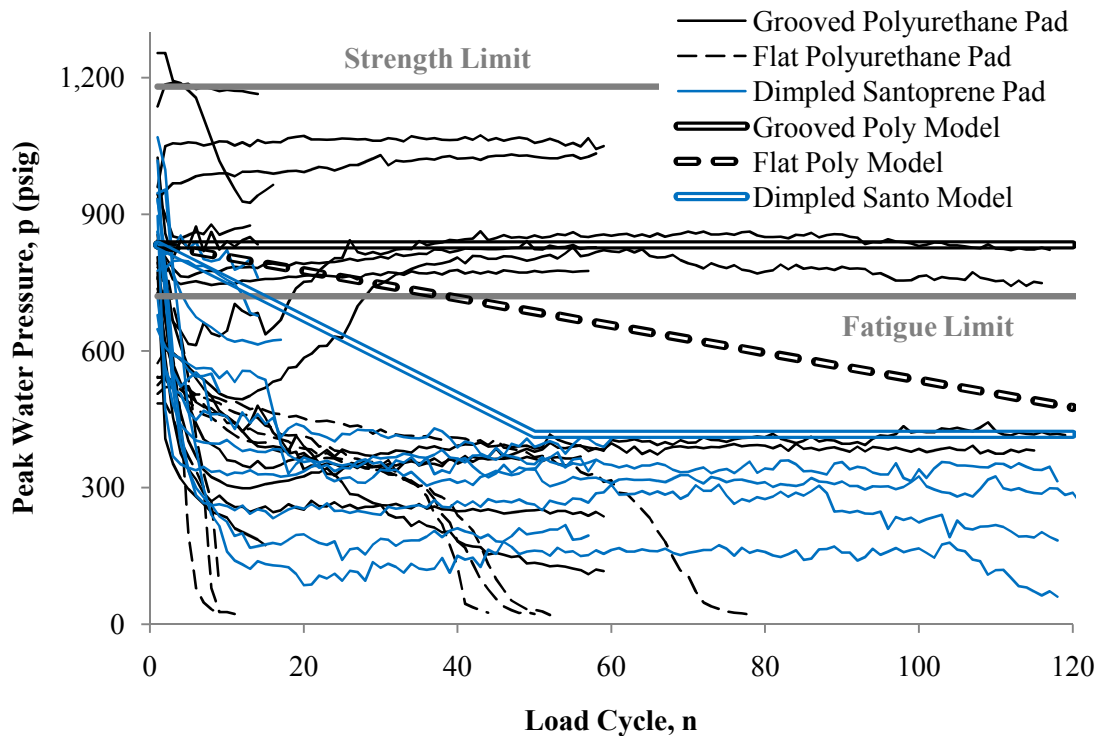

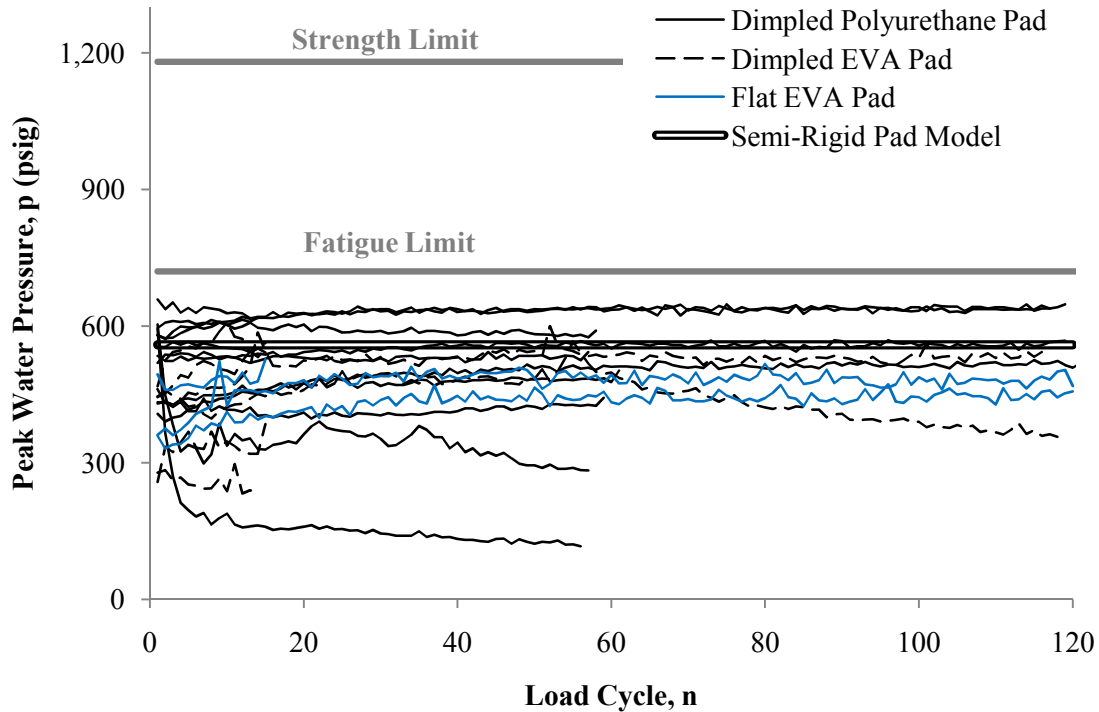**Figure 6.15 Recorded surface pressure peaks for flexible pads, 40-kip applied load**

Figure 6.16 Recorded surface pressure peaks for semi-rigid pads, 40-kip applied load

The curves for flat polyurethane in Figure 6.15 came from two different test days, with the curves dropping to zero within ten cycles occurring separately from the curves dropping to zero after 40 cycles. This difference may have been related to changes in the contact angle at the interface (Figure 6.10).

6.5 Discussion

6.5.1 Sources of Variability

Linear trend lines fit the *p-P* data well for the thermoplastic pads, with the worst R-squared value at 0.72 for the flat polyurethane pad. The rest of the pads with trend lines had R-squared values of at least 0.88. There was significant scatter in the pad assembly data, yielding low R-squared values; however, because the pad assemblies also generated pressures below the predicted damage limits, the variability in their results was not a cause for concern. The *p-P* points plotted in Figures 6.11 through 6.13 include data from tests with different water levels, waveforms, and indentation alignments, where applicable. The fact that the data still plot with a good linear fit suggests that parameters such as surrounding water head and

loading rate (train speed) do not have a strong influence on the surface pressure. Figures 6.6 through 6.8 further suggest that water level, waveform, and indentation alignment do not have a significant influence on the surface pressure developed, since there is no discernable trend in any of these plots. The resulting load-pressure models for the three tie pad groups, showing the R-squared values and number of trials in each sample, are summarized here (Table 6.4).

Table 6.4 Load-pressure models of the three tie-pad sets, including mean and upper-95% regression lines

Load-Pressure Set	Pads	Trend Line, p (psig) and P (k)	R^2	No. of Trials
Flexible Pads	Flat Poly, Grooved Poly, Dimpled Santo	$[p_{max}]_{mean} = 33.7P - 513.9$ $[p_{max}]_{95\%} = 36.1P - 415.2$	0.825	157
Semi-Rigid Pads	Dimpled Poly, Dimpled EVA, Flat EVA	$[p_{max}]_{mean} = 22.7P - 347.8$ $[p_{max}]_{95\%} = 23.8P - 300.0$	0.936	104
Pad Assemblies, Rigid Layer	2-Part B, 2-Part C, 3-Part A	$[p_{max}]_{mean} = 7.7P - 46.3$ $[p_{max}]_{95\%} = 10.5P + 66.6$	0.338	73

The most likely source of variation in the test results was the difficulty in controlling the contact angle between the loading plate and the rail seat block. Advancing the actuator with a nonzero contact angle between the loading plate and the block most likely provided the surface water a path for it to escape more easily. Without a contact angle, there would be a greater chance that a seal would develop between the pad and the concrete before the surface water could be expelled, as considered in Section 4.4.1. This may explain some of the scatter in the maximum pressure generated, as well as the variations in *p-n* behavior, particularly for the flat polyurethane's different pressure loss rates (Figure 6.15). The

potential implications in track are that rail roll or tilt could lead to similar nonzero contact angles between the rail base and the rail seat. If a nonzero contact angle occurs, it may reduce the rail seat surface pressure that is generated in track.

It was difficult to control the contact angle because the test frame was too flexible for this application and a small change in the angle at the actuator's restrained pin connection would result in a significant change in the position of the loading plate. In other words, the unbraced length of the actuator was too long, and the test procedure required dimensional tolerances at the mock rail seat that were difficult to maintain with this test apparatus. A future test apparatus of this type should have a more rigid test frame, as long as adjustment can be made for misaligned surfaces (with a ball-and-socket joint, for example).

As for the variable *p-n* behavior of the grooved polyurethane pad (Figure 6.15), it appears that the trials with the greatest sustained pressure mostly occurred when the groove indentation was directly above the transducer (aligned). The set of trials with the pressure just above the fatigue limit mostly occurred when the transducer was aligned between two indentations (misaligned), and the set of trials with the greatest pressure loss for the grooved polyurethane pad mostly occurred when the transducer was aligned with the long edge of an indentation (half-aligned). For the pads with indentations, some of the variability in *p-n* behavior may be explained by changes in indentation alignment.

6.5.2   *Surface Water Pressure and Velocity*

In Bakharev's model of hydraulic pressure, it was assumed that the surface pressure generated by a load P would be equal to P divided by the area of the rail seat, and this is referred to here as the uniform load stress (same as σ_V in Chapter 4). This assumes that the pad and the rail seat are separated by a film of water that transfers the load. For the surface water to ideally transfer load, a seal must be created between the tie pad and the concrete to prevent water from flowing rather than being pressurized. The *p-P* trend lines for the flexible pads are close to this ideal uniform load stress (Figure 6.17), suggesting that the flexible pads match Bakharev's assumption well.
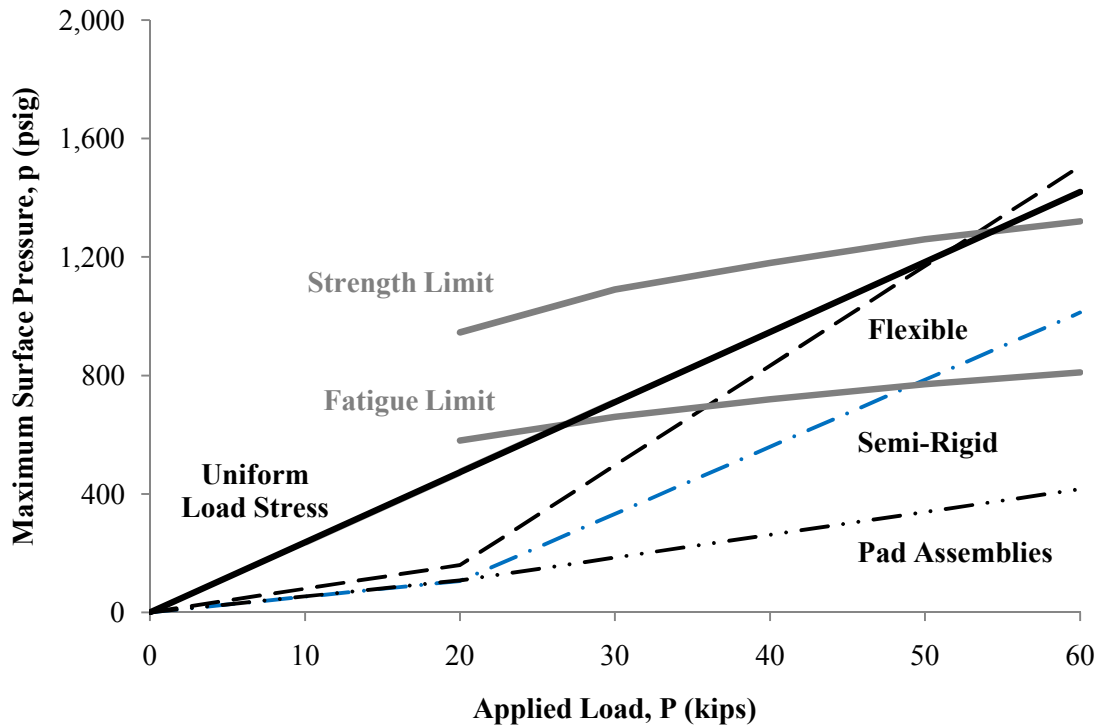
**Figure 6.17 Comparing the mean load-pressure models and
the uniform load stress on the rail seat**

The semi-rigid pads exhibited consistent p-P behavior that was parallel to but significantly below

the ideal uniform load stress assumption. One way to explain these results is to consider the transfer of

energy through the system. The applied load acts as an energy input that is transferred through the pad to

the rail seat block. If water is between the pad and the rail seat, then energy is also transferred to the

water. Borrowing from the Bernoulli equation for pipe flow, neglecting changes in elevation (Munson et

al. 2006), I considered the surface water's total energy as the sum of its pressure energy and velocity

energy. If a perfect seal is created, and there is no air in the transducer chamber, then the load energy

would be transferred as pressure energy in the water. Neglecting any dynamic effects and assuming

uniform load distribution, it can be assumed that the rail seat load stress is a maximum for the surface

pressure that can be generated under a given load – representing the case where the total energy is

pressure energy. If water is allowed to escape, fill air voids, or otherwise flow, then some of the energy

would be manifested as velocity, reducing the pressure that can be generated. Allowing some of the

water to escape or flow rather than become pressurized may explain the difference between the flexible and semi-rigid pads.

Applying the Bernoulli estimate for maximum surface water velocity as a function of applied load and surface water pressure (see Section 4.4.1) to the mean load-pressure models yielded the curves shown here (Figure 6.18). The critical flow velocity for perpendicular flow found in the literature (approximately 400 ft/s) was included for reference (Section 3.4.5). Considering that the critical flow velocity for parallel flow should be considerably higher than the given limit, it seems unlikely that water flow alone would be sufficient to erode the rail seat.
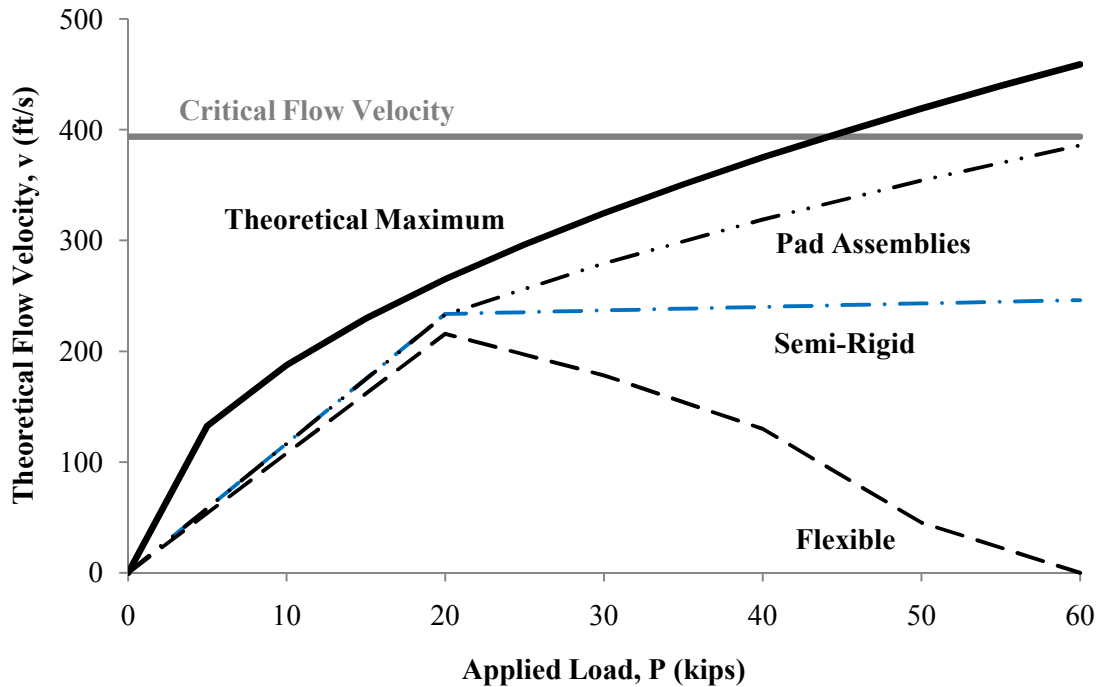

**Figure 6.18 Theoretical flow velocity based on
Bernoulli's equation and the mean load-pressure models**

Considering the observation in the literature that the suspended-particle velocity is up to 72% of the flow velocity, the flow velocity estimates (Figure 6.18) were scaled to estimate the particle velocity for the different tie pad groups (Figure 6.19). The smallest value of particle velocity in the literature that was associated with concrete erosion was approximately 165 ft/s, and this was for flow parallel to the

surface, similar to the case I am considering. Considering these estimates, it appears that hydro-abrasive erosion is feasible in a concrete-tie rail seat. The potential for wear due to this mechanism would need to be evaluated with a different test apparatus than the one used in this study.
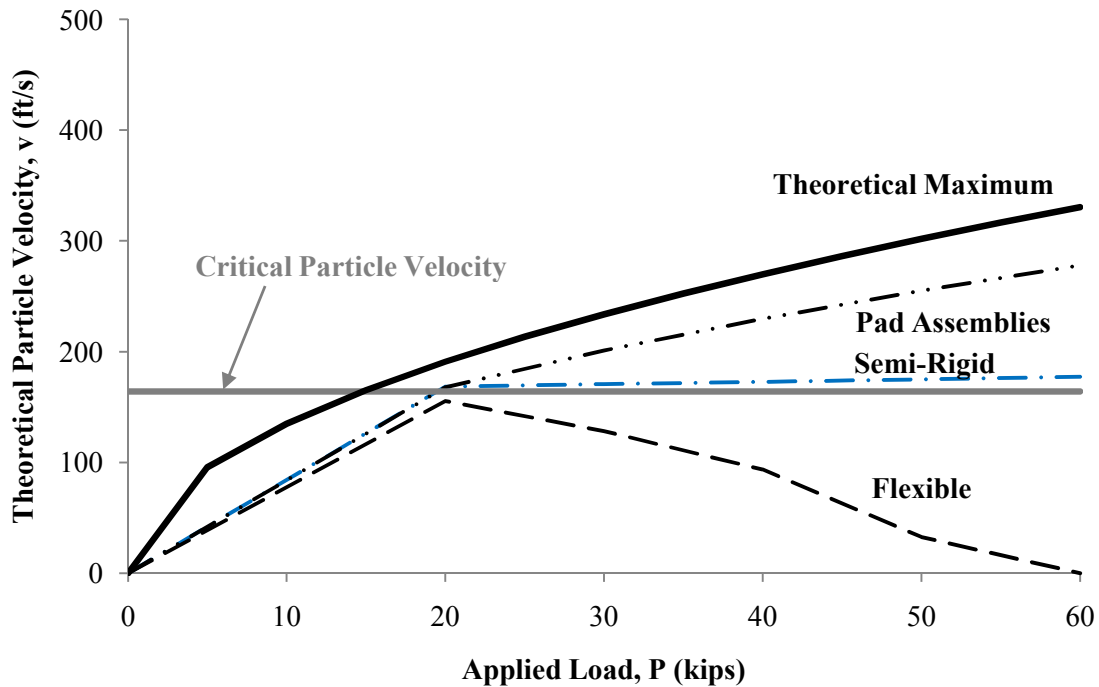

Figure 6.19 Theoretical particle velocity scaled as 72% of the flow velocity

The concept of energy transfer through the water can be applied to offer an explanation for the varied *p-n* results (Figures 6.15 and 6.16). There were three general types of *p-n* behavior observed: constant pressure with continued cycles, pressure loss from a maximum to a steady state value, and pressure loss from a maximum to zero. What may be causing pressure loss with load cycles is that some volume of water is forced out either from the transducer chamber or from the indentations of the pad. As a pad relaxed between cycles, there was still at least five kips of load applied to the pad, so there may have been enough of a seal that water did not return between cycles. Rather, there might have been a reduced volume of water in the chamber or indentations, requiring the pad to locally flex more into the chamber to pressurize the water. As a result of this loss of contact with the water, the stress distribution over the pad may have changed such that most of the stress was transferred away from the transducer's

orifice. If the volume of water in the transducer chamber became low enough, the pad may have been unable to contact the water and pressurize it, resulting in a reading of zero. Though this explanation of pressurization versus ejection was not specifically tested, it was found that the relative ranking of flexural stiffness of each pad aligned with the load-pressure groups (Table 6.4), suggesting that flexural stiffness is a characteristic that relates to surface water pressurization (see Appendix D for more information).

6.5.3   Comparison of Tie Pads

The grooved and flat polyurethane pad surfaces were two sides of the same tie pad. These surfaces generated very similar *p-P* curves but consistently different *p-n* behavior, providing strong evidence that indentations can lead to more sustained pressures with load cycles – the indentations may act as storage compartments for the surface water or they may introduce more tortuous escape paths than a flat surface would. However, the dimpled and flat ethyl-vinyl acetate (EVA) pads generated similar *p-P* and *p-n* graphs, despite the difference in surface geometry. It is important to note that the dimpled EVA and flat EVA are different pads with different thicknesses, so it is not quite the same comparison as with the grooved and flat polyurethane. Generally EVA is a stiffer material than polyurethane. This introduces another complication when comparing these tie pads: though the two EVA pads are nominally the same material, there is room for variation of material properties to fit a specific product, similar to how a concrete mix is adjusted to produce different strengths. The same can be said about the dimpled and the flat polyurethane pads – they appear to have slightly different stiffness and hardness properties. By using some simple tests, it was shown that the grooved polyurethane pad has a relatively higher compressive stiffness and a lower flexural rigidity than the dimpled polyurethane pad (see Appendix D). The major difference between the dimpled santoprene and the dimpled polyurethane pads is that the santoprene rubber was relatively flexible and compressible and underwent permanent deformation after a few trials. The santoprene pad may have deformed enough that the dimples were flattened during the trials, causing it to act more like the flat polyurethane pad, in terms of surface pressure, than the dimpled polyurethane pad. It appears that both the surface geometry and the material properties of the pad determined what surface pressures were generated.

The studded pad, as well as the dimpled and grooved pads which were modified with channels, generated zero pressure for all tests, and this may have been because the surface water had at least one direct path to escape under applied load rather than being pressurized. As long as the escape velocity is less damaging than the pressure that would otherwise be generated, then providing escape channels in a thermoplastic material appears to be an effective way to prevent hydraulic pressure cracking in the rail seat.

Both the hardest material – the plastic bottom of the two-part assemblies – and the softest material – the foam bottom of the three-part assembly – generated pressures lower than the semi-rigid pads. These pad assemblies developed pressures that would require very high rail seat loads – probably 80 to 90 kips or higher – to exceed the fatigue limit (Figure 6.13), assuming that the present data can be extrapolated. For the plastic bottoms, it is possible that it was difficult to create a seal with such a hard, stiff material, allowing water to flow rather than being pressurized. After one trial, the soft foam bottom would become permanently deformed. During the first trial, the foam apparently created an adequate seal and developed pressure not too far below the semi-rigid pads, exhibiting some pressure loss with load cycles. When a subsequent trial was run with the same pad, a lower pressure was obtained, and even lower pressures were generated with subsequently higher loads. This was observed when going from 50 kips to 60 kips (from 30 kips to 40 kips as well) (Figure 6.13). It may be that the deformation of the foam prevented the formation of a seal and allowed the water to escape. Another possible explanation is that the pressure behavior of the three-part assembly was dominated by the stiff metal layer in the middle, which would not readily form a seal. It may be some combination of the deformation of the foam surface and the rigidity of the metal layer.

6.5.4   Potential for Concrete Damage

The strength and fatigue limits from the effective stress model were superimposed on the *p-P* curves (Figures 6.11 through 6.14) for comparison. The flexible pads, on average, exceeded the fatigue limit between 30 and 40 kips applied load and exceeded the strength limit between 50 and 60 kips applied load. On the other hand, the semi-rigid pads exceeded the fatigue limit with 50 kips applied load but did

not exceed the strength limit within 60 kips. So for rail seat loads above 50 kips there is the potential that

a flexible pad could initiate microcracking in the concrete. It is also possible that fatigue damage could

result for either flexible or semi-rigid pads if the proper conditions are met.

Fatigue damage would require millions of cycles of surface pressure exceeding the fatigue limits

and this would require each cycle to have the correct combination of high rail seat loads and moisture in

the concrete and on the rail seat. Considering a 286,000-lb rail car with four axles, approximately 36

million gross tons (MGT) would be required for one million load cycles. To estimate the number of

fatigue cycles per train, under the correct moisture conditions, a set of cycled-pressure models were

selected to envelope the *p-n* behavior of the pad(s) for all loading cases (Table 6.5). The cycled-pressure

models for a 40-kip applied load are illustrated as an example (Figure 6.20). These models were

compared with the fatigue limits for the five loading cases to conservatively estimate the number of

fatigue cycles per train (Table 6.6). One freight train in North America could apply over 400 load cycles

to a rail seat, but it could be less than this, depending on the track modulus (see Section 4.3).

Table 6.5 Cycled-pressure models of the three pad sets

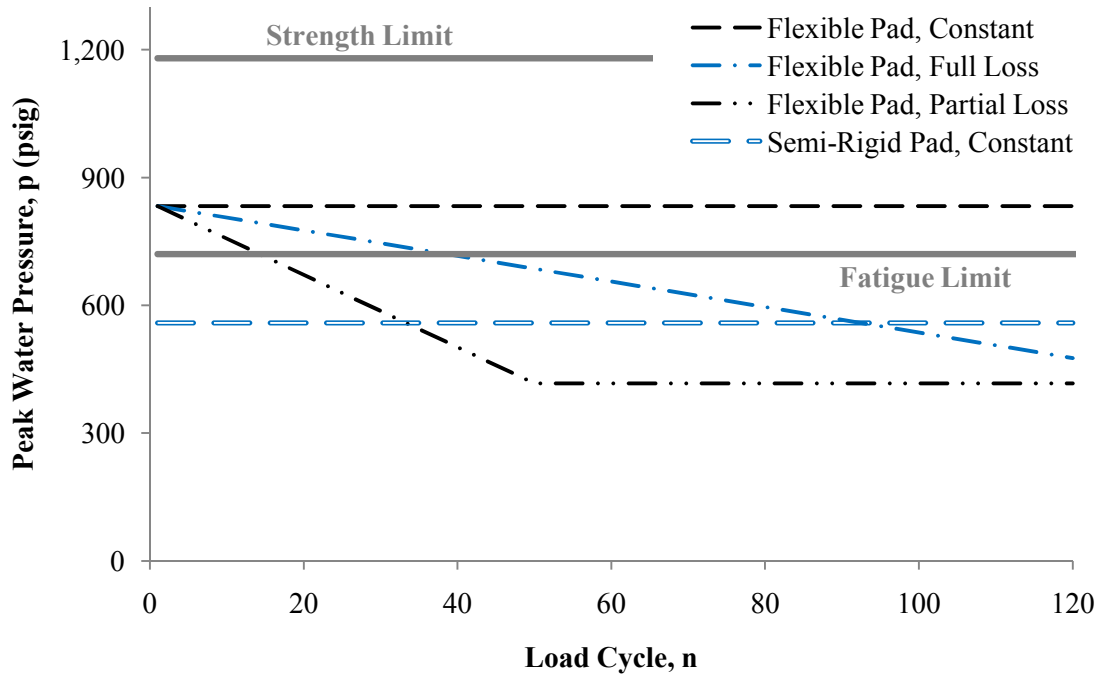| Cycled-Pressure Set	Tie Pads	Envelope Models, p (psig) and P (k)
Constant	Grooved Poly., Semi-Rigid Pads	$p(n) = [p_{max}]_{mean}$
Full Loss	Flat Poly.	$p(n) = [p_{max}]_{mean} - (P - 20)(0.15n)$
Partial Loss	Dimpled Santo.	$p(n) = \begin{cases} [p_{max}]_{mean}(1 - 0.01n) & \text{for } n \leq 50 \\ \frac{1}{2}[p_{max}]_{mean} & \text{for } n > 50 \end{cases}$

**Figure 6.20 Comparing the cycled-pressure models and damage limits,
for 40-kip applied load, assuming saturated concrete**

**Table 6.6 Number of fatigue cycles per train, derived using
the cycled-pressure models, assuming saturated concrete**

Tie Pads	Applied Load, P (kips)				
	20	**30**	**40**	**50**	**60**
Flat EVA	0	0	0	all	all
Dimp. EVA	0	0	0	all	all
Dimp. Poly.	0	0	0	all	all
Dimp. Santo.	0	0	15	35	46*
Flat Poly.	0	0	38	90	116*
Grooved Poly.	0	0	all	all	all*

*For these cases, the initial surface pressure exceeds the strength limit

High rail seat loads could result from high dynamic wheel loads – caused by wheel or rail imperfections or support transitions, such as those found adjacent to bridges and grade crossings – or by poor load distribution among adjacent ties. When 20 kips was taken as the static rail seat load, this

139

assumed that one rail seat supports at most half of a wheel load, with the other half of the load distributed

to adjacent ties (AREMA 2009). If adjacent ties are broken, missing, spaced too far apart, or not

providing good bearing for the rail, a rail seat could take up to 100% of the wheel load. Based on data

from wheel impact load detectors (WILD), the rail seat load could be as high as 90 kips or greater if one

rail seat has to take most of the wheel load (Gemeiner and Mattson 2005, AAR 2010). Table 4.2 shows

example distributions of wheel loads from WILD data.

A short-coming of the load tests was that the loading pattern was more uniform than what a rail

seat would experience in track. Although tests did show that the waveform, or loading rate, did not affect

the surface pressure, cases with a return load, or minimum load, higher than five kips were not tested. As

discussed in Section 4.3, the effective return load between adjacent rail car axles would be, at a minimum,

72% of the full load. However, if this aspect influenced anything, it would probably be the p-n behavior,

not the p-P behavior, since the maximum load would remain the same.

The effective stress model assumed a saturated concrete in order to model the distribution of pore

water pressure from an initial surface water pressure. If the concrete is fully saturated, then all of its

pores are filled with water. In an unsaturated concrete, the pore volume not taken up by water is filled

with air. Considering pressure distribution, a fully saturated concrete is assumed to transfer pressure

immediately, just as water contained in a pressure vessel would. However, if the concrete is not fully

saturated, water pressure will be relieved by flowing through the pores to fill the air voids. In an

unsaturated case, the pressure at some depth beneath the rail seat would be lower than what the model

predicts. In other words, the same surface pressure will potentially do more damage to a saturated

concrete than an unsaturated concrete. An important question is whether concrete ties in track can be

fully saturated, even just locally at the rail seat. If not, then the effective stress model presented here

would represent a conservative but potentially invalid prediction for concrete damage limits. One way

that the unsaturated case could be considered is to redefine the surface pressure damage limit as being

equal to the pore pressure damage limit at the rail seat surface, rather than considering it at some depth as

was done for the saturated case (Figure 4.11).

A significant assumption of the current model is that the concrete damage limits are based on 7,000-psi 28-day strength. This is the minimum strength the American Railway Engineering and Maintenance-of-Way Association (AREMA) Manual for Railway Engineering (2009) recommends for concrete ties. In reality US concrete-tie manufacturers commonly use mixes that produce 28-day strengths well above 7,000 psi, reaching up to 11,000 psi. If the model were modified to incorporate higher concrete strengths, the damage limits would increase. This increase was estimated using the equation in Section 4.5.5 for the pore pressure damage limits and changing the concrete tensile strength.

Also, as mentioned in Section 4.5.2, the effective stress model assumed elastic stress distributions and a Poisson's ratio of 0.5. The effects of each assumption would be to predict higher confining stresses than would be encountered in real concrete ties. The error in these assumptions could be as high as 20%, considering other elastic stress distribution models (Poulos and Davis 1974).

The sensitivity of the damage limits to the above considerations were evaluated and plotted, along with the load-pressure models (Figures 6.21 and 6.22). The fatigue limit was compared with the mean load-pressure model, while the strength limit was compared with the upper-95% load-pressure model. The change in the limits between the base case of saturated, 7,000-psi concrete to unsaturated, 7,000-psi concrete becomes more significant at higher loads, and this is due to the curvature in the pore pressure limits near the rail seat surface (see Section 4.5.5). Considering unsaturated concrete in this manner pushes the strength limit higher than all of the recorded flexible pad pressures except those at the highest rail seat loads and the fatigue limit higher than any of the mean semi-rigid pad pressures. Increasing the concrete strength of the unsaturated case to 10,000 psi shifts the fatigue limit up to the base case's strength limit, making fatigue damage seem very unlikely, even for the flexible pads. In an attempt to consider the overestimate of confinement stresses, the minor principal stress term in the pore pressure limit was reduced by 20%. This consideration did not affect the surface pressure limits significantly.
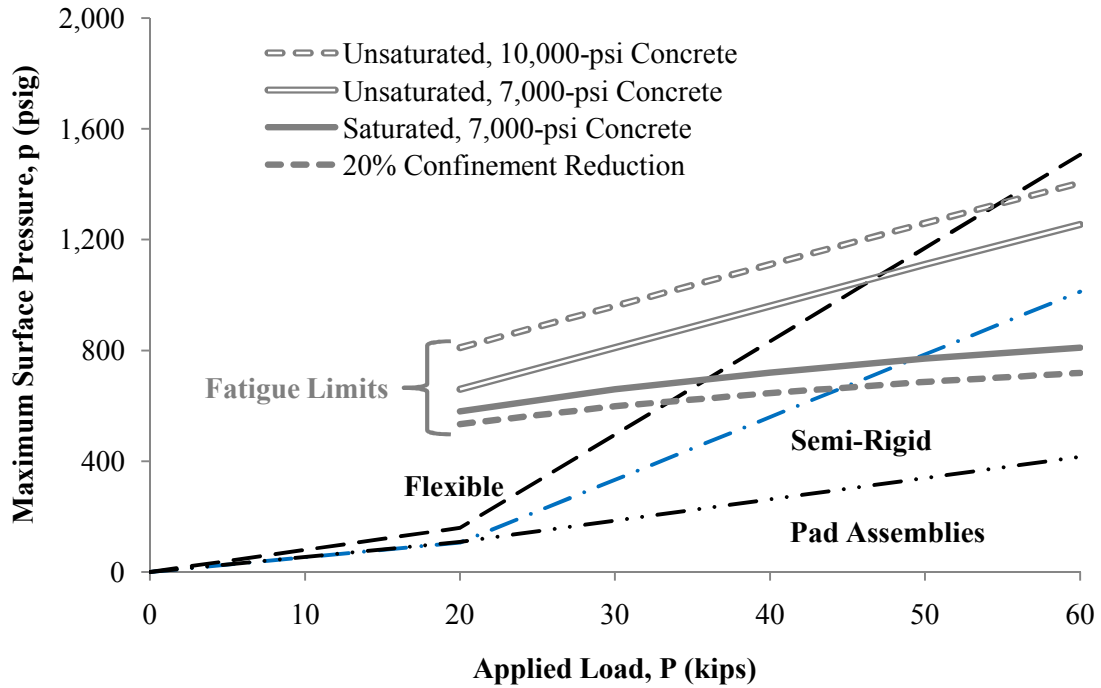
Figure 6.21 Sensitivity of the fatigue limit to changes in concrete strength, confinement, and moisture content, compared with mean load-pressure models
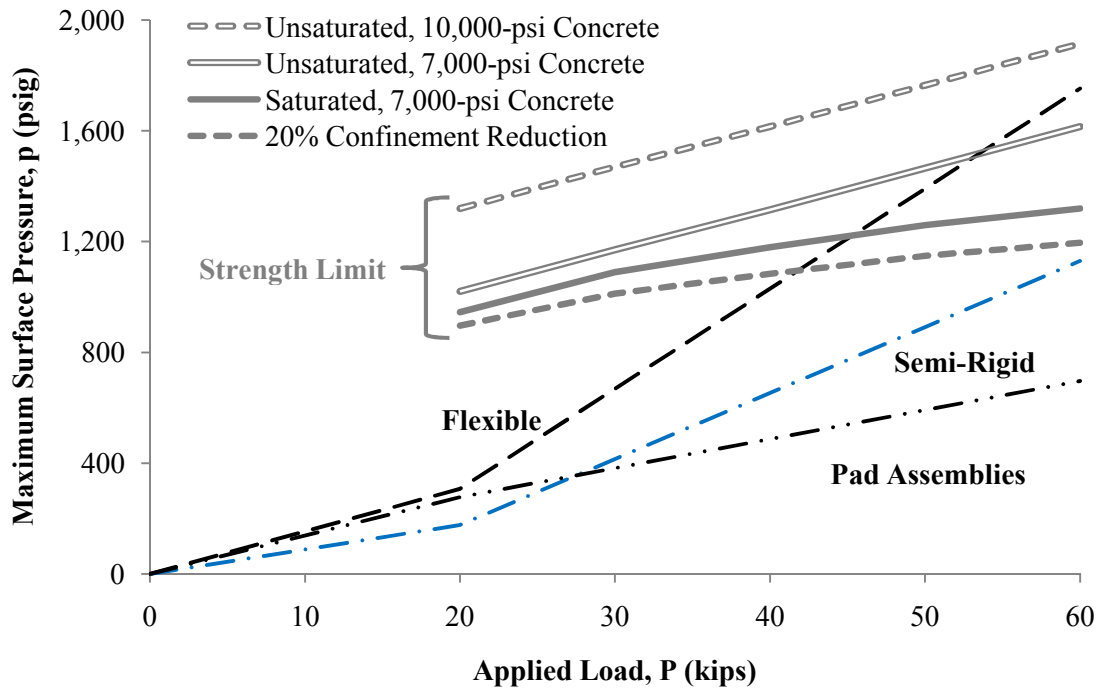

Figure 6.22 Sensitivity of the strength limit to changes in concrete strength, confinement, and moisture content, compared with upper-95% load-pressure models

A hypothetical design scenario was considered to demonstrate how the empirical surface pressure models could be used to consider different tie pad designs for different scenarios. A simple approach to evaluate the potential for fatigue damage is to consider how long it would take to accumulate one million fatigue cycles under different conditions. Fatigue damage typically requires on the order of a million cycles or more of stresses that exceed a fatigue limit, but the actual number of cycles to failure is complex so it is not determined here (Mindess et al. 2003). This example is for a 100-million-gross-ton (MGT) rail line with 120-car coal trains, consisting of 286,000-lb gross-weight cars. The concrete was assumed to have a 28-day compressive strength of 7,000 psi. The moisture content of the concrete should be correlated with the annual number of days with precipitation. The climate of this hypothetical site was assumed to be such that the concrete is saturated 50 days out of the year and is wet but unsaturated 100 days out of the year. The 2003 WILD distribution in Table 4.2 was used in this example. For the given train traffic, and assuming that each of the axles produces an individual load on the tie, the number of load cycles per year is:

$$\text{Daily Traffic} = \frac{(100 \times 10^6 \text{ tons/year})(2 \text{ kips/ton})}{(120 \text{ cars/train})(286 \text{ kips/car})(365 \text{ days/year})} = 16 \text{ trains/day}$$

Annual Load Cycles = (120 cars/train)(4 axles/car)(1 cycle/axle)(16 trains/day)(365 days/year)

Annual Load Cycles = 2.8×10^6 cycles/year

With the assumed climate, the concrete would be saturated 14% of the time (50/365) and wet but unsaturated 27% of the time (100/365). Using the WILD distribution from 2003 in Table 4.2, 40-, 50-, and 60-kip rail seat loads (using the AREMA assumption of half the wheel load) occur 6%, 3%, and 1% of the time, respectively – rail seat loads lower than 40 kips will not incur fatigue cycles. This simple procedure assumes that the different factors are independent, random events so that their probabilities can be multiplied together. Using Table 6.6 to get the number of fatigue cycles per train for the saturated case and modifying these numbers for the unsaturated case using the predictions in Figure 6.21, the number of annual fatigue cycles was calculated to be

$$\frac{\text{fatigue cycles}}{\text{year}} = \frac{\text{load cycles}}{\text{year}}\left[\sum_{i=1}^{2} P(\text{moisture}_i)\sum_{j=1}^{5} P(\text{load}_j)\left(\frac{\text{fatigue cycles}}{\text{load cycle}}\right)_{ij}\right]$$

Semi-Rigid Pads:

$$2.8\times10^6[0.14(0.03+0.01)+0.27(0)] = 15{,}700 \text{ fatigue cycles/year}$$

$$\text{Time to 1 million fatigue cycles} = \frac{1\times10^6}{15{,}700 \text{ fatigue cycles/year}} = 64 \text{ years}$$

Grooved Polyurethane Pad:

$$2.8\times10^6[0.14(0.06+0.03+0.01)+0.27(0.03+0.01)] = 69{,}400 \text{ fatigue cycles/year}$$

$$\text{Time to 1 million fatigue cycles} = \frac{1\times10^6}{69{,}400 \text{ fatigue cycles/year}} = 14 \text{ years}$$

Flat Polyurethane Pad:

$$2.8\times10^6[0.14(0.08\times0.06+0.19\times0.03+0.24\times0.01)+0.27(0.05\times0.03+0.10\times0.01)]$$

$$= 7{,}000 \text{ fatigue cycles/year}$$

$$\text{Time to 1 million fatigue cycles} = \frac{1\times10^6}{7{,}000 \text{ fatigue cycles/year}} = 144 \text{ years}$$

Dimpled Santoprene Pad:

$$2.8\times10^6[0.14(0.03\times0.06+0.07\times0.03+0.10\times0.01)+0.27(0.05\times0.03+0.10\times0.01)]$$

$$= 3{,}800 \text{ fatigue cycles/year}$$

$$\text{Time to 1 million fatigue cycles} = \frac{1\times10^6}{3{,}800 \text{ fatigue cycles/year}} = 262 \text{ years}$$

The semi-rigid, flat polyurethane, and dimpled santoprene pads are not in danger of causing fatigue damage with hydraulic pressure under the assumed conditions. The grooved polyurethane pad would be expected to cause some fatigue damage within 15-45 years, which would be considered within the life cycle of the tie. However, this calculation is very sensitive to the occurrence of high wheel loads – the "tail" of the WILD distribution. This is important because in recent years there has been a decline in high impact wheel loads on major North American freight railroads (Kalay 2010). For example, Kalay

(2010) reported that the number of high wheel loads (greater than 140 kips) have fallen by 75% since October 2004. This trend is apparently confirmed by the two sets of data presented in Table 4.2. If the grooved polyurethane pad is considered again for the same conditions but using a 2008 WILD distribution from a US Class I railroad (Table 4.2), with 0.94% 40-kip, 0.14% 50-kip, and 0.02% 60-kip rail seat loads, the result is:

Grooved Polyurethane Pad:

$$2.8 \times 10^6 [0.14(0.0094+0.0014+0.0002)+0.27(0.0014+0.0002)] = 5,500 \text{ fatigue cycles/year}$$

$$\text{Time to 1 million fatigue cycles} = \frac{1 \times 10^6}{5,500 \text{ fatigue cycles/year}} = 182 \text{ years}$$

This significant change in the fatigue potential demonstrates the major impact that high wheel loads have on hydraulic pressure cracking. In such a design scenario, the engineer would only be able to adjust the concrete strength (increasing the fatigue limit) or select which pad to use. However, the railroad as a whole, by improving the detection and removal of high impact wheels, can substantially reduce the likelihood of fatigue damage due to hydraulic pressure cracking.

6.6   Conclusions

Based on the results of the laboratory experiments and the damage limits defined by the effective stress model, hydraulic pressure cracking appears to have the potential to initiate or contribute to RSD as a concrete deterioration mechanism. It appears that the most effective way to prevent hydraulic pressure is to use pads or pad assembly bottoms that do not seal water. The soft foam with a rigid metal layer and the hard plastic bottoms developed little surface pressure at the rail seat, with the hard plastic being slightly more effective. When thermoplastic pads are in contact with the concrete rail seat, it appears that designing the pad with direct escape channels for the water effectively ejects the surface water upon load application rather than pressurizing it. Thermoplastic pads without escape channels created the highest surface pressures, apparently sealing the water during load application. It seems advisable and relatively simple to incorporate these considerations into future pad and pad assembly designs; however, these design considerations for hydraulic pressure must be balanced with the possibility that allowing water and

145

fines to flow in and out might increase wear due to hydro-abrasive erosion and abrasion. The potential

for hydro-abrasive erosion to damage concrete seems feasible, but more research is needed to understand

how important this mechanism is before design recommendations can be made.

Low rail seat loads, resulting from near-static wheel loads and good load distribution among

adjacent ties, will not generate damaging hydraulic pressure at the rail seat, according to the effective

stress model. In some cases, sufficient moisture for critical saturation is required for hydraulic pressure to

damage the concrete. Furthermore, the concrete strength should play a major role in determining whether

the hydraulic pressures are damaging. Considering this variability in a hypothetical design scenario, it

was demonstrated that by reducing the occurrence of high impact wheels, selecting a proper tie pad, or

increasing the concrete's strength, the likelihood of fatigue damage due to hydraulic pressure could be

reduced to an insignificant level. What remains is the possibility that hydraulic pressure could initiate

microcracking by exceeding the concrete strength. However, according to the results of this

investigation, the same preventive measures listed above could cause the likelihood of this scenario to be

insignificant as well.

CHAPTER 7: UPLIFT TESTS

7.1   Motivation

As discussed in Chapter 3, cavitation erosion is one of the proposed RSD mechanisms, though

there has been little empirical evidence to support this theory. The same laboratory test apparatus used

for the load tests (Chapter 6) was used to measure the suction created by uplift motions, intended to

simulate the motion of the rail. It was hypothesized that the suction (a) would increase with increased

vertical acceleration, (b) would be greatest when the pad adheres to the base-of-rail, (c) would be

independent of the surrounding water level, (d) would be independent of the uplift height, and (e) would

be dependent on the tie pad, similar to what was found with the load tests. Hypotheses (c) and (d)

resulted from observations from the manual tests (Chapter 5). Aside from learning about the factors that

affect the suction under a tie pad, the suction would also be compared with the vapor pressure of water to

evaluate the potential for cavitation in the rail seat.

7.2   Procedure

The same concrete blocks, test frame, water tank, and actuator described in Section 6.2 were used

to conduct the uplift tests described here. The primary distinctions for the uplift tests were that the

actuator was run on position control, the submersible, 135-pounds-per-square-inch-absolute (psia)

pressure transducer (a TDG 03/04 unit from Transducers Direct, see Section 5.2.2) was used to ensure

sufficient resolution to measure suction, and an accelerometer was attached to the top of the loading arm

to measure the vertical acceleration during tests.

The control conditions for the test were six-inch water level, square wave motion at one half

Hertz (Hz), 0.06-inch uplift amplitude, and 0.03-inch compression amplitude. The compression and uplift

motions were programmed relative to the contact position, which was arbitrarily defined as 200-pounds

(lb) of contact force. The compression amplitude could not be varied because further compression would

have generated positive water pressure greater than 120 psi gauge (psig), damaging the transducer, and

the resolution of the actuator's displacement transducer was limited to around 0.03 inches. Initially, the

thermoplastic pads were glued to the loading plate with a two-part epoxy because it was suspected that it

would be difficult to produce significant suction without adhesion between the pad and rail base. However, for comparison similar trials were also conducted without gluing the pads, and this case was referred to as "free contact."

7.3   Results

One trial was operated with manual control to observe the effects of the actuator's rate of motion on the resulting pressure (Figure 7.1). The vertical displacement of the actuator in the upper half of Figure 7.1 was measured relative to an estimated contact elevation, here based on the initiation of positive pressure at approximately 9.5 seconds. The vertical, dotted, gray lines reference points of distinct pressure change. The loading plate began in contact with the rail seat. Between 0.8 and 6.4 seconds it was raised slowly enough that no acceleration was measured. This resulted in a small amount of suction that dissipated around the same time that the loading plate lifted off the rail seat. Beginning at 6.4 seconds, the loading plate was lowered at about the same rate, past the point of contact at 9.5 seconds. Once the loading plate reestablished contact with the rail seat it produced positive pressure approximately proportional to the compressive displacement. Just before 11 seconds, the loading plate was rapidly raised, generating an acceleration of 0.06 g (g = 9.81 m/s^2 = 32.2 ft/s^2) and causing the plate to lose contact with the rail seat. The result was an immediate suction spike that peaked at approximately -16 psig, very close to the time when the loading plate likely lost contact with the rail seat.
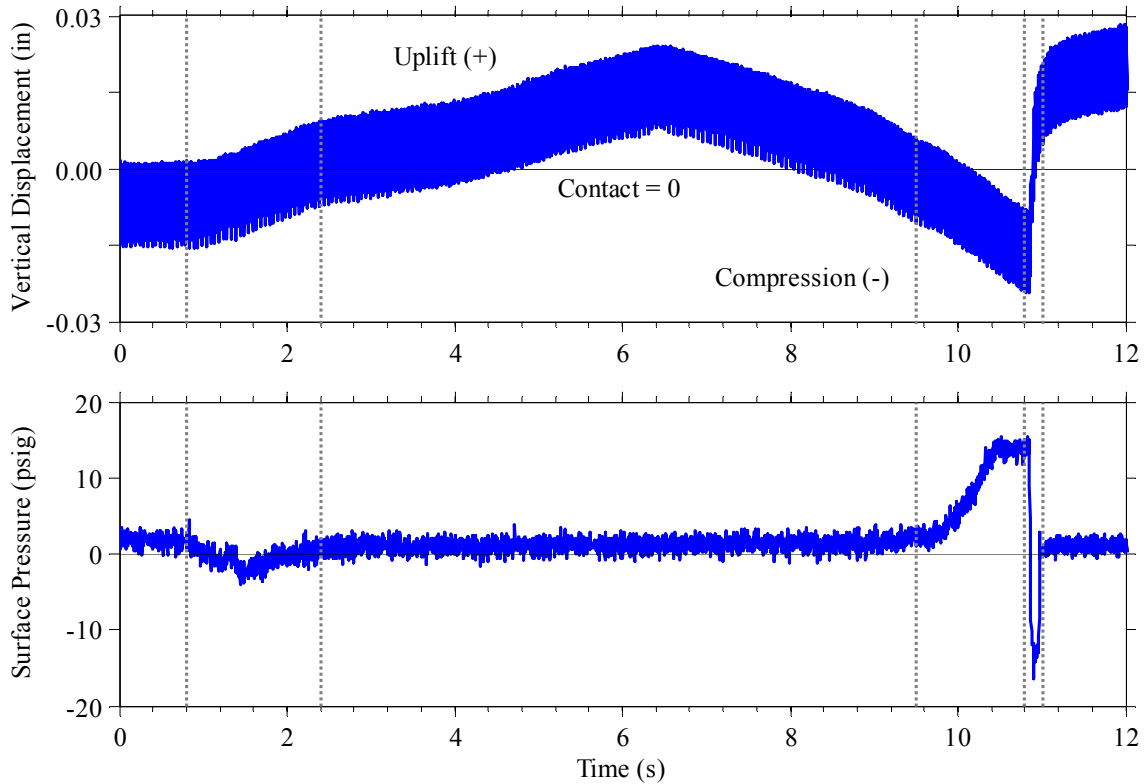
**Figure 7.1 Comparison of loading plate displacement
and surface water pressure; flat polyurethane pad, glued**

For the following figures, the control conditions listed in the procedure were maintained unless otherwise noted (Figures 7.2 through 7.11). In most of the trials, the pressure values provided by the transducer were physically unreasonable. Absolute vacuum is approximately -14.70 psig. It is physically impossible to generate pressures lower than this, yet such levels were frequently recorded in these tests and were due to error in the transducer. This is reflected in the blue lines labeled "error range" in the following figures, showing the absolute vacuum plus/minus approximately 3 psi. The error range was defined by the largest measurement below absolute vacuum, which was approximately -18 psig. The transducer's calibration was checked with a hydraulic hand pump and dial gauge, and it was found that the manufacturer's calibration equation differed substantially from the transducer's actual readings. The calibration curve is given in Appendix D (Figure D.2). It is important to note that this calibration was performed after all of the trials were performed because the transducer's reading of atmospheric pressure

149

fluctuated during the uplift test from 1.33 Volts (V) to 1.40 V, and then returned to 1.34 V. Judging from previous experience of over-pressuring transducers, this transducer may have been exposed to some slight positive overpressure, followed by some slight negative overpressure to cause the atmospheric reading to first increase and then decrease.

In general, the test results were similar for all pads and conditions, except for the studded pad and the 3-part A assembly. In Appendix E, Figures E.6 through E.8 provide examples of the raw data observed for a representative tie pad and the two exceptions. It is interesting to note in Figure E.6 that significant rebound pressure was produced, immediately following the primary suction peaks. Such large rebound peaks (up to 80 psig) were not observed in all trials, and multiple pads that produced nearly the same suction did not consistently generate rebound peaks.

As noted in the procedure, the thermoplastic pads were initially glued to the loading plate. After conducting multiple trials, some pads began to exhibit epoxy debonding. The dimpled santoprene pad eventually debonded from the loading plate, though it continued to partially adhere to the plate during uplift strokes. In general, this debonding did not appear to affect the results.

The surrounding water level was varied for a dimpled polyurethane pad (Figure 7.2). To evaluate the relationship with water level, an analysis of variance (ANOVA) test was performed on the data in Figure 7.2, and those results are given in Appendix E (Table E.5), along with other ANOVA tests. Statistically, the mean varies significantly with water level; however, because all the peak values fell within the error range of the transducer, the results are practically insensitive to water level variations.
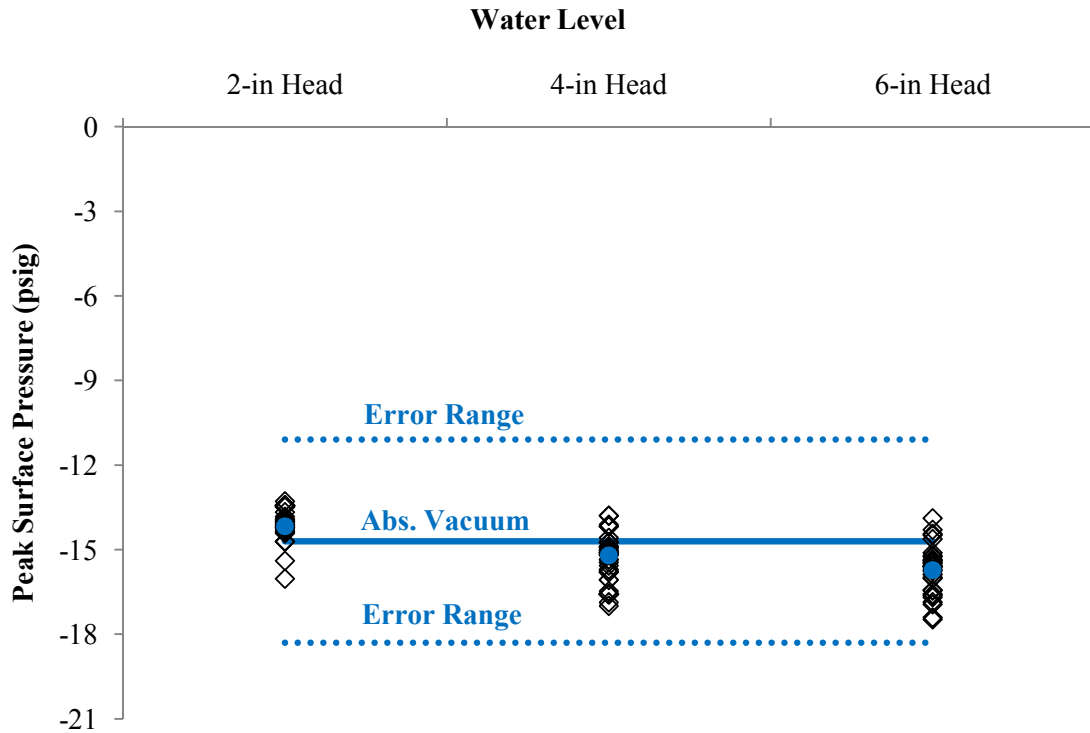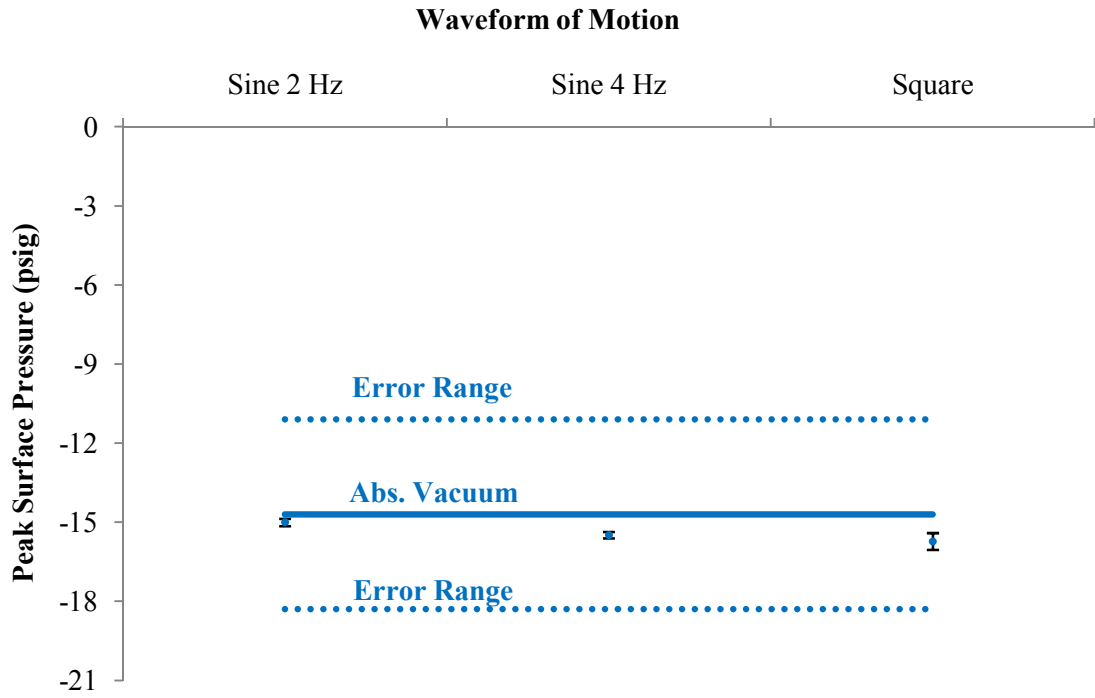
Water Level

Figure 7.2 Comparison of the peak surface pressure for three water levels, dimpled polyurethane pad; the blue dots are averages (0.09-inch uplift, glued)

The waveform of motion was varied for a dimpled polyurethane pad, and the mean for each waveform, plus/minus two standard errors of the mean, was evaluated (Figure 7.3). As with the water level test, the results for this test all fell within the error range of the transducer, though the ANOVA results (Table E.6) suggested that the means were dissimilar. As was considered in the load tests (Chapter 6), varying the waveform of motion resulted in different rates of motion, or accelerations (Figure 7.4). There was a clear trend of increasing acceleration by comparing sine two-Hz and sine four-Hz waveforms, as well as sine wave versus square wave, as was expected.

Figure 7.3 Comparison of the peak surface pressure for three waveforms of motion, dimpled polyurethane pad; the blue dots are averages, and the bars show the average peak pressure ± 2× the standard error of the mean (0.09-inch uplift, glued)
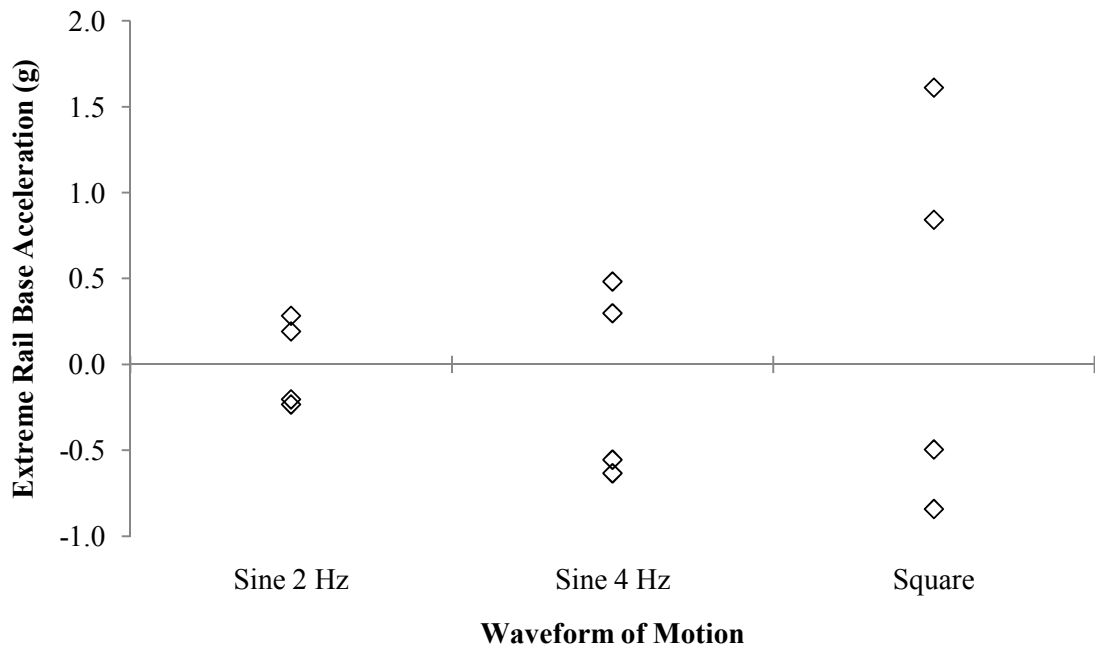
Figure 7.4 Influence of the waveform of motion on the extreme rail base acceleration, dimpled polyurethane pad (0.09-inch uplift, glued)

The results of Figure 7.3 show that although the acceleration varied significantly, the resulting pressure did not. Considering this, the extreme suction readings from all uplift test trials were plotted versus the extreme rail base acceleration (Figure 7.5). There is no evident trend between these two variables, apparently confirming the insensitivity of the suction to acceleration. It is interesting to note, however, that the few points with acceleration less than about 0.25 g were outside the error range of the transducer, suggesting that suction is a function of acceleration below a certain acceleration threshold.
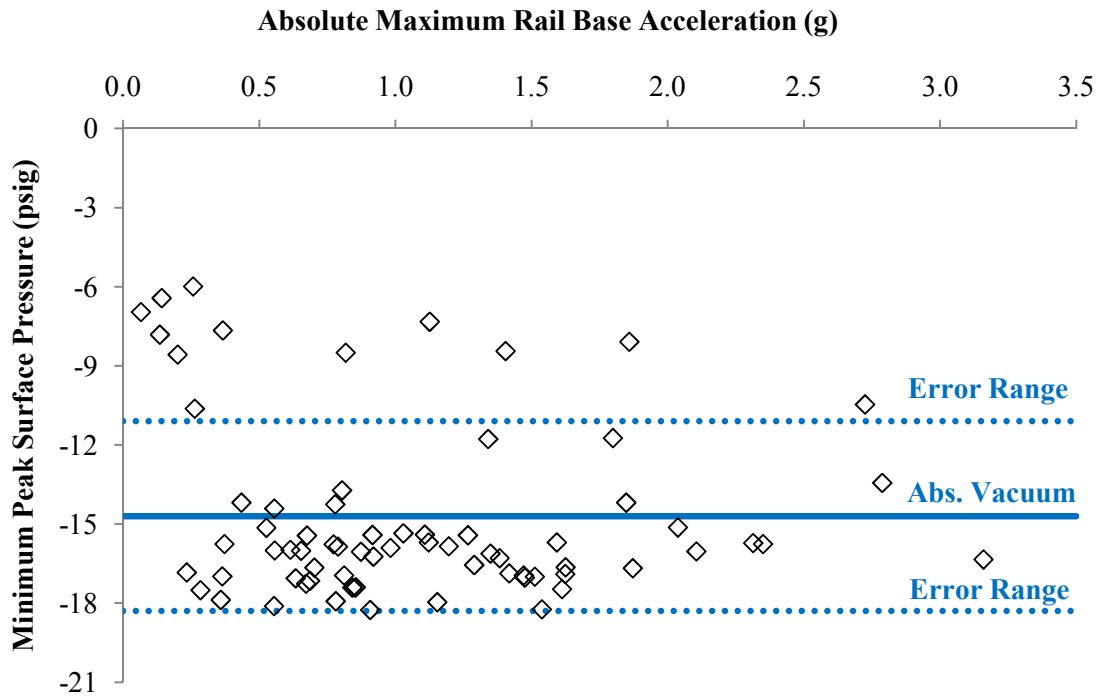
**Figure 7.5 Minimum peak surface pressure versus
the absolute maximum rail base acceleration, all trials**

The mean suction varied depending on whether the various thermoplastic pads were glued to the loading plate or in free contact (Figure 7.6). Only for the studded pad was there a major difference between glued and free contact, namely that the free-contact trial resulted in some suction within the error range of the transducer. The ANOVA test (Table E.7) showed that the grooved and dimpled polyurethane pads had statistically similar results for glued versus free contact, while the rest of the pads had distinctly different mean values for the different configurations.
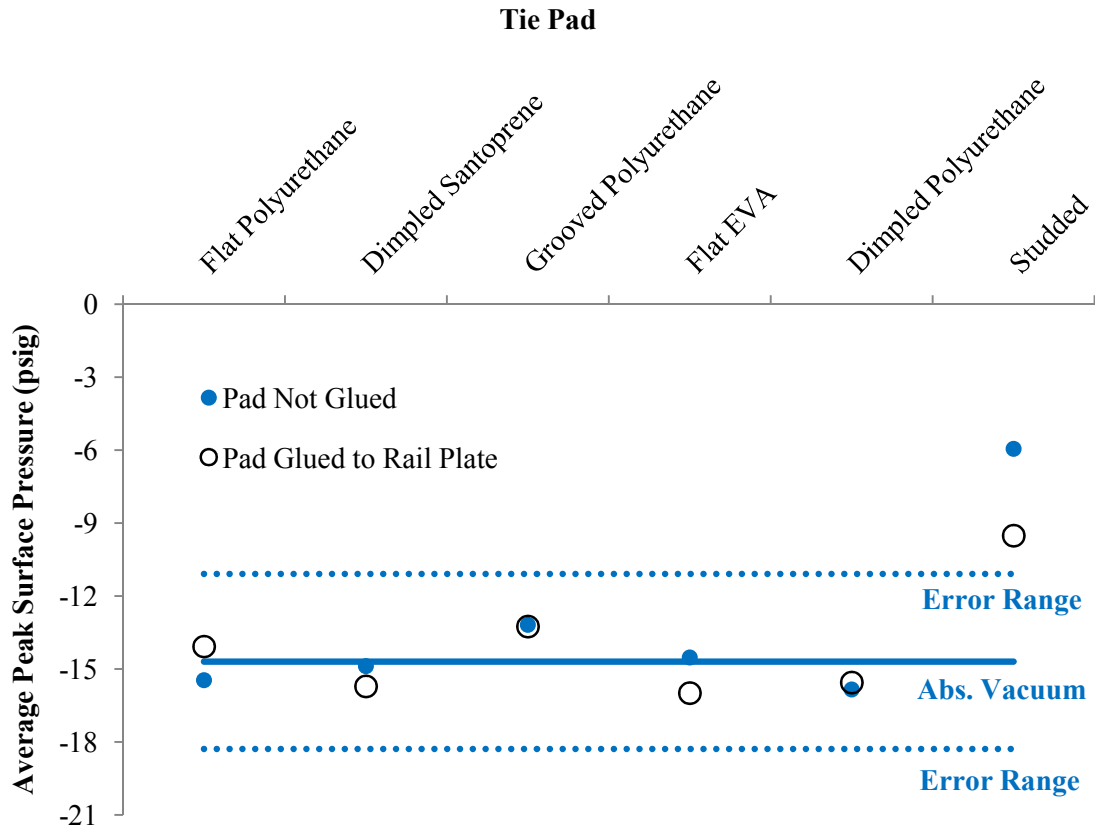
**Figure 7.6 Comparison of the average peak surface pressure
for the thermoplastic pads, glued versus free contact**

The uplift amplitude was varied for all of the pads and assemblies, except for the 2-part C assembly (Figures 7.7, 7.8, and 7.9). The pads were grouped according to their load test behavior (flexible, semi-rigid, rigid layer). The only pad that showed a major change with uplift amplitude was the studded pad, which began to produce suction within the error range of the transducer at uplift between 0.06 and 0.09 inches. The ANOVA results (Table E.8) show that only the flat ethyl-vinyl acetate (EVA) pad, dimpled polyurethane pad, and 3-part A assembly were statistically insensitive to uplift height.
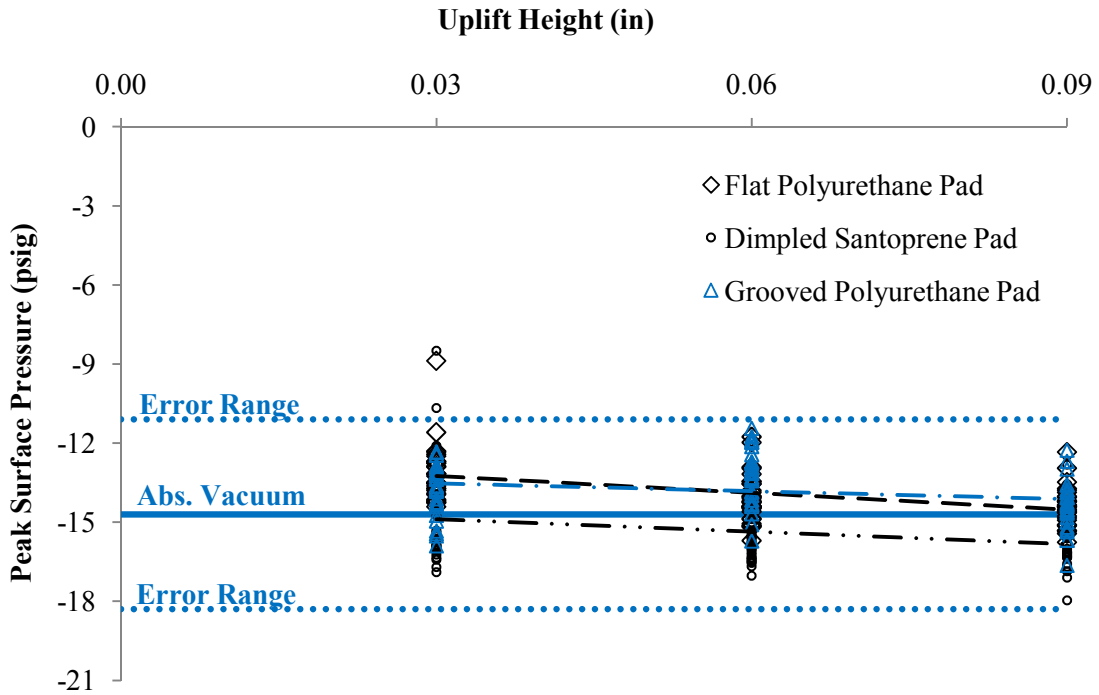
Figure 7.7 Comparison of the peak surface pressure for three uplift amplitudes, using flexible pads, showing mean regression lines (glued)
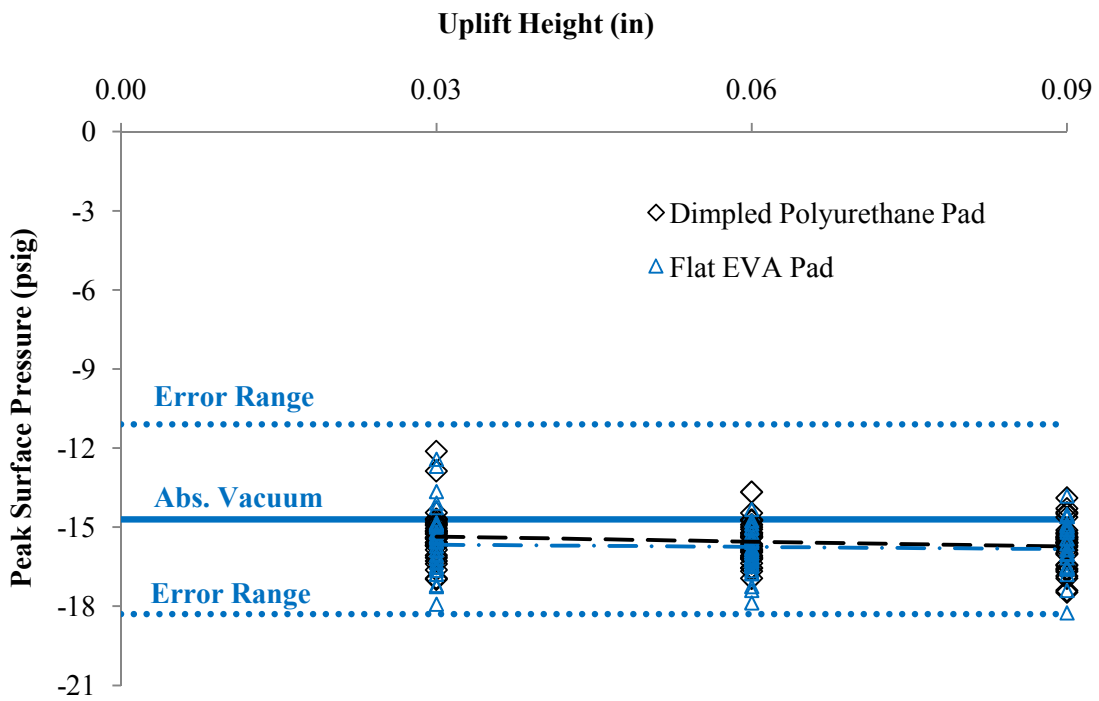

Figure 7.8 Comparison of the peak surface pressure for three uplift amplitudes, using semi-rigid pads, showing mean regression lines (glued)
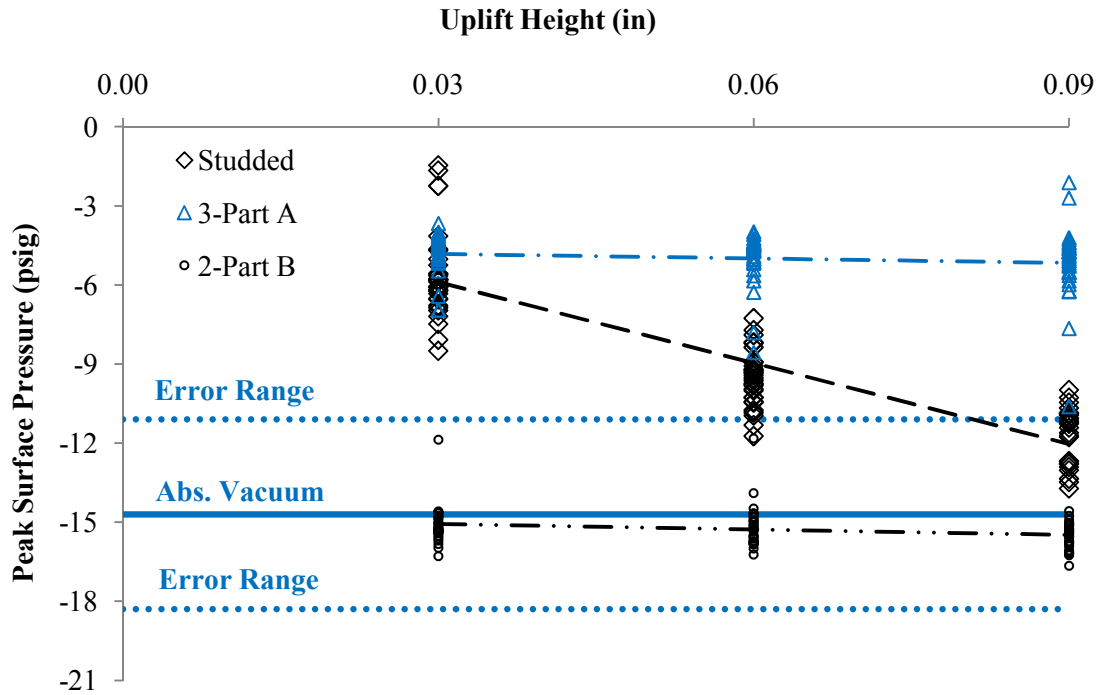
Figure 7.9 Comparison of the peak surface pressure for three uplift amplitudes, using pad assemblies, showing mean regression lines (studded pad was glued; others in free contact)

7.4 Discussion

7.4.1 Sources of Variability

The error range shown in the previous figures is quite significant because it means that the transducer readings were only accurate within approximately three psi. This limits the ability to draw strong conclusions about whether the measured suctions were able to produce cavitation. It can be said, however, that suction measured within the error range presented here had the potential to produce cavitation, due to the proximity of the suction to the vapor pressure of water. The transducer was rated with an accuracy of 0.25% of its range, which translates to accuracy within one-third of a psi. The actual error, observed during the test, was on the order of two percent, and this could have been the result of damage to the transducer, which was also suggested by the fluctuating reading for atmospheric pressure. Whatever the cause, the transducer's error was systematic, providing some confidence that the results are still useful.

As discussed in Chapter 6, there may be many sources of the variance of the peak surface pressure. The most likely sources of variance relate to the quality of the seal that the tie pad creates around the transducer's orifice, and these are the contact angle between the pad and the rail seat, the alignment of the surface indentations (which could not be controlled in the uplift tests), as well as any permanent deformations in the pad's contact surface (as was likely the case for the 3-part A assembly). In comparison, the uplift tests typically had a lower coefficient-of-variation (COV) than what was generally found in the load tests. The uplift test COV was commonly 4% to 20%, while the load test COV was 7% to 30% or higher, with higher variance found with the flexible pads and assemblies with rigid layers.

7.4.2   *Surface Water Pressure and Velocity*

In an attempt to explain the pressurization of the water in the uplift tests, an ideal model of a perfectly sealed piston with its chamber filled with water is considered here. In this model, any force applied to the piston is directly transferred through the water. When an upward force is applied, extending the piston, the water is also placed in tension. Water has a measurable tensile strength, and, though it is a simplification, this tensile strength can be considered to be around -14.3 psig, at which point the water cavitates (Franc and Michel 2004). The resulting vapor bubbles create a discontinuity in the fluid that is analogous to a crack in concrete – this effectively represents tensile rupture. Theoretically, an upward force on a chamber of water increases the suction to cavitation inception, at which point the introduction of air should reduce the suction (Franc and Michel 2004).

The suction magnitude was a function of the rate of piston displacement, not just the displacement itself (Figure 7.1). This was evident when comparing the suction produced by raising the loading plate slowly or rapidly. This was probably because the rapid displacement resulted in higher acceleration, which directly translated to force, and the higher force resulted in higher suction. If the previous analogy is true, that cavitation represents tensile rupture of the water, then any acceleration beyond the minimum required to produce cavitation will result in the same suction. Continuing with the analogy of concrete in tension, if the tensile strength of a concrete sample is 700 psi, attempting to apply 1,000 psi in tension will still result in an ultimate stress of 700 psi. With this consideration, the results

157

shown in Figure 7.5 seem reasonable. There is probably some small amount of upward acceleration that is required to raise the suction to a cavitation limit, and any acceleration above this minimum produces the same suction – assuming that the tie pad creates a good seal. Considering a tie pad with a contact area of 42.25 in^2, only approximately 600 lb of uplift force would be required to generate -14.3 psig suction.

In reality, no seal is perfect, and this appears to hold particularly true for tie pads, which are not necessarily designed with fluid sealing as a criteria. Similar to the positive pressure case considered in Chapter 6, the suction created by an imperfect seal should be less than that produced by the ideal seal. Theoretically, if there is no seal created by the tie pad over the transducer orifice, no suction can result from an upward acceleration of the tie pad.

Reviewing the hypotheses described in the first section of this chapter, the uplift tests addressed some of my misconceptions about suction at the rail seat. I expected that the suction would increase with acceleration, but, considering the previous discussion, this only appears to be true for small accelerations. Once enough suction is produced for cavitation, further acceleration should have little to no effect on the suction. The pads were originally glued to the loading plate under the supposition that this would produce the maximum suction, but there was little difference between gluing the pad and allowing free contact (Figure 7.6). In addition, the glued pad more often produced pressures the same or lower than the free-contact case. As was expected, the suction was largely independent of the surrounding water level and the uplift height – though the studded pad was strongly influenced by the uplift height. One possible explanation would be that as the amplitude of motion increased, the acceleration had to increase to maintain the same frequency of square wave motion. The extreme accelerations recorded during square wave motion for all pads were plotted versus the specified uplift (Figure 7.10), and there appears to be a subtle interaction between the two. Suction appeared to be related to the tie pad, as was found in the load tests, although all tie pads except two behaved practically the same. In addition, the load test groupings did not appear to be related to differences in suction behavior.
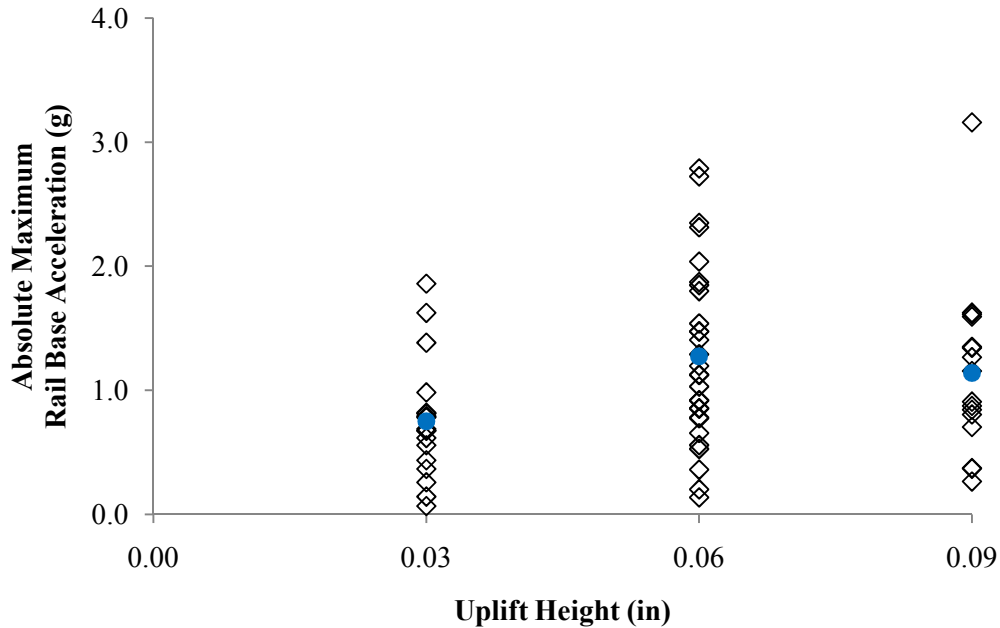
Figure 7.10 Interaction between specified uplift height and resulting rail base acceleration, square waveform, all pads; the blue dots are averages

7.4.3 Comparison of Tie Pads

The results of the free-contact trials were compared for all of the pads (Figure 7.11). This side-by-side comparison highlights the similarity between all pads except for the studded pad and the 3-part A assembly. The groupings that were used for the load tests – flexible, semi-rigid, rigid layer – do not appear to have any relevance to the uplift tests. Despite the fact that the ANOVA test (Table E.4) demonstrated that the pads producing high suction were statistically distinct, they still produced similar results in that their mean suction values were all close to the point of cavitation inception. The pads that consistently produced high suction – within the error range of the transducer – can be said to have the potential to cause cavitation. Due to the error in the transducer measurements, these results do not prove that the vapor pressure of water was achieved or that cavitation actually occurred. They do reveal that most of the pads have a strong potential to produce suction close to what would be required to initiate cavitation.
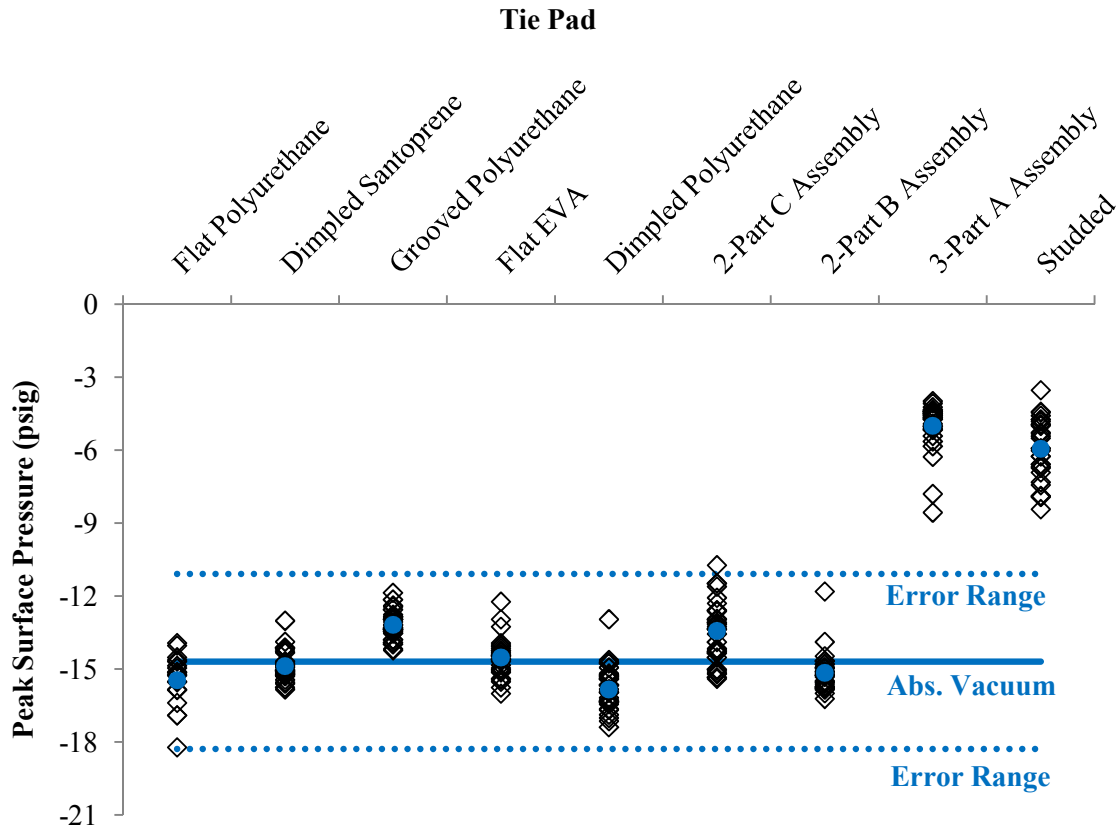
Tie Pad

**Figure 7.11 Comparison of the peak surface pressure of all pads;
the blue dots are averages (free contact)**

7.4.4   *Potential for Concrete Damage*

The loading plate acceleration was typically 0.5-1.5 g, although, in one instance it was as high as 3.0 g. The specified uplift was between 0.03-in and 0.09-in. Comparing this range of motion with the motion predicted by the Talbot model and the motion measured on railroad tracks (Table 4.3), the loading plate's acceleration is quite low, while its uplift is quite high. However, as was discussed in Section 7.4.2, higher accelerations should not affect the suction. Therefore, the actuator's motion was sufficiently representative of railroad track motion under train traffic.

The results from the uplift tests suggest that cavitation is possible in concrete-tie rail seats if the tie pad creates an adequate seal. Such pads are generally thermoplastic pads or pad assemblies with plastic bottoms. The fact that water cavitates does not necessarily mean that cavitation erosion is

occurring. Cavitation can occur in a syringe when the piston is extended too rapidly (Franc and Michel 2004), and it also occurs in geotechnical triaxial tests on soil samples if proper backpressure procedures are not followed. Review of the literature on cavitation in soil samples found no mention of cavitation damaging a soil sample. The primary concern is that it introduces air into the transducer lines such that pore pressure cannot be accurately measured (Terzaghi et al. 1996). Certainly, the cause of cavitation beneath a tie pad is very different from the common cases of cavitation erosion with high-velocity flow in hydraulic structures or high-frequency vibrations (20 kHz or greater), so it is important to consider whether cavitation in the rail seat could result in damaging pressures.

One way to consider the damage potential of cavitation is to consider basic bubble collapse theory. Similar to boiling water, cavitation typically initiates if there are inclusions in the water, particularly microbubbles referred to as "nuclei." These nuclei are commonly one half of a mm or smaller, and cavitation essentially causes them to inflate to bubbles up to ten mm or less. The internal pressure in the cavitation bubbles is a constant, near the vapor pressure of water (-14.3 psig), making them unstable as the bulk (external) water pressure increases. The pressure produced by a collapsing bubble depends on the bulk pressure of the water and the ratio of the bubble radius to its initial radius before collapse began (Figure 7.12) (Franc and Michel 2004). The collapse pressures can be extremely high as the bulk water pressure increases and the collapse progresses. Based on the load test results, 2,000 psia was considered a reasonable upper bound for the bulk water pressure.
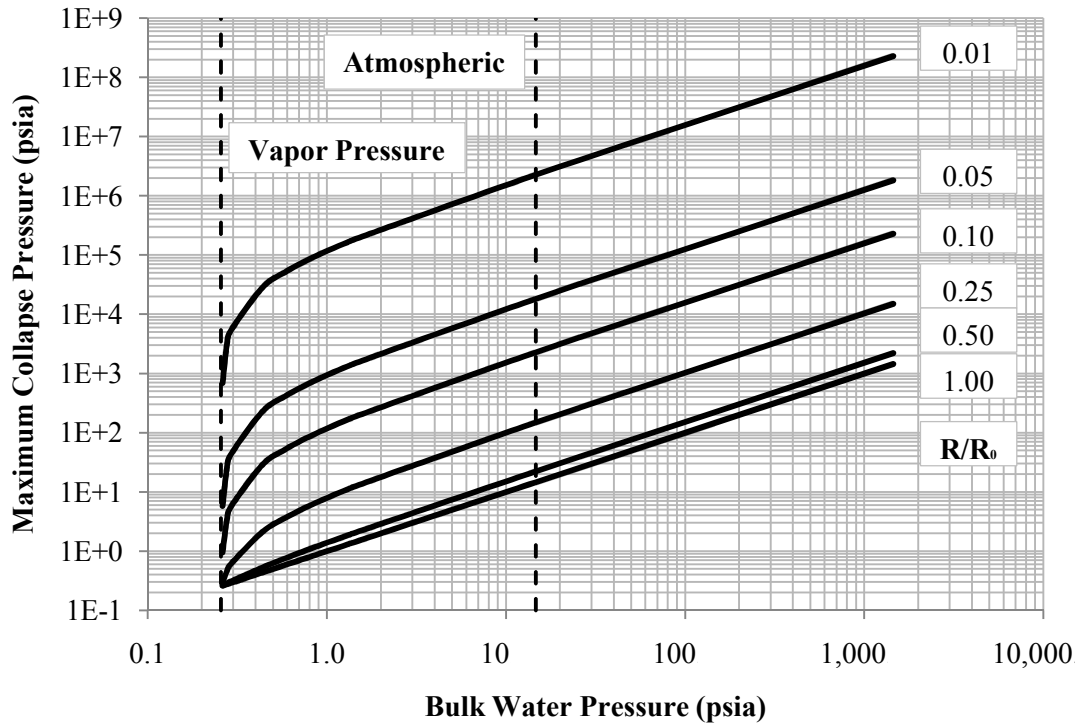
Figure 7.12 Theoretical maximum collapse pressure of cavitation bubbles, as a function of the bulk water pressure and the progression of collapse (R = current radius, R_0 = initial radius)

The pressure that is felt by the rail seat or tie pad will also depend on the initial radius of the bubble (Figure 7.13). As collapse progresses, the location of the maximum collapse pressure is drawn inward, and this collapse pressure decays away from the bubble as the inverse of the radial distance ($1/r$) (Franc and Michel 2004). Considering that the deepest indentation in any of the pads is approximately three mm (grooved pad), it was assumed that the initial bubble diameter could be no larger than two mm, or else the bubble would come in contact with either the tie pad or the rail seat.
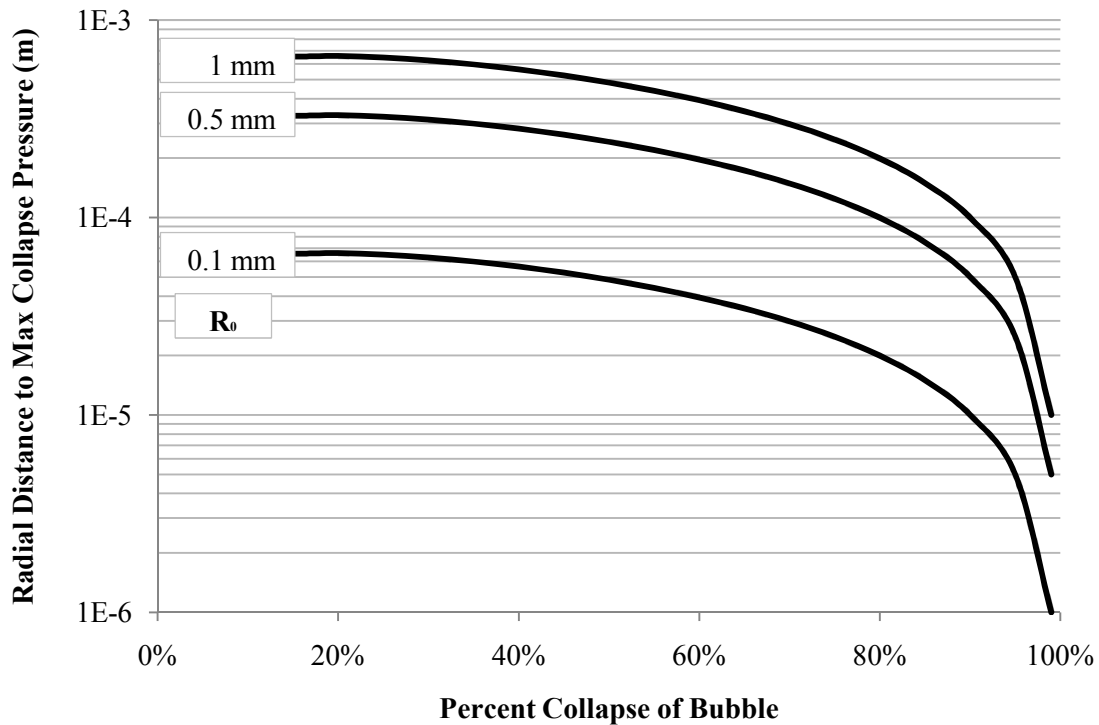
**Figure 7.13 Radial distance to maximum collapse pressure,
as a function of initial bubble radius and the progression of collapse
(R_0 = initial radius)**

The third, and possibly most important, consideration is the time to collapse, which is also a

function of the initial bubble radius and the bulk water pressure. For any bubble with an initial radius

one-mm or smaller, the theoretical time to collapse is less than five milliseconds (ms), regardless of the

bulk water pressure (Figure 7.14) (Franc and Michel 2004). This rapid collapse time is important because

five ms was also the data acquisition period used in the experiment, making it difficult to characterize

such behavior with the transducer. Also, the collapse time is short enough that the bulk water pressure

should only reach atmospheric pressure, at most, during collapse. It was observed in the uplift test data

that the peak suction occurred around the same time that contact would have been lost with the loading

plate. A loss of contact or some other failure of the tie pad seal would very quickly return the water

pressure to atmospheric conditions. This could conceivably occur within the five-ms time to collapse.

Pressurization beyond atmospheric pressure seems unlikely, considering the motion predicted by the

Talbot model. Taking a closer look at the displacement-time curve for a 60-mile-per-hour (mph) train, the complete uplift motion takes about 100 ms, and the motion from peak uplift to closure takes about 20 ms – these times would be longer for a slower train speed. This suggests that if cavitation occurs during the uplift stroke, all cavitation bubbles will expand and collapse before the approaching wheel load pressurizes the surface water.
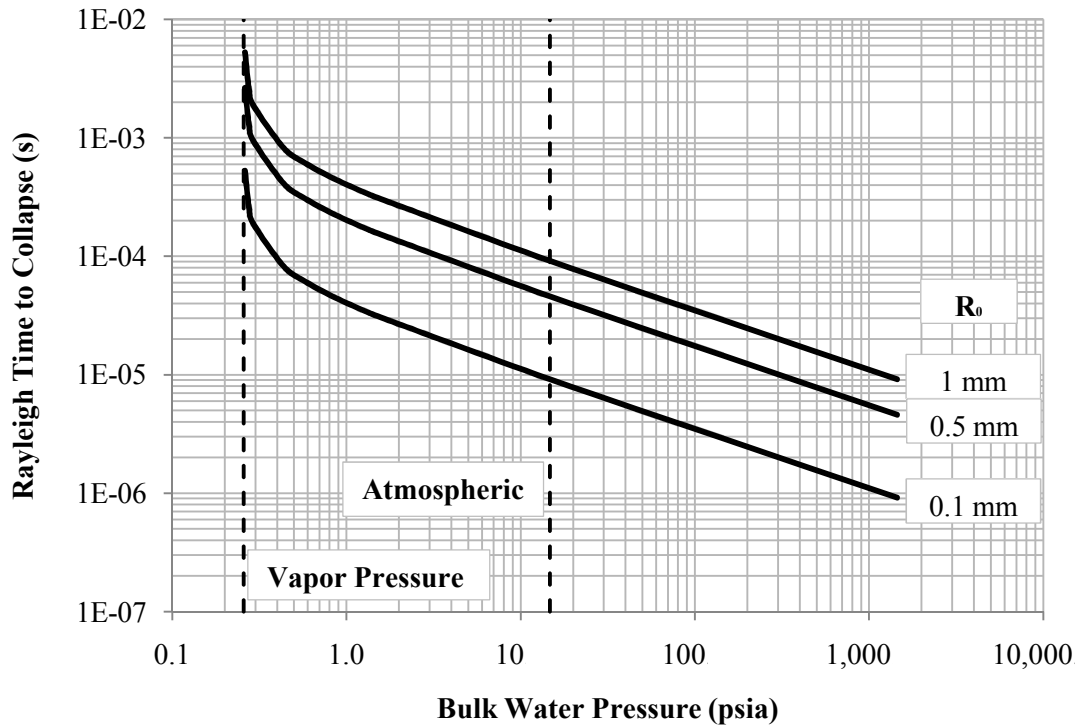

**Figure 7.14 Rayleigh's theoretical time to bubble collapse,
as a function of bulk water pressure and initial bubble radius**

From this discussion of the theory of bubble collapse, the following conclusions were drawn: (1) because they are limited to one-mm radii, the cavitation bubbles will collapse within five ms; (2) considering the short collapse time, a theoretical maximum bulk water pressure during collapse would be atmospheric pressure; and (3) because the maximum collapse pressure is drawn in close to the bubble center as collapse progresses and decays rapidly away from this radius, the collapse pressure felt by the rail seat or the tie pad will probably be less than the maximum predicted (Figure 7.12).

Even though the data acquisition period for the uplift tests was approximately the same duration as the maximum time to collapse, some rebound pressure peaks were recorded that may have been direct results of cavitation collapse. The rebound peaks typically occurred within 5-15 ms of the proceeding suction peak, and they were observed in most of the trials where the suction was within range of the vapor pressure of water. The maximum rebound peaks from all of the uplift tests were plotted against the corresponding minimum peak suction, sorted by the load-pressure pad groups (Figure 7.15). Rebound peaks were most commonly observed in tests that had very high suction and where a thermoplastic pad was being used – exceptions to this are that the grooved pad did not produce any rebound peaks, while the 2-part C assembly did produce minimal peaks. The recorded rebound peaks were all less than 80 psig, and this should not lead to concrete damage. Assuming that these were the result of cavitation collapse, it is likely that the 135-psia transducer would have been unable to measure the theoretical maximum collapse pressures (Figure 7.12). However, it is interesting that, given there were approximately two to three dozen rebound peaks recorded, not a single rebound peak was higher than 80 psig. Along the same lines, if extremely high collapse pressures were felt by the transducer but not recorded, due to the relatively long acquisition period, the transducer would likely have been severely damaged because its rated rupture pressure was only 240 psig. As I experienced in preliminary load tests with a low-range transducer, a transducer rupture is obvious because the reading becomes a constant high-pressure value, even under atmospheric pressure. These results suggest that the likelihood of cavitation leading to damaging collapse pressures at the rail seat is low.
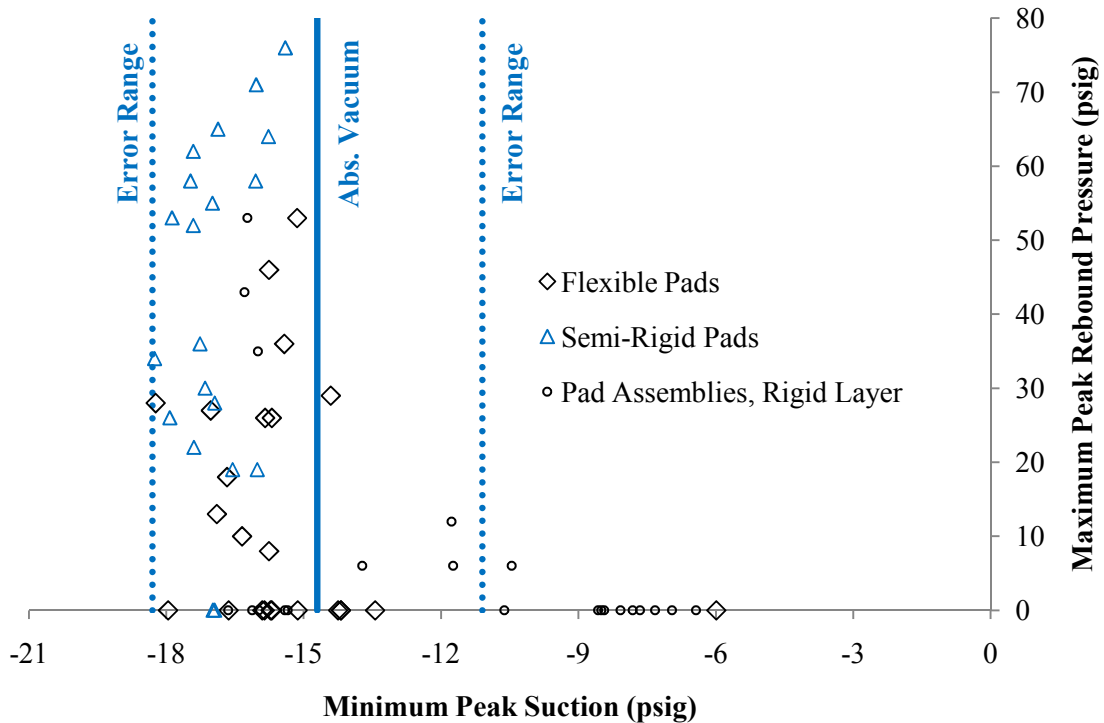
Figure 7.15 Maximum peak rebound pressure versus minimum peak suction for all trials, sorted by load-pressure pad groups

7.5   Conclusions

Based on the results of the laboratory tests, it appears that the surface water at the rail seat can cavitate under uplift forces. By comparing the transducer readings with theories about bubble collapse, cavitation erosion seems unlikely because damaging bubble collapse pressures were not observed during the laboratory tests and probably will not occur in track.

Though cavitation erosion at the rail seat appears to be unlikely, using pad assemblies with rigid layers or thermoplastic pads that do not seal water would further reduce the chances of cavitation occurring. Fortunately, this is compatible with the conclusions from the load tests, where it was found that these same pads produced low pressure under rail seat loads, thus mitigating hydraulic pressure cracking.

CHAPTER 8: SUMMARY

8.1 Conclusions about Hydraulic Mechanisms of Rail Seat Deterioration

Three hydraulic mechanisms of rail seat deterioration (RSD) – hydraulic pressure cracking, hydro-abrasive erosion, and cavitation erosion – were evaluated to consider their likelihood as causes of RSD, and possible mitigation methods. Empirical observations and results from laboratory tests, coupled with a literature review and analysis of theoretical models, were used to individually assess these three potential mechanisms.

8.1.1   Hydraulic Pressure Cracking

Hydraulic pressure cracking appears to be a possible RSD mechanism that can be effectively prevented by implementing one or more of the following approaches: (1) selecting or designing a tie pad that does not seal water and therefore does not generate high surface water pressure, (2) maintaining a low probability of high impact loads by repairing or removing out-of-round wheels and maintaining uniform load distribution among adjacent ties, and (3) producing concrete with compressive strength well above the minimum 7,000 pounds per square inch (psi), with proper air entrainment (particularly near the rail seat surface) and low permeability to increase the resistance to cracking, minimize the effects of pore pressure, and reduce the likelihood of saturated concrete beneath the rail seat surface.

Based on the linear-elastic effective stress model proposed in Chapter 4, the guidelines above can make hydraulic pressure cracking an insignificant mechanism. The primary limitations of the effective stress model are the use of linear-elastic constitutive relationships, simple definitions of fatigue and strength crack-initiation, and an assumed saturation state of the concrete. Above low levels of strain, concrete typically responds non-linearly by displaying strain-softening until rupture. Accounting for this would result in lower confining stresses, and therefore lower resistance to tensile cracking than the current model predicts. A more advanced total stress model would require a non-linear finite element analysis, since superposition could not be employed. Such complex modeling could also result in more realistic predictions of crack initiation and pore pressure distribution. In light of the sensitivity analysis of the

damage limits discussed in Chapter 6, I think that non-linear modeling would not produce significantly different conclusions than the linear model did.

8.1.2 Hydro-Abrasive Erosion

In Chapter 6, a comparison was made between the theoretical water velocity under the rail seat and lower limits of suspended-particle velocity associated with eroding concrete. The results suggest that hydro-abrasive erosion is a feasible RSD mechanism. It is difficult to predict how much this mechanism might contribute to RSD without conducting experiments that specifically measure the velocity of the particles and the resulting wear in a rail seat situation. The theoretical estimates were simple, assuming that all the rail seat load energy is transferred through the water in the form of pressure and velocity, based on the Bernoulli equation. Similar to the considerations for abrasion, caution should be exercised when allowing moisture and fines to intrude. A sealing tie pad may prevent some moisture and fines from intruding when it is undamaged, but once the system begins to wear, moisture and fines may become trapped by the same sealing action of the tie pad. The main question relevant to tie pad design is whether the considerations for hydro-abrasive erosion and abrasion, or the considerations for hydraulic pressure cracking, should dominate the sealing design of the tie pad.

8.1.3 Cavitation Erosion

Cavitation erosion appears to be infeasible – or at least highly improbable – in a concrete-tie rail seat, and it is recommended that it be removed from the list of potential RSD mechanisms. The laboratory experiments described in Chapter 7 provide evidence that cavitation can occur in rail seat surface water when sealing tie pads are used. The analysis of bubble collapse theory in Chapter 7 demonstrated that for the size of bubbles that would be feasible in a rail seat, the collapse would happen so quickly that damaging collapse pressures seem unlikely. This conclusion was potentially confirmed by the fact that a low-range pressure transducer was not damaged by any collapse pressures – even moderately high collapse pressures would have destroyed the transducer's sensor. To further prevent any possibility of cavitation erosion, the laboratory results suggest that selecting or designing tie pads that do not seal water would reduce the chance that cavitation itself occurs.

8.2 Revised Understanding of RSD

Due to the recent resurgence of RSD as a critical concrete tie problem in North America, a second ad hoc committee was formed to address the problem in 2010, this time by the American Railway Engineering and Maintenance-of-Way Association (AREMA) Committee 30 – Ties. The ad hoc RSD working group comprises railroaders, suppliers, and researchers, and among their first actions was to agree on the causes of RSD (Tables 8.1 and 8.2). Cavitation erosion has been removed from the list of potential RSD mechanisms (Table 8.1), resulting in five concrete deterioration mechanisms that should be considered.

Table 8.1 Relevance of the causes of RSD to the different concrete deterioration mechanisms

Causes	Abrasion	Crushing	Freeze-Thaw	Hydraulic Pressure	Hydro-Abrasive
High stresses at rail seat	✔	✔		✔	✔
Relative motion at rail seat	✔	✔		✔	✔
Presence of moisture	✔	✔	✔	✔	✔
Presence of abrasive fines	✔				✔

Table 8.2 Summary of factors, internal and external to the concrete tie, related to the causes of RSD

	High Stresses at the Rail Seat	Relative Motion at the Rail Seat	Presence of Moisture	Presence of Abrasive Fines
Internal Factors	*Loss of proper rail cant* • Loss of material at rail seat • Loss of material at shoulder • Loss of toe load	*Looseness of fastening system (loss of toe load)* • Loss of material at rail seat • Loss of material at shoulder • Yielded or fractured clips *Scrubbing action* • Poisson's ratio of tie pad	*Tie pad seal* • Material properties and surface geometry of tie pad • Looseness of fastening system • Wear of rail seat and tie pad *Concrete saturation* • Permeability of concrete and rail seat surface	*Tie pad seal* • Material properties and surface geometry of tie pad • Looseness of fastening system • Wear of rail seat and tie pad *Fines from wear of rail seat components*
External Factors	*High vertical loads* • Impact loads • Degraded track geometry *High L/V ratio* • Truck hunting • Over-/under-balanced speeds on curves • Sharp curves • Degraded track geometry *High longitudinal loads* • Steep grades • Thermal stresses in rail • Train braking and locomotive traction *Poor load distribution among adjacent ties* • Non-uniform track substructure • Non-uniform tie spacing • Degraded track geometry	*Uplift action* • Low stiffness of track substructure, higher deflections *Lateral action* • Truck hunting • Truck steering around curves (push and pull) • Over-/under-balanced speeds on curves • Sharp curves *Longitudinal action* • Steep grades • Thermal stresses in the rail • Train braking and locomotive traction	*Climate* • Average annual rainfall, days with precipitation, humidity, etc. • Average evaporation rate, etc. • Extreme daily or annual temperatures • Number of annual freeze/thaw cycles	*Environment* • Wind-blown sand or dust • Moisture to transport the abrasive fines under the tie pad *Track maintenance* • Ground ballast • Metal shavings from rail grinding *Train operations* • Application of locomotive sand for braking (especially on grades) • Coal dust and other abrasive commodities

Table 8.2 separates factors that contribute to the causes of RSD into internal and external factors,

considering that some factors are within the realm of concrete-tie design and some are functions of track

alignment, track maintenance, train operations, or the climate/environment. It can be advantageous to organize the factors in this way so that the different stakeholders – concrete tie manufacturers and suppliers, and the railroads that purchase concrete ties – identify their roles in preventing or mitigating RSD. However, considering Tables 8.1 and 8.2 together highlights the fact that RSD is a complex interaction of different deterioration mechanisms and causes. For example, the importance of tie pad sealing has been demonstrated through this research on the hydraulic mechanisms of RSD. Tie pad sealing depends not just on the design of the tie pad, but also the toe load or looseness of the fastening assembly, as well as the amount of wear on the rail seat surface.

Table 8.2 is a summary of factors that affect the demand on the rail seat and the fastening assembly. The different factors that affect resistance to wear and damage, such as strength, hardness, stiffness, and ductility, are not listed here. The most effective way to address resistance to RSD is to consider it as a system problem because the demands (causes) are functions of all aspects of the track system, including train operations. For example, to resist high stresses at the rail seat, the system has to be designed with proper load paths such that no single component wears too quickly and thus compromises the life cycle of the system. In other words, the system is only as durable as its least durable component. Also, a proper balance must be achieved between the distinct objectives of maintaining a tight fastening system and providing a sustainable load path. An extremely stiff fastening system and track substructure that allows no relative motion will have higher stress concentrations because there is much less energy absorption, or dynamic damping, in the track system.

8.3 Proposals for Future Rail Seat Deterioration and Concrete Tie Research

8.3.1 Intrusion of Moisture and Fines

In this research on the hydraulic mechanisms of RSD, general assumptions were made about moisture under the tie pad and saturation of the concrete. In order to predict the potential for hydraulic pressure cracking, as well as other RSD mechanisms, it would be beneficial to investigate how different precipitation or pooling events on the track result in the intrusion of moisture and fines beneath the tie pad and how saturated the concrete actually is. In this research I attempted to quantify different properties of

tie pads, such as their compressibility and rigidity that would contribute to their ability to seal water. A simple test could be developed to evaluate this sealing potential directly by placing a matrix of dots of litmus paper under the tie pad in a fully assembled tie attached to a rail section. Litmus paper with a pH range from 3.0 to 5.5 changes color when exposed to tap water, so it could give a simple yes/no answer as to whether water penetrates under the tie pad when it is applied to a fully assembled tie. Water could be applied while the tie is at rest (when only the clip toe load is acting) or while a static wheel load is applied. Dynamic loading would probably damage the litmus paper. The intrusion of fines could be another aspect of the experiment and this could be measured by simply weighing the mass of fines found under the tie pad at various intervals and at the end of some allotted time period.

8.3.2   *Laboratory Abrasion Test with Polymers, Moisture, and Fines*

The literature and standard tests on abrasion resistance typically involve steel grinding against concrete, but there has been little research on the kind of polymer-concrete or polymer-abrasive slurry-concrete wear regime that characterizes RSD. It would be beneficial to develop simple, laboratory abrasion tests that incorporate these different materials (including different rail seat surface treatments) with chosen lateral loads/displacements and vertical loads. The test could be scaled down so that the wear surfaces are smaller and the loads are lower, but at the same time maintaining the same stresses. Such a test would be useful to select combinations of tie pads and concrete (or rail seat treatments) that provide adequate abrasion resistance at a reasonable cost. These combinations could be further tested in a full-scale laboratory or field test of a fully assembled concrete tie and rail assembly.

The other advantage of a simple laboratory abrasion test for RSD would be to understand the demands on the materials. How will the rate of abrasion be influenced by the amount of lateral displacement/load, the loading rate, the normal force, the effective coefficient of friction between the pad and the rail seat, the amount of water, the amount and type of abrasive fines, the hardness of the pad relative to that of the rail seat, the strength of the materials, and the ductility of the materials? Developing experiments and research programs to answer these questions could significantly improve the design of concrete ties for resistance to RSD.

8.3.3   *Measuring Rail Seat Stresses*

The stress demand on the different components of the track system under heavy-axle-load operation is complex. These stresses depend on wheel loads, the wheel/rail interface, track support, and lateral-to-vertical load ratio (L/V). It would be beneficial if a concrete-tie rail seat and its fastening components (particularly the insulators and shoulders) could be properly instrumented to measure the actual stresses they develop under different loading conditions. Traditional strain gauges could be one option, if the strain gauges can be placed without being damaged during loading. Another option that might be viable is casting fiber optic strain sensors into concrete ties. Fiber optic sensors have been demonstrated to be useful for measuring strain in concrete cylinders and along sections of rail (Calero et al. 1994, Signore et al. 1997). The advantage of a fiber optic cable is that it can measure strain along its length (Calero et al. 1994).

What is important for the rail seat is not just the maximum stress but the distribution of stresses, particularly when high L/V ratios are applied. A better understanding of the transferred loads and stress distribution as a function of the input normal force (P) and L/V ratio would be applicable to abrasion, crushing, hydraulic pressure cracking, and hydro-abrasive erosion. The stress distribution on an eccentrically-loaded rail seat could help match different pairs of P and L/V with concrete damage. This would be a worthwhile follow-up to the work by Choros et al (2007) on the crushing mechanism of RSD.

8.3.4   *Dynamic Vehicle-Track Interaction Model*

In addition to correlating the rail seat normal force (P) and the L/V ratio with concrete damage, it would also be important to determine which P and L/V pairs could result from different configurations of track alignment, track support, and different train operating conditions. The most accurate way to estimate such relationships may be with a three-dimensional, dynamic vehicle-track interaction model, where the elasticity and dynamics of the track and train components are modeled with masses, springs, and dampers. A robust program that could incorporate non-uniformity in the wheel loads, track support, and track alignment would be very powerful. In particular, these non-uniformities can lead to dynamic concentrations of stresses that would be difficult to predict without a model. Significant work has been

done in the area of vehicle-track interaction models, and the literature would be the best place to start.

Table 8.3 summarizes what the vehicle-track interaction model should do, with the primary objective of finding combinations of track and train parameters that lead to high concentrated stresses on the rail seat components. If feasible, such a model could substantially advance the understanding of the dynamic load path in the track structure.

Table 8.3 Possible input parameters for, and output from,
a dynamic vehicle-track interaction model

Track Parameters		Train Parameters	
• Length and degree of curve	• Superelevation	• Train speed	• Train length
• Geometry of spirals	• Rail friction	• Gross car load	• Power distribution
• Alignment deviations	• Grade	• Wheel tread condition	• Axle spacing and arrangement
• Tie stiffness and damping (downward)	• Gauge deviations	• Braking and traction forces	• Stiffness and damping of truck and car components
• Shoulder stiffness and damping (lateral)	• Cross-level deviations		
	• Thermal rail stresses		
• Clip stiffness and damping (upward, longitudinal, rotational)	• Track substructure stiffness and damping (downward, lateral, longitudinal)		
	• Tie pad stiffness and damping (downward)		
Output per Rail Seat:	*Normal force*	*L/V ratio*	*Dynamic impact factor*

8.3.5   *Assorted Concrete-Tie Research Topics*

A major component that is currently missing from RSD research are quantitative data on the geography, conditions, and rate of RSD occurrence in track. Through the ad hoc RSD working group, some system could be instituted by railroads to record instances of RSD along with the conditions and age of the tie. The data would be further enriched by similar information along with characteristics of ties, tracks, and train operations in locations elsewhere in the world where RSD has not been observed (see

Chapter 3). This could be one way to advance the industry's knowledge of RSD from anecdotal to data-driven.

As discussed in Chapter 1, the AREMA recommendations for tie design, particularly in terms of design moments and ballast pressures, need to be updated. The recommendations are currently unable to adjust to different scenarios of axle loads or support conditions – each of which can strongly influence the demand on the tie (see the sensitivity analysis of the beam model in Appendix C). Speed and annual tonnage are considered through the use of empirical factors, but the design process is not intuitive. It is not clear how the design charts were derived or how to modify them for different conditions. Comparisons between the AREMA design procedure and the relevant European code have revealed that AREMA has relatively stringent rail seat moment requirements but less stringent center moment requirements (Haban 2009). This is interesting when one considers that center cracking was listed as one of the top problems with concrete ties in the industry survey (Chapter 2). An analytical approach that is validated by laboratory tests and field installations should be pursued that can improve the AREMA design guidelines and procedures. Although in actuality AREMA provides a set of "recommended best practices," for concrete ties it is effectively used as a design manual, and it should have physically-based design procedures and similar detail as that found in the American Concrete Institute (ACI) building code and commentary or the American Institute of Steel Construction (AISC) construction manual.

REFERENCES

American Concrete Institute (ACI), 2008, *Building Code Requirements for Structural Concrete and Commentary*, ACI 318-08, American Concrete Institute, Farmington Hills, Michigan.

American Institute of Steel Construction, Inc. (AISC), 2006, *Steel Construction Manual*, 13th ed, American Institute of Steel Construction, Inc., Chicago, Illinois.

American Railway Engineering and Maintenance-of-Way Association (AREMA), 2009, *AREMA Manual for Railway Engineering*, v 1, ch. 30, parts 2 and 4, American Railway Engineering and Maintenance-of-Way Association, Landover, Maryland.

American Railway Engineering Association (AREA), 1910, "Report of Committee III – On Ties: Appendix D – Metal and Composite Ties," *Proceedings of the American Railway Engineering Association*, v 11, pt. 2, Chicago, Illinois, pp. 876-899.

American Railway Engineering Association (AREA), 1912, "Report of Committee III – On Ties: (3) Metal Composite and Concrete Ties," *Proceedings of the American Railway Engineering Association*, v 13, Chicago, Illinois, pp. 352-363.

American Railway Engineering Association (AREA), 1920, "Second Progress Report of the Special Committee on Stresses in Railroad Track," *Proceedings of the American Railway Engineering Association*, v 21, Chicago, Illinois, pp. 648-814.

American Railway Engineering Association (AREA), 1923, "Report of Committee III – Ties: Exhibit A – Fundamentals to Be Considered in Designs of Substitute Ties," *Proceedings of the American Railway Engineering Association*, v 24, Chicago, Illinois, pp. 249-250.

American Railway Engineering Association (AREA), 1947, "Report of Committee 3 – Ties: Report on Assignment 3 – Substitutes for Wood Ties," *Proceedings of the American Railway Engineering Association*, v 48, Chicago, Illinois, pp. 378-379.

American Railway Engineering Association (AREA), 1954, "Discussion on Ties: Assignment 3 – Substitutes for Wood Ties," *Proceedings of the American Railway Engineering Association*, v 55, Chicago, Illinois, pp. 1074-1076.

American Railway Engineering Association (AREA), 1960, "Report of Committee 3 – Ties: Report on Assignment 3 – Substitutes for Wood Ties," *Proceedings of the American Railway Engineering Association*, v 61, Chicago, Illinois, pp. 408-412.

American Railway Engineering Association (AREA), 1962, "Discussion on Ties and Wood Preservation: Assignment 7 – Substitutes for Wood Ties," *American Railway Engineering Association Bulletin*, v 63, bulletin 572, Chicago, Illinois, p. 745.

American Railway Engineering Association (AREA), 1975, "Special Committee on Concrete Ties – Manual Recommendations," *American Railway Engineering Association Bulletin*, v 77, bulletin 655, Chicago, Illinois, pp. 193-236.

American Railway Engineering Association (AREA), 1976, "Special Committee on Concrete Ties – Manual Recommendations," *American Railway Engineering Association Bulletin*, v 78, bulletin 660, Chicago, Illinois, pp. 133-138.

American Railway Engineering Association (AREA), 1981, "Manual Recommendations Committee 10 – Concrete Ties," *American Railway Engineering Association Bulletin*, v 83, bulletin 685, Washington, DC, pp. 192-195.

American Railway Engineering Association (AREA), 1988, "Proposed 1988 Manual Revisions to Chapter 10 – Concrete Ties," *American Railway Engineering Association Bulletin*, v 89, bulletin 714, Washington, DC, pp. 124-132.

American Railway Engineering Association (AREA), 1991, "Proposed 1991 Manual Revisions to Chapter 10 – Concrete Ties," *American Railway Engineering Association Bulletin*, v 92, bulletin 729, Washington, DC, p. 64.

Amtrak, 2006, National Passenger Railroad Corporation, "Standard Track Plan Concrete Tie," dwg. no. AM76008B, Philadelphia, Pennsylvania, revised 3 April, sheet no. 1 of 2.

Association of American Railroads (AAR), 2010, *Field Manual of the AAR Interchange Rules*, Association of American Railroads, Washington, DC.

Bakharev, T., 1994, *Microstructural Features of Railseat Deterioration in Concrete Railroad Ties*, M.S. Thesis, University of Illinois at Urbana-Champaign, Urbana, Illinois.

Bhatnager, P., 2009, "Dedicated Freight Corridors in India," third keynote presentation at the opening ceremony of the 9th International Heavy Haul Conference, Shanghai, China, 21-24 June.

Bhatti, M.H., V.K. Garg, K.H. Chu, 1985, "Dynamic Interaction between Freight Train and Steel Bridge," *Journal of Dynamic Systems, Measurement, and Control*, v 107, no. 1, pp. 60-66.

Bosshart, J., 2009, phone interview, John Bosshart was Director of Track Standards and Procedures for the BNSF Railway when this research was conducted, 6 February.

Cai, Z., G.P. Raymond, R.J. Bathurst, 1994, "Estimate of Static Track Modulus Using Elastic Foundation Models," *Transportation Research Record*, v 1470, pp. 65-72.

Calero, J., S.P. Wu, C. Pope, S.L. Chuang, J.P. Murtha, 1994, "Theory and Experiments on Birefringent Optical Fibers Embedded in Concrete Structures," *Journal of Lightwave Technology*, v 12, no. 6, pp. 1081-1091.

Carrasquillo, P.M., 1987, "Durability of Concrete Containing Fly Ash for Use in Highway Applications," *Concrete Durability: Proceedings of Katharine and Bryant Mather International Symposium*, American Concrete Institute (ACI) Special Publication 100-47, pp. 843-862.

Choros, J., B. Marquis, M. Coltman, 2007, "Prevention of Derailments due to Concrete Tie Rail Seat Deterioration," Proceedings of the ASME/IEEE Joint Rail Conference and the ASME Internal Combustion Engine Division, Spring Technical Conference 2007, pp. 173-181.

Choros, J., 2009, phone interview, John Choros was a Mechanical Engineer for the Volpe National Transportation Systems Center when this research was conducted, 17 February.

Clark, D.W., J. Bosshart, 2010, "Fastener Systems," presentation at the Transportation Research Board 89th Annual Meeting, Washington, DC, January.

Craig, R.R., 2000, *Mechanics of Materials*, 2nd ed., John Wiley & Sons, Inc., New York City, New York, pp. 81-84.

De Almeida, I.R., 1994, "Abrasion Resistance of High Strength Concrete with Chemical and Mineral Admixtures," *Durability of Concrete – Proceedings Third CANMET – ACI International Conference*, American Concrete Institute (ACI) Special Publication 145-60, pp. 1099-1114.

Degrande, G., L. Schillemans, 2001, "Free Field Vibrations During the Passage of a Thalys High-Speed Train at Variable Speed," *Journal of Sound and Vibration*, v 247, no. 1, pp. 131-144.

Dhir, R.K., M.R. Jones, E.A. Byars, I.G. Shaaban, 1994, "Predicting Concrete Durability from its Absorption," *Durability of Concrete – Proceedings Third CANMET – ACI International Conference*, American Concrete Institute Special Publicaiton 145-64, pp. 1177-1194.

Finnie, I., 1960, "Erosion of Surfaces by Solid Particles," *Wear*, v 3, pp. 87-103.

Fort, O.E., 1968, "Experience of the Frisco with Prestressed Concrete Cross Ties," *American Railway Engineering Association Bulletin*, v 69, bulletin 612, Chicago, Illinois, pp. 545-549.

FRA, 2010, US Department of Transportation, Federal Railroad Administration, Office of Safety, Code of Federal Regulations Title 49, Federal Track Safety Standards, Part 213.

Franc, J.-P., J.-M. Michel, 2004, *Fundamentals of Cavitation*, Fluid Mechanics and Its Applications Series, v 76, Kluwer Academic Publishers, Dordrecht, The Netherlands, pp. 1-56 and 265-291.

Gallamore, R., 1999, "Regulation and Innovation: Lessons from the American Railroad Industry," in J.A. Gomez-Ibanez, W.B. Tye, C. Winston (eds.), *Essays in Transportation Policy and Economics*, Brookings Institution Press, Washington, DC.

Gemeiner, B., S. Mattson, 2005, "Wheel Impact Loads and Transmission into Track Structure," presentation at the Transportation Research Board 84th Annual Meeting before Committee AR060 for Railway Maintenance, Washington, DC, January.

Goretta, K.C., M.L. Burdt, M.M. Cuber, L.A. Perry, D. Singh, A.S. Wagh, J.L. Routbort, W.J. Weber, 1999, "Solid-Particle Erosion of Portland Cement and Concrete," *Wear*, v 224, pp. 106-112.

Haban, F., 2009, "Comparison EN 13230 and AREMA," presentation to AREMA Committee 30 in Pueblo, Colorado, 3 March.

Haestad Methods, T.M. Walski, D.V. Chase, D.A. Savic, W. Grayman, S. Beckwith, E. Koelle, 2003, *Advanced Water Distribution Modeling and Management*, 1st ed., Haestad Press, Waterbury, Connecticut, pp. 573-623.

Hay, W.W., 1982, *Railroad Engineering*, 2nd ed., John Wiley & Sons, Inc, New York City, New York, pp. 239-244, 247-266, 415-416, 469-477, 542-550, 593-597, and 667.

Hendry, M.T., 2007, *Train-induced Dynamic Response of Railway Track and Embankments on Soft Peaty Foundations*, M.S. Thesis, University of Saskatchewan, Saskatoon, Canada.

Heritage, A. (ed.), 2007, *World Reference Atlas*, revised 3rd ed., Dorling Kindersley Publishing, Inc., New York, New York, pp. 2, 49, 69, 87, 133.

Hetenyi, M., 1946, *Beams on Elastic Foundation*, University of Michigan Press, Ann Arbor, Michigan, pp. 1-9 and 56-58.

Hjelmstad, K.D., 2005, *Fundamentals of Structural Mechanics*, 2nd ed., Springer Science + Business Media, LLC, New York City, New York, pp. 103-124 and 241-282.

Hoff, G.C., 1987, "Durability of Fiber Reinforced Concrete in a Severe Marine Environment," *Concrete Durability: Proceedings of Katharine and Bryant Mather International Symposium*, American Concrete Institute (ACI) Special Publication 100-55, pp. 997-1042.

Hu, X.G., A.W. Momber, Y.G. Yin, 2002, "Hydro-Abrasive Erosion of Steel-Fibre Reinforced Hydraulic Concrete," *Wear*, v 253, pp. 848-854.

Humphreys, D., 2007, "In-Track Repair of Concrete Ties," *AREMA Conference Proceedings 2007*, American Railway Engineering and Maintenance-of-way Association (AREMA), Landover, Maryland.

Jimenez, R., J. LoPresti, 2004, "Performance of Alternative Tie Material under Heavy-Axle-Load Traffic," *Railway Track & Structures*, v 100, no. 1, pp. 16-18.

Johns, T., 2009, phone interview, Tim Johns was the Manager of Rail Products for Exova Canada, Inc. when this research was conducted, 11 February.

Judge, T., 2003, "What's on M/W Shopping Lists for '03?," *Railway Track and Structures*, v. 99, no. 1, pp. 19-23.

Kalay, S., 2010, "AAR Strategic Research Implementation Safety and Efficiency," *Transportation Technology Center Institute (TTCI) 15th Annual Research Review*, Pueblo, Colorado, 2-3 March.

Kettil, P., G. Engstrom, N.-E. Wiberg, 2005, "Coupled Hydro-Mechanical Wave Propagation in Road Structures," *Computers and Structures*, v 83, pp. 1719-1729.

Kettle, R.J. and M. Sadegzadeh, 1987, "Influence of Construction Procedures on Abrasion Resistance," *Concrete Durability: Proceedings of Katharine and Bryant Mather International Symposium*, American Concrete Institute (ACI) Special Publication 100-71, pp. 1385-1410.

Kutay, M.E., A.H. Aydilek, 2007, "Dynamic Effects of Moisture Transport in Asphalt Concrete," *Journal of Transportation Engineering*, American Society of Civil Engineers, v 133, no. 7, pp. 406-414.

Kuys, W., 2009, "Heavy Haul Developments in South Africa," fifth keynote presentation at the opening ceremony of the 9th International Heavy Haul Conference, Shanghai, China, 21-24 June.

Magee, G.M., 1966, "Current Status of Prestressed Concrete Ties on Railroads in the United States," *American Railway Engineering Association Bulletin*, v 67, bulletin 600, Chicago, Illinois, pp. 621-641.

Magee, G.M. and Ruble, E.J., 1960, "Progress Report: Service Tests of Prestressed Concrete Ties," *Railway Track & Structures*, v. 56, no. 9, pp. 33-36, 82, 84, and 88.

Mattson, S., 2010, interviews and email correspondence, Steve Mattson was a Technical Manager for VAE Nortrak when this research was conducted, January to April.

McQueen, J., 2006, "Flexural Performance Requirements for Prestressed Concrete Ties by Factoring," *Proceedings of the AREMA Seminar "Concrete Ties…Into the Next Century,"* Skokie, Illinois, 10-11 May.

Mindess, S., J.F. Young, D. Darwin, 2003, *Concrete*, 2nd ed., Pearson Education Inc., Upper Saddle River, New Jersey, pp. 68-76 and 342-344.

Momber, A.W., 2000, "Short-Time Cavitation Erosion of Concrete," *Wear*, v 241, pp. 47-52.

Momber, A.W., R. Kovacevic, 1994, "Fundamental Investigations on Concrete Wear by High Velocity Water Flow," *Wear*, v 177, pp. 55-62.

Munson, B.R, D.F. Young, T.H. Okiishi, 2006, *Fundamentals of Fluid Mechanics*, 5th ed., John Wiley & Sons, Inc., Hoboken, New Jersey, pp. 39, 402-407, 489-492, 761.

Naaman, A.E., 2004, *Prestressed Concrete Analysis and Design Fundamentals*, 2nd ed., Techno Press 3000, Ann Arbor, Michigan, pp. 193-195.

Naik, T.R., S.S. Sing, B. Ramme, 1997, "Effect of Source and Amount of Fly Ash on Mechanical and Durability Properties of Concrete," *Fourth CANMET/ACI International Conference on Durability of Concrete*, American Concrete Institute Special Publication 170-8, pp. 157-188.

Nanni, A., 1989, "Abrasion Resistance of Roller Compacted Concrete," *American Concrete Institute Materials Journal,* v 86, no. 6, pp. 559-565.

National Transportation Safety Board (NTSB), 2006, "Railroad Accident Brief, Accident No. DCA-05-FR-010 (NTSB/RAB-06/03)," 18 October.

Norfolk Southern Railway Company (NS Railway), 2001, "Rail Sections," design drawing, Atlanta, Georgia, revised 9 August.

Oregon Climate Service, "PRISM Precipitation Maps: 1961-90," online reference, URL: http://www.wrcc.dri.edu/precip.html.

Pandrol USA, 2004a, "'e' Series Clip," product brochure, Pandrol USA, LP, Bridgeport, New Jersey.

Pandrol USA, 2004b, "Pandrol Safelok," product brochure, Pandrol USA, LP, Bridgeport, New Jersey.

Peters, N., S. Mattson, 2004, "CN 60E Concrete Tie Development," *AREMA Conference Proceedings 2004*, American Railway Engineering and Maintenance-of-way Association (AREMA), Landover, Maryland.

Poulos, H.G., E.H. Davis, 1974, *Elastic Solutions for Soil and Rock Mechanics*, John Wiley and Sons, New York City, New York, pp. 1-2, 54, 66, and 162-164.

Read, D., S. Kalay, 1996, "Results of Phase II Heavy Axle Load Tests at FAST," *American Railway Engineering Association Bulletin*, v 97, bulletin 757, Washington, DC, pp. 467-476.

Reiff, R., 1995, "An Evaluation of Remediation Technologies for Concrete Tie Rail Seat Abrasion in the FAST Environment," *American Railway Engineering Association Bulletin*, v 96, bulletin 753, Washington, DC, pp. 406-418.

Reiff, R., 2009a, "Evaluation of Concrete Tie Rail Seat Abrasion Detection/Measurement Systems," AAR Research Report RS-09-001.

Reiff, R., 2009b, email correspondence, Richard Reiff was a Principal Engineer for the Transportation Technology Center, Inc. when this research was conducted, 11 February.

Riehl, W., 2008, interview, William Riehl was the Director of Structures for RailAmerica, Inc. when this research was conducted, 27 October.

Sahu, S., N. Thaulow, 2004, "Delayed Ettringite Formation in Swedish Concrete Railroad Ties," *Cement and Concrete Research*, v 34, no. 9, pp. 1675-1681.

Schoch, W., A. Frick, 2007, "Development of the Grinding Practice at Malmbanan," *Proceedings of the International Heavy Haul Association Specialist Technical Session*, International Heavy Haul Association, Kiruna, Sweden, 11-13 June, pp. 245-254.

Selig, E.T., D. Li, 1994, "Track Modulus: Its Meaning and Factors Influencing It," *Transportation Research Record*, v 1470, pp. 47-54.

Senbetta, E., G.A. Malchow Jr., 1987, "Studies on Control of Durability of Concrete through Proper Curing," *Concrete Durability: Proceedings of Katharine and Bryant Mather International Symposium*, American Concrete Institute (ACI) Special Publication 100-7, pp. 73-88.

Signore, J.M., M.G. Abdel-Maksoud, B.J. Dempsey, 1997, "Fiber-optic Sensing Technology for Rail-buckling Detection," *Transportation Research Record*, v 1584, pp. 41-45.

Stamatis, D.H., 1995, *Failure Mode and Effect Analysis: FMEA from Theory to Execution*, American Society for Quality (ASQ) Quality Press, Milwaukee, Wisconsin, pp. xix-xxviii and 1-83.

Sustersic, J., E. Mali, S. Urvancic, 1991, "Erosion-Abrasion Resistance of Steel Fiber Reinforced Concrete," *Durability of Concrete: Second International Conference*, American Concrete Institute Special Publication 126-39, pp. 729-744.

Terzaghi, K., R.B. Peck, G. Mesri, 1996, *Soil Mechanics in Engineering Practice*, 3rd ed., John Wiley and Sons, Inc., New York City, New York, pp. 125 and 184.

Thomas, P., 2009, "Construction of New Iron Ore Line in Australia," fourth keynote presentation at the opening ceremony of the 9th International Heavy Haul Conference, Shanghai, China, 21-24 June.

Trainiax.net, 2010, "Johnstown America Bethgon II Coalporter, later version," rail car drawing, online reference, URL: http://trainiax.net/me55-rs.php.

Unsworth, J., 2003, "Heavy Axle Load (HAL) Effects on Fatigue Life of Steel Bridges," *Proceedings of the 83rd Transportation Research Board Annual Meeting Annual Meeting*, Washington, DC, January.

Wamani, W.T., C. Villar, 2009, "Aurora Automated Railroad Tie Condition Assessment System: The Quest for Accuracy," *AREMA Conference Proceedings 2009*, American Railway Engineering and Maintenance-of-way Association (AREMA), Landover, Maryland.

Weber, J.W., 1969, "Concrete Crossties in the United States," *Prestressed Concrete Institute Journal*, v 14, no. 1, pp. 46-57.

Weed, D., C. Lonsdale, 2004, "Review and Analysis of Wheel Impact Load Detector (WILD) and Wheel Removal Data," *Proceedings of the 2004 Mechanical Association Railcar Technical Services (MARTS) Technical Conference*.

White, J.G., 1984, "Concrete Tie Track System," *Transportation Research Record*, v 953, pp. 5-11.

Wight, J.K, J.G. MacGregor, 2009, *Reinforced Concrete: Mechanics and Design*, 5th ed., Pearson Prentice Hall, Upper Saddle River, New Jersey, p. 47.

Woodhead, H.R., 1991, "Barges Topped with Abrasion Resistant Concrete," *Durability of Concrete: Second International Conference*, American Concrete Institute (ACI) Special Publication 126-63, pp. 1185-1196.

Zeman, J.C., J.R. Edwards, C.P.L. Barkan, D.A. Lange, 2009a, "Failure Mode and Effect Analysis of Concrete Ties in North America," *Proc. of the 9th International Heavy Haul Conference*, Shanghai, China, June, pp. 270-278.

Zeman, J.C., J.R. Edwards, C.P.L. Barkan, D.A. Lange, 2009b, "Investigating the Role of Moisture in Concrete Tie Rail Seat Deterioration," *AREMA Conference Proceedings 2009*, American Railway Engineering and Maintenance-of-way Association (AREMA), Landover, Maryland.

Zeman, J.C., J.R. Edwards, C.P.L. Barkan, D.A. Lange, 2010a, "Investigation of Potential Concrete Tie Rail Seat Deterioration Mechanisms: Cavitation Erosion and Hydraulic Pressure Cracking," *Proceedings of the Transportation Research Board 89th Annual Meeting*, Washington, DC, January.

Zeman, J.C., J.R. Edwards, C.P.L. Barkan, D.A. Lange, 2010b, "Evaluating the Potential for Damaging Hydraulic Pressure in the Concrete Tie Rail Seat," *Proceedings of the 2010 Joint Rail Conference,* Urbana, Illinois, April.

Zeman, J.C., J.R. Edwards, C.P.L. Barkan, D.A. Lange, 2010c, "Sealing Characteristics of Tie Pads on Concrete Crossties," *AREMA Conference Proceedings 2010*, American Railway Engineering and Maintenance-of-way Association (AREMA), Landover, Maryland.

Zhang, T., R.L. Armstrong, J. Smith, 2003, "Investigation of the Near-Surface Soil Freeze-Thaw Cycle in the Contiguous United States: Algorithm Development and Validation," *Journal of Geophysical Research*, v 108, no. D22 8860, pp. 21-1 – 21-14.

Zhixiu, G., 2009, "Innovation in Practice and Development of Da-Qin Railway," second keynote presentation at the opening ceremony of the 9th International Heavy Haul Conference, Shanghai, China, 21-24 June.

APPENDIX A: SUMMARY OF CONCRETE TIE SURVEY RESULTS

1) What are the most critical problems with concrete ties on your railroad?

Major Railroads:

- Insulator and pad wear out resulting in concrete abrasion.
- Rail seat abrasion. Concrete tie shoulder becoming loose or breaking off. Derailment damage. Tie ends breaking off.
- Rail seat abrasion; loss of toe load due to rail seat abrasion and due to failure of pads
- Shoulder and insulator wear; cracking (weak tensile strength of concrete)
- There are several problems with concrete ties on [our railroad]. I firmly believe that concrete ties should not be utilized unless MGT's are in excess of 150; or, the line is operated by passenger trains in excess of 100 miles per hour. Concrete ties for the initial costs, coupled with the ongoing maintenance expectations such as (1) rail seat abrasion, (2) continual surfacing, (3) complete foul ballast and mud removal, (4) repetitive rail grinding, (5) continual fastener monitoring, (6) gage correction, (7) derailment repair, are not the best economical solution for [us]. The most critical problem with concrete ties is supporting these maintenance expectations which are more costly and labor intensive than wood ties.
- Tie breakage.

Regional and Shortline Railroads:

- The majority of [our] ties are legacy design ... These ties have incredible concrete strength but relatively low pretension stress which leads to rail seat positive bending failure. Additionally, these ties use a bolted fastener that is poor in accommodating lateral load. Conversely, these ties have virtually no railseat abrasion after 30-40 years in service … Creation of mud in the ballast section.
- Ties are aging and some are first generation ties and the fastening systems are broken and repair parts not available.

Commuter Agencies and Transit Authorities:

- Broken (cracked) ties not been able to be replaced without incurring high expenses.
- Concrete Ties were first installed on [our track] approximately 10 years ago. Because of the light loads associated with a Passenger Service environment we have not had any critical problems. One downfall with Concrete Ties is that it is very difficult to handle as opposed to wood and remove and replace in an emergency situation. But as a whole, many of the benefits of Concrete Ties far outweigh the negatives
- Premature failure
- Very few problems directly with concrete ties. The fastening systems including the pads and insulators fail prematurely in some cases.

2)   **When concrete ties require maintenance or replacement in your track,
        what are the most common reasons?**

The following table summarizes the rank assigned to each concrete tie problem based on the average
ranking value from each group of responses. Participants responded to the survey by indicating "1" as the
most critical to "8" as the least critical problems. Some participants left some spots blank. It was
assumed that the intended meaning was that these problems were not issues for that participant. To give a
blank response the meaning of least critical, the ranking variables were inverted, making 8.00 the most
critical and 0.00 the least. For example, the average responses from all survey participants ranked
"shoulder / fastener wear or fatigue" as the most critical problem because it had the highest average
ranking value of 5.75.

Table A.1 Rankings assigned to concrete tie problems by different groups

Concrete Tie Problems	Rank (Average Value)			
	All Responses	**Major Railroads**	**Regional & Shortline**	**Commuter & Transit**
Cracking from environmental or chemical degradation	**8** (1.63)	**8** (1.25)	**5** (3.00)	**6** (1.50)
Cracking from dynamic loads	**7** (2.00)	**5** (1.83)	**--** (0.00)	**4** (3.25)
Cracking from center binding	**3** (3.71)	**4** (4.58)	**3** (3.50)	**5** (2.50)
Rail seat deterioration (RSD)	**2** (3.75)	**1** (6.83)	**--** (0.00)	**7** (1.00)
Shoulder/ fastener wear or fatigue	**1** (5.75)	**2** (6.67)	**1** (6.50)	**3** (4.00)
Derailment damage	**4** (3.25)	**3** (4.83)	**3** (3.50)	**8** (0.75)
Tamping damage	**5** (3.00)	**5** (1.83)	**2** (4.00)	**2** (4.25)
Other (ex: manufactured defect, installation damage)	**6** (2.50)	**7** (1.33)	**--** (0.00)	**1** (5.50)

3) What specifically do you do to repair distressed, worn, or damaged concrete ties in track?

Major Railroads:

- Fill abrasion with…urethane and install new pads & insulators. Cast steel plates installed on sharp curves. Broken ties replaced with new concrete or wood depending on amount.
- Really there are only about two repairs that we try to do. First is the repair of any RSA. This is typically done in conjunction with any rail replacement. The other is some different types of repairs to shoulders as they wear.
- Replace worn or damage pads; apply…epoxy on rail seat to bring back to original profile
- [We have] very limited amount of concrete ties in track. Other than making corrections on concrete ties from rail seat abrasion, [we have] historically removed concrete ties out of face from track after noticeable wear, damage or failure to perform.
- We level the rail seat to establish the proper cant. We may also place stainless steel shoulder face to establish the shoulder face again. We always place new clips, pads and clips.
- We use epoxy or polyurethane to repair rail seats. Method too slow requires 5 to 6 hours track time. We have discontinued using this process and are exploring other options to repair rail seat abrasion. Almost all other damages we replace the tie.

Regional and Shortline Railroads:

- Tighten bolts / replace insulators…Replace them.
- We have very few concrete ties and if the tie fails it is removed and replaced with a wood tie

Commuter and Transit Authorities:

- Replace
- No concrete ties replaced to date after being accepted and placed in service. The fasteners, insulators and pads have been replaced
- It really depends what the problem is. On the standard 8'3" we have not had any concrete ties that have worn out to date. We have some standard and switch ties impacted by the tamper or other equipment. We have successfully replaced shoulders in the rail bearing areas using procedures developed jointly by concrete tie and cast shoulder manufacturers. Parts of concrete that has chipped out is typically been reset using epoxy. One major concern is water getting into cracks and chipped areas and the exposure of the wire tendons to the elements. Since we do not have freeze and thaw type temperatures on a "normal basis" our environment is considered very mild.
- Try to replace them with new ones.

4)   What would convince your railroad to use more concrete ties on your system?

Major Railroads:

- If concrete ties truly had the service life that was promised – 40 to 50 years – and that their use was supported by a realistic business case – one that recognized the reality that at some point maintenance will be required at possibly significant cost – that pads wear out and need to be replaced, that shoulders get worn, that the current concrete tie is subject to rail seat abrasion which must be repaired.
- Maybe major track expansion … where rot is high and curves gentle. Install cost would have to be competitive with wood due to wider spacing and expected longer life in high rot zone. [We] stopped using concrete ties a few years ago except for capacity projects due to on going rail seat problems.
- Money. We are doing a lot of concrete tie replacement. It is now pretty much economics.
- Nothing at the present time.
- Reduce the cost of the concrete tie system or an increase in cost of the wood ties……
- Solution of the rail seat problem and cost. Replacing insulators to control wide gauge issue is a major concern. Exploring material which will last longer thus increasing the replacement cycle will be very beneficial. Protecting rail seats and preventing rail Seat abrasion is extremely important.

Regional and shortline Railroads:

- Our system is entirely concrete on main tracks and sidings…Committed to concrete ties.
- We operate light tonnage railroad and see no economic benefit to using concrete

Commuter and Transit Authorities:

- Decrease in costs and improvements in the fastening system
- None. We are convinced that concrete ties are a good solution for at-grade and open cut ballasted tracks when compared with wood ties.
- Nothing. They are too heavy to mix with wood or plastic ties.
- We are pretty convinced based on the performance of our own concrete ties. If the initial price to procure and install became lower it makes the justification for concrete ties all that much easier.
- We have no concrete ties in the segment of [track] owned, operated and maintained by [our agency]. We don't generate the tonnage that makes them economical. We'd have to purchase new tie cranes for our production tie gangs to handle them. We run on a cycle (approx 7 year) basis for running a production tie gang through a territory. Intermixing concrete with timber just doesn't work because of the difference in track modulus. There are a few curves where we probably ought to use them. But in the mid $40 range for timber vs concrete cost and we can still get 30 years out of timber in open track, I don't think the justification is there. We're not all that thrilled with the elastic fasteners either. When they break they typically break in multiples. I know everybody out there is using them, but we are just a little bit leery.

5) **Would your railroad be willing to provide the University of Illinois research team with data on concrete tie use and performance? Information of interest includes amount of required maintenance, actual service life, and reasons for maintenance or replacement with the track location, curvature, grade, tonnage, and train speed.**

[Confidential responses]

6) **Would your railroad be willing to provide the University of Illinois research team with concrete tie design specifications and standards, including those that apply to the fastening assembly and standards on the maintenance and inspection of concrete ties?**

[Confidential responses]

7) **If your railroad has conducted its own research on concrete ties, would you be willing to share relevant information with the University of Illinois research team? If research has been conducted, what were the primary topics?**

[Confidential responses]

8) **Please rank the following areas of concrete tie research from most to least beneficial.**

The following table summarizes the rank assigned to each area of concrete tie research based on the average ranking value from each group of responses. As an example, an average of all responses ranked "fastener design" as the most beneficial area of research with the highest ranking value of 4.25 (see Question 2 for an explanation of the ranking value).

Table A.2 Rankings assigned to areas of concrete tie research by different groups

| Areas of Concrete Tie Research | Rank (Average Value) | | | |
	All Responses	Major Railroads	Regional & Shortline	Commuter & Transit
Fastener design: clips, insulators, inserts, tie pads	**1** (4.25)	**1** (3.83)	**1** (4.00)	**1** (5.00)
Materials design: concrete mix, prestress strand arrangement	**3** (2.96)	**3** (2.75)	**2** (3.00)	**3** (3.25)
Optimize tie design: spacing, cross-section, body shape, for specific uses (curves, grades, etc.)	**2** (3.00)	**4** (2.67)	**2** (3.00)	**2** (3.50)
Prevention of rail seat deterioration (RSD) or repair of abraded ties	**4** (2.75)	**2** (3.67)	**2** (3.00)	**5** (1.25)
Track system design: determining the track service environment and required tie characteristics	**5** (1.79)	**5** (1.58)	**5** (2.00)	**4** (2.00)

APPENDIX B: MATLAB CODE FOR MODELS AND DATA PROCESSING

B.1　　Track Motion Model

```matlab
% By Lingfei Zhang and John Zeman
% Talbot's equation for track deflection
% March 2010

% "talbot.m"

clear all; close all;
syms t real
P = 40000; % wheel load, lbs
I = 94.9; % rail moment of inertia, in4
u = 8000; % track modulus, lb/in/in
E = 30*10^6; % Young's modulus of the rail
l = (u/(4*E*I))^.25; % damping term
v = 60; % train speed, mph
v = v*5280/3600*12; % train speed converted to in/s
x = v*t-v/3; % position along the track as a function of time, with an x0
offset of v/3

% Sixteen axles, from four 50-foot cars
% Using the following spacing per car: 3ft-axle-6ft-axle-32ft-axle-6ft-
axle-3ft
% The following offsets are in inches
x01 = x - 0;
x02 = x - 6*12;
x03 = x - 38*12;
x04 = x - 44*12;
x05 = x - 50*12;
x06 = x - 56*12;
x07 = x - 88*12;
x08 = x - 94*12;
x09 = x - 100*12;
x10 = x - 106*12;
x11 = x - 138*12;
x12 = x - 144*12;
x13 = x - 150*12;
x14 = x - 156*12;
x15 = x - 188*12;
x16 = x - 194*12;

% Vertical track deflection under each axle, in
z01 = (P/((64*E*I*u^3)^.25))*(exp(-abs(-l*x01)))*(cos(abs(l*x01))
+sin(abs(l*x01)));
z02 = (P/((64*E*I*u^3)^.25))*(exp(-abs(-l*x02)))*(cos(abs(l*x02))
+sin(abs(l*x02)));
z03 = (P/((64*E*I*u^3)^.25))*(exp(-abs(-l*x03)))*(cos(abs(l*x03))
+sin(abs(l*x03)));
z04 = (P/((64*E*I*u^3)^.25))*(exp(-abs(-l*x04)))*(cos(abs(l*x04))
+sin(abs(l*x04)));
z05 = (P/((64*E*I*u^3)^.25))*(exp(-abs(-l*x05)))*(cos(abs(l*x05))
+sin(abs(l*x05)));
z06 = (P/((64*E*I*u^3)^.25))*(exp(-abs(-l*x06)))*(cos(abs(l*x06))
+sin(abs(l*x06)));
```

```matlab
    z07 = (P/((64*E*I*u^3)^.25))*(exp(-abs(-l*x07)))*(cos(abs(l*x07))
+sin(abs(l*x07)));
    z08 = (P/((64*E*I*u^3)^.25))*(exp(-abs(-l*x08)))*(cos(abs(l*x08))
+sin(abs(l*x08)));
    z09 = (P/((64*E*I*u^3)^.25))*(exp(-abs(-l*x09)))*(cos(abs(l*x09))
+sin(abs(l*x09)));
    z10 = (P/((64*E*I*u^3)^.25))*(exp(-abs(-l*x10)))*(cos(abs(l*x10))
+sin(abs(l*x10)));
    z11 = (P/((64*E*I*u^3)^.25))*(exp(-abs(-l*x11)))*(cos(abs(l*x11))
+sin(abs(l*x11)));
    z12 = (P/((64*E*I*u^3)^.25))*(exp(-abs(-l*x12)))*(cos(abs(l*x12))
+sin(abs(l*x12)));
    z13 = (P/((64*E*I*u^3)^.25))*(exp(-abs(-l*x13)))*(cos(abs(l*x13))
+sin(abs(l*x13)));
    z14 = (P/((64*E*I*u^3)^.25))*(exp(-abs(-l*x14)))*(cos(abs(l*x14))
+sin(abs(l*x14)));
    z15 = (P/((64*E*I*u^3)^.25))*(exp(-abs(-l*x15)))*(cos(abs(l*x15))
+sin(abs(l*x15)));
    z16 = (P/((64*E*I*u^3)^.25))*(exp(-abs(-l*x16)))*(cos(abs(l*x16))
+sin(abs(l*x16)));

    % Superposition of all individual deflection terms, in
    z = z01 + z02 + z03 + z04 + z05 + z06 + z07 + z08 + z09 + z10 + z11 + z12
+ z13 + z14 + z15 + z16;

    t = 0:0.005:3; % vector of time for 0 to 3 seconds
    z = subs(z,t);
    dt = t(2:length(t));
    zdot = diff(z)./diff(t); % numerical differentiation for vertical track
velocity, in/s
    ddt = dt(2:length(dt));
    zdotdot = diff(zdot)./diff(dt)./117.72; % numerical differentiation for
vertical track acceleration, g

    subplot(3,1,1)
    plot(t,z)
    set(gca,'YDir','reverse');
    title('')
    axis tight
    xlabel('Time (t)','FontSize',16);
    ylabel('Deflection (in)','FontSize',16);
    title('\it{Rail Deflection}','FontSize',16);
    subplot(3,1,2)
    plot(dt,zdot)
    set(gca,'YDir','reverse');
    title('')
    axis tight
    xlabel('Time (t)','FontSize',16);
    ylabel('Velocity (in/s)','FontSize',16);
    title('\it{Rail Velcoity}','FontSize',16);
    subplot(3,1,3)
    plot(ddt,zdotdot)
    set(gca,'YDir','reverse');
    title('')
    axis tight
    xlabel('Time (t)','FontSize',16);
```

189

```matlab
    ylabel('Acceleration (g)','FontSize',16);
    title('\it{Rail Acceleration}','FontSize',16);
```

B.2   Effective Stress Model

```matlab
% An adaptation of Bakharev's approach to find the effective stress in a
% concrete tie, using Holl's expressions for a loaded rectangular area,
% with v = 0.5, and under the corner of the loaded area (here I split the
% loaded area into 4 equal areas for the center)
% Also includes contributions from the prestressed beam on an elastic
% foundation model

% "bakharev.m"

% John Zeman
% Winter 2009-2010
% University of Illinois at Urbana-Champaign

clear all; close all;

syms x y z sigv sigh P real

% coordinates here are z as vertical, y as the axis of the tie, and x as
% the axis of the rail

% Bakharev's pore water pressure model
w = 6.5; % assumed width of the rail seat
p = 1; % set surface pressure as 1 psi for now, then multiply later by p
Q1x = atan(x./z);
Q2x = atan((x-w)./z);
Q1y = atan(y./z);
Q2y = atan((y-w)./z);
ux = p/2/pi.*(Q1x-Q2x); % porewater pressure in xz plane, assuming Darcy flow
uy = p/2/pi.*(Q1y-Q2y);
u = ux+uy; % porewater pressure in 3-D, superposition of xz and yz planes

% Considering the center of the rail seat
x = w/2;
y = w/2;
u = subs(u);
l = w/2; % half of the width of the rail seat
b = w/2; % half of the width of the rail seat

% Holl's radial distance terms
R1 = sqrt(l^2+z^2);
R2 = sqrt(b^2+z^2);
R3 = sqrt(l^2+b^2+z^2);

% Holl's equations for uniform vertical load (taken from Poulos and Davis,
1974), multiplying each by
% 4 to apply superposition:
sigzV = 4*sigv/2/pi*(atan(l*b/z/R3)+l*b*z/R3*(1/R1^2+1/R2^2));
sigxV = 4*sigv/2/pi*(atan(l*b/z/R3)-l*b*z/R1^2/R3);
```

```matlab
sigyV = 4*sigv/2/pi*(atan(l*b/z/R3)-l*b*z/R2^2/R3);
tauxzV = 4*sigv/2/pi*(b/R2-z^2*b/R1^2/R3);
tauyzV = 4*sigv/2/pi*(l/R1-z^2*l/R2^2/R3);
tauxyV = 4*sigv/2/pi*(1+z/R3-z*(1/R1+1/R2));
SV = [sigxV tauxyV tauxzV; tauxyV sigyV tauyzV; tauxzV tauyzV sigzV]; %
contributions of vertical load to total stress

% Holl's equations for uniform horizontal load (taken from Poulos and
% Davis, 1974), multiplying each by 4 to apply superposition:
% From Holl, with horizontal load in positive x-direction, with z downward:
sigzH = 4*sigh/2/pi*(b/R2-z^2*b/R1^2/R3);
sigxH = 4*sigh/pi*(log((R1*(b+R2))/(z*(b+R3)))-l^2*b/2/R1^2/R3);
sigyH = 4*sigh/2/pi*(log((R1*(b+R2))/(z*(b+R3)))-b*(1/R2-1/R3));
tauxzH = 4*sigh/2/pi*(atan(l*b/z/R3)-l*b*z/R1^2/R3);
tauyzH = 4*sigh/2/pi*(1+z/R3-z*(1/R1+1/R2));
tauxyH = 4*sigh/2/pi*(log((R1+l)*(R3-l)/z/R2)+l*(1/R3-1/R1));
SH = [sigxH tauxyH tauxzH; tauxyH sigyH tauyzH; tauxzH tauyzH sigzH]; %
contributions of horizontal load to total stress
% But our coordinates have the horizontal load in the negative y-direction,
% with z downward
A = [0 1 0; -1 0 0; 0 0 1]; % Transformation map to go from Holl's
coordinates to our coordinates (rotation of -90 deg)
SH = A*SH*A.'; % Transformed horizontal load contributions

% Model of a prestressed Timoshenko beam on an elastic foundation
% Copy and paste outputs from the "galerkin" code as functions of z and P
% This is just one example of the stresses resulting from the beam model
% Different conditions will yield different stress functions
% Because it was found that SB has little effect on the damage limits,
% this example case was used
sigyB = (.52888067533518464510343162642709e-2*P-
267.46073931812952544171560376090)*(2.7273-z)+2000;
tauyzB = -.22180863799453304382213777871663e-
2*P+2.9548366557245037510923520086;
SB = [0 0 0; 0 sigyB tauyzB; 0 tauyzB 0]; % contributions of bending and
prestress to total stress, psi

% Assemble the total stress matrix:
Sxyz = SV+SH+SB;

P0 = [20000 30000 40000 50000 60000]; % applied vertical loads, kips
L_V = 0.52; % the assumed L/V (lateral/vertical loads) ratio
H0 = L_V.*P0;
SIGV = P0./w^2; % uniformly applied vertical load, psi
SIGH = H0./w^2; % uniformly applied horizontal load, psi
Z = [0.1 0.25 0.5 0.75 1 1.5 2 3 4 5 6 6.5]; % depths below rail seat
surface, inches

% Create empty matrices to fill in the following "for" loop
m = length(Z);
n = length(SIGV);
Ustr1 = zeros(m,n);
Ufat1 = zeros(m,n);
Ustr2 = zeros(m,n);
Ufat2 = zeros(m,n);
Ustr3 = zeros(m,n);
```

```matlab
Ufat3 = zeros(m,n);
U = zeros(m,1);
S1 = zeros(m,n);
S2 = zeros(m,n);
S3 = zeros(m,n);
Sxx = zeros(m,n);
Syy = zeros(m,n);
Szz = zeros(m,n);
Sxy = zeros(m,n);
Syz = zeros(m,n);
Sxz = zeros(m,n);

fc = 7000; % the assumed compressive strength of concrete, psi

for j = 1:length(SIGV) % "j" serves as the applied load index
    sigv = SIGV(j);
    sigh = SIGH(j);
    P = P0(j);
    for i = 1:length(Z) % "i" serves as the depth index
        z = Z(i);
        S = subs(Sxyz);
        [V,D] = eig(S); % V is a matrix of the normalized eigenvectors, while
D contains the eigenvalues
        d = max(D) + min(D); % vector of the principal stresses
        S1(i,j) = max(d); % major principal stress
        S2(i,j) = median(d); % intermediate principal stress
        S3(i,j) = min(d); % minor principal stress
        Sxx(i,j) = S(1,1); % normal stress in x direction
        Syy(i,j) = S(2,2); % normal stress in y direction
        Szz(i,j) = S(3,3); % normal stress in z direction
        Sxy(i,j) = S(1,2); % shear stress with xy orientation
        Syz(i,j) = S(2,3); % shear stress with yz orientation
        Sxz(i,j) = S(1,3); % shear stress with xz orientation
        Ustr3(i,j) = min(d)+fc*0.1; % strength limit using S3
        Ufat3(i,j) = min(d)+fc*0.05; % fatigue limit using S3
        U(i) = subs(u);
    end
    % plots of a family of pore pressure curves
    figure(j) % creates a new figure for each applied load
    plot(250*U,Z);
    hold on
    plot(500*U,Z);
    plot(750*U,Z);
    plot(1000*U,Z);
    plot(1250*U,Z);
    plot(1500*U,Z);
    plot(1750*U,Z);
    plot(2000*U,Z);
    % plots of the pore pressure damage limits
    plot(Ustr3(:,j),Z,'r'); % strength limit
    plot(Ufat3(:,j),Z,'g'); % fatigue limit
    % plots of the stress or the principal stress with depth
    % (currently shows the shear stress, Sxy, Syz, Sxz)
    figure(10)
    plot(Sxy(:,j),Z);
    hold on
```

```matlab
    figure(11)
    plot(Syz(:,j),Z);
    hold on
    figure(12)
    plot(Sxz(:,j),Z);
    hold on
end
```

B.3   Beam on an Elastic Foundation – Galerkin Model

```matlab
% Model of a Timoshenko beam on an elastic foundation.
% Represents a prestressed concrete tie, with vertical loads.
% Applies the Galerkin Method, an approximate solution to the virtual work
% equations, following Keith Hjelmstad's Fundamentals of Structural
% Mechanics, 2nd ed.

% "galerkin.m"
% John Zeman
% March 2010
% University of Illinois at Urbana-Champaign


close all; clear all;
syms y real % y is the axis of the tie

% Define the constants (the base case is given)
    l = 102; % length of the tie, in
    As = 100; % area of the shoulder section, in2
    Is = 700; % moment of inertia of the shoulder section, in4
    Am = 80; % area of the mid-section, in2
    Im = 360; % moment of inertia of the mid-section, in4
    fpc = 2000; % precompression, psi
    bt = 11; % base width of the tie, in
    P = 40000; % applied rail seat load, lbs
    h1 = 12; % height of the ballast layer, in
    h2 = 6; % height of the subballast layer, in
    E1 = 40000; % resilient modulus of the ballast layer, psi
    E2 = 20000; % resilient modulus of the subballast layer, psi
    E3 = 6000; % resilient modulus of the subgrade, psi
    vf = 0.2; % Poisson's ratio for the foundation
    Cs = 1.0; % factor for reducing the shoulder-section foundation modulus
    Cm = 1.0; % factor for reducing the mid-section foundation modulus
    vc = 0.2; % Poisson's ratio for the concrete
    E = 4800000; % modulus of elasticity for the tie, psi
    Ni = fpc*As; % nominal axial precompression force at shoulder-section,
lbs
    Nii = fpc*(Am+As)/2; % nominal axial precompression force at transition
of sections, lbs
    dw = 5/25.4; % diameter of wire or strand, mm converted to in
    br = 6; % rail base width, in
    ls = (l-60)/2; % length of shoulder (end of tie to center of rail seat)
    lm = 36; % length of smaller mid-section
    le = l/2-ls-lm/2; % length from center of rail seat to shorter section in
tie center
    e0 = 0.25; de = -0.25; % initial eccentricity and change in eccentricity
from shoulder to center
    ld = 60*dw; % approx. development length of prestress
```

193

```matlab
    G = E/(2*(1+vc)); % shear modulus, psi (assuming a v = 0.2 for concrete)
    % Approximating the transition of A and I from shoulder to mid-section
    % The transition occurs between 3-in before and 6-in after the edge
    % of the mid-section
    AyL = (Am-As)/9*(y-(l-lm)/2+3)+As; AyR = (As-Am)/9*(y-(l+lm)/2-6)+Am;
    hs = (As/bt); hm = Am/bt;
    hyL = (hm-hs)/9*(y-(l-lm)/2+3)+hs; hyR = (hs-hm)/9*(y-(l+lm)/2-6)+hm;
    IyL = (hyL/hs)^3*Is; IyR = (hyR/hm)^3*Im;

    % Odemark's method for approximating the effective modulus of a
    % three-layer foundation
    aeff = sqrt(l*bt/pi); % the radius of a circle with equal area to the
bottom of the tie
    T = h1+h2; % granular layer thickness, in
    Em = (E1+E2+E3)/3; % guess a value for Em, effective modulus for the
foundation, psi
    error = 1;
    N1 = 0.9*h1/T;
    count = 0;
    while abs(error) > 0.01
        Q = Em;
        N2 = N1*(E1/Em)^(1/3);
        N21 = N2+0.9*h2/T;
        N3 = N2+0.9*h2/T*(E2/E3)^(1/3);
        Em = E3 / (sqrt((1+N2^2*(T/aeff)^2)/(1+N3^2*(T/aeff)^2))+E3/E2*(1-
sqrt((1+N2^2*(T/aeff)^2)/(1+N21^2*(T/aeff)^2)))); % effective modulus for the
foundation, psi
        error = Em-Q;
        count = count + 1;
    end
    Efs = Cs*Em; % shoulder-section foundation modulus
    Efm = Cm*Em; % mid-section foundation modulus
    % Vesic and Johnson's method for approximating the effective spring
    % stiffness of the elastic foundation
    ks = 0.65*Efs/(1-vf)^2*sqrt(Efs*bt^4/E/Is); % shoulder-section stiffness
in psi
    km = 0.65*Efm/(1-vf)^2*sqrt(Efm*bt^4/E/Im); % mid-section stiffness in
psi

        % Applied Loads
        q1 = -P/br; % distributed rail seat load, lb/in
%         q2s = ks*w; % shoulder-section foundation reaction, lb/in
%         q2m = km*w; % mid-section foundation reaction, lb/in
        % Applied moment from prestress, split into piecewise components, lb-
in/in
        m1 = Ni*e0/ld; % development of the full prestress on the shoulders
        m2 = -Nii/le*(2*e0+de); % change in the eccentricity inside the rail
seats

        % Ritz Approximation
        o = pi*y/l;
%         a = [a0;a1;a2;a3;a4]; % Coefficients for w
        h = [1;sin(o);sin(3*o);sin(5*o);sin(7*o)]; % shape function for
deflection
        g = [1;cos(o);cos(3*o);cos(5*o);cos(7*o)]; % shape function for
rotation
```

```matlab
%          w = a'*h; % vertical displacement, in
%          q2s = subs(q2s);
%          q2m = subs(q2m);
        dh = diff(h,y);
        dg = diff(g,y);
        Kaa = int(G.*As.*dh*dh',y,0,(l-lm)/2-3)+int(G.*AyL.*dh*dh',y,(l-
lm)/2-3,(l-lm)/2+6)+int(G.*Am.*dh*dh',y,(l-lm)/2+6,(l+lm)/2-6)...
            +int(G.*AyR.*dh*dh',y,(l+lm)/2-
6,(l+lm)/2+3)+int(G.*As.*dh*dh',y,(l+lm)/2+3,l);
        Kab = -int(G.*As.*dh*g',y,0,(l-lm)/2-3)-int(G.*AyL.*dh*g',y,(l-lm)/2-
3,(l-lm)/2+6)-int(G.*Am.*dh*g',y,(l-lm)/2+6,(l+lm)/2-6)...
            -int(G.*AyR.*dh*g',y,(l+lm)/2-6,(l+lm)/2+3)-
int(G.*As.*dh*g',y,(l+lm)/2+3,l);
        Kba = -int(G.*As.*g*dh',y,0,(l-lm)/2-3)-int(G.*AyL.*g*dh',y,(l-lm)/2-
3,(l-lm)/2+6)-int(G.*Am.*g*dh',y,(l-lm)/2+6,(l+lm)/2-6)...
            -int(G.*AyR.*g*dh',y,(l+lm)/2-6,(l+lm)/2+3)-
int(G.*As.*g*dh',y,(l+lm)/2+3,l);
        Kbb = int(E.*Is.*dg*dg'+G.*As.*g*g',y,0,(l-lm)/2-
3)+int(E.*IyL.*dg*dg'+G.*AyL.*g*g',y,(l-lm)/2-3,(l-lm)/2+6)...
            +int(E.*Im.*dg*dg'+G.*Am.*g*g',y,(l-lm)/2+6,(l+lm)/2-
6)+int(E.*IyR.*dg*dg'+G.*AyR.*g*g',y,(l+lm)/2-6,(l+lm)/2+3)...
            +int(E.*Is.*dg*dg'+G.*As.*g*g',y,(l+lm)/2+3,l);
%          faL = int(q2s.*h,y,0,(l/2-lm/2))+int(q2m.*h,y,(l/2-
lm/2),(l/2+lm/2))+int(q2s.*h,y,(l/2+lm/2),l);
        faR = int(q1.*h,y,(ls-br/2),(ls+br/2))+int(q1.*h,y,(l-(ls+br/2)),(l-
(ls-br/2)));
        fb = int(m1.*g,y,0,ld)+int(m2.*g,y,(ls+br/2),(ls+br/2+le))+int(-
m2.*g,y,(l-(ls+br/2+le)),(l-ls-br/2))+int(-m1.*g,y,(l-ld),l);
%          faL = simple(faL);
%          faL


        % Use the output from "faL" to manually create "FaL", since it is a
        % function of the coefficients a0,...,a5
        % FaL only changes if the shape function for h(y) changes or if the
number
        % of terms included in h(y) changes


%      % the influence of the foundation reaction on the stiffness matrix

X = pi/l*lm; D01 = sin(1/2*X); D02 = sin(3/2*X); D03 = sin(5/2*X); D04 =
sin(7/2*X);
D05 = sin(X); D06 = sin(2*X); D07 = sin(3*X); D08 = sin(4*X); D09 = sin(5*X);
D10 = sin(6*X); D11 = sin(7*X);


A11 =105*ks*pi-105*ks*X+105*km*X;
A12 =-210*ks*D01+210*ks+210*km*D01;
A13 =+70*ks*D02+70*ks-70*km*D02;
A14 = -42*ks*D03+42*ks+42*km*D03;
A15 =+30*ks*D04 +30*ks -30*km*D04;
A1 = 1./105.*[A11 A12 A13 A14 A15];


A21 = -48*ks*D01+48*ks+48*km*D01;
A22 =+12*ks*pi-12*ks*X-12*ks*D05+12*km*D05+12*km*X;
A23 =+12*ks*D05+6*ks*D06-6*km*D06-12*km*D05;
A24 = -4*ks*D07-6*ks*D06+4*km*D07+6*km*D06;
A25 =+3*ks*D08 +4*ks*D07 -3*km*D08 -4*km*D07;
```

```
A2 = 1./24.*[A21 A22 A23 A24 A25];


A31 =+80*ks*D02+80*ks-80*km*D02;
A32 =+60*ks*D05+30*ks*D06-30*km*D06-60*km*D05;
A33 =+60*ks*pi-60*ks*X-20*ks*D07+20*km*D07 +60*km*X;
A34 = 15*ks*D08+60*ks*D05-60*km*D05-15*km*D08;
A35 =-30*ks*D06 -12*ks*D09 +12*km*D09 +30*km*D06;
A3 = 1./120.*[A31 A32 A33 A34 A35];


A41 =-48*ks*D03+48*ks+48*km*D03;
A42 =-30*ks*D06-20*ks*D07+20*km*D07+30*km*D06;
A43 =+60*ks*D05+15*ks*D08-60*km*D05-15*km*D08;
A44 = -60*ks*X+60*ks*pi-12*ks*D09+60*km*X+12*km*D09;
A45 =+60*ks*D05 +10*ks*D10 -60*km*D05-10*km*D10;
A4 = 1./120.*[A41 A42 A43 A44 A45];


A51 =+240*ks+240*ks*D04-240*km*D04;
A52 =+140*ks*D07+105*ks*D08-140*km*D07-105*km*D08;
A53 =-210*ks*D06-84*ks*D09+210*km*D06+84*km*D09;
A54 = +420*ks*D05+70*ks*D10-420*km*D05-70*km*D10;
A55 =+420*ks*pi-420*ks*X -60*ks*D11 +420*km*X +60*km*D11;
A5 = 1./840.*[A51 A52 A53 A54 A55];


FaL = l./pi.*[A1;A2;A3;A4;A5];


        Kaa = Kaa + FaL; % The foundation reaction supplements the stiffness
term Kaa


        % Solution
        K = vpa([Kaa Kab; Kba Kbb]); % "Stiffness" matrix
        f = vpa([faR;fb]); % "Force" matrix
        c = simple(K\f); % Solution for the coefficients
        a = c(1:length(h)); % deflection coefficients
        b = c(length(h)+1:length(c)); % rotation coefficients
        w = a'*h; % Vertical displacement, in
        th = b'*g; % In-plane rotation, rad
        Qs = -G.*As.*(diff(w,y)-th)./1000; % shoulder shear, kips
        Ms = E.*Is.*diff(th,y)./1000; % shoulder moment, kip-inches
        QyL = -G.*AyL.*(diff(w,y)-th)./1000; % left transition shear, kips
        MyL = E.*IyL.*diff(th,y)./1000; % left transition moment, kip-inches
        Qm = -G.*Am.*(diff(w,y)-th)./1000; % mid shear, kips
        Mm = E.*Im.*diff(th,y)./1000; % mid moment, kip-inches
        VyR = -G.*AyR.*(diff(w,y)-th)./1000; % right transition shear, kips
        MyR = E.*IyR.*diff(th,y)./1000; % right transition moment, kip-inches
        q2s = w.*ks./bt; % shoulder ballast pressure, psi
        q2m = w.*km./bt; % mid ballast pressure, psi

        % Plots
        figure(1)
        subplot(1,2,1)
        ezplot(q2s, [0 (l-lm)/2])
        title('Ballast Pressure, q_2 (psi)')
        xlabel('y (in)')
        subplot(1,2,2)
        ezplot(q2m, [(l-lm)/2 l/2])
```

```matlab
        title('Ballast Pressure, q_2 (psi)')
        xlabel('y (in)')
        figure(2)
        subplot(2,3,1)
        ezplot(Qs, [0 ((l-lm)/2-3)])
        title('Shear, Q (k)')
        xlabel('y (in)')
        subplot(2,3,2)
        ezplot(QyL, [((l-lm)/2-3) ((l-lm)/2+6)])
        title('Shear, Q (k)')
        xlabel('y (in)')
        subplot(2,3,3)
        ezplot(Qm, [((l-lm)/2+6) (l/2)])
        title('Shear, Q (k)')
        xlabel('y (in)')
        subplot(2,3,4)
        ezplot(Ms, [0 ((l-lm)/2-3)])
        title('Moment, M (k-in)')
        xlabel('y (in)')
        subplot(2,3,5)
        ezplot(MyL, [((l-lm)/2-3) ((l-lm)/2+6)])
        title('Moment, M (k-in)')
        xlabel('y (in)')
        subplot(2,3,6)
        ezplot(Mm, [((l-lm)/2+6) (l/2)])
        title('Moment, M (k-in)')
        xlabel('y (in)')


        % Calculate the resulting stresses
        Mrs = subs(Ms,ls)*1000; % moment at the rail seat, lb-inches
        Qrs = subs(Qs,ls)*1000; % shear at the rail seat, lbs
        Nrs = abs(Ni); % axial force at the rail seat, lbs
        tauyzB = Qrs/As; % shear stress, psi
        sigymomcoeffB = Mrs/Is; % to be multiplied by (z-yt) for flexural
stress, psi
        sigynormB = Nrs/As; % to be added to the flexural stress, psi
        yt = As/bt/2; % distance to neutral axis assuming a homogeneous
section, in
```

B.4   Beam on an Elastic Foundation – Hetenyi Model

```matlab
% Hetenyi verification, to compare Hetenyi's model with the Galerkin model.
% Based on Hetenyi's solution to beam of finite length on an elastic
% foundation, with two symmetric point loads, at a certain gauge length
% apart.
% Hetenyi's model uses an Euler-Bernoulli beam and point loads

% "hetenyi.m"

% Hammad Khalil and John Zeman
% Winter 2009-2010


close all; clear all;

syms y real % y is the axis of the tie, y=0 at the left end
```

197

```matlab
P = 40000; % applied rail seat load, lbs
E = 4800000; % modulus of elasticity, psi
I = 700; % average moment of inertia, in^4
l = 102; % length of the tie, in
ls = (l-60)/2; % length from end of tie to rail seat center, in
c = 60/2; % assume 60 inches between rail seat centers, or 2c, in
bt = 11; % tie base width, in

% Odemark's method for approximating the effective modulus of a
% three-layer foundation
aeff = sqrt(l*bt/pi); % the radius of a circle with equal area to the bottom
of the tie
h1 = 12; % ballast layer thickness, in
h2 = 6; % subballast layer thickness, in
T = h1+h2; % granular layer thickness, in
E1 = 40000; % resilient modulus of the ballast, psi
E2 = 20000; % resilient modulus of the subballast, psi
E3 = 6000; % resilient modulus of the subgrade, psi
Em = (E1+E2+E3)/3; % guess a value for Em, effective modulus for the
foundation, psi
error = 1;
N1 = 0.9*h1/T;
count = 0;
while abs(error) > 0.01
    Q = Em;
    N2 = N1*(E1/Em)^(1/3);
    N21 = N2+0.9*h2/T;
    N3 = N2+0.9*h2/T*(E2/E3)^(1/3);
    Em = E3 / (sqrt((1+N2^2*(T/aeff)^2)/(1+N3^2*(T/aeff)^2))+E3/E2*(1-
sqrt((1+N2^2*(T/aeff)^2)/(1+N21^2*(T/aeff)^2)))); % effective modulus for the
foundation, psi
    error = Em-Q;
    count = count + 1;
end
% Vesic and Johnson's method for approximating the effective spring
% stiffness of the elastic foundation
v = 0.2; % assume this value for the foundation, which could reasonably be
between 0.1 and 0.4
k = 0.65*Em/(1-v)^2*sqrt(Em*bt^4/E/I); % stiffness in psi

h = (k/4/E/I)^(.25); % damping term

% Deflection from y=0 to y=ls
W = ((P.*h)./(k)).*(1./(sinh(h.*l) + sin(h.*l)));
w = (2.*cosh(h.*y).* cos(h.*y)).*(cosh(h.*ls).*cos(h.*(l-ls))+cosh(h.*(l-
ls)).*cos(h.*ls))+(cosh(h.*y).*sin(h.*y)...
    + sinh(h.*y).*cos(h.*y)).*(cosh(h.*ls).*sin(h.*(l-ls)) -
sinh(h.*ls).*cos(h.*(l-ls)) + cosh(h.*(l-ls)).*sin(h.*ls) - sinh(h.*(l-
ls)).*cos(h.*ls));
w = W.*w;

% Deflection at midpoint,
w0 = cosh(h.*c).*(cos(h.*(l-c))+cos(h.*c))+cos(h.*c).*(cosh(h.*(l-
c))+cosh(h.*c))-sinh(h.*c).*sin(h.*(l-c))+sin(h.*c).*sinh(h.*(l-c));
w0 = W.*w0;
```

```matlab
% Beam Rotation from y=0 to y=ls,
TH = (2.*P.*(h.^2))./k.*(1./(sinh(h.*l) + sin(h.*l)));
th = TH.*((sinh(h.*y).*cos(h.*y)-
cosh(h.*y).*sin(h.*y)).*(cosh(h.*ls).*cos(h.*(l-ls))+cosh(h.*(l-
ls)).*cos(h.*ls))...
    +(cosh(h.*y).*cos(h.*y)).*(cosh(h.*ls).*sin(h.*(l-ls)) - sinh(h.*ls) .*
cos(h.*(l-ls)) + (cosh(h.*(l-ls)).*sin(h.*ls)) - sinh(h.*(l-
ls)).*cos(h.*ls)));

% Shear from y=0 to y=ls,
Q = (P./(sinh(h.*l) + sin(h.*l))).*((sinh(h.*y).*cos(h.*y)+
cosh(h.*y).*sin(h.*y)).*(cosh(h.*ls).*cos(h.*(l-ls))...
+ cosh(h.*(l-ls)).*cos(h.*ls)) +
(sinh(h.*y).*sin(h.*y)).*(cosh(h.*ls).*sin(h.*(l-ls)) -
sinh(h.*ls).*cos(h.*(l-ls))...
+ cosh(h.*(l-ls)).*sin(h.*ls) - sinh(h.*(l-ls)).*cos(h.*ls)));

% Moment from y=0 to y=ls,
C = P ./ (2.*h.*(sinh(h.*l)+sin(h.*l)));
M = (2.*sin(h.*y).*sin(h.*y)).*(cosh(h.*ls).*cos(h.*(l-ls)) + cosh(h.*(l-
ls)).*cos(h.*ls))...
    + (cosh(h.*y).*sin(h.*y) -
sinh(h.*y).*cos(h.*y)).*(cosh(h.*ls).*sin(h.*(l-ls)) -
sinh(h.*ls).*cos(h.*(l-ls))...
    + cosh(h.*(l-ls)).*sin(h.*ls) - sinh(h.*(l-ls)).*cos(h.*ls));
M = C.*M;

% Moment at midpoint,
M0 = -C.*(sinh(h.*c).*(sin(h.*c)+sin(h.*(l-
c)))+sin(h.*c).*(sinh(h.*c)+sinh(h.*(l-c)))+cosh(h.*c).*cos(h.*(l-c))-
cos(h.*c).*cosh(h.*(l-c)));
```

B.5   Data Processing Code

```matlab
% HALF HERTZ Data Processing File for LOAD TEST data
% Place all ".dat" files needing to be processed into the Matlab directory
% This file should contain only those tests run at 0.5 Hz
% To process other loading frequencies, change the period T specified in the
code

% "processdatahalfHz.m"

% John Zeman
% Fall 2009

clear all; close all;
datfiles = dir('*.dat');

for i = 1:length(datfiles)
    filename = datfiles(i).name;
    [p,u,t] = textread(filename,'%f %f %f','headerlines',2);
    p = p*1500-1500; % converting voltage to psig
    dt = t(2)-t(1);
    T = 2000; %period SPECIFIED in milliseconds
```

```matlab
    dT = T/dt; %period converted to steps
    peakp = 0;
    peakt = 0;
    e = 1;
    for d = 1:round(dT/2)
        if (p(d) == max(p(1:round(dT/2))))
            if p(d) > 20
                peakp(e) = p(d);
                peakt(e) = t(d);
                e = e + 1;
            else
            end
        end
    end
    for d = (1+round(dT/2)):(length(p)-round(dT/2))
        if (p(d) > max(p((d-round(dT/2)):(d-1))) && p(d) >
max(p((d+1):(d+round(dT/2))))))
            if p(d) > 20
                peakp(e) = p(d);
                peakt(e) = t(d);
                e = e + 1;
            else
            end
        end
    end

    figure(i);
    plot(t,p);
    hold on
    scatter(peakt,peakp,'o','r');

    halfHzdata(i).name = strrep(filename,'d1.dat','');
    halfHzdata(i).p = p;
    halfHzdata(i).u = u;
    halfHzdata(i).t = t;
    halfHzdata(i).f = 1000/T;
    halfHzdata(i).pmax = max(p);
    halfHzdata(i).ppeak = peakp;
    halfHzdata(i).tpeak = peakt;
    halfHzdata(i).npeak = length(peakp);

    saveas(i,halfHzdata(i).name,'fig');
    close all;
    clear peakp;
    clear peakt;

end
save halfHzdata;
```

B.6   Spreadsheet Assembly Code

```matlab
% Create arrays and matrices of the processed data and print these in Excel
% The proper data structure must be loaded before running this file

% "assemble.m"
```

```matlab
% John Zeman
% Fall 2009

clear all; close all;
load halfHzdata; % change this name to the structure file to be processed

N = size(halfHzdata); % make sure this is the same name as the structure
n = N(2);
warning off MATLAB:xlswrite:AddSheet;
for i = 1:n
    Lp(i) = length(halfHzdata(i).ppeak);
    Lt(i) = length(halfHzdata(i).tpeak);
end
lp = max(Lp);
lt = max(Lt);
Ppeak(1:n,1:lp) = 0;
Tpeak(1:n,1:lt) = 0;
for i = 1:n
    if length(halfHzdata(i).name) == 3
        halfHzdata(i).name(4) = ' ';
        halfHzdata(i).name(5) = ' ';
    end
    if length(halfHzdata(i).name) == 4
        halfHzdata(i).name(5) = ' ';
    end
    f(i) = halfHzdata(i).f;
    Pmax(i) = halfHzdata(i).pmax;
    Ai = strcat('A',int2str(i));
    xlswrite('Results',{halfHzdata(i).name},'Summary',Ai);
    Ppeak(i,1:Lp(i)) = halfHzdata(i).ppeak;
    Tpeak(i,1:Lt(i)) = halfHzdata(i).tpeak;
end
xlswrite('Results',Ppeak,'Peak Pressure','B2');
xlswrite('Results',Tpeak,'Peak Time','B2');
A = [f;Pmax];
xlswrite('Results',A,'Summary','F1');
```

APPENDIX C: DETAILED RESULTS OF THE ANALYTICAL MODELS

**Table C.1 Parameters used in the analytical models,
with the selected base values and ranges
(AREMA 2009, Mindess et al. 2003, FRA 2010, Selig and Li 1994, Mattson 2010)**

Parameter	Units	Base Value	Min	Max
Train speed	mph	60	10	80
Wheel load	lb	40,000	10,000	140,000
Rail moment of inertia	in^4	94.9	--	--
Base width of the rail	in	6	--	--
Applied load, normal to rail seat surface	lb	40,000	5,000	70,000
Length of the tie	in	102	99	102
Area at the shoulder	in^2	100	60	130
Area at the midsection	in^2	80	60	130
Moment of inertia at the shoulder	in^4	700	300	700
Moment of inertia at the midsection	in^4	360	200	360
Base width of the tie	in	11	10	13
Length of the middle section	in	36	18	36
Precompression	psi	2,000	0	2,500
Wire diameter	mm	5	--	--
Prestress eccentricity at the shoulder	in	0.25	--	--
Poisson's ratio of the tie	---	0.2	--	--
Concrete 28-day strength	psi	7,000	7,000	10,000
Young's modulus for the tie	psi	4,800,000	4,800,000	5,700,000
Track modulus	lb/in/in	10,000	2,000	15,000
Height of ballast	in	12	6	24
Height of subballast	in	6	6	18
Resilient modulus of ballast	psi	40,000	20,000	80,000
Resilient modulus of subballast	psi	20,000	10,000	40,000
Resilient modulus of subgrade	psi	6,000	2,000	20,000
Poisson's ratio of the foundation	---	0.2	0.1	0.4

C.1   Track Motion Model
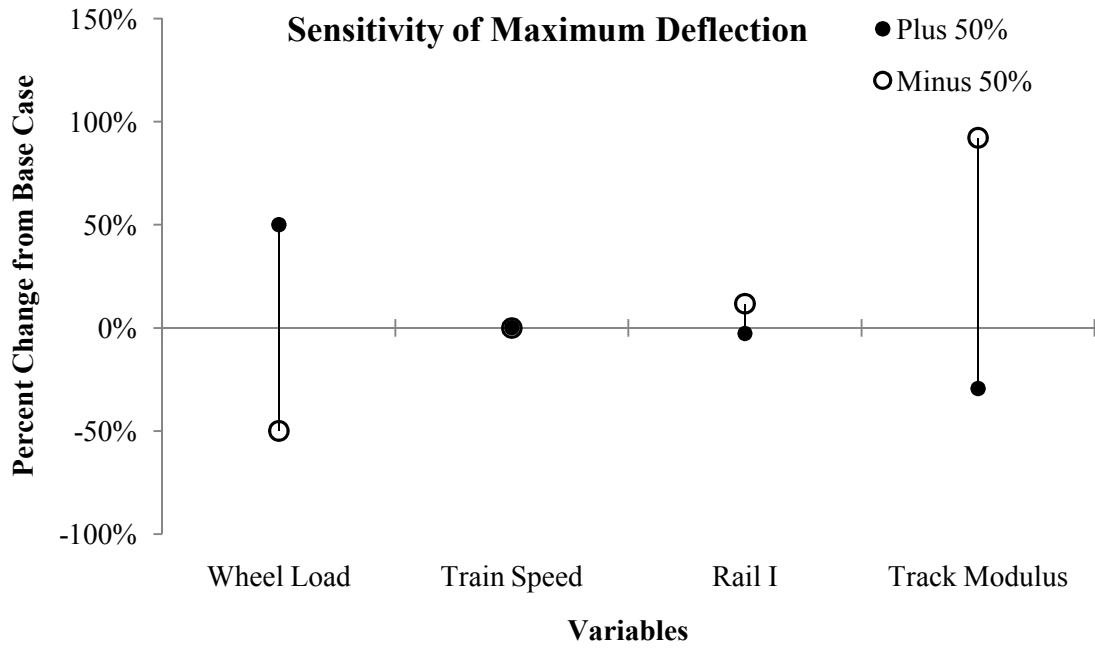
**Figure C.1 Sensitivity of maximum vertical deflection
to variations in track motion model parameters**
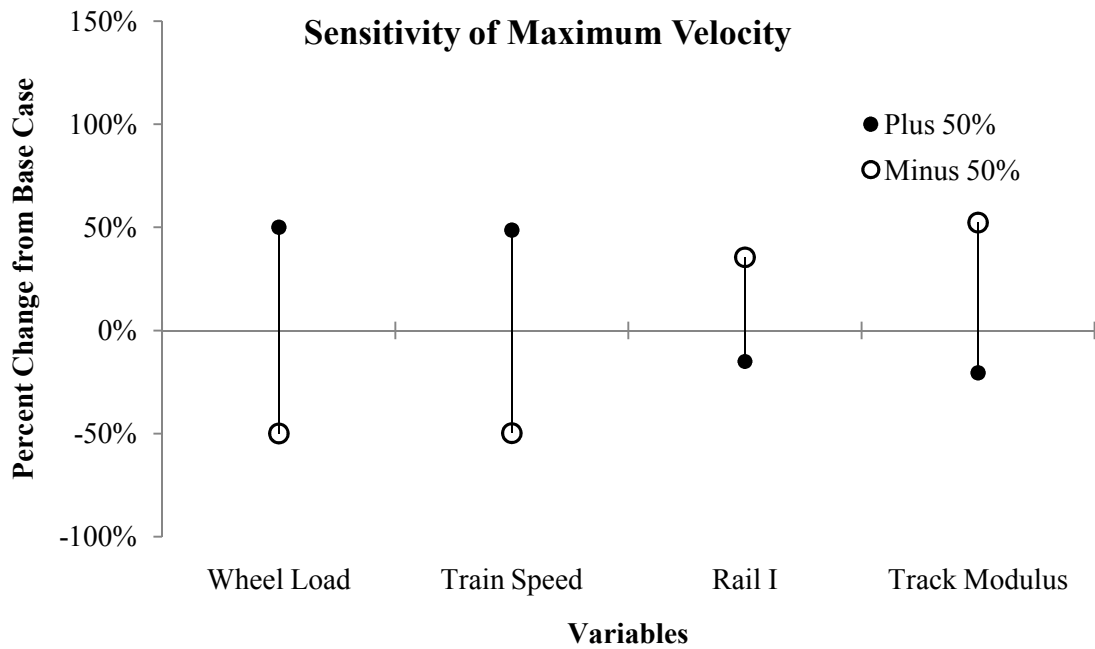
**Figure C.2 Sensitivity of maximum vertical velocity
to variations in track motion model parameters**
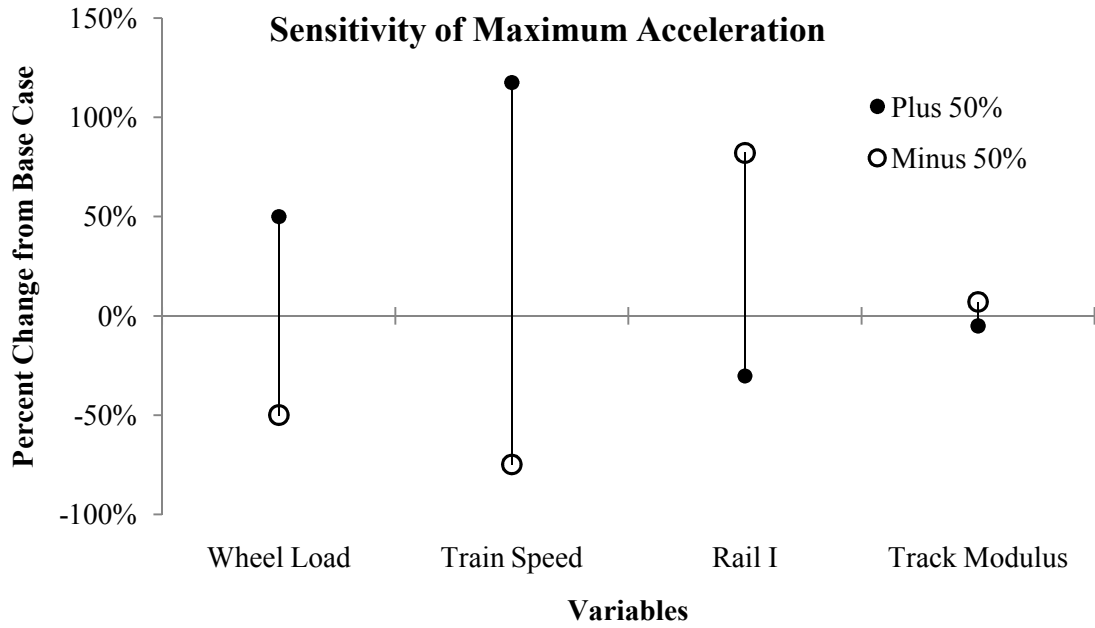
**Figure C.3 Sensitivity of maximum vertical acceleration
to variations in track motion model parameters**
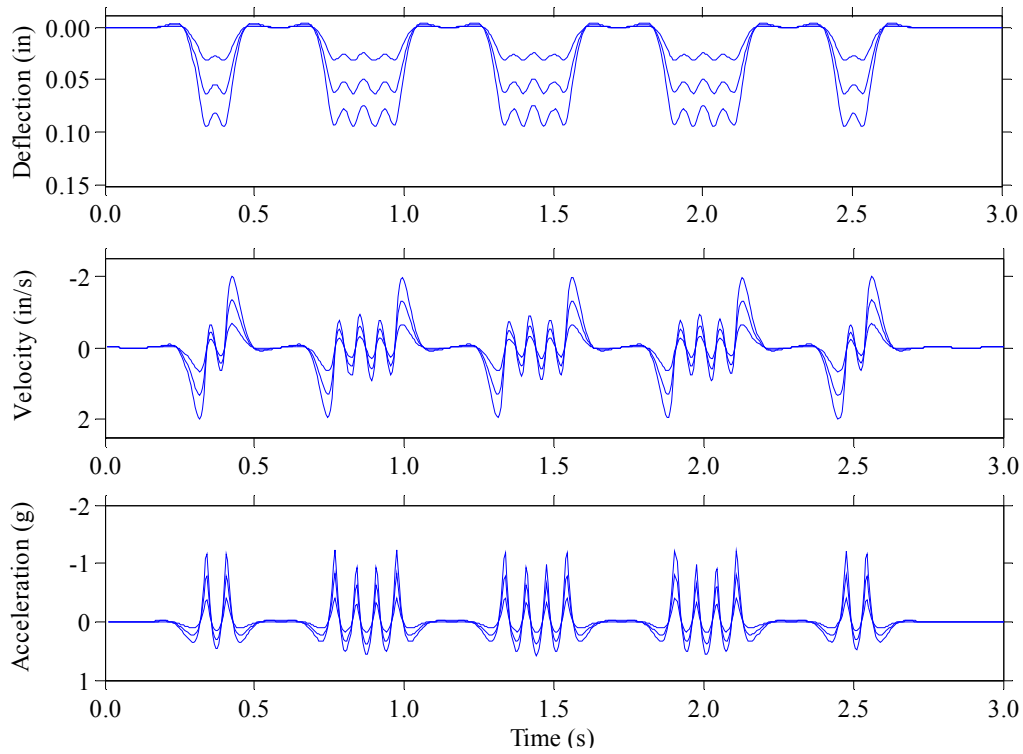
**Figure C.4 Variations in track motion for three wheel load cases:
20 kips, 40 kips, and 60 kips**
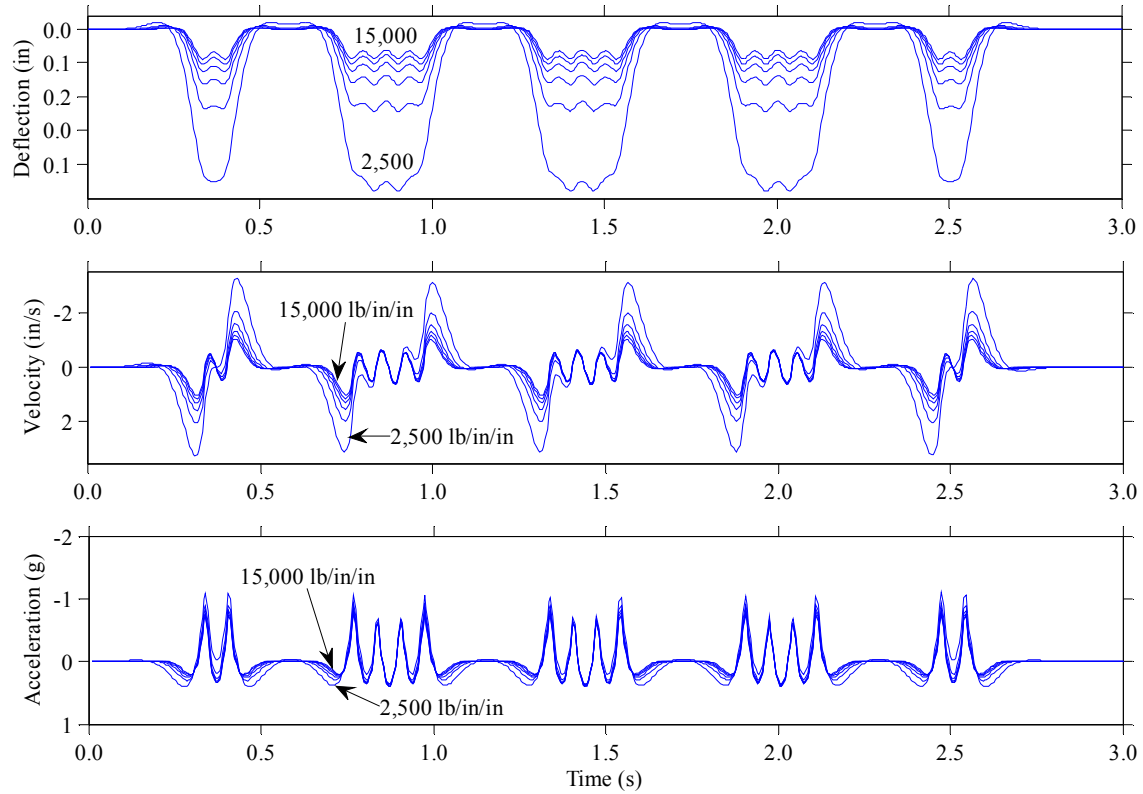
Figure C.5 Variations in track motion for a range of track modulus values, from 2,500 lb/in/in to 15,000 lb/in/in at intervals of 2,500 lb/in/in
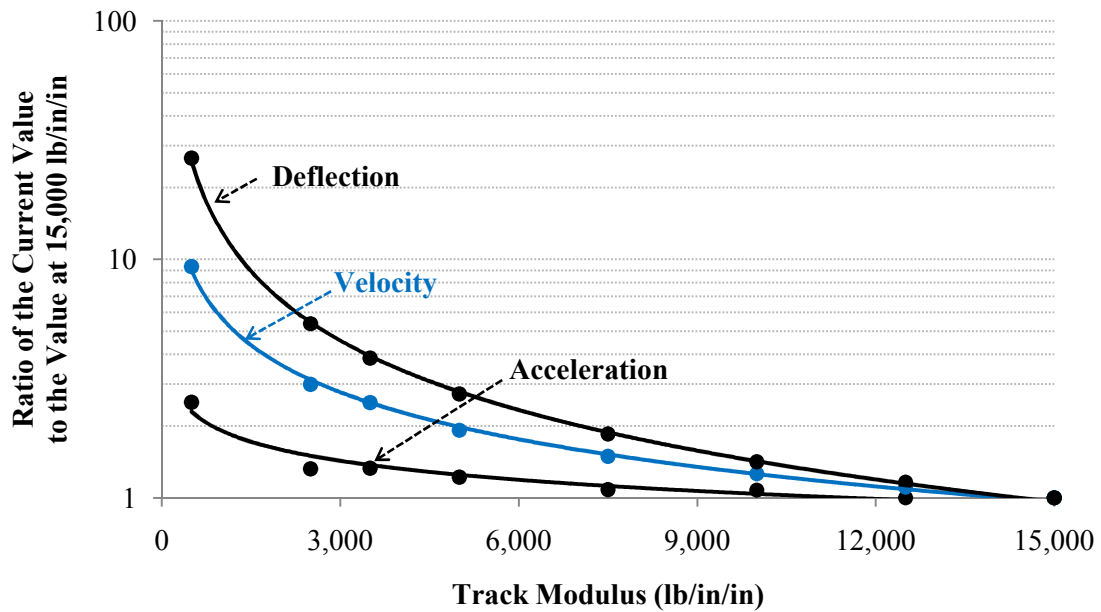
Figure C.6 Log-linear representation of relationship between peak track motion and track modulus
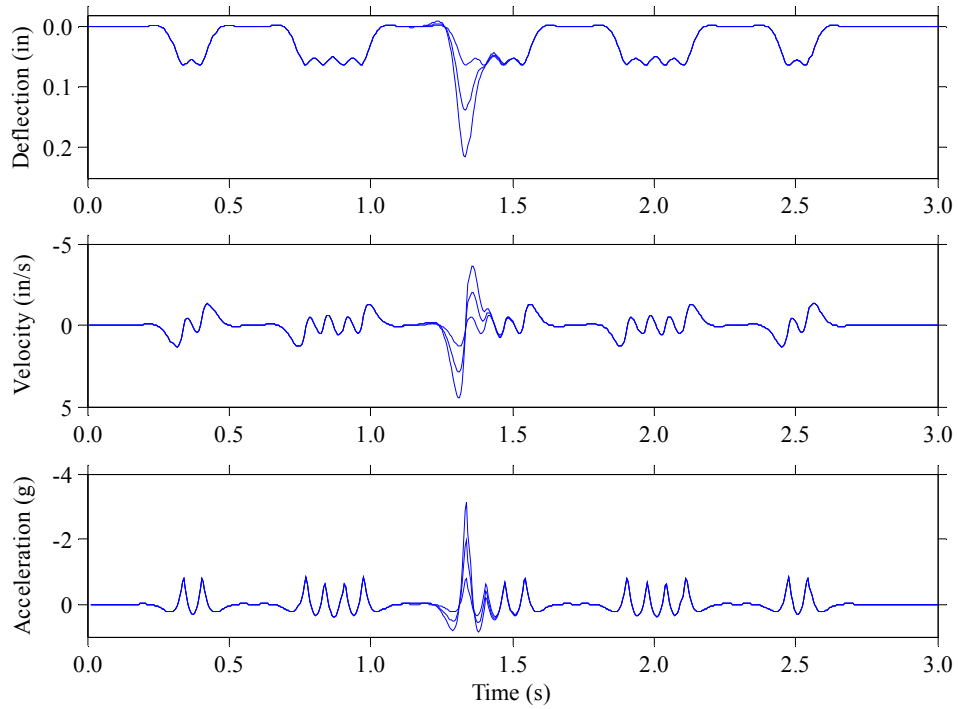
Figure C.7 Introduction of a high impact wheel at an inner axle, showing the base case, a 90-kip wheel, and a 140-kip wheel
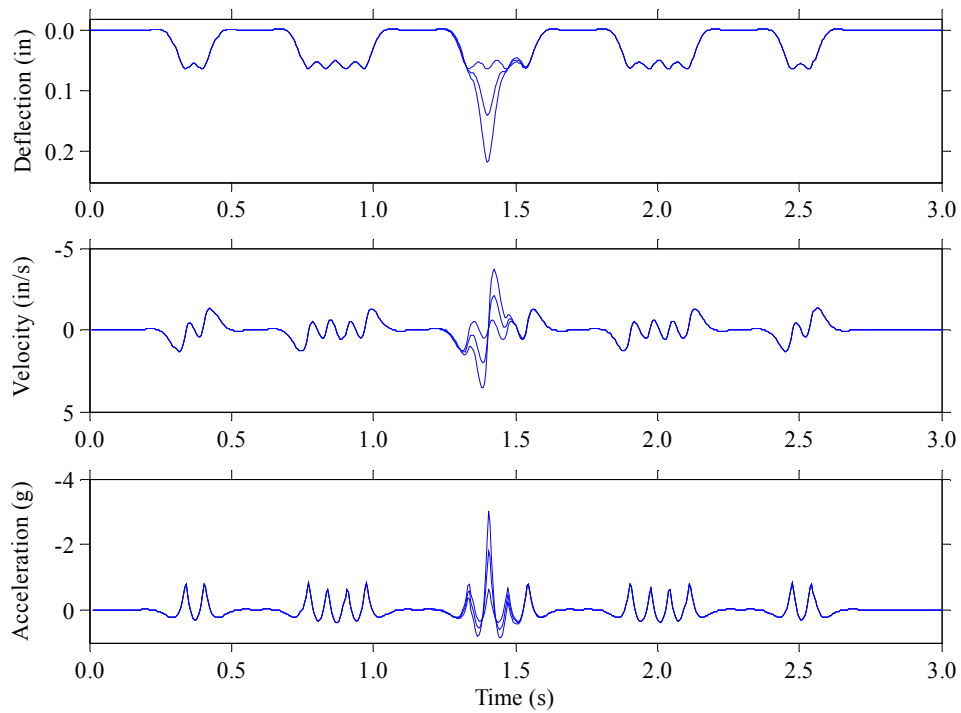
Figure C.8 Introduction of a high impact wheel at an outer axle, showing the base case, a 90-kip wheel, and a 140-kip wheel

206

C.2   Effective Stress Model
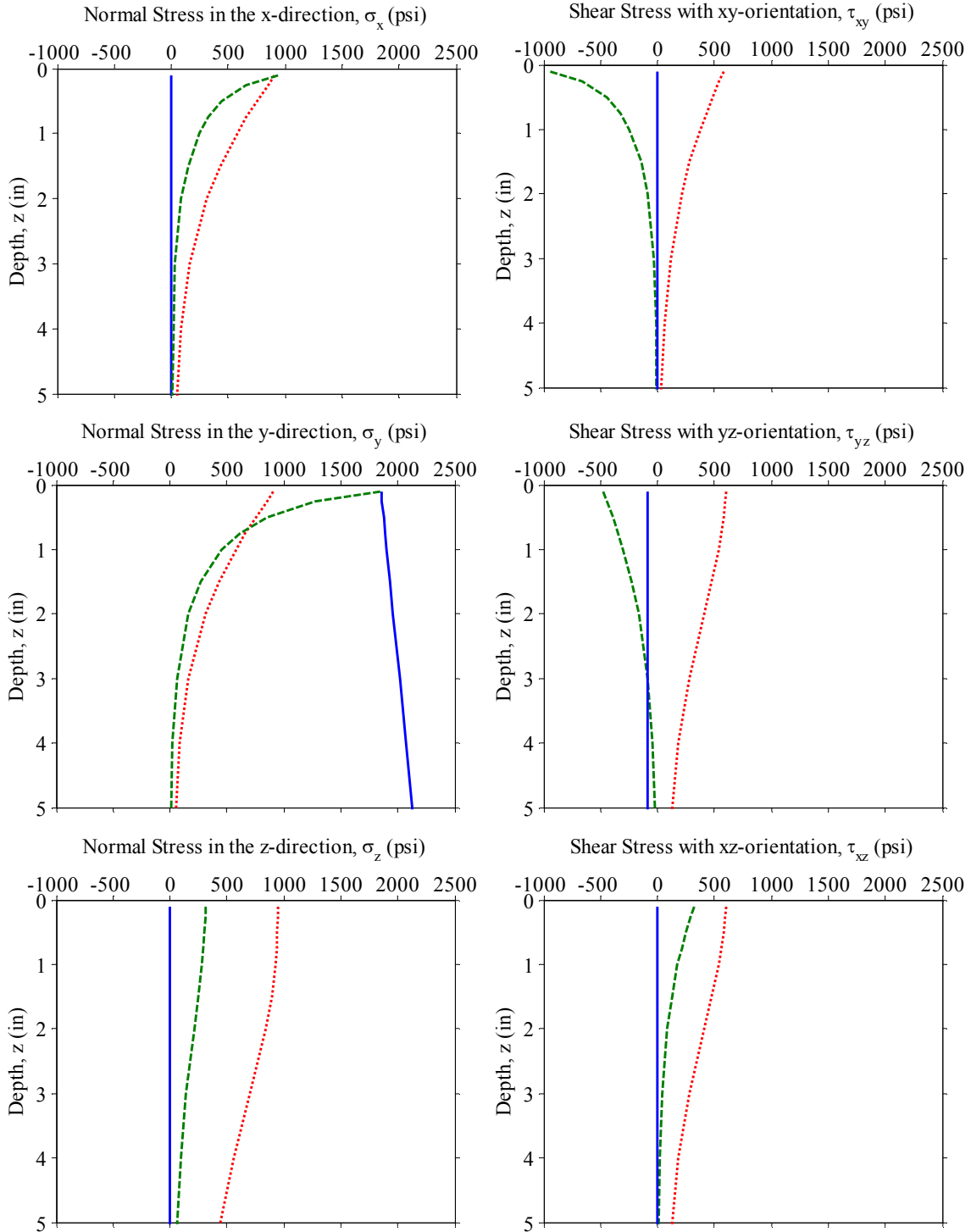
Figure C.9 Individual components of the "*xyz*" total stress with depth from the rail seat surface: uniform vertical stress S_V (dotted red), uniform horizontal stress S_H (dashed green), prestressed beam on an elastic foundation S_B (solid blue)
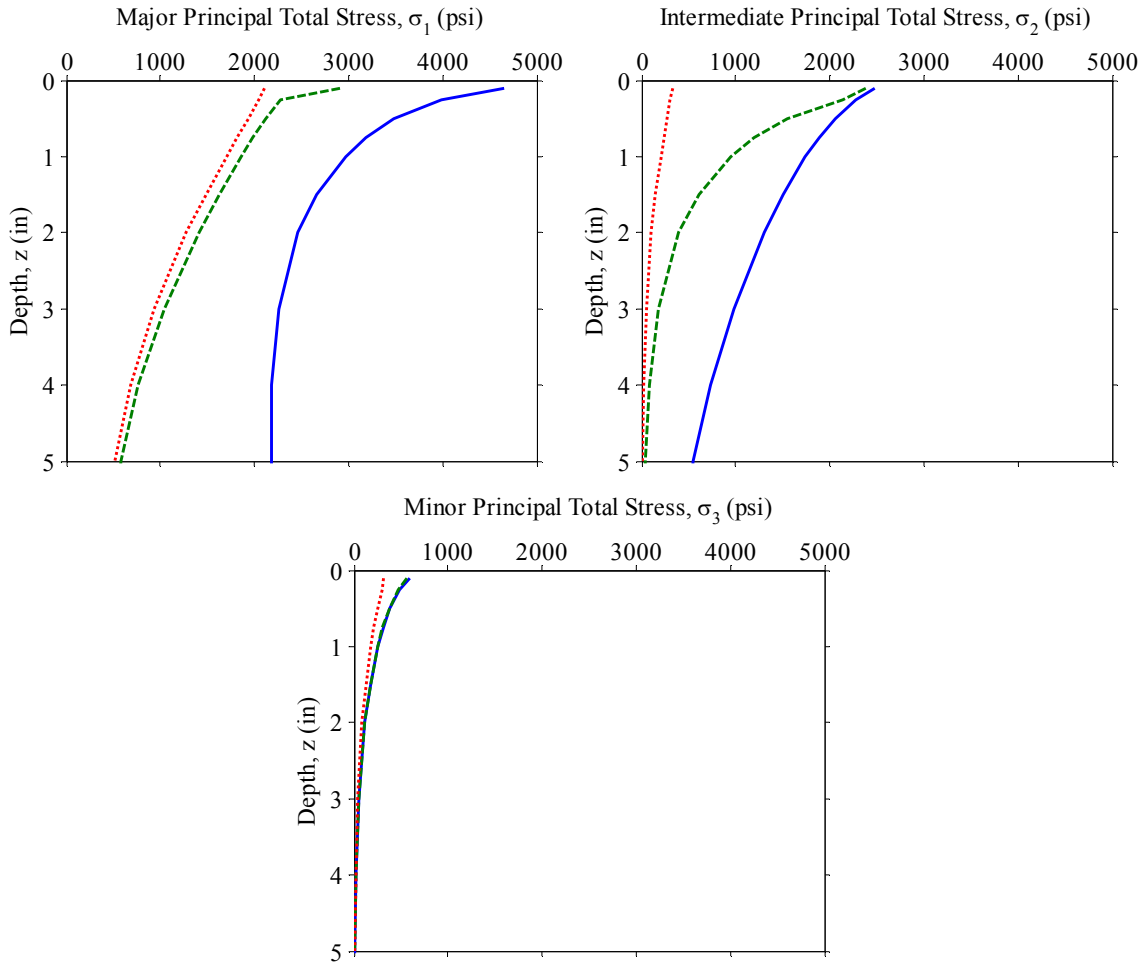
Figure C.10 Comparison of principal total stress models with depth from the rail seat surface: S = S$_V$ (dotted red), S = S$_V$ + S$_H$ (dashed green), S = S$_V$ + S$_H$ + S$_B$ (solid blue)

C.3   Beam on an Elastic Foundation – Galerkin Model

Sensitivity of Modulus of Foundation Reaction
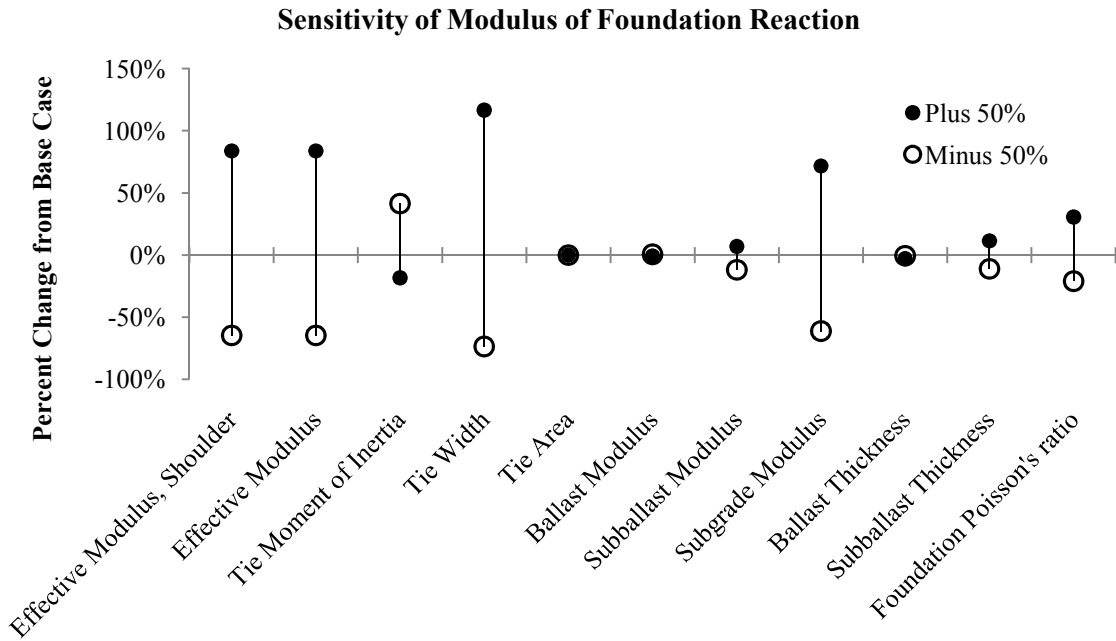
Figure C.11 Sensitivity of shoulder support stiffness to variations in Galerkin model parameters

Sensitivity of Effective Modulus
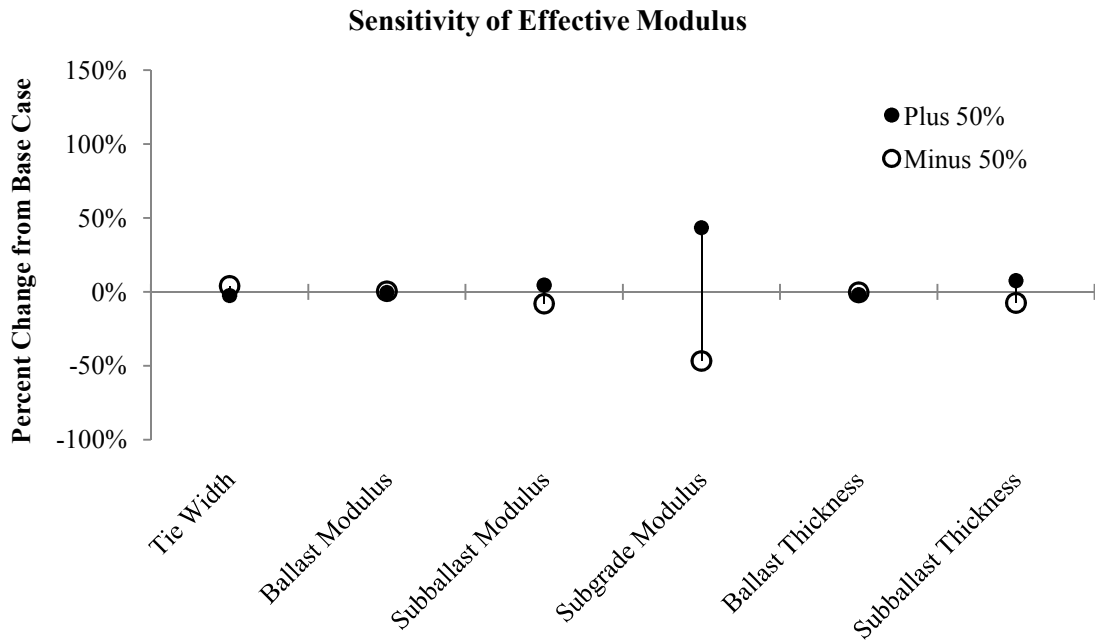
Figure C.12 Sensitivity of effective resilient modulus to variations in Galerkin model parameters
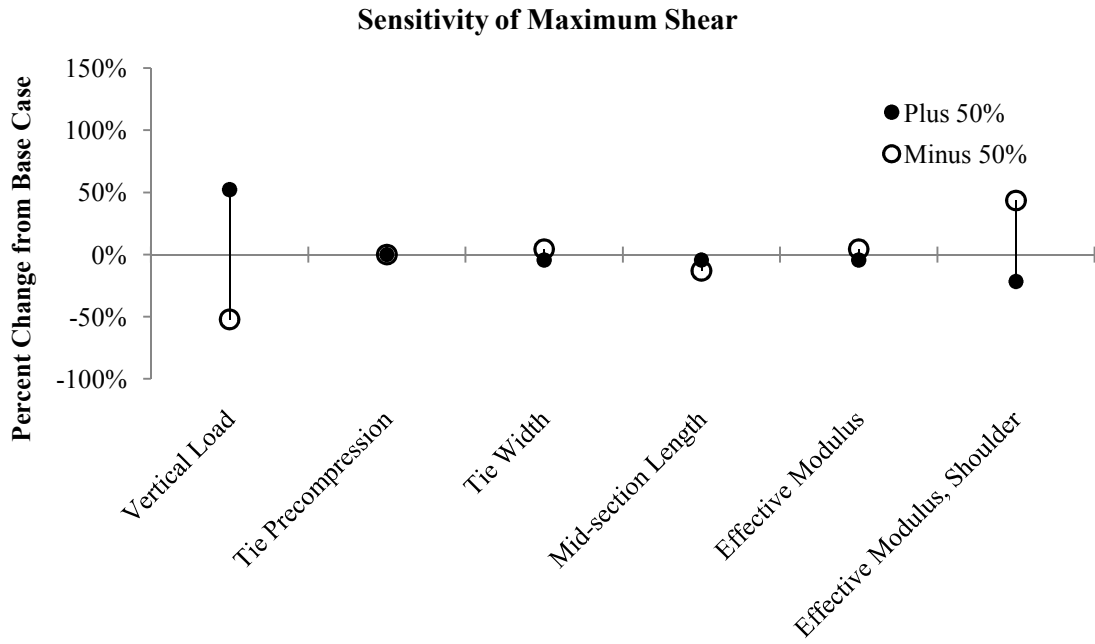
Figure C.13 Sensitivity of maximum shear to variations in Galerkin model parameters
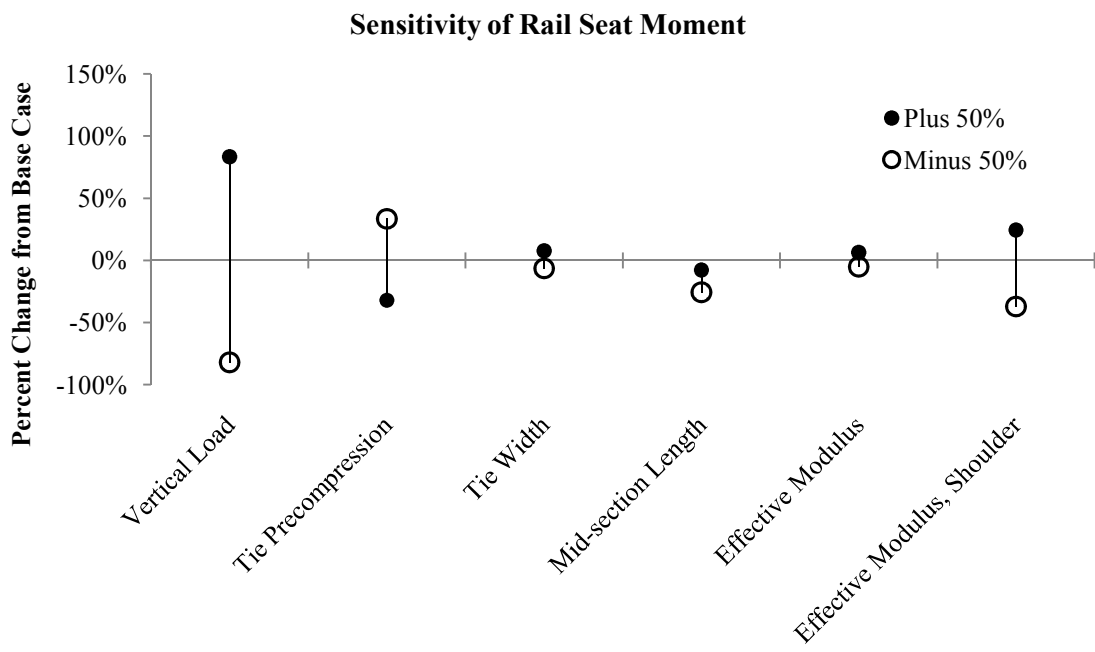
Figure C.14 Sensitivity of rail seat moment to variations in Galerkin model parameters

Sensitivity of Center Moment
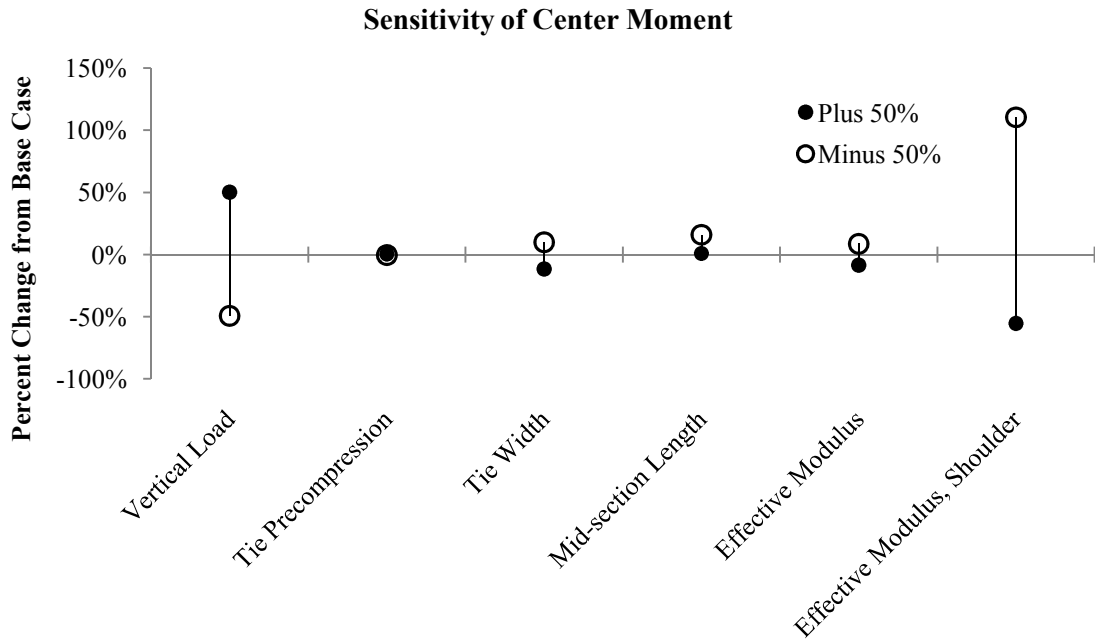
Figure C.15 Sensitivity of center moment to variations in Galerkin model parameters

Sensitivity of Maximum Ballast Pressure
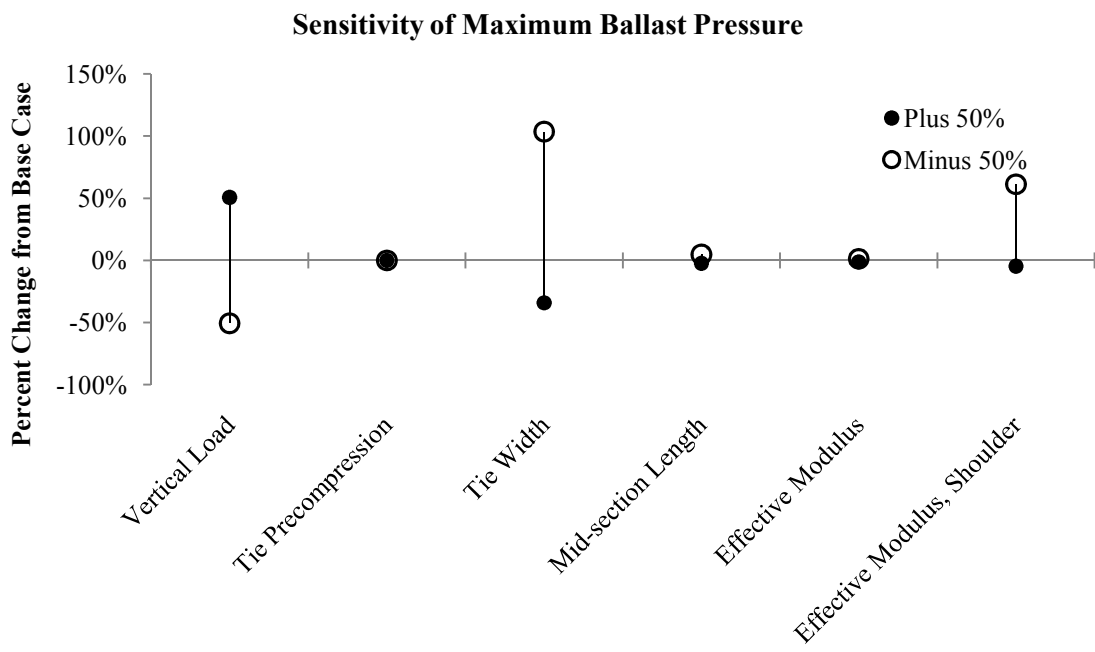
Figure C.16 Sensitivity of maximum ballast pressure to variations in Galerkin model parameters
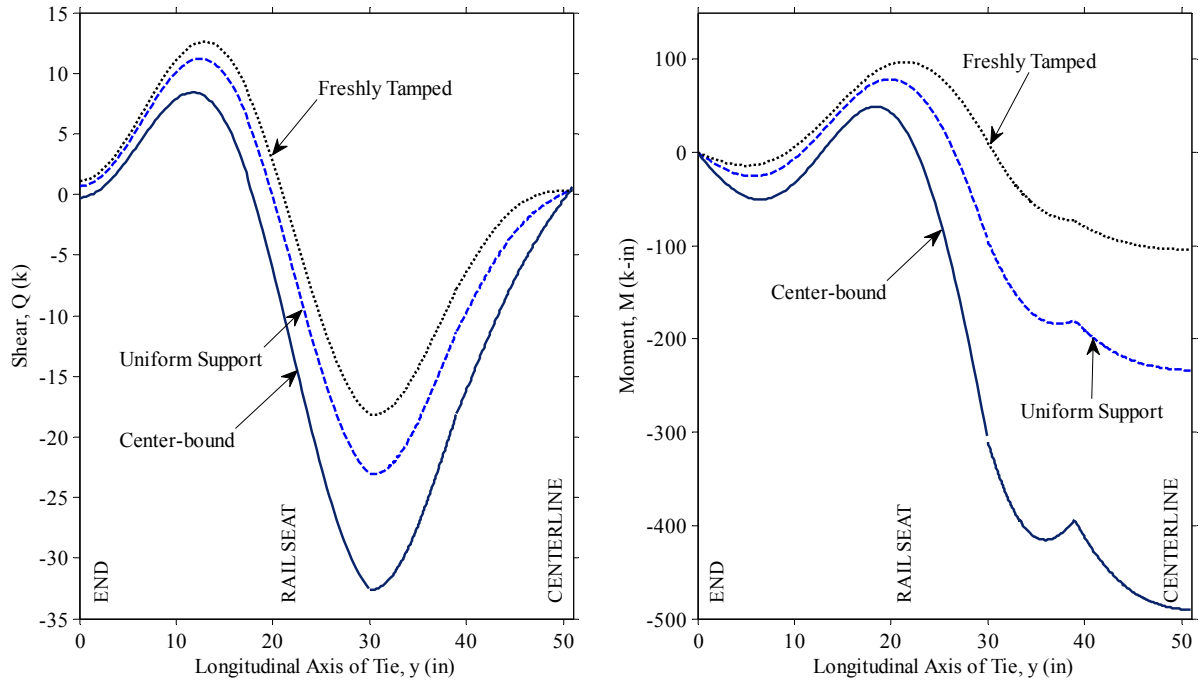
Figure C.17 Comparison of support conditions for prestressed, sectioned Galerkin model: E_{fs}:E_{fm} = 1.5 for freshly tamped and E_{fs}:E_{fm} = 0.5 for center-bound
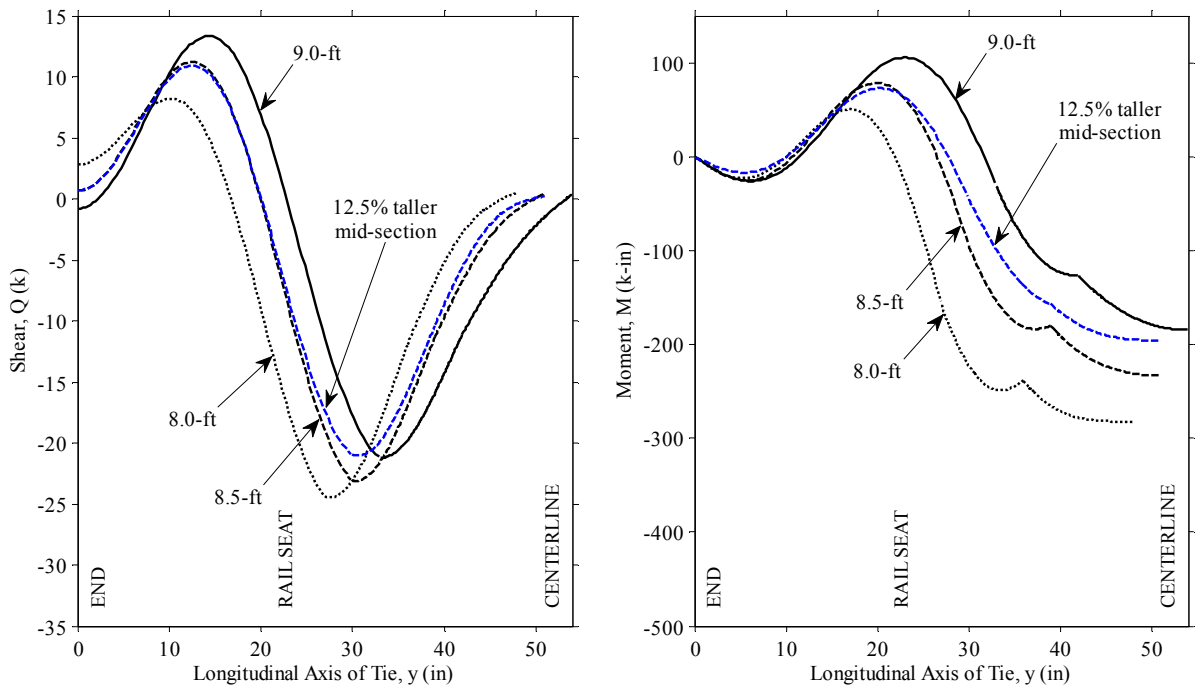
Figure C.18 Comparison of tie dimensions for prestressed, sectioned Galerkin model

The following figures provide a simple procedure to derive the values for ballast pressure, shear, and moment by applying factors to the base case. These graphs were created for the base tie dimensions listed in Table C.1. It was found that changing the tie dimensions (other than the base width) results in interaction between different changes in the model that cannot be scaled directly with factors. The purpose of pursuing such a procedure is to make the output of the model accessible for engineers who do not use Matlab.

Table C.2 Base case values for the Galerkin model, under base conditions

Maximum Ballast Pressure (psi)	Maximum Shear (kips)	Rail Seat Moment (k-in)	Center Moment (k-in)
85	23	78	-233
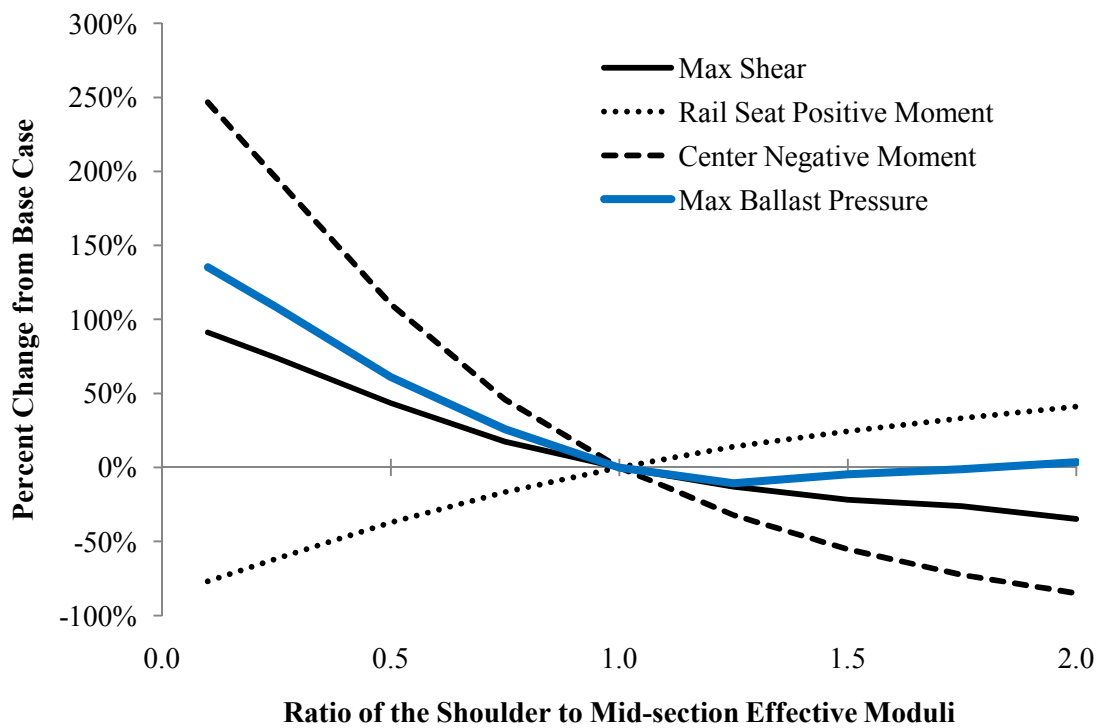
**Figure C.19 Percent change from base case,
varying ratio of shoulder to mid-section effective resilient moduli**
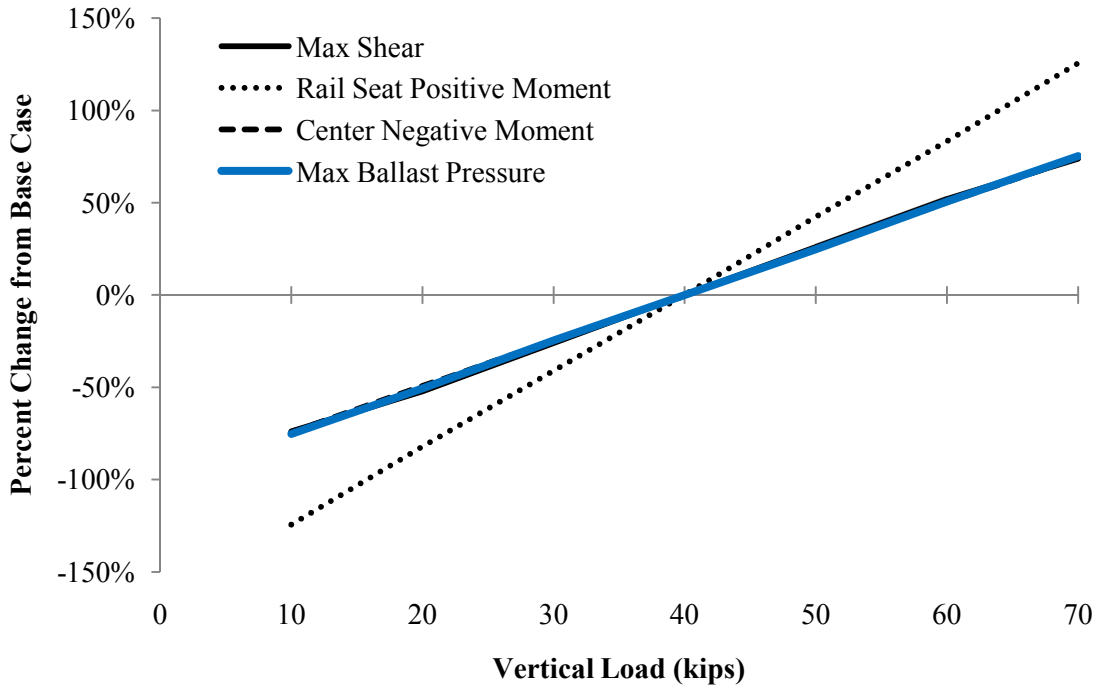
Figure C.20 Percent change from base case, varying vertical load
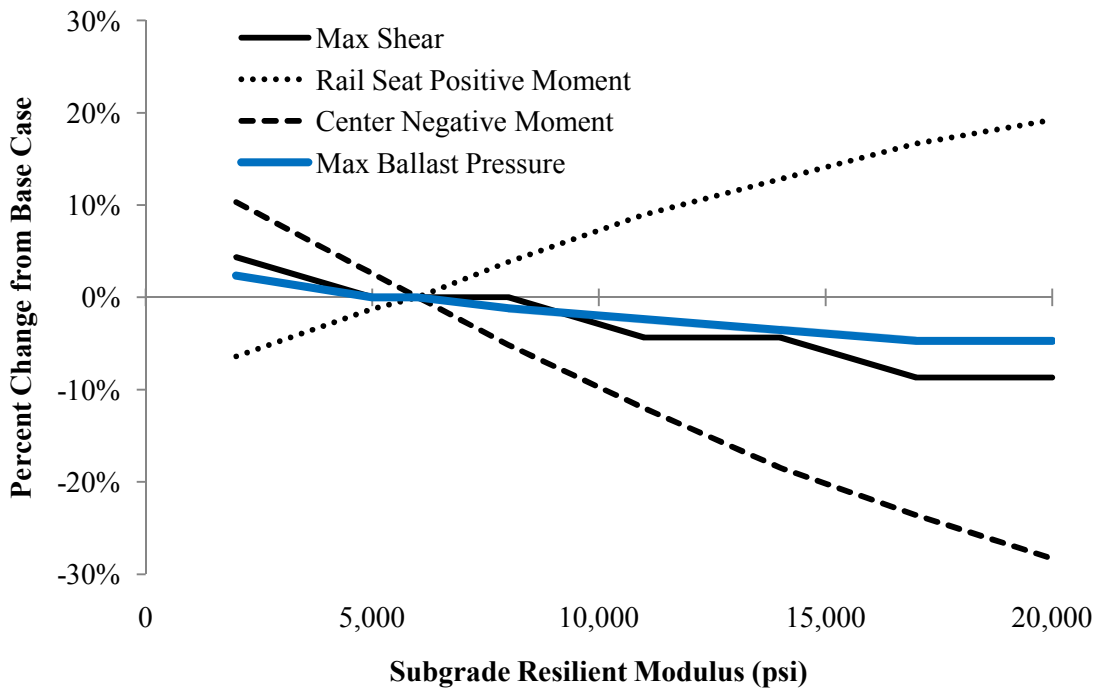
Figure C.21 Percent change from base case, varying subgrade resilient modulus
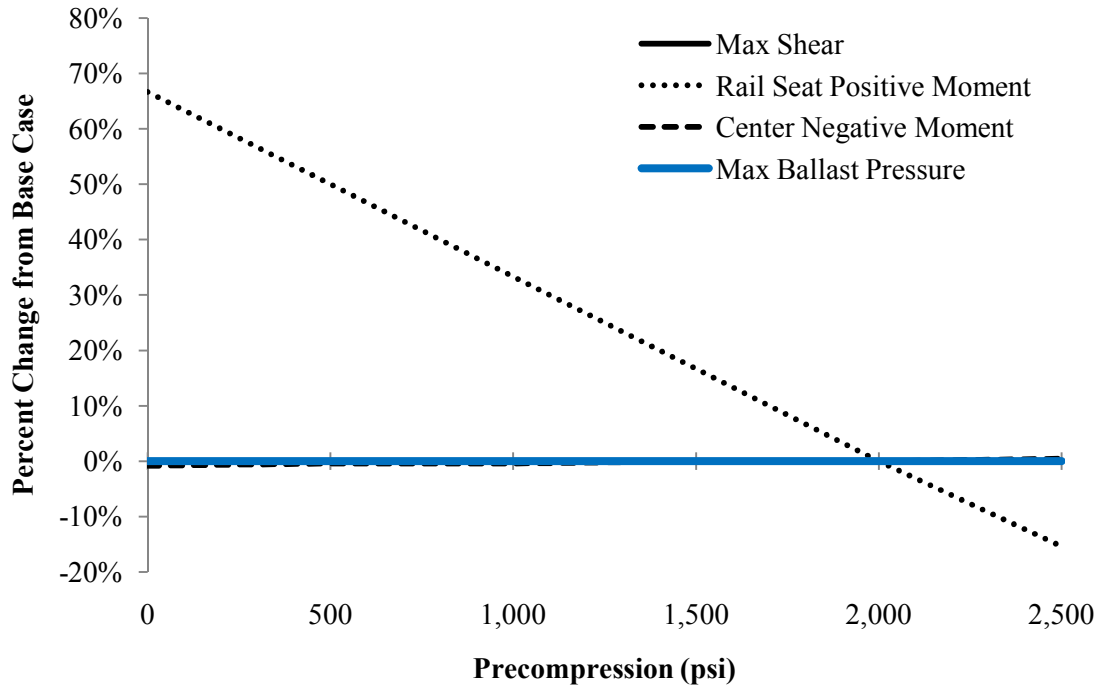
Figure C.22 Percent change from base case, varying precompression
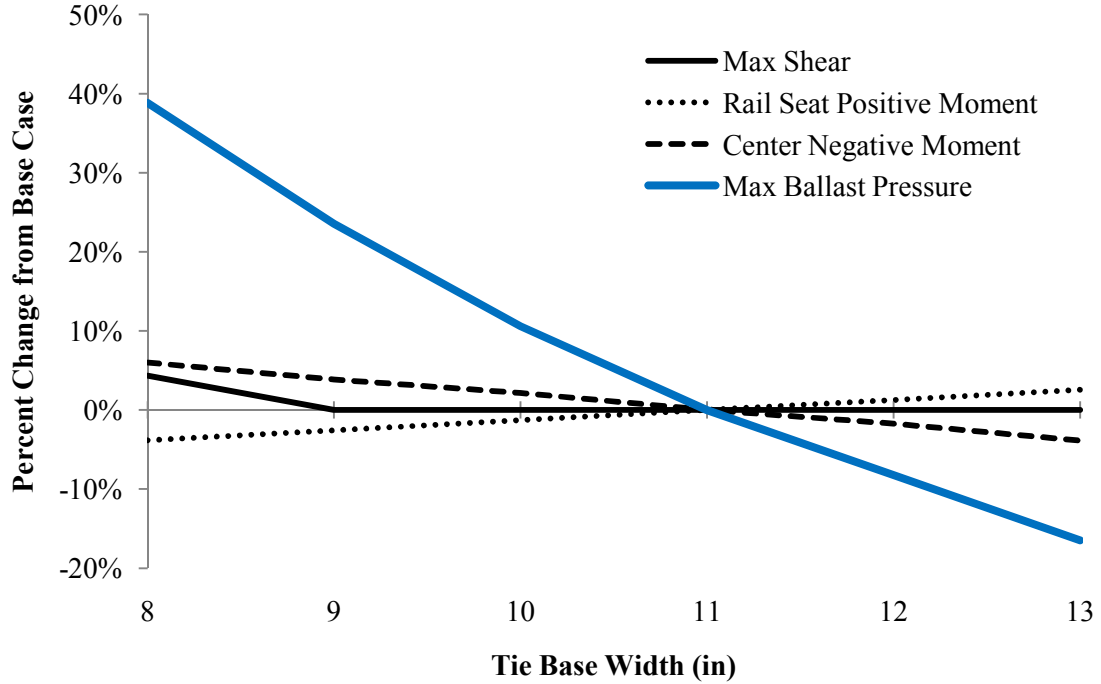
Figure C.23 Percent change from base case, varying tie base width

215

APPENDIX D: SPECIFICATIONS FOR MATERIALS AND EQUIPMENT

The length and width of the tie pads, summarized in the following tables, were defined as the dimensions of the general bearing surface – neglecting the dimensions of tabs or other protruding sections that would not bear much load. The thickness was defined as the external thickness, not accounting for the reduced thickness at indentations.

The surface area of the dimpled pads was estimated as follows:

$$\text{Net Contact Area} = (7.09")(6.69") - (88 \text{ dimples})\frac{\pi(0.41")^2}{4} = 35.8 in^2$$

For the indentation volume, the dimples were assumed to be truncated spheres, knowing that the chord length, c, was 0.41 inch and the height above the chord, h, was 0.074 inch. To find the radius of this sphere, r, the central angle θ was found by geometry:

$$c = 2r\sin\tfrac{\theta}{2} \qquad h = r(1 - \cos\tfrac{\theta}{2}) \qquad \frac{2h}{c} = \frac{1 - \cos\tfrac{\theta}{2}}{\sin\tfrac{\theta}{2}} = \tan\tfrac{\theta}{4}$$

$$\theta = 4\arctan\left(\frac{2(0.074")}{0.41"}\right) = 79.4° \qquad r = \frac{c}{2\sin\tfrac{\theta}{2}} = \frac{0.41"}{2\sin\frac{79.4°}{2}} = 0.321"$$

Then the volume of the spherical segment was calculated by taking the integral:

$$V = \int_{r-h}^{r} \pi\left(r^2 - z^2\right)dz = \pi\left(z(0.321")^2\Big|_{0.247"}^{0.321"} - \tfrac{1}{3}z^3\Big|_{0.247"}^{0.321"}\right) = 0.005 in^3$$

Making the volume of voids on a dimpled surface equal to $88(0.005 \text{ in}^3) = 0.44 \text{ in}^3$.

For the grooved pad, the indentations were approximated as rectangular prisms:

$$\text{Net Contact Area} = (6.90")(6.42") - (10 \text{ grooves})(2.72")(0.34") = 35.1 in^2$$

$$V = 10(2.72")(0.34")(0.121") = 1.12 in^3$$

Simple, non-standard laboratory tests were conducted to measure the relative compressive and flexural stiffness of the different tie pads and assemblies. The primary motivation was to identify

properties of the pads and assemblies that could begin to explain their distinct water pressurization

behaviors[6].

     The compressive stiffness was approximated by measuring the load-deflection curve for each pad

under deflection-control, up to a 50-kip applied load. The P-δ curves shown in the following tables have

been corrected by removing the corresponding machine deflections from the deflection measurements.

These curves typically had two distinct slopes, and these tangent slopes, as well as the secant slope at 50

kips, are shown on the plots. To convert the load-deflection slope to a compressive stiffness that is

similar to a Young's modulus, the engineering strain was approximated as the deflection over the initial

thickness and the normal stress was approximated as the load over the contact area between the pad and

the 8.5-inch diameter steel plate. This contact area was estimated by using a computer-aided drafting

program to calculate the intersection between the two areas. Thus, the compressive stiffness is:

$$\frac{\sigma}{\varepsilon_{eng}} = \frac{P}{\delta} \frac{t_{pad}}{A_{contact}}$$

     For a simple test to estimate the flexural stiffness of the pads and assemblies, a 4.1-lb weight was

attached to the end of a pad/assembly fixed to a table's edge, with a cantilever length of 5 inches.

Because the moment of inertia of the pads was not easy to estimate, the stiffness of the pads and

assemblies were considered with the flexural rigidity, EI, by rearranging the deflection (Δ) of a cantilever

beam under a point load (Craig 2000):

$$EI = \frac{PL^3}{3\Delta}$$

     The results of these simple lab tests are summarized in Table D.1, and it appears that the relative

cantilever rigidity of the pads aligns with the three load-pressure groups that were proposed in Chapter 6.

However, other factors that contribute to the contact surface's ability to seal water should relate to

---

[6] A more extensive discussion of this topic has been published in the Proceedings of the 2010 AREMA Annual
Conference in Orlando, Florida, USA (Zeman et al. 2010c)

hardness and surface geometry as well – properties of just the contact surface, rather than the full pad/assembly.

Table D.1 Summary of tie pad characteristics relevant to the load-pressure relationships

Load-Pressure Group	Tie Pad	2nd Tangent Stiffness (ksi)	Cantilever Deflection (in)	Cantilever Rigidity (lb-in^2)
Flexible	Dimpled Santoprene	11.8	2.63	65
	Grooved Polyurethane	30.6	2.25	76
Semi-Rigid	Flat EVA	64.3	2.19	78
	Dimpled EVA	17.7	2.00	85
	Dimpled Polyurethane	20.2	1.81	94
Assemblies, Rigid Layer	2-Part Assembly B	18.6	1.50	114
	2-Part Assembly C	31.3	0.56	304
	3-Part Assembly A	24.0	0.06	2,733

As an example of the distinction between compressive stiffness and flexural rigidity, 3-part assembly A has the lowest secant stiffness and one of the lowest 2nd tangent stiffness, but it has the highest cantilever rigidity by an order of magnitude. For an assembly of different materials, the compressive stiffness is dominated by the least stiff material, while the flexural rigidity is dominated by the most rigid material.

Table D.2 Characteristics of the grooved polyurethane pad

Grooved Polyurethane Pad

$K_s = 2,024$ k/in

$K_{t2} = 4,534$ k/in

Length, x-direction (in)	6.90
Width, y-direction (in)	6.42
Thickness (in)	0.24
Flex. Rigid. (lb-in^2)	76
Notes	

Tangent Comp. Stiff. (ksi)	30.6
Indentation geometry (in)	2.72 x 0.34 x 0.12
Net contact area (in^2)	35.1
Volume of voids (in^3)	1.12
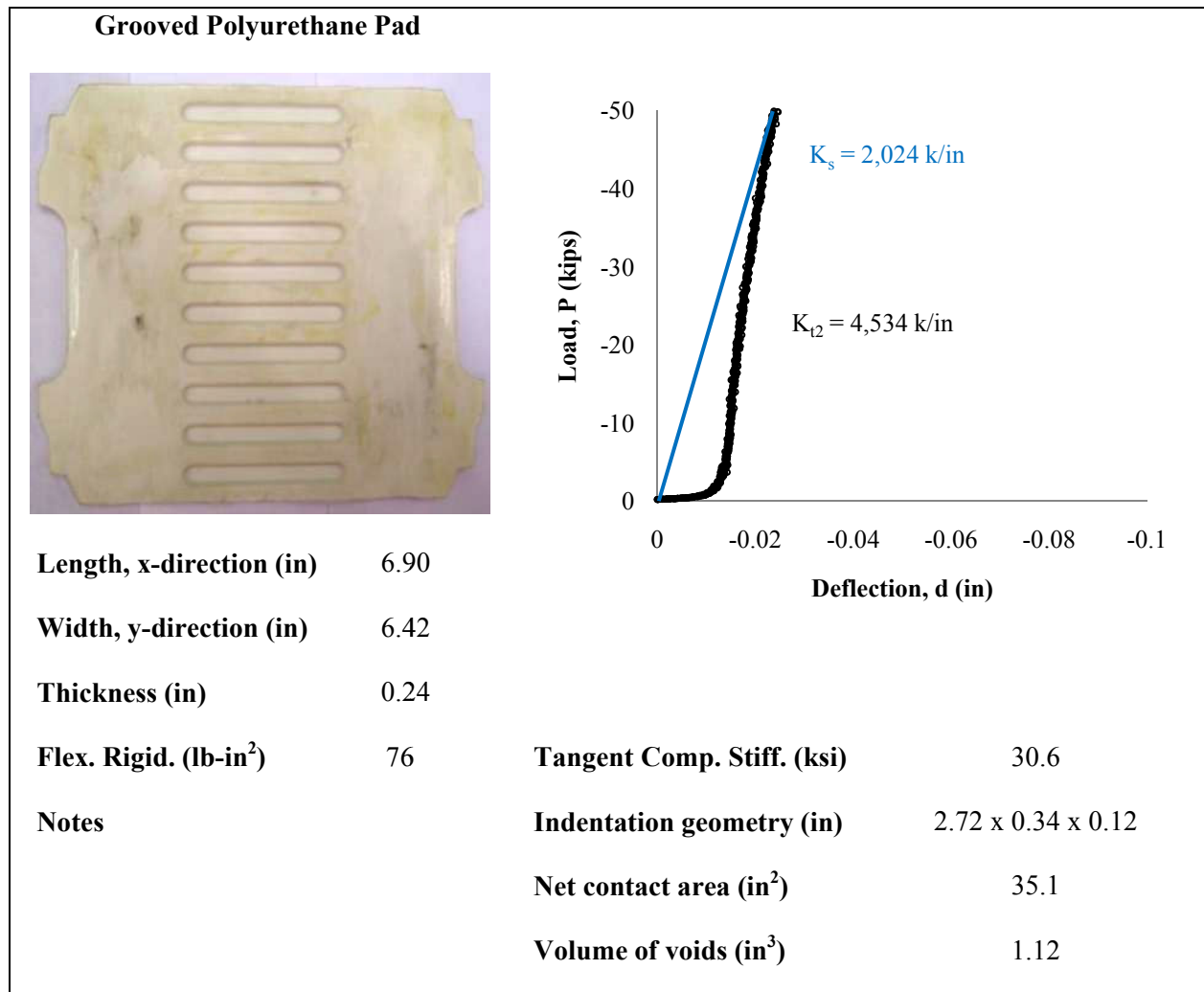
Table D.3 Characteristics of the dimpled santoprene pad

Dimpled Santoprene Pad

Length, x-direction (in)	7.09		
Width, y-direction (in)	6.69		
Thickness (in)	0.23		
Flex. Rigid. (lb-in^2)	65	**Tangent Comp. Stiff. (ksi)**	11.8
Notes		**Indentation geometry (in)**	0.41 diam, 0.074 deep
		Net contact area (in^2)	35.8
		Volume of voids (in^3)	0.44

In the graph:
$K_s = 891$ k/in
$K_{t2} = 1{,}710$ k/in
$K_{t1} = 159$ k/in

Load, P (kips)
Deflection, d (in)
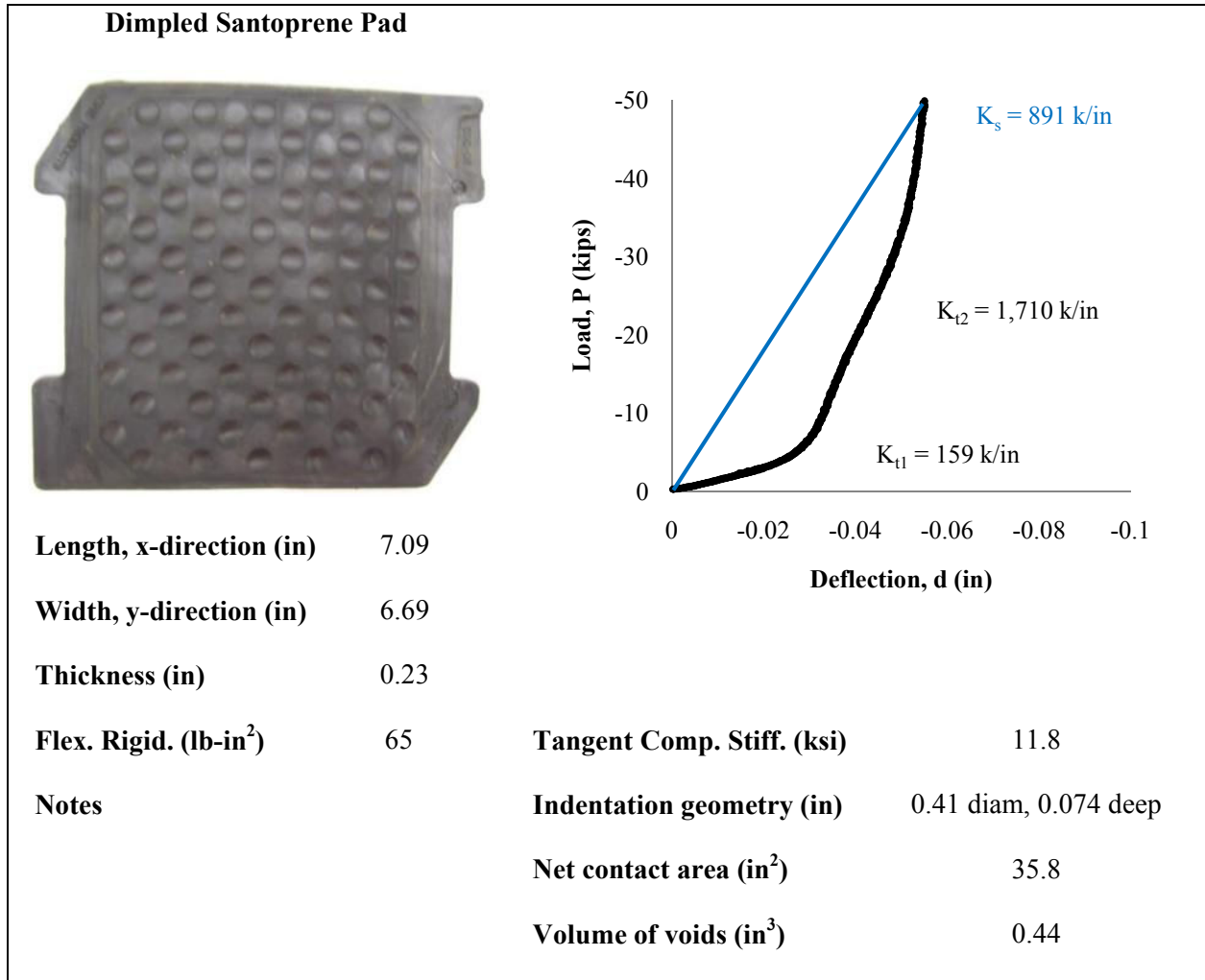
Table D.4 Characteristics of the dimpled polyurethane pad

Dimpled Polyurethane Pad

$K_s = 1,024$ k/in

$K_{t2} = 2,800$ k/in

$K_{t1} = 382$ k/in

Length, x-direction (in)	7.09
Width, y-direction (in)	6.69
Thickness (in)	0.24
Flex. Rigid. (lb-in^2)	94
Notes	

Tangent Comp. Stiff. (ksi)	20.2
Indentation geometry (in)	0.41 diam, 0.074 deep
Net contact area (in^2)	35.8
Volume of voids (in^3)	0.44
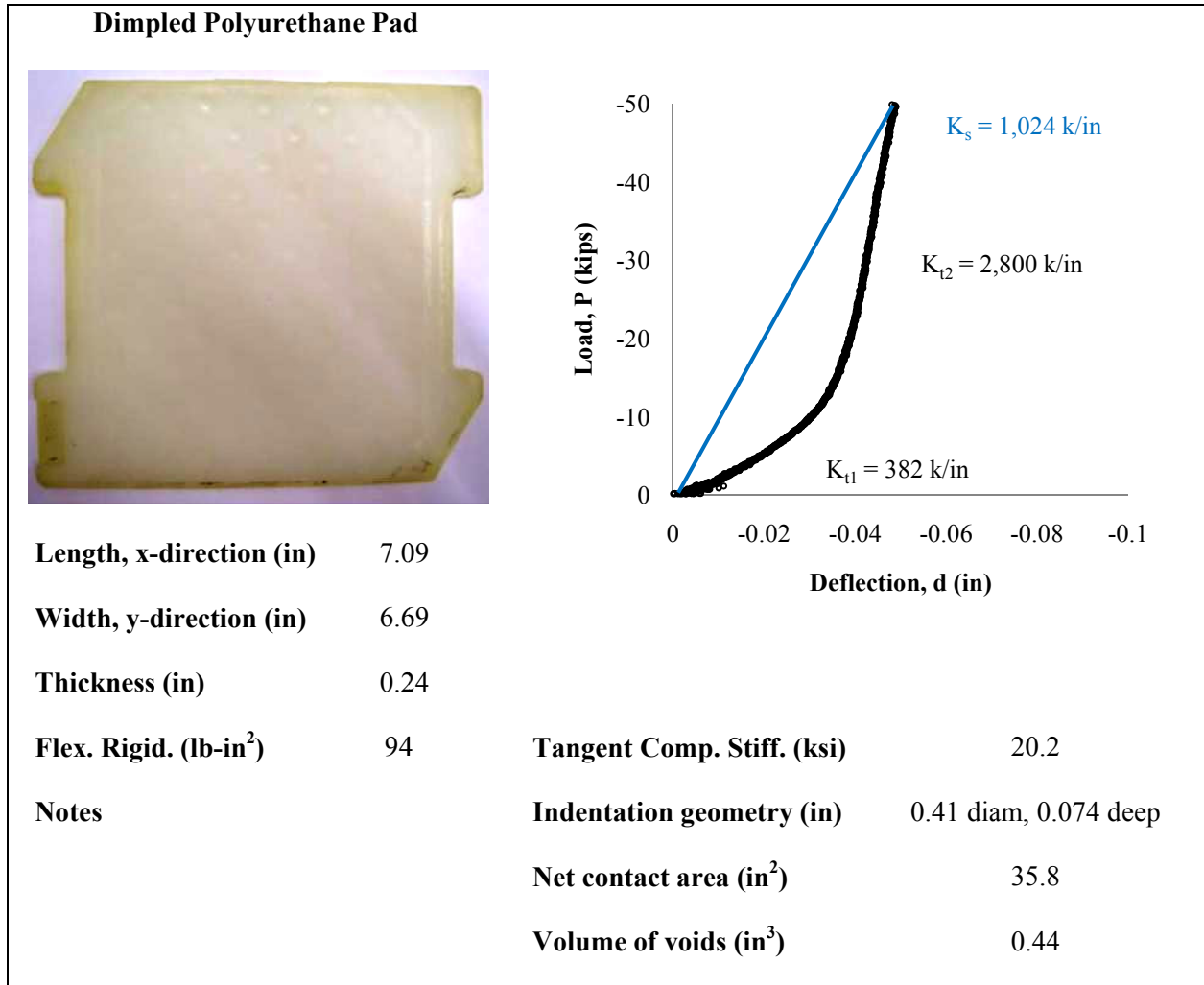
Table D.5 Characteristics of the flat EVA pad

Flat Ethyl-Vinyl Acetate Pad

$K_s = 4,757$ k/in

$K_{t2} = 14,957$ k/in

Length, x-direction (in)	7.48		
Width, y-direction (in)	6.30		
Thickness (in)	0.20		
Flex. Rigid. (lb-in^2)	78	Tangent Comp. Stiff. (ksi)	64.3
Notes		Indentation geometry (in)	--
		Net contact area (in^2)	47.1
		Volume of voids (in^3)	0

Table D.6 Characteristics of the dimpled EVA pad
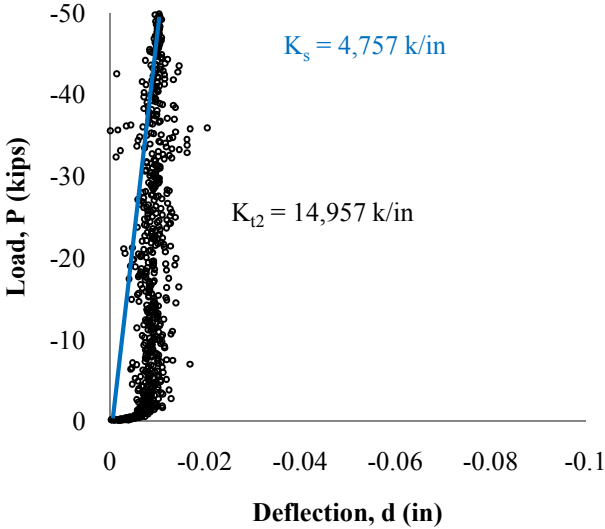
Dimpled Ethyl-Vinyl Acetate Pad
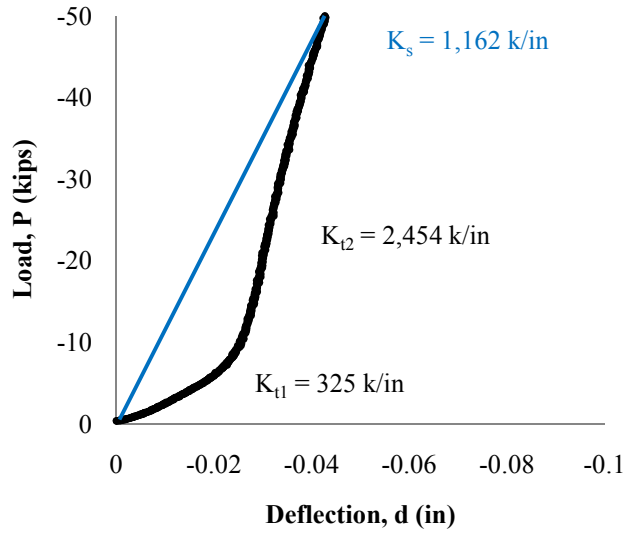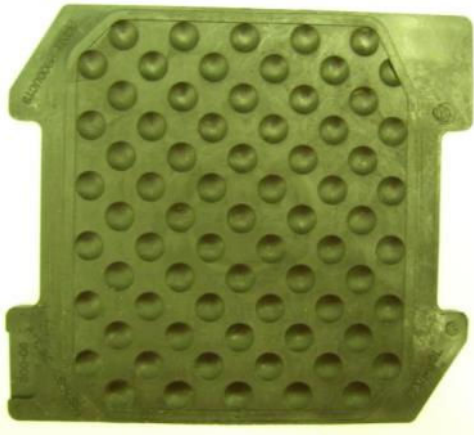
Length, x-direction (in)	7.09
Width, y-direction (in)	6.69
Thickness (in)	0.24
Flex. Rigid. (lb-in^2)	85

$K_s = 1,162$ k/in

$K_{t2} = 2,454$ k/in

$K_{t1} = 325$ k/in

Tangent Comp. Stiff. (ksi)	17.7
Indentation geometry (in)	0.41 diam, 0.074 deep
Net contact area (in^2)	35.8
Volume of voids (in^3)	0.44

Notes

Table D.7 Characteristics of the 3-part assembly A

3-Part Assembly A

Length, x-direction (in)	6.90
Width, y-direction (in)	6.42
Thickness (in)	0.33
Flex. Rigid. (lb-in^2)	2,733

Notes	Top: poly.	
	Middle: steel	
	Bottom: foam	

Tangent Comp. Stiff. (ksi)	24.0
Indentation geometry (in)	--
Net contact area (in^2)	44.3
Volume of voids (in^3)	--

$K_s = 526$ k/in

$K_{t2} = 3{,}174$ k/in

$K_{t1} = 33$ k/in
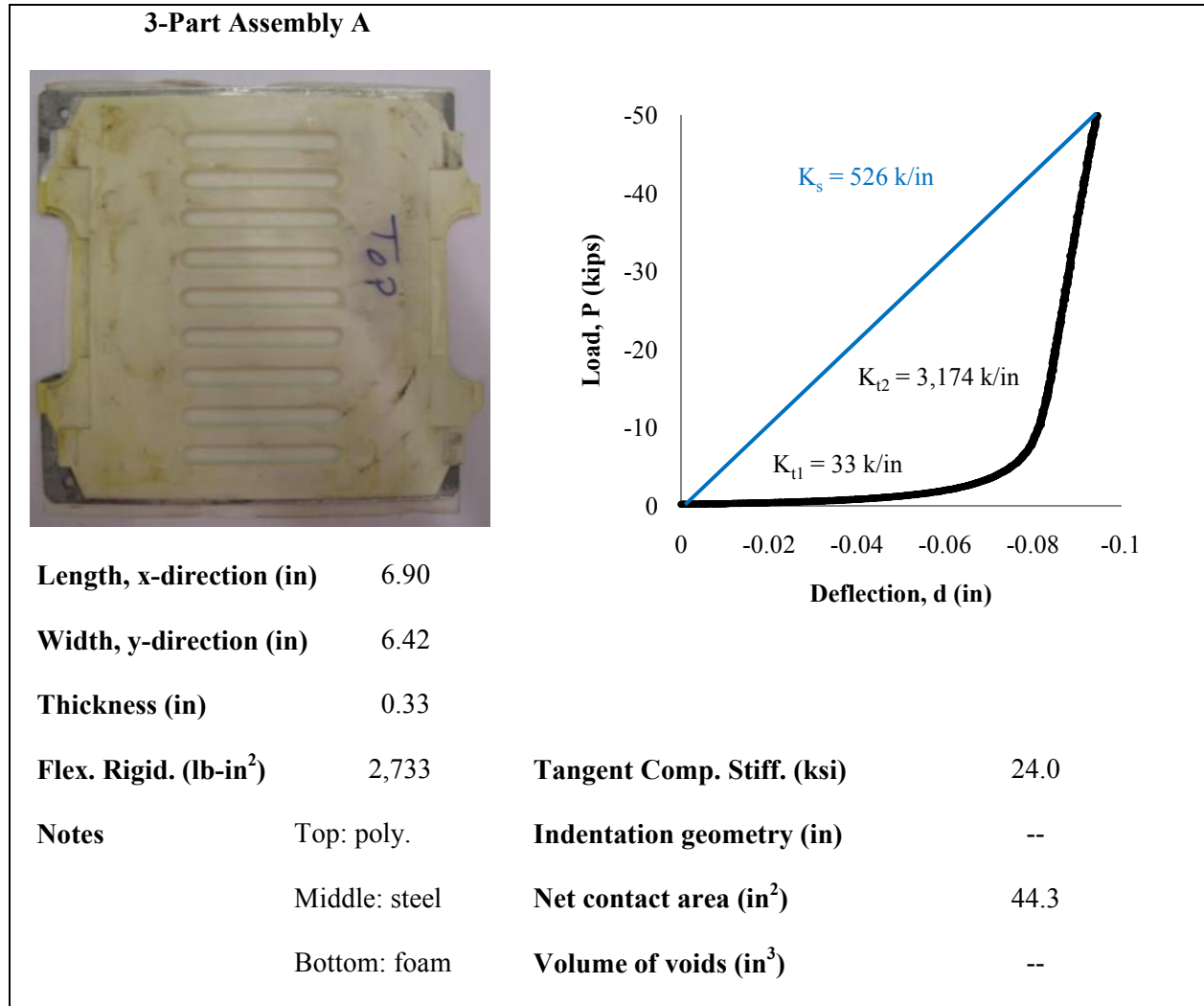
Table D.8 Characteristics of the 2-part assembly B
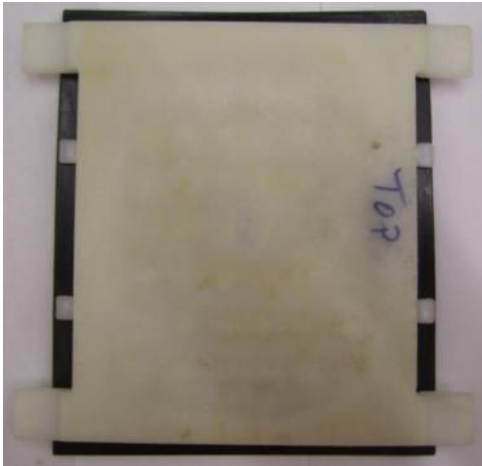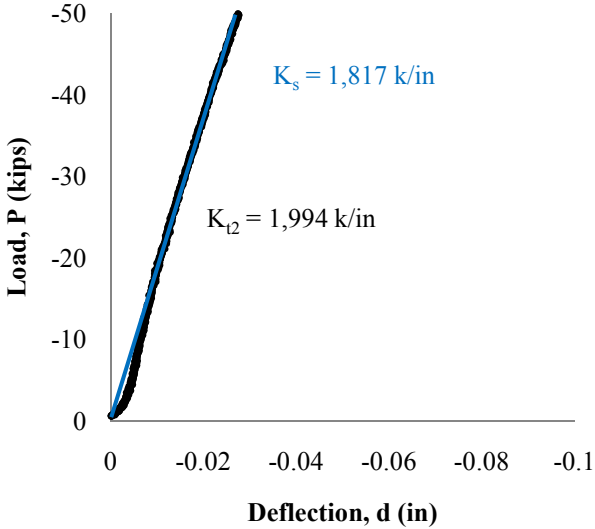
2-Part Assembly B

Length, x-direction (in)	6.89		
Width, y-direction (in)	5.51		
Thickness (in)	0.35		
Flex. Rigid. (lb-in^2)	114	**Tangent Comp. Stiff. (ksi)**	18.6
Notes	Top: poly.	**Indentation geometry (in)**	--
	Bottom: plastic	**Net contact area (in^2)**	38.0
		Volume of voids (in^3)	--

The plot shows Load, P (kips) versus Deflection, d (in) with annotations:
$K_s = 1{,}817$ k/in
$K_{t2} = 1{,}994$ k/in

Table D.9 Characteristics of the 2-part assembly C

2-Part Assembly C

Length, x-direction (in)	6.13		
Width, y-direction (in)	5.63		
Thickness (in)	0.31		
Flex. Rigid. (lb-in^2)	304	**Tangent Comp. Stiff. (ksi)**	31.3
Notes	Top: material NA	**Indentation geometry (in)**	--
	("studded pad")	**Net contact area (in^2)**	34.5
	Bottom: plastic	**Volume of voids (in^3)**	--

From the graph: $K_s = 3{,}125$ k/in, $K_{t2} = 3{,}420$ k/in
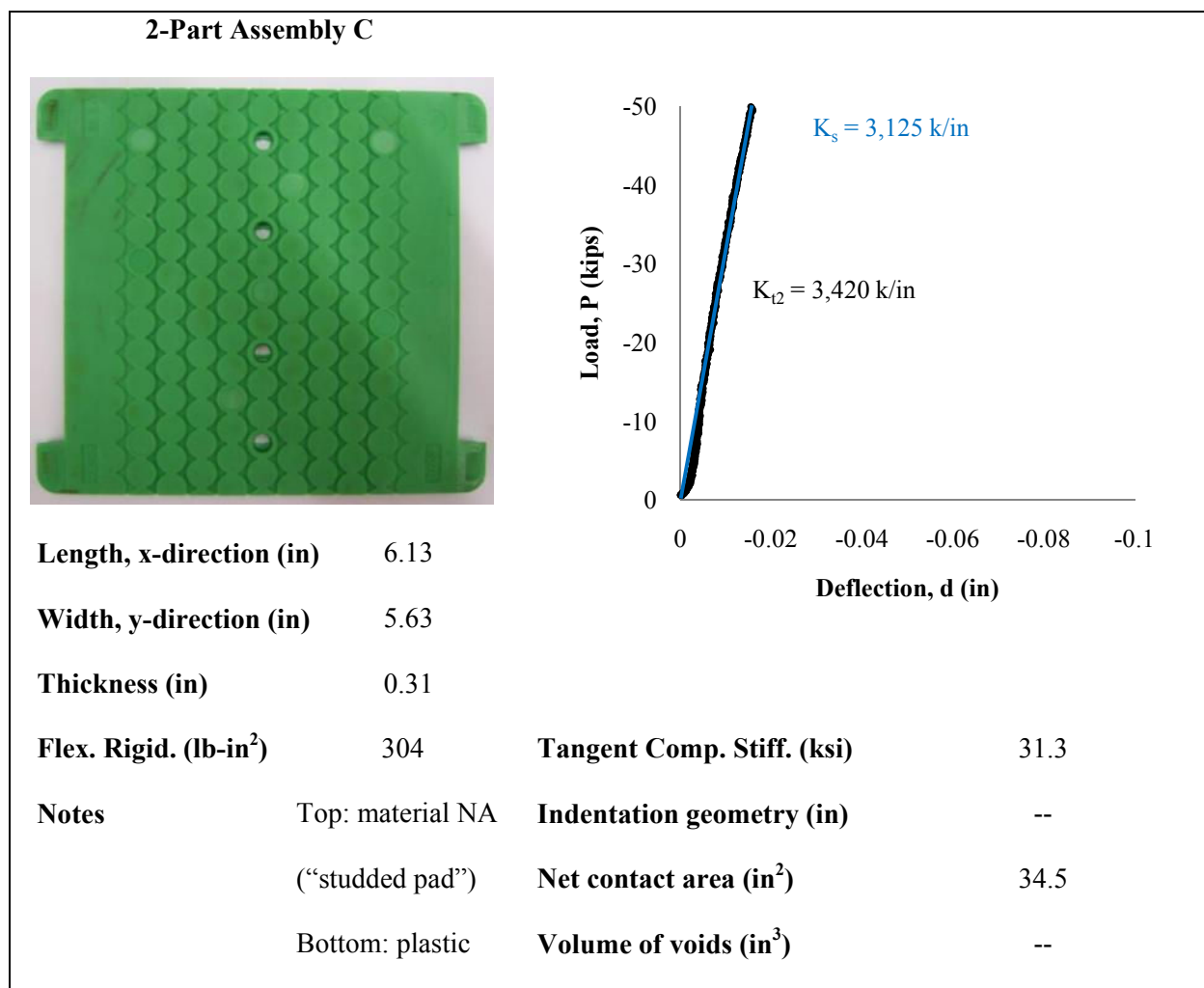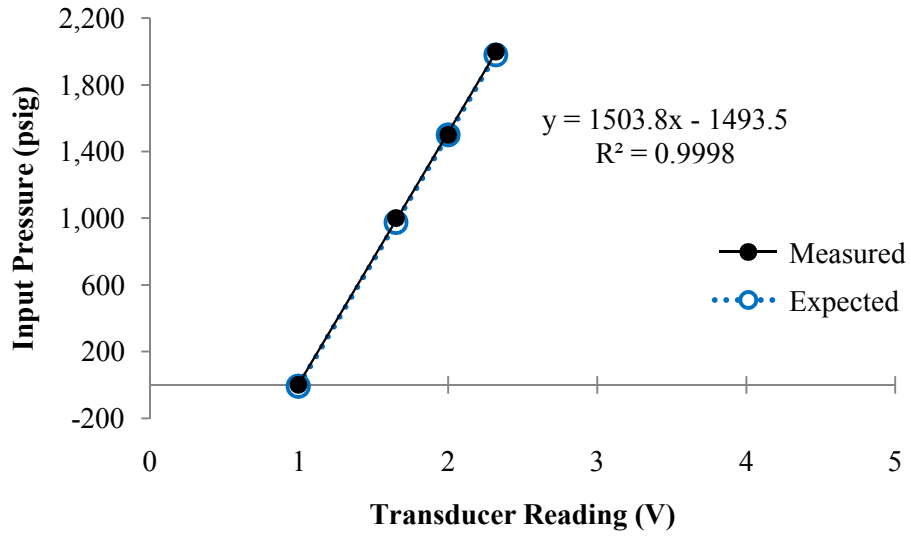
Figure D.1 Comparison of calibration measurements and expected transducer readings, 6000-psig transducer
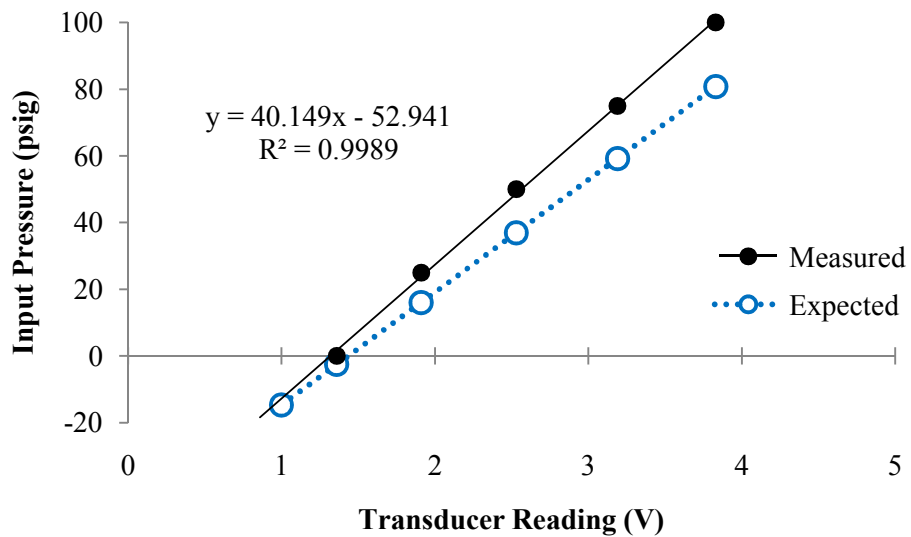
Figure D.2 Comparison of calibration measurements and expected transducer readings, 135-psia transducer
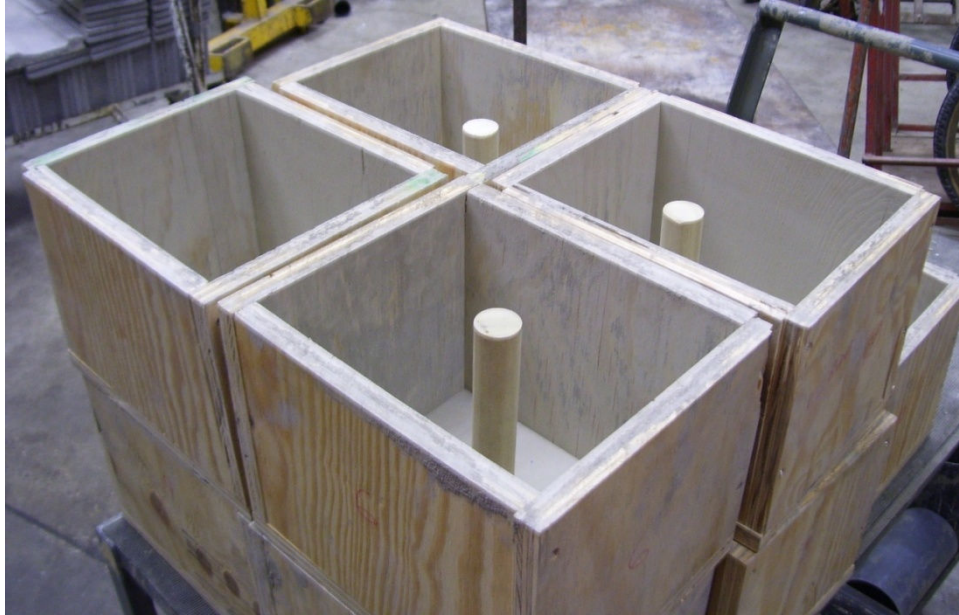
Figure D.3 Plywood forms used to cast the rail seat blocks

Figure D.4 Bottoms of the rail seat blocks during the first 24 hours of curing

Figure D.5 Wooden dowel and cylindrical piece removed during demolding
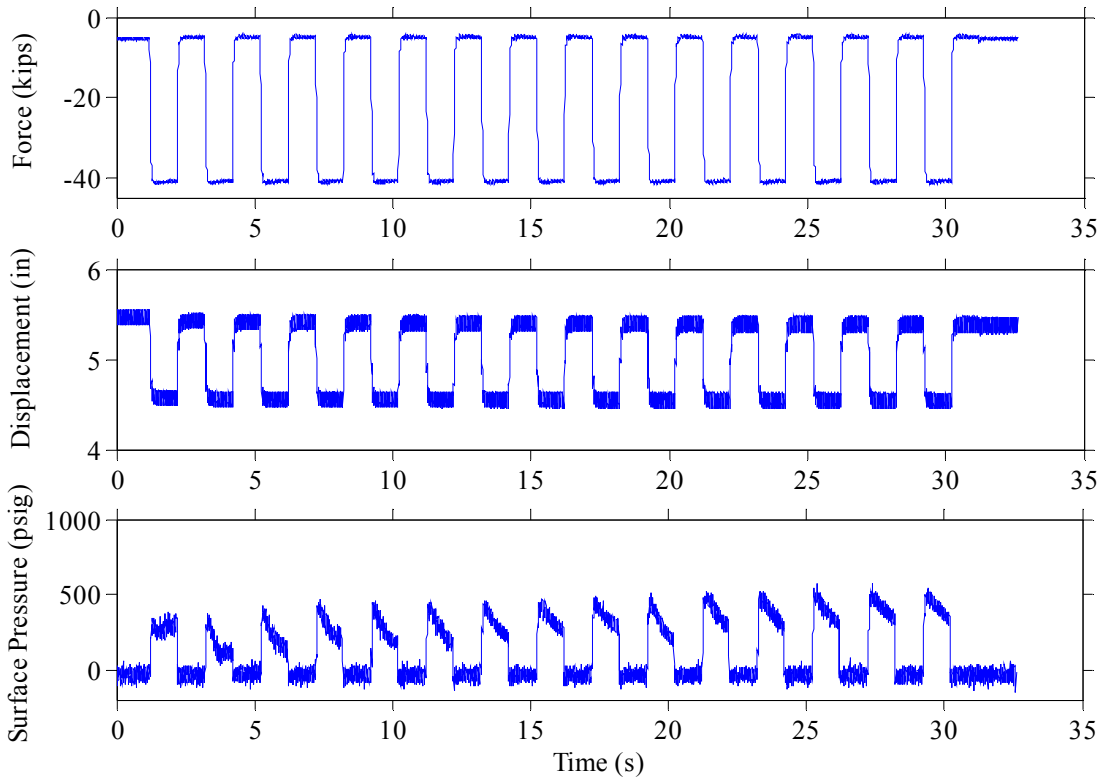
Figure E.1 Sample load test on dimpled EVA under square wave loading
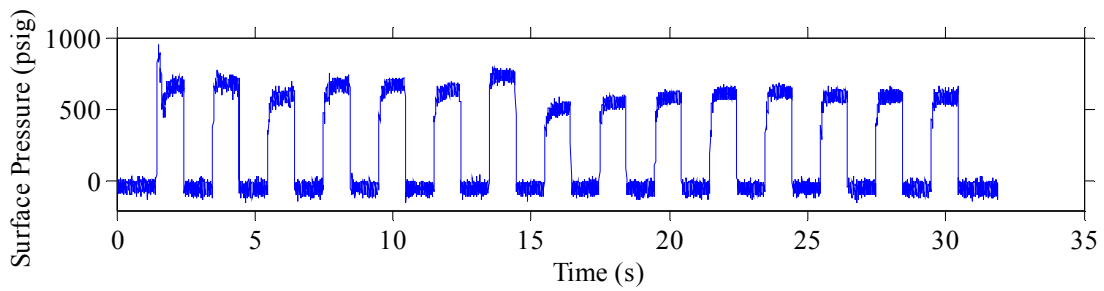
Figure E.2 Sample load test on dimpled santoprene under square wave loading
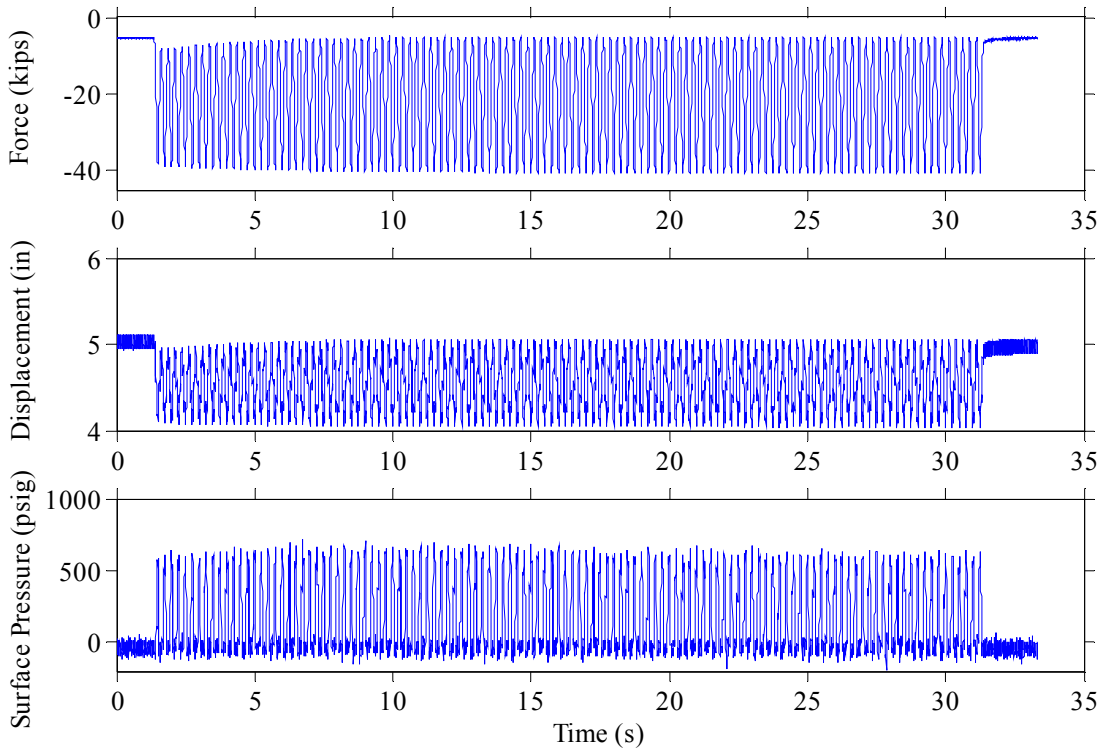
Figure E.3 Sample load test on flat EVA under 4-Hz sine wave loading
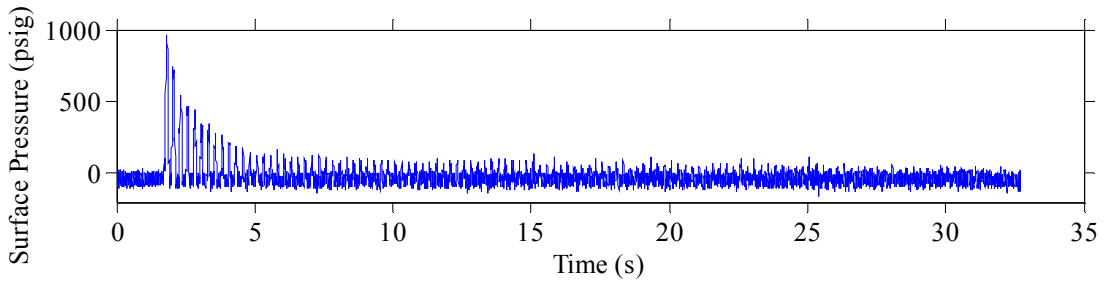
Figure E.4 Sample load test on dimpled santoprene under 4-Hz sine wave loading
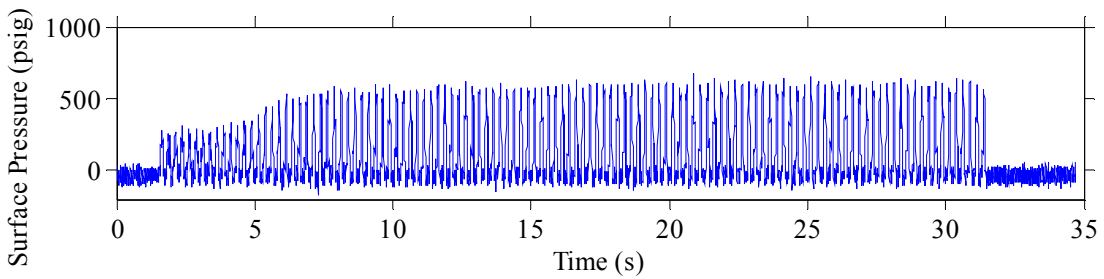
Figure E.5 Sample load test on dimpled EVA under 4-Hz sine wave loading
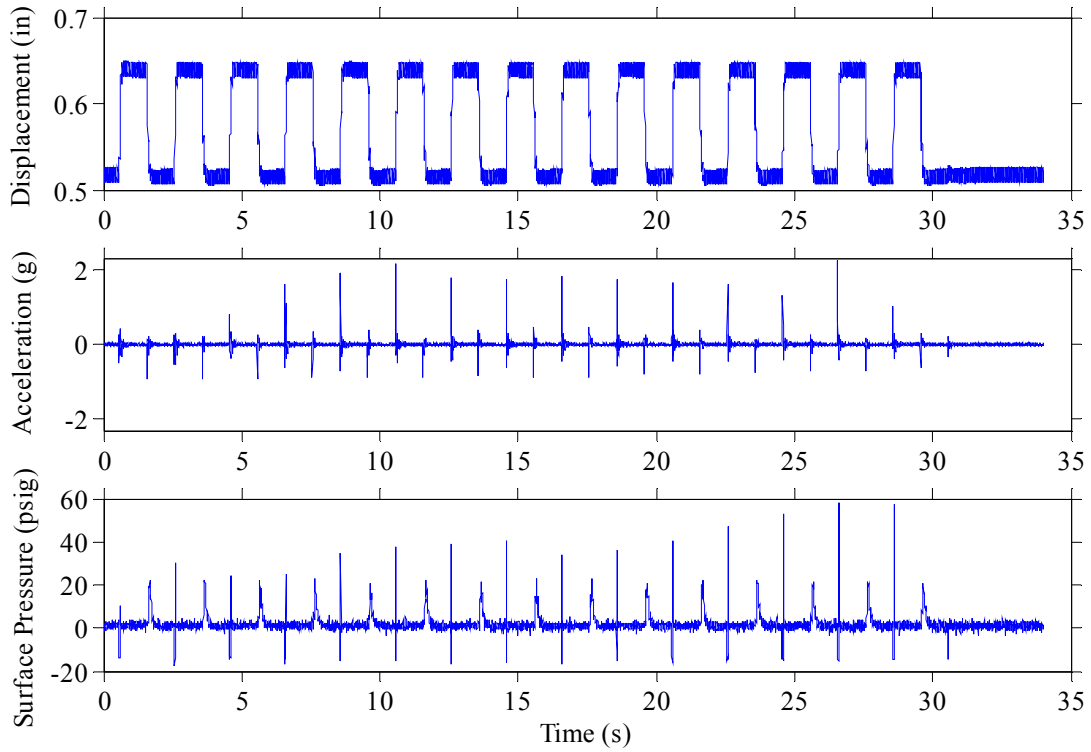
Figure E.6 Sample uplift test on dimpled polyurethane under square wave motion
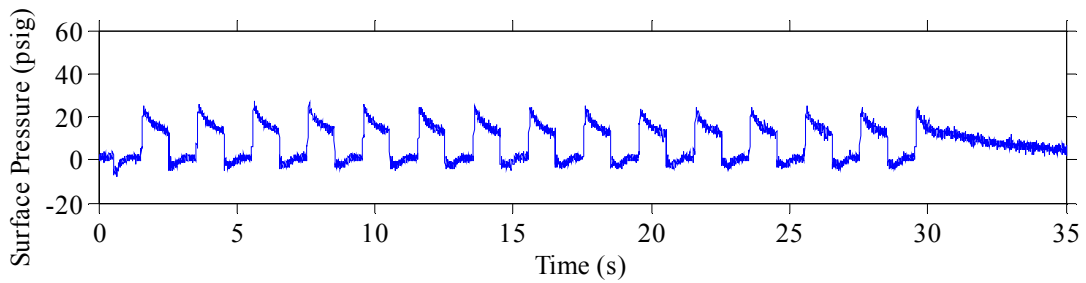
Figure E.7 Sample uplift test on 3-part assembly A under square wave motion
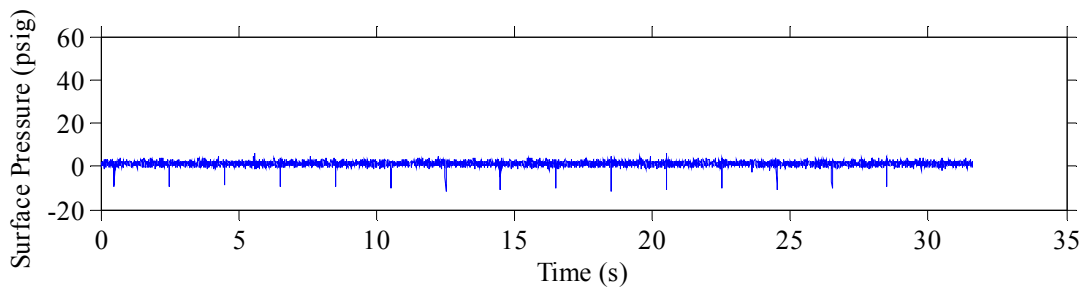
Figure E.8 Sample uplift test on studded pad under square wave motion
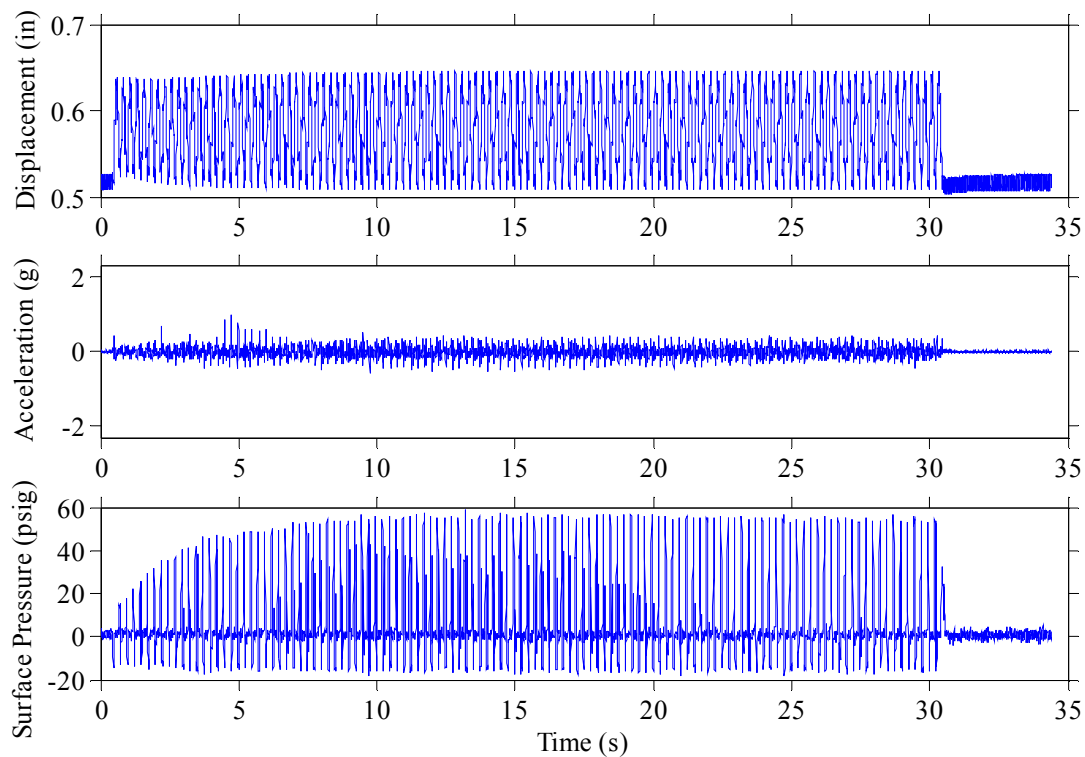
Figure E.9 Sample uplift test on dimpled polyurethane under 4-Hz sine wave motion

As reference, the p-values for various analysis of variance (ANOVA) tests performed on the experimental results are included here. Single factor ANOVA evaluates whether the mean of different samples is the same. The case where the samples all have the same mean is often termed the null hypothesis. The larger the p-value, the more statistical confidence we have in the null hypothesis, whereas a very small p-value suggests we should reject the null hypothesis. It is common to use 0.05 as a minimum cutoff (or α) for the p-value – in other words, if the p-value is less than 0.05, then we should reject the null hypothesis. This is a very useful procedure to statistically consider the influence of different experimental factors on the measured surface water pressure. In the following tables, cases where the null hypothesis should be rejected – meaning that the set of samples are statistically different – have been italicized.

Table E.1 ANOVA results for waveform of loading, load tests

Pad Group	Waveform	Count	Average	Variance	P-value
Flexible	Square	22	811.0825	58,892.89	0.572646
	4 Hz Sine	13	727.5486	16,315.77	
	2 Hz Sine	18	745.4073	46,228.85	
	200 k/s Ramp	12	797.9356	18,153.11	
Semi-Rigid	Square	14	540.2201	9,558.209	0.8756
	4 Hz Sine	10	563.8731	3,235.961	
	2 Hz Sine	10	557.282	3,596.911	
	200 k/s Ramp	6	556.3508	1,820.804	
Assemblies	Square	10	202.1027	7,901.151	0.221981
	4 Hz Sine	7	291.2946	3,8587.35	

Table E.2 ANOVA results for water level, load tests

Pad Group	Water Level	Count	Average	Variance	P-value
Flexible	Thin Film	5	695.4348	80,052.89	0.091875
	3-in Head	8	694.4046	43,348.82	
	6-in Head	48	820.2707	26,663.82	
Semi-Rigid	Thin Film	4	612.351	942.4752	0.163247
	3-in Head	4	522.2858	2,983.307	
	6-in Head	34	551.2929	5,207.731	

Table E.3 ANOVA results for indentation alignment, load tests

Pad Geometry	Indent. Align.	Count	Average	Variance	P-value
Grooved	Aligned	14	837.1126	22,055.01	0.176713
	Half-aligned	8	825.6684	5,310.035	
	Misaligned	8	943.9431	29,792.38	
Dimpled	*Aligned*	*16*	*595.9857*	*2,961.793*	*0.000236*
	Half-aligned	*8*	*574.2416*	*152.2961*	
	Misaligned	*8*	*513.8169*	*140.5572*	

Table E.4 ANOVA results for grouping tie pads by suction generated, uplift tests

Pad Group	Tie Pad	Count	Average	Variance	P-value
High-Suction Pads	Flat Poly.	19	-15.46	1.132093	1.02E-30
	Dimp. Santo.	31	-14.8839	0.380318	
	Grooved. Poly.	30	-13.1902	0.329394	
	Flat EVA	32	-14.5363	0.586363	
	Dimp. Poly.	31	-15.8503	0.822709	
	2-Part C	30	-13.4381	1.628177	
	2-Part B	32	-15.1662	0.629605	
Low-Suction Pads	3-Part A	30	-5.01248	1.022393	0.002073
	Studded	30	-5.95919	1.563314	

Table E.5 ANOVA results for water level, uplift tests

Pad	Water Level	Count	Average	Variance	P-value
Dimpled Poly.	2-in Head	29	-14.1669	0.338303	4.01E-11
	4-in Head	32	-15.209	0.642508	
	6-in Head	31	-15.7282	0.783085	

Table E.6 ANOVA results for waveform of motion, uplift tests

Pad	Waveform	Count	Average	Variance	P-value
Dimpled Poly. (all data)	2 Hz Sine	118	-15.007	0.573002	9.17E-07
	4 Hz Sine	239	-15.4901	0.906885	
	Square	31	-15.7282	0.783085	
Dimpled Poly. (same sample size)	2 Hz Sine	31	-15.1772	0.583638	0.002946
	4 Hz Sine	31	-14.9333	1.111694	
	Square	31	-15.7282	0.783085	

Table E.7 ANOVA results for pads glued to loading plate or in free contact, uplift tests

Pad	Glued	Count	Average	Variance	P-value
Flat Poly.	*Yes*	*32*	*-14.0837*	*0.780368*	*8.22E-6*
	No	*19*	*-15.46*	*1.132093*	
Dimp. Santo.	*Yes*	*30*	*-15.7253*	*0.524653*	*8.11E-6*
	No	*31*	*-14.8839*	*0.380318*	
Grooved Poly.	Yes	29	-13.2627	1.103724	0.74213
	No	30	-13.1902	0.329394	
Flat EVA	*Yes*	*32*	*-15.9963*	*0.619425*	*2.68E-10*
	No	*32*	*-14.5363*	*0.586363*	
Dimp. Poly.	Yes	30	-15.5668	0.546454	0.186781
	No	31	-15.8503	0.822709	
Studded	*Yes*	*29*	*-9.52912*	*1.17641*	*8.8E-17*
	No	*30*	*-5.95919*	*1.563314*	

Table E.8 ANOVA results for varied uplift, uplift tests

Pad	Uplift (in)	Count	Average	Variance	P-value
Dimp. Poly.	0.03	32	-15.3568	0.962562	0.246549
	0.06	30	-15.5668	0.546454	
	0.09	31	-15.7282	0.783085	
Flat Poly.	*0.03*	*31*	*-13.1413*	*1.097664*	*3.33E-7*
	0.06	*32*	*-14.0837*	*0.780368*	
	0.09	*32*	*-14.4283*	*0.503356*	
Studded	*0.03*	*33*	*-5.61849*	*2.787864*	*1.22E-30*
	0.06	*31*	*-9.54382*	*1.13205*	
	0.09	*27*	*-11.6995*	*1.136667*	
Dimp. Santo.	*0.03*	*32*	*-14.7231*	*3.231442*	*0.003734*
	0.06	*30*	*-15.7253*	*0.524653*	
	0.09	*30*	*-15.6591*	*1.086372*	
Flat EVA	0.03	32	-15.5364	1.535975	0.187199
	0.06	32	-15.9963	0.619425	
	0.09	31	-15.7001	0.89518	
Grooved Poly.	*0.03*	*30*	*-13.7959*	*0.931328*	*0.000141*
	0.06	*29*	*-13.2627*	*1.103724*	
	0.09	*30*	*-14.3938*	*0.849093*	
2-Part B	*0.03*	*32*	*-15.1325*	*0.511126*	*0.030331*
	0.06	*32*	*-15.1662*	*0.629605*	
	0.09	*32*	*-15.5433*	*0.235091*	
3-Part A	0.03	31	-4.81514	0.589566	0.471017
	0.06	30	-5.01248	1.022393	
	0.09	32	-5.15394	1.953594	